TAMPEREEN TEKNILLINEN YLIOPISTO
TAMPERE UNIVERSITY OF TECHNOLOGY

Arto Aho

Dilute Nitride Multijunction Solar Cells Grown by Molecular Beam Epitaxy

Julkaisu 1343 • Publication 1343

Tampere 2015

Tampereen teknillinen yliopisto. Julkaisu 1343
Tampere University of Technology. Publication 1343

Arto Aho

Dilute Nitride Multijunction Solar Cells Grown by Molecular Beam Epitaxy

Thesis for the degree of Doctor of Science in Technology to be presented with due permission for public examination and criticism in Tietotalo Building, Auditorium TB104, at Tampere University of Technology, on the 14th of November 2015, at 12 noon.

Tampereen teknillinen yliopisto - Tampere University of Technology
Tampere 2015

ISBN 978-952-15-3613-7 (printed)
ISBN 978-952-15-3661-8 (PDF)
ISSN 1459-2045

Abstract

Solar cells generate green energy directly from sunlight. The energy conversion efficiency of solar cells depends strongly on materials used as absorbers and the cell architecture. Currently, the best solar cells convert sunlight energy to electricity with an efficiency of up to 46%. This thesis focuses on the development of dilute-nitride materials and related solar cells, which are one of the most promising approaches for achieving even higher efficiencies. Applications for these cells include concentrated photovoltaic and space power systems. In particular, the thesis focuses on developing solar cell materials based on GaInNAsSb, which can provide efficient light absorption and energy conversion for a photon energy range of 0.8 eV- 1eV, typically challenging for conventional III-V semiconductors. The GaInNAsSb semiconductor materials were synthesized by molecular beam epitaxy.

The experimental work of this thesis explored the dependence of the fabrication parameters on the GaInNAsSb material and solar cell properties. It was observed that for many of the growth parameters even a slight change of the value can have a significant effect on the solar cell performance. A N incorporation model was developed to help the iteration process for growth parameter tuning. For optimized growth conditions, nearly ideal current generation for GaInNAsSb based material was achieved. Based on external quantum efficiency measurements it was possible to collect up to ~90% of the photons in the spectral range of the GaInNAsSb junction. In addition, an excellent fill factor of 0.7 and voltages in the range of 0.5 V for a 1 eV GaInNAsSb junction were measured.

Simulation based on a state-of-the-art GaInP/GaAs double junction cell, a commercial GaInP/GaAs/Ge triple junction cell and GaInNAsSb single junction cells studied in this thesis, revealed that a GaInP/GaAs/GaInNAsSb/Ge cell at the one sun concentration can have 1.7 percentage points higher efficiency than GaInP/GaAs/GaInNAsSb cell. In addition, the estimated efficiency of a four junction cell at 300 suns would be 3.6 percentage points higher than for a GaInP/GaAs/GaInNAsSb cell. The optimized single junction GaInNAsSb cell was experimentally tested into a GaInP/GaAs/GaInNAsSb cell in this work. The one sun efficiency of the cell under AM1.5G spectral conditions was 31% and the efficiency of the cell at 70 suns concentration was 37-39%. The one sun result is 91% of the projected efficiency. The results under concentrated conditions are expected to be improved by optimizing of the cell top grid

design, layer structure and interfaces. As future concepts are concerned, a nanopatterned moth eye antireflection coating was fabricated on top of the GaInP/GaAs/GaInNAs cell, which was then compared to a cell that had a traditional two layer TiO_2/SiO_2 coating. The moth eye nanostructure had a low average reflection of 2% in the spectral range of 400-1700 nm, being less than half of the reflectance of the TiO_2/SiO_2 coating. For future work, the absorption loss for the nanostructure coating at wavelengths below 500 nm needs to be reduced.

Acknowledgements

The research has been carried out at the Optoelectronics Research Centre (ORC) of the Tampere University of Technology. I acknowledge ORC for giving me an opportunity and support to study the material physics of III-V semiconductors. I also acknowledge the financial support received from Finnish Founding Agency for Technology and Innovation (TEKES), European Space Agency (ESA), National Graduate School in Material Physics, Graduate School in Electronics, Telecommunications and Automation (GETA), Doctoral training network in Electronics, Telecommunications and Automation (DELTA), Ulla Tuominen Foundation, Finnish Foundation for Technology Promotion, and Wärtsilä Foundation.

For the opportunity to work in a team of solar cell and dilute nitride specialists I would like to thank Professor Mircea Guina, who built a team of professionals conducting frontier research in photovoltaics. I also acknowledge Professor Mircea Guina for supervising my doctoral studies. For hiring me to work at ORC and supervising my master studies, I would like to thank Professor Emeritus Markus Pessa. I would like to thank director Dr. Pekka Savolainen for managing the ORC during the years of my PhD studies. For the excellent support with many administrative tasks, I would like to thank Mrs. Anne Viherkoski and Mrs. Eija Heliniemi.

Dr. Antti Tukiainen has been my MBE mentor and my scientific advisor since the beginning of my MBE career. In particular, the learning years at 8-port MBE system gave me smooth start to MBE basics as we were studying the synthesis of InAs quantum dots and were developing AlGaInP epitaxy. I also own great gratitude for Dr. Antti Tukiainen for the deep analysis of solar cell materials, in particular the modelling and designing of the dilute nitride cell structures, and for developing realistic simulation models for single and multijunction cells.

Ville-Markus Korpijärvi gave me the first introductory and guiding for dilute nitride epitaxy, and shared the response for the GEN20 system ramp ups, maintenances and crystal growth development discussions with me. Together we made it possible to have almost production base development speed for lasers and solar cells. I also greatly appreciate the analytic discussions that we have had for endless hours on the facts how particular dilute nitride and also all other layers should be grown for the best device performance. I also want to acknowledge the younger GEN20 MBE team mates in particular Pekka Malinen was the guy who just gets the

jobs done. The newest MBE teammate Riku Isoaho, passionate young scientist, has shown that by dedicating to the team-effort well, extremely good results can be obtained. For Pekka and Riku I am grateful for the numerous wafer analyses, for which I certainly would have not have time to do it by my own for every sample. I also greatly acknowledge Janne Puustinen for the dilute nitride MBE growth on V80H reactor and analysis of the samples for the plasma paper, which made the model for the N incorporation even more convincing. I also acknowledge Janne for analytic discussions on the MBE epitaxy dynamics itself.

Solar cell wafers would be nothing without post processing and packing them to ready solar cells. To his end, my greatest gratitude I own to Ville Polojärvi who has had the main response for the processing and defect analyses of the dilute nitride based solar cells. Owing to Ville's effort, we were able to do numerous different post growth treatments for the same wafer, which made it possible to have faster iteration processes for the dilute nitride growth and post process optimization. Also at the beginning of the solar cell research, Joel Salmi showed to be a dedicate researcher with the analysis of different process parameters on the cell performances and definitely still part of our success is due to his pertinent analysis. For the solar cell processing, I would also like to acknowledge the work of Wenxin Zhang, Timo Aho and Marianna Raappana. In particular for the CPV-cell chip development and for the highest efficiencies, I would like to mention the efforts of Timo and Marianna and their enrichment of the team as hard core chemists.

For the new solar cell processing concepts, I want to acknowledge Professor Tapio Niemi and Dr. Juha Tommila who contributed to the research and development of moth eye based antireflection coatings. In particular I want to thank Dr. Juha Tommila for making made it possible to have extremely fast and analytic process development with very little need for iterative steps.

For the material characteristics analysis and for mentoring I would like to cordially mention Professor Pekka Laukkanen from the University of Turku for the RHEED, XPS and LEED analysis of the dilute nitride materials. In addition, for the time resolved photoluminescence analysis I would like to thank Alexander Gubanov and Professor Nikolai Tkachenko. For compositional analysis with SEM-EDS, I would like to thank Dr. Mari Honkanen.

For the sub-systems needed for MBE and their continuous operation without interruptions, I thank the efforts of Ilkka Hirvonen and Bengt-Olof Holmström. I want to also mention Timo Lindqvist for the fabrication of high quality vacuum parts needed for the MBE system.

For the supporting of GEN20 team in MBE maintenance and heavy lifting jobs, the support of Miki Tavast and Riku Koskinen made my job easier. Also the other MBE group members have been lovely to work with and have shared the good and bad times of MBE with me. In addition all other ORC co-workers have made my years at ORC excellent.

For the last but not least, I would like to mention my family, friends and Jenni for the support that I have needed during the PhD research and studies.

Tampere, October 2015
Arto Aho

Table of Contents

List of Publications

The following journal and conference proceeding publications P1 to P11 are included in this thesis as appendices and referred to in the text as [P1]–[P11]. All papers have been reviewed by peer review process coordinated by the journal editor or by the conference committee.

P1 Aho, A., Polojärvi, V., Korpijärvi, V.-M., Salmi, J., Tukiainen, A., Laukkanen, P. & Guina M. Composition dependent growth dynamics in molecular beam epitaxy of GaInNAs solar cells. Solar Energy Materials and Solar Cells 124 (2014), pp. 150-158.

P2 Aho, A., Korpijärvi, V.-M., Tukiainen, A., Puustinen, J. & Guina, M. Incorporation model of N into GaInNAs alloys grown by radio-frequency plasma-assisted molecular beam epitaxy. Journal of Applied Physics 116 (2014) 21.

P3 Aho, A., Tukiainen, A., Polojärvi, V., Salmi, J. & Guina, M. High current generation in dilute nitride solar cells grown by molecular beam epitaxy. SPIE Conference Proceedings 8620 (2013) 55, pp. 1-6.

P4 Aho, A., Tukiainen, A., Korpijärvi, V.-M., Polojärvi, V., Salmi, J. & Guina, M. Comparison of GaInNAs and GaInNAsSb solar cells grown by plasma-assisted molecular beam epitaxy. AIP Conference Proceedings 1477 (2012), pp. 49-52.

P5 Aho, A., Tukiainen, A., Polojärvi, V. & Guina, M. Performance assessment of multijunction solar cells incorporating GaInNAsSb. Nanoscale Research Letters 9 (2014) 1, pp. 1-7.

P6 Aho, A., Tommila, J., Tukiainen, A., Polojärvi, V., Niemi, T. & Guina, M. Moth eye antireflection coated GaInP/GaAs/GaInNAs solar cell. AIP Conference Proceedings 1616 (2014), pp. 33-36.

P7 Aho, A., Isoaho, R., Tukiainen, A., Polojärvi, V., Aho, T., Raappana, M. & Guina M. Temperature Coefficients for GaInP/GaAs/GaInNAsSb Solar Cells, AIP Conference Proceedings 1679 (2015) 050001.

P8 Aho, A., Korpijärvi, V.-M., Isoaho, R., Malinen, P., Tukiainen, A., Honkanen, M. & Guina, M. Determination of composition and energy gaps of GaInNAsSb layers grown by MBE, (Submitted to Journal of Crystal Growth).

P9 Aho, A., Tukiainen, A., Polojärvi, V., Korpijärvi, V.-M., Gubanov, A., Salmi, J. & Guina, M. and P. Laukkanen Lattice matched dilute nitride materials for III-V high-efficiency multi-junction solar cells: growth parameter optimization in molecular beam

epitaxy, European Photovoltaic Solar Energy Conference and Exhibition EU PVSEC (2011), pp. 58-61.

P10 Aho, A., Tukiainen, A., Polojärvi, V., Salmi J., & Guina, M. MBE Growth of High Current Dilute III-V-N Single and Triple Junction Solar Cells, European Photovoltaic Solar Energy Conference (2012), pp. 290-292.

P11 Aho, A., Tukiainen, A., Polojärvi, V., & Guina, M. Dilute Nitride Space Solar Cells: Towards 4 Junctions, 10th European Space Power Conference ESPC 2014, 13-17 April, 2014, Noordwijkerhout, the Netherlands, vol. 719 (2014), pp. 1-3.

Author's Contribution

The results presented have been largely obtained by teamwork. A summary of the author's contribution to the research work and to the manuscript preparation is given in the list below. The main aspects provided by the coworkers listed in the publications include wafer processing, nanopatterning, solar cell and material characterization, and structure and result simulation.

P1: *The author planned and performed the epitaxial experiments, participated in the characterization of GaInNAs crystal and solar cell properties, analyzed the results and prepared the manuscript.*

P2: *The author shared the contribution to epitaxial design and experiments, and crystal characterization with the second and fourth author. The author developed the incorporation model by brainstorming together with the co-authors and prepared the manuscript.*

P3: *The author participated in epitaxial layer structure design and performed epitaxial experiments. The author also contributed to the solar cell characterization and analysis as team work. The author participated in the manuscript writing as team work, which was finalized by the second and the last author.*

P4: *The author participated in epitaxial layer structure design and performed epitaxial experiments. The author also contributed to the solar cell characterization and analysis as team work. The author participated in the manuscript writing as team work, which was finalized by the second author.*

P5: *The author participated in epitaxial layer structure design and performed epitaxial experiments. The author also calculated the efficiency projections for terrestrial applications of triple and four junction cells, performed solar cell characterization and prepared the manuscript.*

P6: *The author participated in epitaxial layer structure design and performed epitaxial experiments. The author also made solar cell characterization, in particular the quantum efficiency analysis for each sub-cell. The author also prepared the manuscript.*

P7: *The author participated in epitaxial layer structure design and performed the epitaxy experiments. The author also made temperature dependent quantum efficiency analysis and prepared the manuscript.*

P8: *The author designed the experiments, epitaxial structures and performed epitaxial experiments. The characterization and analysis work was coordinated by the author and*

performed as team work with the co-authors. The composition analysis was performed and modified band anti-crossing model was developed by the author. The author also prepared the manuscript.

P9: *The author participated in epitaxial layer structure design and performed the epitaxy work. The author also participated in the solar cell characterization and analysis. The author drafted first version of the paper and participated in the paper writing, which was finalized by the second author.*

P10: *The author participated in epitaxial layer structure design, performed the epitaxy experiments and analyzed the results. The author also participated in the solar cell characterization and prepared the manuscript.*

P11: *The author participated in epitaxial layer structure design, performed the epitaxy experiments and analyzed the results. The solar cell characterization was performed as team work. In addition, the author calculated the efficiency projections for triple and four junction cells for space applications, and prepared the manuscript.*

List of Abbreviations and Symbols

AFM	Atomic force microscopy
AlGaAs	Aluminum gallium arsenide
AlGaInP	Aluminum gallium indium phosphide
AlInP	Aluminum indium phosphide
ARC	Anti reflection coating
As	Arsenic
A_{sc}	Area of solar cell
B, *D*	Fitting factors for N incorporation rate calculation taking into account system and plasma geometrics
Be	Beryllium
BEP	Beam equivalent pressure
BOL	Beginning of life
C	Light concentration level
CdTe	Cadmium telluride
CO_2	Carbon dioxide
CPV	Concentrated photovoltaics
CV	Capacitance-voltage
DLTS	Deep level transient spectroscopy
DNI	Direct normal irradiance
E_+	Higher energy band generated by N incorporation
E_-	Lower energy band generated by N incorporation
E_{ad}	Effective activation energy for N_2 molecule dissociation processes
E_g	Band gap
E_{gi}	Band gap of the i^{th} sub cell sub-cell
E_M	Host material band gap in band anti-crossing model
E_N	N induced energy level

EOL	End of life
EQE	External quantum efficiency
EQE_{avi}	Average EQE the i^{th} sub cell sub-cell
F	N_2 molecular flow
FF	Fill factor
Ga	Gallium
GaAs	Gallium arsenide
GaInAs	Gallium indium arsenide
GaInNAs	Gallium indium nitride arsenide
GaInNAsSb	Gallium indium nitride arsenide antimonide
GaInP	Gallium indium phosphide
GaNPAs	Gallium nitride phosphide arsenide
Ge	Germanium
GR_{III}	Growth rate determined by group III atoms
HCPV	High concentration concentrated photovoltaics
I	Current of two terminal cell
i	Sub-cell index
I_0	Reverse saturation current of solar cell
I_{0i}	Reverse saturation current of the i^{th} sub cell sub-cell
$I_{1\text{-sun}}$	Light intensity corresponding to one sun illumination
I_i	Current of the i^{th} sub cell sub-cell
I_{Li}	Photocurrent generated by the i^{th} sub cell sub-cell
I_{mp}	Current at maximum power point
In	Indium
InP	Indium phosphide
IQE	Internal quantum efficiency
I_{sc}	Short circuit current
$I_{sc\text{-}1\text{-}sun}$	Short circuit current at one sun concentration
I_{sun}	Sunlight intensity at solar cell
IV	Current-voltage
J_{sc}	Short circuit current density
k_b	Boltzmann constant
KPFM	Kelvin probe force microscopy

LCPV	Low concentration concentrated photovoltaics
LIV	Light biased current-voltage measurements
MBE	Molecular beam epitaxy
MJSC	Multijunction solar cell
MOCVD	Metalorganic chemical vapor deposition
N	Nitrogen
n_i	Ideality factor of the i^{th} sub cell
NREL	National Renewable research laboratory
ORC	Optoelectronics Research Centre
PL	Photoluminescence
P_{opt}	Optical radiation power
P_{RF}	Plasma primary power
q	Charge of electron
RF	Radio frequency
RHEED	Reflection high energy electron diffraction
R_s	Total series resistance of multijunction cell
R_{si}	Series resistance of the i^{th} sub cell
R_{sp}	Plasma system primary resistance
RTA	Rapid thermal annealing
Sb	Antimony
SC	Solar cell
Si	Silicon
T	Solar cell temperature
UHV	Ultra-high vacuum
V	Interaction potential
V_i	Voltage of i^{th} sub cell sub-cell
V_{mp}	Voltage at maximum power point
V_{oc}	Open circuit voltage
V_{sc}	Voltage of two terminal solar cell
W_{oc}	Band gap voltage offset
x	In composition in $Ga_{1-x}In_xN_zAs_{1-y-z}Sb_y$
XRD	X-ray diffraction
y	Sb composition in $Ga_{1-x}In_xN_zAs_{1-y-z}Sb_y$

z	N composition in $Ga_{1-x}In_xN_zAs_{1-y-z}Sb_y$
z_1	N composition in lattice matched GaInNAs
z_2	N composition in lattice matched GaNAsSb
3J	Triple junction cell
4J	Four junction cell

Symbols, Greek Alphabet

f	Photon flux
h	Efficiency

Chapter 1

1 Introduction

Since the introduction of first pn-junction solar cell (SC) [1], patented by Russell Ohl in 1946 and developed in 1954 by Bell Laboratories, the energy conversion efficiency of solar cells has grown steadily [2]. Starting from the 1980s, the efficiency has been improved by an average of 1 percentage points per year [2] and currently the best solar cell converts 46% of the energy of sunlight to electricity [3] (see Figure 1.1). During the past 20 years, steady growth has been enabled by the development of solar cells based on thin film III-V semiconductors and on their band gap tailoring option for multijunction solar cells (MJSC) [4]. III-V solar cells are constructed from crystalline compounds that are made of group III and group V elements of the periodic table. During the last five years, new materials such as Perovskites have shown promise, reaching a maximum efficiency of about 20% [3]. We should also not forgot so called thin film technologies including CdTe ~21%, dye sensitive cells ~12% and ~11% organic solar cells which make the spectrum of photovoltaic technologies even wider [3]. Emerging technologies, such as intermediate band solar cells and hot carrier solar cells, may also play a significant role in future renewable energy generation [5]. In an ideal situation, the efficiency is high and cost of the solar cell material per area is low. Unfortunately for many simple and cheap solar cell technologies, the limit for solar cell efficiency can be rather low and therefore the additional installation, system costs and cost of space will make the solar energy expensive. If the solar cell is based on a single current generating material with a pn-junction diode, the ideal efficiency is determined mainly by the light absorption edge and the density of absorption states of the material.

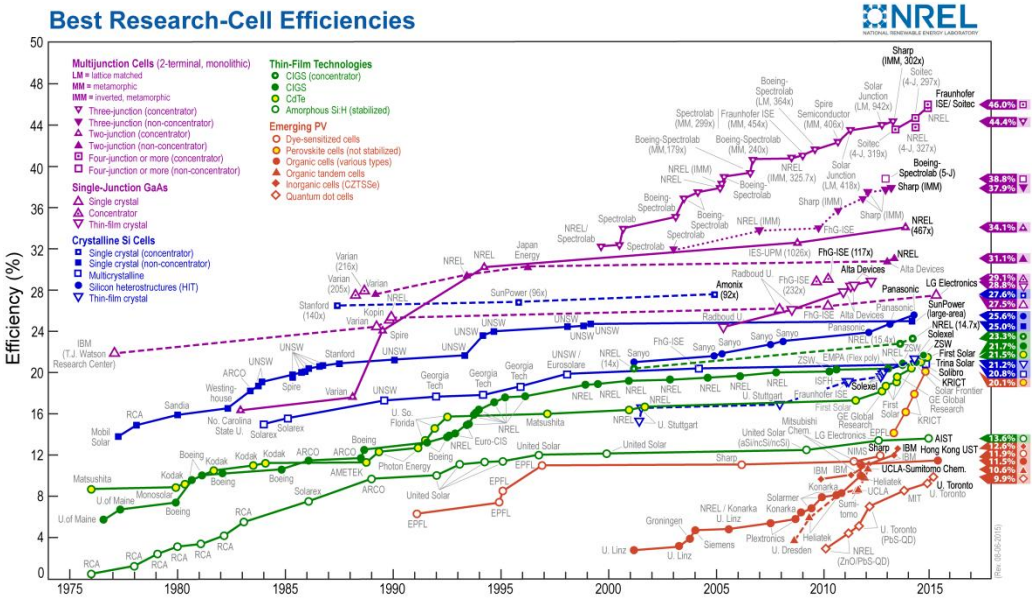

Figure 1.1. *Best research solar cell efficiencies starting from 1975 [2].*

The efficiency limit of a single pn-junction solar cell was calculated by Shockley-Queisser in 1960 [6] to be 30%, corresponding to materials with an absorption edge of 1.2-1.4 eV. The ideal efficiency of such a solar cell is low due to many loss mechanisms, of which the most important are transmission losses and energy losses as heat. The transmission losses can be reduced significantly by reducing the energy of the band edge. Unfortunately for single junction cells, in this case the thermalization losses are increased and the overall energy conversion efficiency is decreased. To increase the efficiency above the single junction limit, multijunction architecture cells are needed [7]. In this concept, solar cells with different band gaps are stacked on top of one another to reduce both transmission and thermalization losses. The idea behind such a solar cell is that the photons that are not absorbed at the junction above will be passed to the junction below and be partly absorbed. The actual stacking of the cells can be performed in many ways, the most important being monolithic integration.

The applications of solar cells and benefits of III-V solar cells

The III-V solar cells are prime choices for concentrated photovoltaic (CPV) power plants, space photovoltaics and in applications where solar cells are required to have a high power to weight ratio and low area [4]. For large area terrestrial flat panel usage, III-V cells are at the moment

too expensive, when compared to Si or thin film technologies (see Figure 1.2) [4]. Currently, for III-V multijunction cells, the efficiency can be ~38% under one sun conditions, and with high light concentration, typically from 300 to 1000 suns, efficiencies of over 45% can be reached [3].

Figure 1.2. *Solar panel installations in operation. On the left, Si flat panel installation connected to large batteries. On the right, an image of a 1 MW installation showing the back of the CPV panels. The panels are located in Albuquerque, New Mexico, USA.*

CPV technology was introduced in the 1960s [8] and pioneering work in CPV was led by Sandia National Laboratories starting from 1976 [9]. In CPV technology, the sunlight is concentrated from a large area to a smaller area, and therefore the active solar cell material area can be significantly reduced. The light concentration also has another benefit: with concentrated light, the solar cell efficiency increases, up to a certain concentration. For III-V solar cells, the improvement continues with concentrations of several hundreds of suns, and in theory the cell can be improved nearly up to the concentration limit of the Sun. The light of the Sun has a concentration limit of 46200 suns that is given by the size of the Sun and the distance between the Earth and the Sun [7], although up to 56000 suns is possible using non-imaging optics [10]. The benefit of CPV-technology is definitely superior efficiency, but the disadvantages are the need for an incorporated sun tracking system, and that the optical concentration design needs to be good in order to achieve high panel efficiency. Currently, only direct, almost collimated sunlight can be focused to a small spot with simple optics. Fortunately, there are multiple locations in the world that have many clear sky, sunny days, where CPV-systems can deliver large amounts of electricity. CPV-systems are currently divided into two different groups according to their concentration factor [11]. For high concentration systems (HCPV) the concentration is over 300 and for low concentrations (LCPV) the concentration is below 100

[11]. III-V cells are used in high concentration systems and other types of solar cells, typically silicon based, are used with lower concentration levels. There are predictions that with production volume and the next development steps in CPV technology, the energy price could go down to 0.045 Euro/kWh by 2030 [12]. The fabrication cost of CPV system will strongly depend on the concentration level [13]. If above 1000x concentrations are considered, only a minor part of the costs will be due to the CPV solar cell chip and the major part will be due to other parts of the system. Developing the cell efficiency will, however, lead to savings on the system level, since it directly improves the investment payback time and the price of energy.

In addition to semiconductor material science, smart product design can reduce the tracker costs and installation related costs, by optimizing power electronics and mechanical designs. For example, light weight designs minimize the logistics costs and enable a much cheaper and less CO_2 intensive production chain. In addition, new approaches in the CPV field are constantly being developed, reflecting almost endless possibilities for III-V CPV solar cell technology. Based on calculations reported in 2013 by the Fraunhofer ISE, the costs of CPV energy in sunny locations with a direct normal irradiance (DNI) of 2500 kWh/year/m^2 and 2200 kWh/year/m^2, is currently 0.08 to 0.12 €/kWh, respectively [11]. Some calculations suggest that the costs might be significantly lower, in the range of 0.04 to 0.05 $/kWh, depending on location [14]. In January 2015, the total amount of installed CPV-power was 330 MW (peak power) and all larger plants were delivering energy corresponding to 74-80% of their nominal performance [11]. Also, field tests by Soitec and National Renewable Energy Laboratory (NREL) reported that their panel installations show no measurable degradation during up to six years operation [15; 16], which is further evidence that CPV technology is not just a scientific exercise. These observations indicate a highly promising future for CPV-technology in sunny locations, where the produced energy can be predicted very accurately and produced without degradation of the output power.

While CPV is an emerging technology, space applications have been the largest application for III-V solar cells for a long time. This is first of all because the III-V cells have the highest efficiencies reported and smallest is area needed per unit power generation. Efficient area utilization saves room for the other essential equipment in the satellite or space station. In addition, the thermal efficiency coefficient for III-V cells has a lower negative slope than it does for Si cells, and therefore high solar power generation can be achieved even at elevated

temperatures. III-V cells also have excellent radiation durability [17; 18] in space, and this means by far the largest energy production in the space environment during the whole panel lifetime. The beginning of life (BOL) efficiency and the end of life (EOL) efficiency of optimized III-V cells are close to each other, when for the next best Si cell technology EOL can be significantly less than BOL. The EOL of III-V cells after a space mission can be as high as 90% of the BOL, while for Si solar cells it can be as low as 74% [19]. The III-V solar cells can also be fabricated as thin film devices to reduce the weight and increase the power to weight ratio. Currently, III-V solar cells with power to weight ratios of over 1000 W/kg can be fabricated [20]. The weight saving possibility makes satellite launches significantly cheaper. III-V solar cells might also be used in the future to produce hydrogen directly from sunlight and water for hydrogen based energy storing applications [21].

Currently III-V multijunction solar cells can be produced by two different epitaxial technologies. The technologies are metal organic chemical vapor deposition (MOCVD) and molecular beam epitaxy (MBE). With both techniques it is possible to grow all III-V solar cell junctions, but the techniques currently have different focuses due to their respective advantages in the production of different materials. MOCVD, at least for GaInAs materials, is a faster growth method than MBE. Therefore, MOCVD has been used as the development tool for III-V semiconductor solar cells in the past. MBE, on the other hand, has been shown to be a significantly better growth method for dilute nitrides, including GaInNAsSb compounds, and also has significant advantages in the fabrication of high performance tunnel junctions [22].

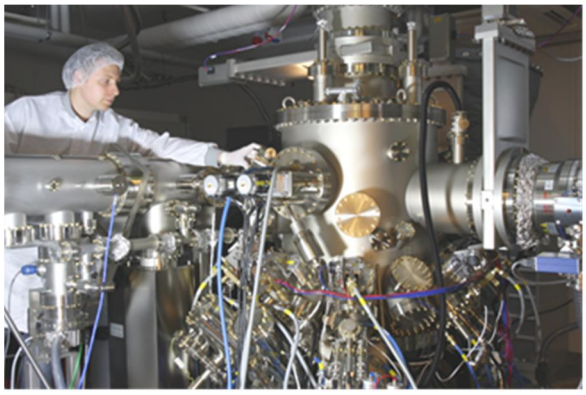

Figure 1.3. *Veeco Gen20 MBE system used in this study.*

To overcome the 50% efficiency limit, III-V multijunction solar cell research groups are adopting new schemes. We have chosen to use 1 eV band gap GaInNAsSb as the key element for the breaking of the 50% efficiency barrier. We have developed GaInNAsSb solar cell materials by exploring MBE synthesis dynamics and determining the physical properties of GaInNAsSb solar cells. This thesis summarizes the research carried between 2009 and 2015 and focuses on the MBE of GaInNAsSb materials for multijunction solar cells. In particular, the thesis focuses on GaInNAsSb multijunction solar cell MBE growth (See Figure 1.3) and on the performance of the fabricated GaInNAsSb single and multijunction solar cells. The thesis also studies the potential of monolithic integration of a nanopattern antireflection coating on top of a triple junction cell in order to achieve minimal reflection losses on top of the cell. Papers 1, 2 and 8 focus on the epitaxy dynamics and characteristics of GaInNAsSb crystals. Paper 1 and papers 3 to 5 focus on GaInNAsSb single junction cell and material properties. Papers 1, 2, 5, 6 and 7 focus on dilute nitride multijunction solar cells. In addition to journal papers, conference proceeding papers 9 to 11 focus on single and multijunction cells. These topics have been addressed in an iterative fashion, following the initial steps of material synthesis to single, and then multijunction device demonstration. The performance of a nanopatterned antireflection coating on a triple junction cell is presented in paper 6.

Chapter 2

2 Physics of III-V multijunction solar cells

For the understanding and optimization of solar cell performance, it is essential to understand the physics behind the photovoltaic phenomenon. This chapter briefly introduces solar cell physics, especially for III-V semiconductors and III-V dilute nitride compounds. The theoretical limitations and potentials of III-V solar cell materials are also discussed in this chapter.

2.1 Solar cell operation principle

Solar cells convert photons into charge carriers and transfer them to positive and negative contacts biased by an internal electric field formed in the solar cell. Solar cells are often based on semiconductor crystals [23]. Charge carriers in semiconductors are electrons for negative charges (n) and holes for positive charges (p), the density of electrons and holes can be tuned by introducing doping atoms to the crystal. Semiconductors are used in solar cells due to their tunable absorption, emission, recombination and charge transport properties [7; 13; 23; 24]. These properties are dependent on the electronic band structure (Figure 2.1), which can be tailored in many ways for compound semiconductors. The tailoring options include tuning the type and the width of the band gap (E_g). The band gap makes it possible to have materials that

will exhibit efficient photon absorption between the valence and conduction bands of the electronic band structure. High absorption is possible due to the high density of states that enable many different absorption transitions. The formation of pn-junction with doping makes possible the separation of the photon generated electron hole pairs from the absorption area, and their efficient collection at the metal contacts without the use of external electric fields. [23; 25]

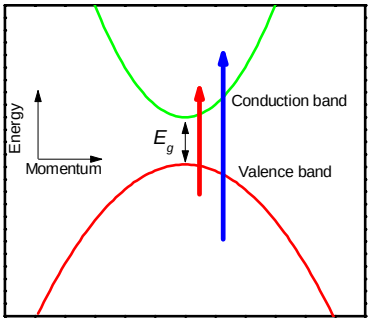

Figure 2.1. *Simplified band diagram for direct band gap bulk semiconductor. Photons can be efficiently absorbed if photon energy is at least* E_g.

In a semiconductor solar cell, the photons generate electron-hole pairs that are separated due to electric field created in the depletion region of the pn-junction. In addition to field aided separation, the charge carriers are collected at roughly the diffusion length [23] away from the junction. For the short circuit condition, the carrier collection to the contacts can be assumed to be complete and no accumulation of charges on the n or the p side of the junction occurs. If external load is placed in series with the solar cell, buildup of charges on the n side for electrons and on the p side for holes will result in building of voltage to the cell output. This voltage can increase up to the point in which the diffusion current cancels out the photocurrent, a level is called open circuit voltage. The current-voltage dependence can be modelled by diode equation for solar cells [23]. A pn-junction can be formed by either the implanting or diffusion of dopants to the crystal or by epitaxially forming an area which is p-type or n-type [25]. In the epitaxial growth, the dopant atoms are mixed on the growth plane during the growth of the epitaxial layer. The n- and p-type semiconductors are formed by introducing crystal lattice impurities that cause an electron density increase or a shortage of electrons, i.e. creating holes. An epitaxial pn-junction can be formed by changing the type of the impurity and continuing the growth. The diffusion length of the charge carriers [25] depends on the purity of the lattice and plays a critical role in the collection performance of the fabricated solar cell [23]. The second

critical parameter for solar cell design is the light absorption, determined by the solar cell material thickness, energy state densities and band gap energy [23]. Absorption strength is strongly dependent on the chosen material and the energy of the incident photon. For semiconductors with a direct band gap, the absorption near the band edge is much stronger than for indirect band gap semiconductors [23]. The difference between indirect and direct semiconductors arises from their electronic band structure. Near the band edges for direct band gap semiconductors, also at minimum absorption energies, the photon electron excitation interaction can occur without the presence of lattice vibrations, and is therefore a more probable phenomenon [23]. On the other hand, the direct band gap semiconductors also have a significantly higher probability to re-emit the photon compared to indirect band gap semiconductors, leading to shorter charge carrier lifetimes for direct gap semiconductors. Typical charge carrier lifetimes and physical constants are listed in Table 2.1. The charge carrier lifetimes are determined by recombination processes which include optical and thermal interactions. The recombination can take place in the bulk or at the interfaces. In the case of solar cells, optical emission is spontaneous emission. The recombination processes producing heat are based on impurity state recombination, also known as Shockley-Read-Hall recombination, or on Auger recombination [23]. At a given temperature, the rate of impurity recombination is dependent on the defect density, the cross section of the defect state, and the energy. Auger recombination is a different process and it is dependent on the free charge carrier densities in the bands. For III-V solar cells it is important to have low bulk recombination and surface recombination rates. For high quality defect-free bulk material and the correct choice of interface materials, significant improvements can be achieved, resulting in higher voltages, currents, and conversion efficiencies [26-28].

Table 2.1. Physical constants for semiconductors which are relevant for the design of semiconductor solar cells.

Semiconductor	Hole mobility ($cm^2/V \cdot s$)	Electron mobility ($cm^2/V \cdot s$)	Charge carrier lifetime (ns)	Absorption coefficient near band edge (1/cm)
Si	~500 [25; 29]	1000-1300 [25; 30]	< $9*10^5$ [31; 32]	10^3 [33]
Ge	1900 [25]	3900 [25]	~10000 [34], 2200 [35]	~10^3 [36]
GaAs	400 [35]	8900 [35]	14 [35], 2-5 [37]	8›10^3 [38]
GaInP	200 [35], 41 [37]	4000 [35],175 [37]	13 [35], 5 [37]	3›10^4 [39]
GaInNAs (1 eV, LM)	100 [37]	350 [37], 400 [40]	1 ns [41]	8‹10^3 [42]

A simplified structure of a single material pn-junction solar cell is presented in Figure 2.2. a. Single material solar cells are also multilayer devices combining, at least, an antireflection coating (ARC), back and front metal contacts, cell interconnector bonds, and some electronics to match the cell to a load that consumes the produced energy. The ARC can be a single, multilayer or micro/nanopatterned surface that is used to minimize the light reflection on the semiconductor-air interface [43]. Back and front metal contacts minimize the resistive losses of photocurrent and photovoltage to the electronic matching unit. The front contact typically has a finger pattern to maximize light transmission. The back contact typically covers the whole back side of the solar cell crystal. In addition to these layers, in modern high efficiency solar cells the semiconductor crystal itself is composed of multiple semiconductor layers from different semiconductors having different purposes and functionalities. These devices are called heterointerface devices and they are widely used also in light emitting diodes, semiconductor lasers, transistors, and photodetectors. A simplified structure of a modern single junction III-V solar cell is presented in Figure 2.2 b.

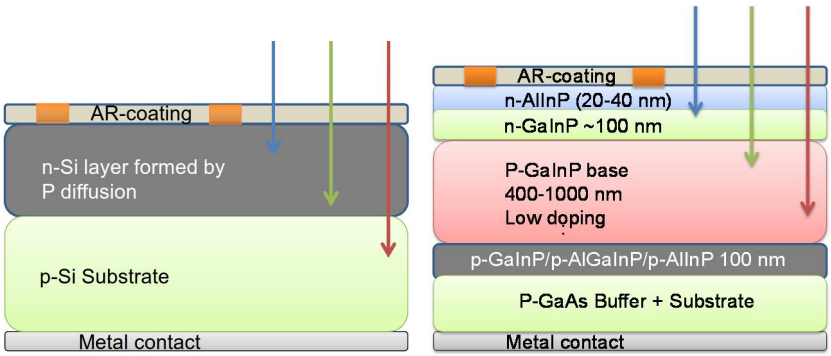

Figure 2.2. *On the left a schematic structure of a simple Si solar cell and on the right the structure of a GaInP top cell. Short wavelengths are absorbed near the top of the cell (blue arrow) and the longest wavelengths (red arrow) are absorbed near the bottom of the cell junction, or travel through the cell.*

The cell has an ARC to maximize the light transmission to the active material. Metal contacts are also formed on the top, typically in a finger pattern. The metal contacts are made on an epitaxial layer of highly doped n-GaAs and the ARC is grown on a high band gap n-AlInP window layer. To form this structure a selective etching step is needed. The purpose of the AlInP is to reflect holes back to the pn-junction and minimize the surface recombination rate. N-doped GaInP forms the n side of the junction and low doping p-GaInP forms the p-side. The depletion region is mainly formed on the p-side of the junction, the low doped region is p-type because the diffusion length of electrons is longer than for holes. Highly doped p-GaInP, p-AlGaInP, or p-AlInP is needed to reflect back electrons to the junction and minimize surface recombination rates at the back side. The purpose of the p-GaAs buffer and substrate is to provide a platform for the device to be grown. A back metal contact is needed for good ohmic contact.

Depending on the application, this kind of device may already satisfy the performance needs, but if even higher performance is preferred, multijunction concepts need to be introduced. In multijunction architectures, solar cells with different absorption band edges are used to absorb the solar energy as efficiently as possible, and the remaining photons are recycled to a second junction that can use them efficiently. The process is efficient because in this way the energy consumed by the relaxation of the photon excited electron to the conduction band minimum has a smaller total energy when losses are integrated for all photons of the solar spectrum. Usually

these devices are III-V semiconductor devices and from now on we will focus only on III-V multijunction solar cells.

Multijunction solar cell architectures

Different III-V solar cells can be connected together by mechanical stacking, spectral splitting, monolithically or by wafer bonding or wafer fusion [44-52]. Each approach has different challenges at different phases of the solar cell panel manufacturing. The advantages and disadvantages of the different approaches are compared in Table 2.2

Table 2.2. Comparison of different MJSC architectures.

MJSC architecture	Advantages	Disadvantages
Spectral splitting	+ Simple epitaxy + No material / lattice matching limitations + No current matching needed between the different junctions	- Complex optics - Multi terminal device and complex electronics - Panel fabrication has many phases - Multiple growths and wafers
Mechanical stacking	+ Simple epitaxy + No lattice constant limitations + Current matching is not necessary	- Complex assembly - Multi terminal device - Multiple growths and wafers
Wafer fusion	+ Two terminal device + Easy panel fabrication + Easy epitaxy + Simple electronics	- Multiple growths and wafers - Complex fusion process
Monolithic	+ Only one wafer and growth + Simple electronics + Easy panel fabrication	- Most of the challenges are on the epitaxy level - Tunnel junctions necessary - Limited amount of lattice matched junctions
Metamorphic (inverted or upright)	+ Lattice matched and metamorphic junctions can be used in the same cell + Only one wafer and growth + Simple electronics + Easy panel fabrication	- Most of the challenges are on the epitaxy level - Multiple different tunnel junctions necessary - Thick metamorphic buffers needed
Monolithic dilute N	+ Multiple material possibilities which all are lattice matched + Only one wafer and growth + Simple electronics + Easy panel fabrication + Only one or two different tunnel junctions need to be developed + No thick buffers needed (thin and fast epitaxy)	- Most of the challenges are on the epitaxy level

For the associated electronics, monolithic and wafer fusion approaches have simpler solutions. On the other hand, the growth of mechanically stacked solar cells is much simpler since only single junction devices are needed, and they do not need to be current matched to each other. Currently, almost all III-V multijunction solar cells are two terminal devices as it is simply easier to resolve the problems on a wafer level than at the system level. Unfortunately, traditional III-V materials easily limit the number of available lattice matched junctions to three. Fortunately, there are new lattice matched materials that can enable multiple new junctions. These materials are based on GaInNAsSb compounds, which are the topic of this thesis.

2.2 Monolithic multijunction solar cells

Monolithic multijunction solar cells are composed of single solar cells that are connected together by electrical polarity inverting tunnel junctions. Tunnel junctions are needed to connect all the junctions in series and gain a voltage increment from each sub-cell. A schematic picture of a monolithic multijunction solar cell is presented in Figure 2.3. In a monolithic multijunction solar cell the topmost cell must have the highest band gap energy and the bottom cell the lowest. This allows equalization of the photon flux for all the junctions, which is based on the absorption properties of III-V cell materials (see Figure 2.1).

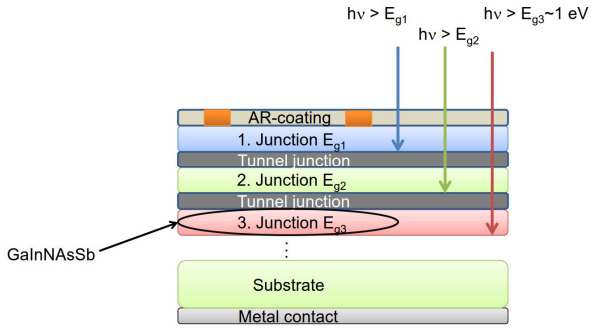

Figure 2.3. *Schematic structure of multijunction solar cell.*

Most of the commercial monolithic III-V solar cells are currently triple junction solar cells and they are made of GaInP, Ga(In)As and Ge junctions. $Ga_{1-x}In_xP$ is lattice matched on GaAs and Ge when x is approximately 0.5. This configuration sets the band gaps of the current generating materials to 1.9 eV, 1.4 eV and 0.7 eV, for GaInP, GaAs and Ge respectively. In practice this

approach limits the solar cell efficiency in production to ~40% and the production panel efficiency of ~30% when installed in a CPV system. [53]

Monolithic multijunction solar cells require tunnel junctions that have low series resistance and high tunneling currents. First of all, the tunnel junction should be transparent to the photons that are not generating current in the junction above. If it is not highly transparent, it will lead to a drop in current generation of the junction below. Secondly, the tunnel junction should have high probability for electron tunneling through the barrier that is formed in a pn-junction between the n-side conduction band and the p-side valence band. If tunneling is not efficient, it will result in unideal operation of the whole multijunction device. In practice, the tunneling between these bands is achieved by introducing extremely high active doping concentrations on both sides of an abrupt pn-junction. The minimum active electron concentration for the n-side is ~1×10^{19} 1/cm^3 and the minimum p-side hole concentration is ~4×10^{19} 1/cm^3 [54-56]. If these minimum concentration levels are achieved, the barrier between conduction and valence bands becomes so narrow that the tunneling phenomenon becomes highly probable for electron in a GaAs pn-junction. The peak tunneling current is strongly dependent on the pn junction doping and band gap [4; 56]. The band diagram of a GaInP/GaAs multijunction cell is presented in Figure 2.4 (a). The corresponding current voltage characteristics of the tunnel junction are presented in Figure 2.4 (b). In a multijunction solar cell, the tunnel junction is operating in the forward bias condition [4].

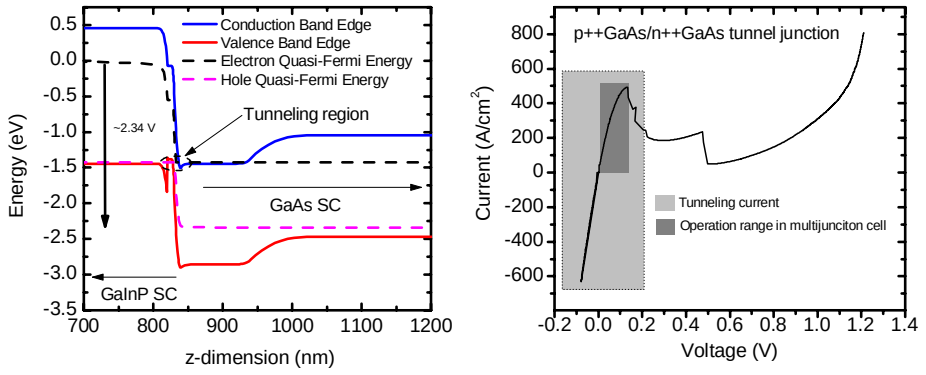

Figure 2.4. *(a) Simulated band diagram of GaInP/GaAs solar cell for open circuit voltage bias (courtesy of Dr. Antti Tukiainen). (b) Current-voltage characteristics of abrupt p++GaAs/n++GaAs tunnel junction fabricated by MBE in this work. The grey marked area shows the voltage and current region where the tunneling current occurs.*

The fabrication of tunnel junctions for MJSC devices is challenging, because ensuring both high doping and good material quality is not trivial. The challenge comes from the fact that high active doping levels require large amounts of impurity atoms to be incorporated to the crystal lattice, making the crystal in crystallographic perspective worse. High concentrations of impurity atoms make the two-dimensional growth of semiconductor crystals challenging, and epitaxial compromises are needed. Typically, use of lower synthesis temperatures is the minimum requirement needed to ensure two-dimensional growth in the presence of impurity atoms [57; 58].

For monolithic design, the junction band gaps and thicknesses need to be chosen properly so that the sunlight photons are shared equally between the junctions, resulting in current balance between the junctions [4]. The efficiency improves with the number of junctions and concentration. These dependences are presented in Figure 2.5 (a). Depending on the number of junctions integrated, the optimal band gap values for the different junctions vary roughly from 0.7 eV to 2.3 eV. An example of the correspondence between the band gaps of GaInP/GaAs/GaInNAsSb/Ge cell and the solar spectral bands can be seen from Figure 2.5 (b).

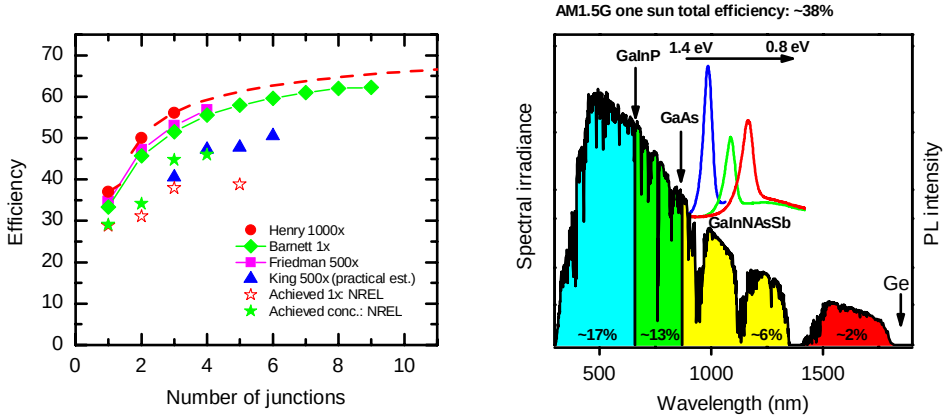

Figure 2.5. *(a) Calculated and measured efficiencies from III-V solar cells as a function of number of junctions [2; 3; 7; 59-61]. Currently triple junction cells have almost reached the maximum performance and subsequently four or more junction cells will continue the trend. (b) Operation bands of potential four junction cell (GaInP/GaAs/GaInNAs/Ge) and AM1.5G spectrum. The operation bands of the four junction cell are colored with different colors. The estimated total efficiency of the four junction cell is the sum of the efficiencies produced by the sub cells – 17%, 13%, 6% and 2%, yielding 38% altogether in this example.*

The traditional materials, lattice matched on GaAs, can cover band gaps from about 1.4 eV to 2 eV well, and these materials can be grown on Ge substrate which has a 0.7 eV band gap. For the energy gaps between 0.7 to 1.4 eV there are no traditional semiconductors lattice matched to GaAs or Ge, but this band gap window is crucial for the efficiency development of III-V multijunction solar cells (see Figure 2.5 (b) revealing the correspondence between the solar spectrum and band gaps). The potential materials with band gaps between 0.7 and 2.3 eV are listed in Table 2.3.

Table 2.3. Materials for multijunction design [24].

Material	E_g **(max, eV)**	E_g **(min, eV)**
AlGaInP	2.30	1.86
GaInAsP	1.9	1.42
AlGaAs	1.9	1.42
GaAs	1.42	1.42
GaInAs	1.42	0.35
GaInNAsSb	1.42	0.8 eV (this work, [62; 63])
Ge	0.7	0.7

To cover the band gaps from 0.7 eV to 1.4 eV, there are at least three practical solutions. The first solution is to epitaxially prepare virtual substrates that have matching lattice constant with junctions having smaller band gap energies than 1.4 eV. These layers are designed to change the lattice parameter of the host lattice and bury the lattice imperfections caused by the lattice strain relaxation, and to prepare a suitable surface for the growth of the smaller band gap semiconductor. In this approach GaInAs sub-cells are typically used. The challenge of this approach is that the metamorphic buffer layer usually needs to be several micrometers thick, making the epitaxy utilization worse and the cell more expensive.

The second approach is to grow lattice matched multijunction solar cells on different substrates and bond them using wafer fusion. For instance, a dual junction cell can be grown on GaAs and InP substrates, and then after growth the wafers are fused together to combine single four junction solar cell wafer. This approach is, however, hampered by the fact that multiple wafers and growths are needed, adding cost to a single cell, and more complex wafer processing is also required.

The third option is to use a relatively new lattice matched III-V semiconductor group called dilute nitrides [64; 65]. Typically, dilute nitride III-V solar cells are prepared from GaInNAsSb compounds that can be grown lattice matched on GaAs and have a widely tunable band gap, at least down to 0.8 eV [62],[P4]. The dilute nitrides can also provide a wide band gap range with lattice matching to Si if GaNPAs with an appropriate composition is used [66]. The growth of dilute nitrides is associated with several challenges, which are discussed later in more detail.

Despite the challenges for dilute nitride epitaxy, close to 100% external quantum efficiency (EQE) results have been demonstrated, and dilute nitrides have been proven to have applications both in lasers and solar cells [67-71]. The advantage of dilute nitrides is that the growth can be done in one repeatable run and only one substrate is needed, even if the multijunction solar cell has more than 3 junctions. Also the total thickness which needs to be grown is not limited by the thickness of metamorphic buffer layers and can be freely optimized.

2.3 Current voltage characteristics of III-V multijunction solar cells

The maximum current generated by a solar cell is determined by the absorption and the material characteristics of the crystal. The maximum charge generation performance can be estimated from the short circuit current density (J_{sc}), which is defined as the ratio of the short circuit current (I_{sc}) and the solar cell area (A_{SC}). Other key parameters for solar cell characterization are the open circuit voltage (V_{oc}) and the fill factor (FF), which is defined as

$$FF = \frac{V_{mp} I_{mp}}{V_{oc} I_{sc}} \quad (2.1),$$

where V_{pm} and I_{mp} represent the voltage and current values recorded at the maximum power point [23]. The cell efficiency (η) is defined as

$$\eta = \frac{V_{mp} I_{mp}}{P_{opt}} \quad (2.2),$$

where P_{opt} is the total power radiated by the sun. Moreover the optical power received depends on the particular application as a function of geographical position and altitude. For characterization of terrestrial flat panels, the input power spectrum is termed AM1.5G and corresponds to 1000 W/m^2 optical power. The standard spectrum for CPV-systems is termed AM1.5D and corresponds to 900 W/m^2 or 1000 W/cm^2 [72]. For space applications, with more intense UV components, the spectrum is denominated AM0. The AM0 spectrum also differs from AM1.5 spectra by other atmospheric losses in the infra-red caused for example by water. The determination of the whole current-voltage (IV) characteristics of the solar cell can be done by voltage sweeps and can be modelled with standard diode equations (2.3-2.5) for multijunction solar cells. These equations have been used in [P5] and [P11] for the cell performance projections and were derived from series connected diodes with two terminals using Kirchhoff laws. The model is useful for projecting solar cell performance under different conditions and with different sub-cell performances. Similar models have been also used elsewhere [59].

$$I = I_i, \; i = 1,2,3..., n \quad (2.3)$$

$$V_i(I) = \frac{n_i k_B T}{e} \ln\left(\frac{I_{Li}(E_{g_i}, EQE_{avi}) - I}{I_{0i}(T, E_{g_i})}\right) - IR_{si} \quad (2.4)$$

$$V_{sc}(I) = \sum_{1}^{n} V_i(I) \quad (2.5)$$

Here I is the current of the two terminal solar cell, I_i is the current through an individual sub-cell, $V_i(I)$ is the voltage of a sub-cell, n_i is the quality factor of the i^{th} sub-cell diode, k_B is the Boltzmann coefficient, T is the device temperature (T = 300 K), I_{Li} is the current generated by the junction i, E_{gi} is the band gap (300 K) of the i^{th} junction, I_{0i} is the reverse saturation current of the i^{th} junction at 300 K, R_{si} is the series resistance of i^{th} junction, EQE_{avi} is the average EQE of each junction, and V_{sc} is the device total voltage. We have neglected the shunt resistance for simplicity, which is a good approximation for most high quality SC devices. In case of low shunt resistance, the cell is self-shorted due to improper processing or non-ideal material characteristics. Figure 2.6 utilizes the model for fitting of the diode characteristics.

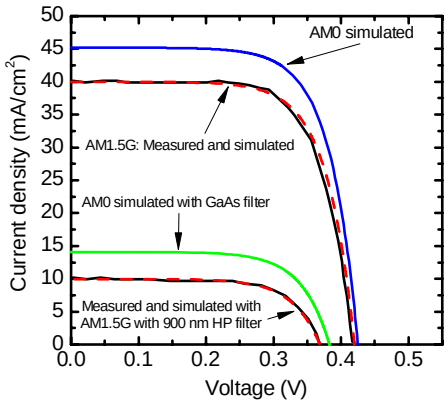

Figure 2.6. *Fitted and projected performances of a GaInNAs single junction solar cell with different spectral conditions reported in [P11].*

In the same way, the IV-characteristics of a multijunction device can be modelled or projected by summing the IV-curves of each sub-junction at a certain operation current. The tunnel junction losses, transport losses within the SCs and the losses in the metal contacts can be modelled by a lump series resistance R_s, which is the sum of sub-junction resistances. This can be done if the tunnel junction is operating in the first linear regime (see Figure 2.4 (b) for details). Typically, for MJSCs the series resistance terms caused by current spreading in sub-cells and the contact resistances limit the operation earlier than the saturation of the first linear regime of the tunnel junctions.

The effect of cell temperature on the III-V multijunction cell performance

For semiconductors, room temperature provides sufficient energy for the ionization of many typical dopant atoms in the crystal lattice [25]. If the operation temperature of the solar cell is changed from standard measurement conditions (25°C), the active doping concentrations do not change remarkably. However, significant changes in the cell performance are seen if the cell temperature is changed by even a few degrees [23; 73]. When the solar cell heats up, the charge carrier recombination rate in the crystal increases, leading to an increase of the recombination current that reduces the cell open circuit voltage. On the other hand, the solar cell current generation increases because the semiconductor band gap shrinks with increasing temperature [24]. The temperature coefficients measured in connection with this work are discussed in chapter 5.3 and in paper [P7].

Altogether, the efficiency of III-V multijunction solar cell drops only slightly with increasing temperature, and the drop is significantly less than for Si solar cells [74]. The target operation spectrum also has significance for the cell design, since the band gap temperature coefficients for the different junctions of a III-V multijunction solar cell might in some cases lead to a situation where a certain junction is current limited, while under other conditions the same sub-cell is not limiting the performance [75]. Figure 2.7 shows an example of IV-measurements carried out for a GaInP/GaAs/GaInNAsSb solar cell fabricated in this work and measured at 25°C and 90°C, the cell is illuminated close to AM0 intensity.

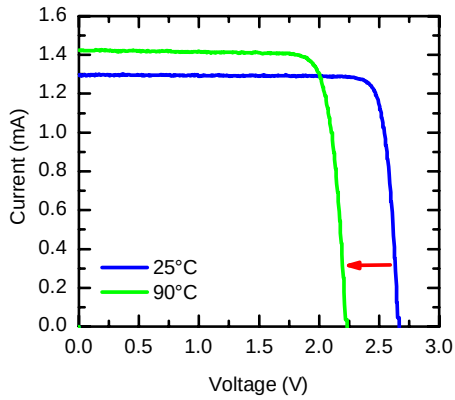

Figure 2.7. *GaInP/GaAs/GaInNAsSb solar cell performance at standard and elevated temperatures measured with Oriel xenon simulator.*

The physics behind increased efficiency with concentrated sun light

The semiconductor properties of III-V semiconductors make them excellent choices for CPV solar cells, since their efficiency can significantly improve up to concentration of hundreds of suns. This property is related to the fact that for III-V solar cells the recombination current I_0 does not significantly change with the concentration and therefore the cell operation voltage can improve significantly, thus making it possible to achieve an efficiency improvement by almost 10 percentage points [4; 23; 62]. A second important characteristic of III-V semiconductors is that they can be fabricated in such a way that the total series resistance of the cell will be low, ensuring high fill factors and efficient utilization of the voltage improvement. Typically, for MJSCs the I_{sc} grows linearly with concentration [76], although luminescent coupling might result in slight over linearity at high concentrations [77-79]. Luminescent coupling is possible if

over generating higher band gap cell is emitting extra charge carriers as photons to lower band gap cell(s) that utilize the photons generating higher current. Solar cell efficiency under CPV conditions, $h_{eff}(C)$, can be estimated with equation 2.6, which can be achieved by combining equations 2.1 to 2.5.

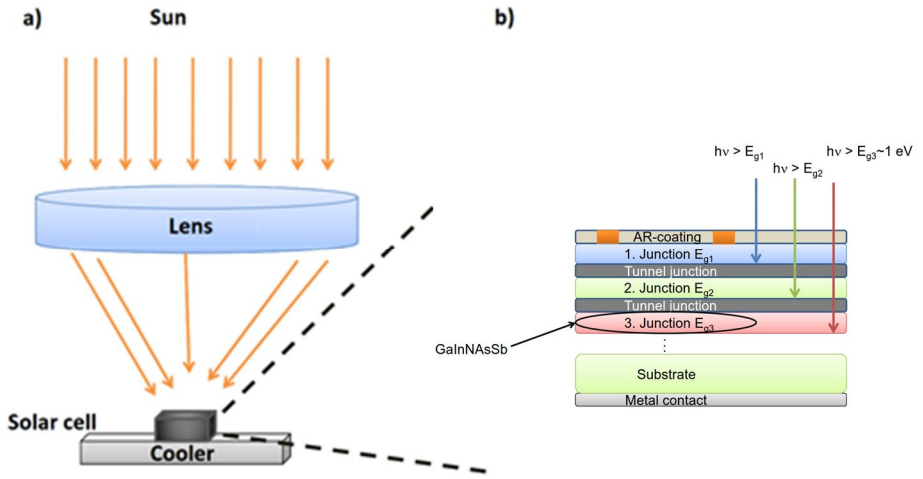

Figure 2.8. Operation principle of CPV solar cell. In CPV technology light is focused from a large area to a small III-V solar cell that converts light efficiently to electricity.

$$h_{eff}(C)=\frac{V_{oc}(C)\times I_{sc}(C)\times FF(C)}{I_{sun}\times A_{SC}}=\frac{\frac{n(C)kT}{q}\ln\left(\frac{CI_{sc\text{-}1sun}}{I_0}\right)\times CI_{sc\text{-}1sun}\times FF(C)}{CI_{1\text{-}sun}\times A_{SC}} \quad (2.6)$$

, where C is the concentration level, $n(C)$ is a C dependent diode ideality factor, $I_{sc\text{-}1sun}$ is the short circuit current generated by the cell under one sun conditions, I_{sun} is sunlight intensity at solar cell, $I_{1\text{-}sun}$ corresponds to the intensity of one sun illumination, q is the electron charge and $FF(C)$ is a C dependent fill factor. Typically, $n(C)$ remains close to constant up to high concentrations, if the cell temperature can be kept constant then the ultimate efficiency is limited by $FF(C)$. FF typically starts to drop at 400-1000 suns concentration, depending on the cell and the front metallization design [80]. One important point for CPV is that the cells will heat up and the maximum efficiency will drop, but not as significantly as for one sun conditions, since the I_0 growth with temperature does not have such a strong effect on the operation voltage of the MJSC at high light concentrations. CPV cells may operate significantly over the ambient temperature (30-50°C) [81] and temperature is also dependent on wind speed [53] and module

design. Elevated operation temperatures will reduce the cell efficiency by 1 to 3 percentage points [73; 76]. The panel designs are often only passively cooled by the panel back plate.

A CPV multijunction solar cell requires careful design in such a way that all the stacked cells will produce close to the same current. Significant losses in the energy production result if the sub-junction band gaps and thicknesses are not well optimized. Depending on the location, the spectrum may differ at morning, noon and evening. The spectrum also has seasonal variations, during some seasons the UV and the blue part of the spectrum might be stronger, and on the other hand the air humidity has an effect on the IR part of the spectrum [35; 75; 82]. However, there are studies that report on the effects of seasonal and daily spectral variations on the performance of CPV solar cells with multiple junctions, and the result is that the total energy produced as a function of number of junctions will have positive slope [59].

Chapter 3

3 Growth dynamics of GaInNAsSb

This chapter focuses on the properties of GaInNAsSb semiconductor and on the growth dynamics of GaInNAsSb crystals. The GaInNAsSb crystals were grown by MBE.

MBE growth

MBE growth is based on thermal evaporation of molecules and atoms in ultra high vacuum (UHV) from solid or liquid high purity elements to a heated substrate that typically has a specific crystal structure and orientation. The UHV conditions are maintained by pumping the system by vacuum pumps and by the liquid nitrogen cooled inner walls of the deposition chamber, and by transferring the substrate through different pumping stages to the growth chamber. If the mixture of the elements and the substrate temperature is in the correct range, a layer of the evaporated elements will be grown which will copy the orientation and crystal structure of the substrate. Many epitaxial layers can be stacked on top of each other. For growth of thick epitaxial layers, a minimal difference between substrate and epitaxial layer lattice constants is preferred. For growth of nanostructures such as quantum wells, wires and dots, the restriction for the lattice constant is not so strict. For growing III-V bulk crystals, the group III fluxes typically limit the growth rate and significant overpressure is used for group V fluxes. The optimal conditions for epitaxial growth depend on the formation energies of the epitaxial crystal and defects. The molecular mixture can be alternated rapidly by mechanical shutter plates and/or valves, and each thermal evaporator cell may have different temperature regions for different purposes. The evaporation rate can be also controlled by the cell evaporator temperature(s). In addition to purely thermal evaporation, the MBE system can also incorporate

gas phase sources. In this work, we have used high purity N_2 gas molecules for the incorporation of nitrogen to GaInNAsSb compounds. Unfortunately the N_2 sticking coefficient is insufficient at typical GaInNAsSb compound growth temperatures and therefore N_2 needs to be cracked into N atoms, which have a close to unity sticking coefficient in the growth parameter range of GaInNAsSb compounds. The N_2 molecules can be cracked into N atoms by transferring the N_2 molecular flow through a radio frequency (RF) plasma chamber that uses a coil antenna to transfer the RF energy to the plasma, which also takes place in vacuum. The MBE growth processes can be monitored by many methods in real time, providing data on the surface structure and substrate temperature, for example. Further reading and more technology details can be found in references [83-85].

3.1 2D growth of GaInNAsSb single crystals

High efficiency III-V solar cells require stacking of single crystal materials with homogenic atomic distribution and smooth heterointerfaces. In general, the epitaxy of metastable highly mismatched materials such as GaInNAsSb is challenging, and in particular when the N concentration is increased close to 3%, the typical composition needed for 1 eV solar cells, the fabrication of smooth surfaces having uniform atomic distribution becomes a great challenge. This is because highly mismatched materials are composed of atoms that have large differences in their size, electronegativity and ionization potential [86]. These materials cannot be fabricated in thermal equilibrium with smooth surfaces, uniform atomic distribution and abrupt heterointerfaces [87-91]. This property of highly mismatched materials drives the grown film to phase separate during the growth, to at least two phases [90-92]. Studies have shown that, especially for GaInNAs, the crystal separates to Ga-N bond rich areas and In-As bond rich areas if the chosen growth parameters are not properly selected [93]. Fortunately, the crystallization processes can be controlled and phase separation effects can be limited by growing the highly mismatched alloys far from thermal equilibrium, resulting in smooth and uniform epitaxial layers. The GaInNAsSb growth can be controlled by keeping the N composition as low as possible, using ~200 to 300°C lower growth temperatures than typical for GaAs [87; 91; 94-96], and by using surfactants such as Sb and Bi [97-101]. The controlling of these conditions bring challenges to dilute nitride epitaxy and a deep understanding of the growth dynamics is essential for high quality devices.

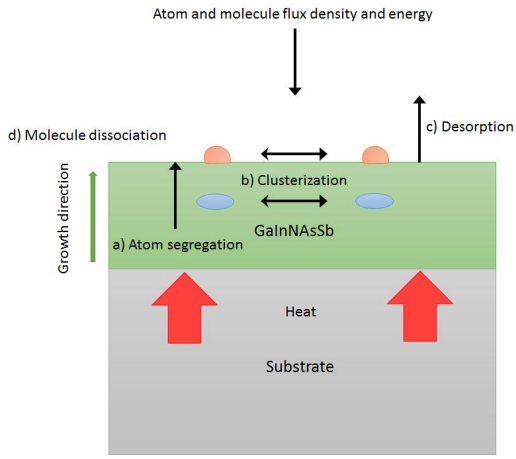

Figure 3.1. *Schematic illustration of processes during growth of GaInNAsSb crystal.*

Due to the many atomic species in GaInNAsSb crystal, there are many fundamental processes interacting together at the GaInNAsSb growth front. The main processes are illustrated in Figure 3.1 and can be divided into: a) atom segregation from bulk face to surface [87], b) formation of clusters on surface and at bulk face, c) desorption of atoms and molecules from the surface, and d) molecule dissociation on the surface. The resulting crystal is defined by the surface energy, where the resultant crystal is driven by minimization of the surface energy [102]. Growth front processes can be controlled by selection of the substrate material and orientation, by control of the substrate temperature and the atom and molecular flux densities and their energies. It is clear that if all atoms and molecules for the growth of the GaInNAsSb crystal have two independently tunable parameters in addition to the substrate temperature selection, the optimization space in the ideal case would be enormous, with a total of 11 independent parameters for a single substrate selection and orientation. In addition, the nature of the incorporation of N by an RF plasma assisted system introduces parameters that are related to the control of the ion flux by, for instance, electric field induced ion deflection [103; 104]. Therefore, many simplifications and approximations need to be used as compromises to reach high quality growth conditions. The safest way to understand the dynamics is to analyze the effect of each parameter one at time using physically intuitive directions and models.

N incorporation is also responsible for introducing point defects that change the charge carrier dynamics, i.e. the defects reduce the lifetimes and mobilities of the charge carries. The defects in dilute nitrides can be, for example, group-III vacancies, arsenic antisites and interstitial

nitrogen [95; 105]. N incorporation also increases the background/unintentional doping of the crystal. Increased background doping results in the formation of a narrow depletion region in the p-i-n structure. Also, increased doping combined with short diffusion lengths often results in low internal quantum efficiency (IQE).

Fortunately, part of the characteristic defects of dilute nitrides can be changed or cured after the growth. Thermal annealing is a well-known method for curing and introducing defects to semiconductor crystals, especially for GaInNAs [95; 106-108]. The main idea of post growth annealing is to manipulate the bonding environment of the grown crystal. The applied thermal energy pulse will make short range atomic rearrangements plausible in the crystal, while remain surface characteristics as intact as possible in the inert atmosphere. In this work, the annealing studies were done using rapid thermal annealing (RTA), where the crystal can be heated up rapidly in a controlled manner by using infrared radiation in an N_2 gas background. The following chapters discuss the growth dynamics and material characteristics of the GaInNAsSb crystals grown in this thesis. [41; 67; 109; 110]

Lattice matched GaInNAsSb crystals

For lattice matched III-V solar cells grown on GaAs, the lattice parameter of the GaInNAsSb layer needs to be well matched to GaAs to avoid misfit dislocations. Misfit dislocations reduce the solar cell performance if they are located in or near the active area of the solar cell [111; 112]. They are generated when the total tensile or compressive strain is too high [111]. The relaxation mechanisms are dependent on the strain type [113], but these effects are not discussed in detail in this thesis since the majority of the studied GaInNAsSb layers are grown almost fully lattice matched, and the used thicknesses are well below the critical thickness limiting the presence of misfit dislocations. For lattice matching of GaInNAs and GaNAsSb, the In and Sb compositions need to be suitable to achieve a lattice constant of 5.65325 Å, which corresponds to the lattice constant of GaAs [24]. The indium composition in $Ga_{1-2.7z1}In_{2.7\ z1}N_{\ z1}As_{1-\ z1}$ needs to be roughly $2.7z_1$, where z_1 is the composition of N that has substituted As. For $GaN_{z2}As_{1-3.4z2}Sb_{2.4z2}$ the Sb composition needs to be $2.4\ z_2$, where z_2 is the composition of N. These composition dependencies are based on the lattice constants of cubic GaInSb, GaInN and GaInAs and Vegard's law [24; 63].

3.2 Modelling of N incorporation

For the growth of GaInNAsSb crystals it is essential to understand the incorporation kinetics of the different atomic species. For the group III-atoms, when using MBE it is relatively easy to define the In/Ga ratio below the high desorption range of In, which starts to be significant at growth temperatures above 520°C [114]. Fortunately, the In desorption is negligible in the growth temperature range optimal for dilute nitrides [87; 91; 94-96] and the In composition can be determined from the calibrated flux ratios of In and Ga measured in-situ by an ion gauge. On the other hand, for N composition, the situation is far more complex. In the early days of dilute nitride epitaxy, it was observed that the N incorporation rate is inversely proportional to the group III atom growth rate [115; 116]. On the other hand, it has also been observed that the N incorporation rate is close to constant in a wide range of As/III beam equivalent pressure (BEP) but may vary significantly at small As fluxes [116-118]. The complexity of N incorporation is compounded further by the fact that it has been observed to be a function of the growth temperature [94; 119].

To control the composition using different growth conditions, it is therefore crucial to understand how the plasma source is used for cracking of the N molecules and how it can be controlled to yield the desired N incorporation rate under the given growth conditions. For traditional RF plasma sources used for the growth of dilute nitrides in MBE, the control parameters are the primary power of the plasma system and the flow of N molecules through the plasma tube. The operation range can also be tuned by introduction of nozzles to the end of the plasma source that can be used for tuning of the flux distribution and the pressure difference between the MBE system and the plasma. The N incorporation dependence has been modelled previously [118; 120; 121]. To this end, in this thesis work [P2] we have introduced an analytical model, which needs only the plasma primary coil power and N_2 molecular flow as inputs to determine the N incorporation. Thus, the dependence of the N composition on power and flow can be determined using the equation:

$$N(\%) = \frac{B}{GR_{III}} F\left(R_{sp}P_{RF}\right)^{1/2} \exp\left(\frac{E_{ad}D}{R_{sp}P_{RF}}\right) \quad (3.1),$$

where GR_{III} is the group III growth rate, B and D are factors that take into account system and plasma geometrics, F is molecular flow, P_{RF} plasma primary power, R_{sp} is plasma system primary resistance, and E_{ad} is the activation energy for the dissociation process. E_{ad} is an effective energy which takes into account all the dissociation/collision processes, including molecule dissociation into atoms, molecule ionization and atom ionization. This equation is based on the Maxwell-Boltzmann electron energy distribution and assumes that electrons are confined to an effective volume. A detailed explanation for the derivation of the model is given in the paper [P2]. The accuracy of the model can be assessed from the graphs shown in Figure 3.2.

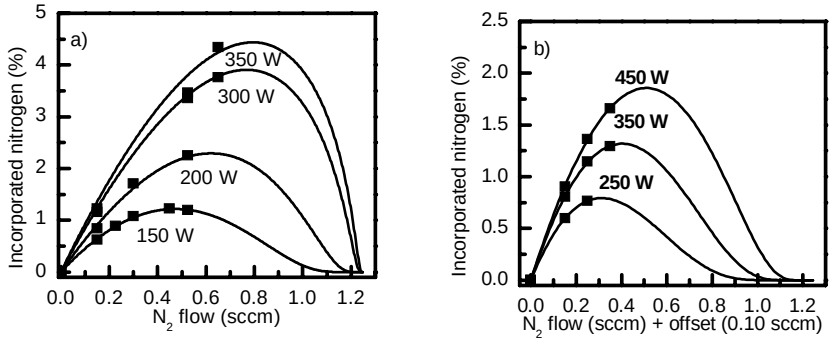

Figure 3.2. *The incorporation kinetics of N as the function of plasma primary power and molecular flow of N. (a) Results fitted for Veeco Gen20 MBE and (b) fitting obtained for V80H reactor. Both systems had Veeco Uni-bulb plasma sources.*

In Figure 3.3 we have used the equation 3.1 to predict the N composition for the growth of lattice matched bulk samples. The maximum error within the tests was 6%. The error analysis shows that the deviation from the model is 4±1%. This shows that the absolute accuracy of the model with well calibrated group-III fluxes would be 1%. In practice this is close to the same accuracy with which the group-III fluxes can be determined by using nude ion gauges for the flux measurement.

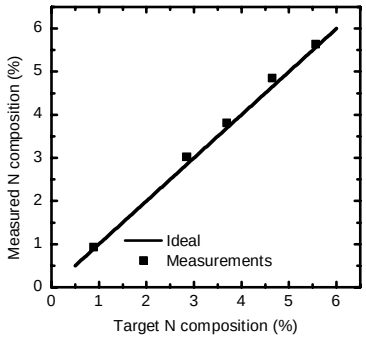

Figure 3.3. *Forecasting accuracy of the derived model for Gen20 reactor. The results show that the model is accurate and has a calibration related drift of only ~4%.*

N related ion incorporation can also be controlled. Control of the ions is essential, as they can easily introduce additional defects to the crystal at the growth front. The ion fluxes have been typically controlled by deflecting them with electric or magnetic fields placed in between the plasma cell and sample surface [103; 104; 122]. The N flux energy also plays a role in the formation of the bonds at the growth front; our preliminary results show that with higher N flux energies a phase separation of the material is more likely. However, in our set-up we have not been able to separate the effects of ions and the energies of N species on the surface properties of GaInNAs and more research is needed for conclusive results.

3.3 Band gaps of GaInNAsSb compounds

One crucial design parameter for any optoelectronic application is the material band gap. For GaInNAsSb there are many possible compositions that can be used to achieve the same band gap and lattice constant, yet they will exhibit different behavior in terms of other material parameters. Therefore, understanding the band gap dependence on In, Sb and N composition is essential for successful epitaxy and applications of GaInNAsSb.

For traditional semiconductors such as GaInAs the band gap can be calculated using a second order polynomic function [24]. However, for dilute nitrides this does not work, because introduction of N splits the conduction band into two different bands termed E_+ and E_- [63]. An accurate estimate of the band gap for dilute nitrides led to the introduction of a band anti

crossing model that takes into account the strong band gap bowing caused by the N atoms incorporated into the crystal lattice [63].

The band gap dependence of GaInNAsSb is more complex to determine: it is not enough to measure the lattice constant by x-ray diffraction (XRD) and determine the band gap by photoluminescence (PL) or transmission spectroscopy, since the material can have many different compositions with the same band gap and lattice constant, unlike the case for GaInNAs. Therefore, a different method is needed in which the In, N or Sb compositions can be fixed. For spectroscopy N is a challenging atom and many methods are considered to be nearly impossible for measuring low N compositions with high precision. In and Sb atoms on the other hand are heavy atoms that are more easy for spectroscopic methods. In paper [P8] we used energy dispersive x-ray spectroscopy analysis to measure the atomic densities of Sb and In atoms from core electron transitions. In addition, we used PL and XRD data to calculate the band gap dependence on the material composition of GaInNAsSb. In addition to the composition dependence, we modified the band anticrossing model for GaInNAsSb. For the modified model, we replaced the band gap of GaInAs with a band gap of GaInAsSb that was interpolated from the band gaps of As and Sb compounds. The excellent accuracy of the new model we devised can be seen in Figure 3.4 (a). The modified band anti crossing model is presented in equation 3.2 for the estimation of the band gap ($E_{g\pm}$).

$$E_{g\pm}(Ga_{1-x}In_xN_zAs_{1-y-z}Sb_y) = \frac{1}{2}\left\{E_M(x,y)+E_N \pm \sqrt{(E_M(x,y)+E_N)^2+4V^2z}\right\} \qquad (3.2),$$

where E_M is the host material band gap, E_N is the nitrogen state, V is the interaction potential, x is In composition, y is Sb composition and z is N composition.

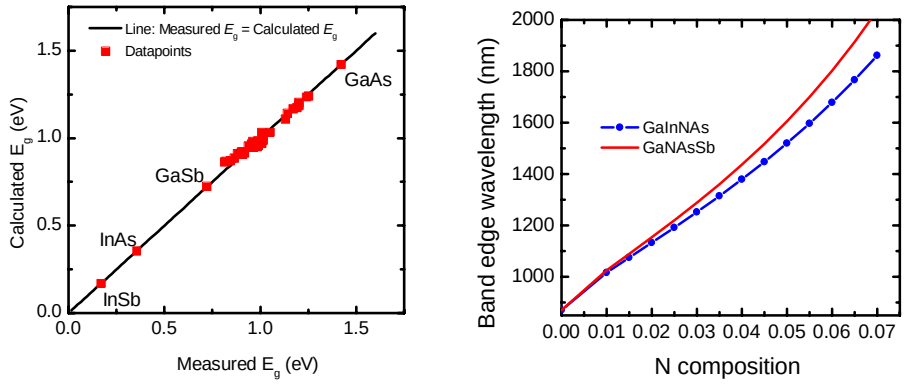

Figure 3.4. *(a) Comparison of calculated band gaps and the corresponding measured values determined with the method presented in [P8]. The accuracy of the model is better than 20 meV for the band gap. (b) Projected band edge wavelengths for lattice matched GaInNAs and GaNAsSb compounds on GaAs.*

In addition to measuring the characteristics of the core electrons of the incorporated elements [123; 124], it is also possible to determine the atomic composition by measuring the properties of atomic nucleus utilizing methods such as Rutherford back scattering [86]. Possible band gaps of the lattice matched GaInNAs/GaAs and GaNAsSb/GaAs compounds as a function of N concentration can be seen in Figure 3.4 (b).

The band gap of GaInNAsSb compounds also has a significant dependence on the bonding environment of the introduced atoms. It is highly probable that the grown GaInNAs crystals will have Ga bonded near N and In bonded near As [102]. It has also been observed that growth conditions and thermal annealing have a great effect on the bonding environment in the crystals [95; 119; 125-128]. For instance, an increase in growth temperature is observed to increase the degree of ordering (see Figure 3.5.) and annealing reduces ordering, which causes a band gap blue shift [119]. The annealing induced blue shift is observed to increase linearly with the growth temperature, revealing growth temperature enhanced ordering effects during the GaInNAs growth. The ordering dependent blue-shift also increases as a function of the In and N composition [129].

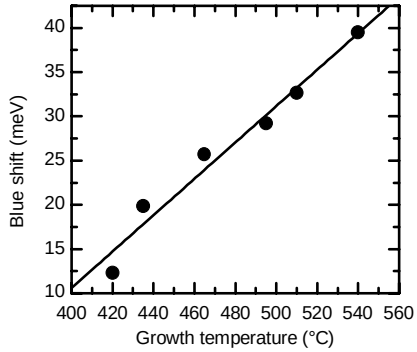

Figure 3.5. *The dependence of GaInNAs blue shift as the function of growth temperature data taken from the publication by Korpijärvi et al. [119]*

3.4 N composition dependent growth dynamics of GaInNAs crystals

For the design of GaInNAs crystal growth, the target N composition is an essential parameter. Generally speaking, the more nitrogen is needed the narrower the growth parameter window becomes, due to the low solubility of N in GaInAs. The ultimate N composition at a certain growth temperature is limited by phase separation. For typical GaInNAs grown at a temperature of 440°C, the N composition limit is approximately 5%, as observed in P1. For an N composition of 3%, the phase separation starts near 500°C. In Figure 3.6, the XRD spectra measured from GaInNAs structures grown at 440°C with different N compositions are presented. The XRD results reveal a widening and lowering of the intensity of the XRD peak corresponding to the GaInNAs epitaxial layer, and less intense spectral oscillations as a function of N composition. These observations suggest that the interface sharpness is deteriorating and the lattice parameter distribution is widening with N composition increase. Ideally, the XRD measurement of the grown GaInNAs structure should look like the simulated single crystal layer XRD-peak presented on top of the measured spectrum for the GaInNAs sample that had 6% of N. For N compositions above 4%, the deviation from the simulated curve is significant. The modelled peak has uniform lattice constant distribution and abrupt interfaces.

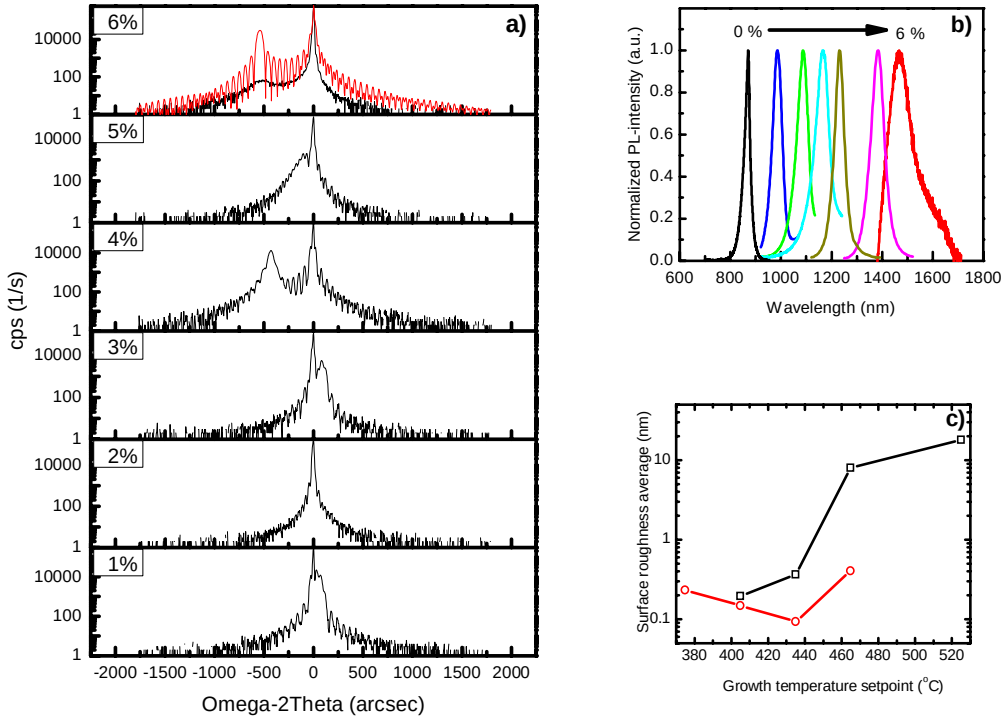

Figure 3.6. *(a) Measured XRD spectrum from lattice matched GaInNAs crystals. The N composition was varied from 1% to 6%. Above 4% N compositions clear evidence of material degradation is observed as a reduction of epilayer peak intensity and widening of the peak. For the 6% N sample the red curve represents a simulated curve calculated by Rads Mercury software. XRD results are published in [P9]. (b) Photoluminescence measurements of lattice matched GaInNAs crystals with 0 to 6% N composition. (c) Roughness averages of GaInNAs surfaces measured by AFM. AFM results were published in paper [P1].*

The phase separation effects of the GaInNAs crystals are also reflected in the charge carrier lifetimes, resulting in lower intensities of PL signals even after optimal RTA (see Figure 3.8). This indicates that not only is the epitaxy roughness limited, but also the charge carrier dynamics are changed significantly and this will reflect negatively on GaInNAs solar cell performance, as will be discussed later.

In [P1] the surface morphology was characterized by atomic force microscopy (AFM). AFM results summarized in Figure 3.6 reveal that even at N composition of 5%, one can achieve smooth layers when using growth temperatures below 440°C. On the other hand, in situ

analysis using high energy electron diffraction (RHEED) corroborated by AFM surface roughness analyses, revealed smooth surfaces for a growth temperature of 440°C when N composition was 3%. AFM analysis also revealed that the phase separation leading to cluster formation is dependent on the crystal directions of the GaAs(100) substrate. The size of such clusters are on the order of tens of nanometers.

In addition to enhancing the phase separation processes, the increase of growth temperature has been observed to result in enhanced N incorporation and activated desorption processes. The results in [P1] and [119], reported on the enhanced incorporation of N (see Figure 3.7). In the paper by Korpijärvi et al. [119] we modelled and analyzed the observed processes with two exponential Arrhenius components from which we calculated the activation energy for enhanced incorporation as 0.1 eV and the activated desorption as 2.1 eV.

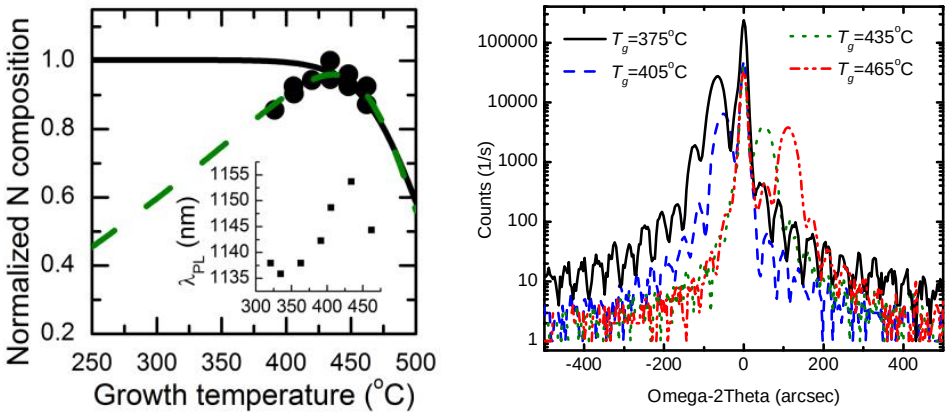

Figure 3.7. *(a) Model for activated N incorporation in the case of thin quantum well samples [119]. (b) XRD measurements for thick GaInNAs samples. The enhanced N incorporation is observed as an epitaxial layer peak position transition from compressive to tensile strain as a function of the growth temperature. The growth temperature enhanced N incorporation has been proved by many methods in paper [P1] and by Korpijärvi et al. [119].*

The effect of the chosen growth temperature on the optical activity after an optimized RTA process was studied by measuring PL. Figure 3.8 shows how the PL intensity is maximized at 415°C growth temperature for all N compositions (i.e. 1%, 2% and 3%). The same trend was observed also from time resolved PL measurements. When the N composition was increased from 2% to 4% the lifetime after optimized RTA dropped from 0.9 ns to 0.3 ns for GaInNAs, as reported in proceedings paper P9. Without annealing, the lifetimes are in the range of 0.02 ns.

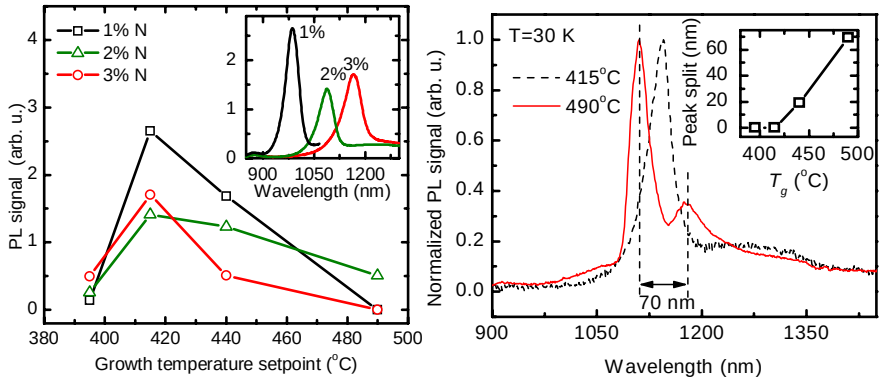

Figure 3.8. *(a) PL intensities of GaInNAs solar cells grown at different growth temperatures. The insert presents the PL spectra from samples grown at 415°C. (b) Low temperature PL measurement from samples grown at 415°C and 490°C. Insert: Observed peak splitting as a function of GaInNAs SC growth temperature. Results published in P1.*

The growth temperature dependence of the PL can be explained by formation of point defects of different kinds [105; 130-132] at the low end of the temperature range, and phase separation effects at the high end of the growth temperature range. The phase separation related effects are also seen in low temperature PL measurements, where phase separation ordering splits the PL spectrum into different components, which become wider when the growth temperature is increased (reported in [P1]). The point defects on the other hand are more difficult to see, and for their characterization we have used deep level transient spectroscopy (DLTS). Thus, we have identified many different impurity levels and the results of the analysis will be published soon. In this thesis, we mainly focus on electrical characterization by Hall-effect measurements, capacitance voltage spectroscopy (CV), light biased current voltage measurements (LIV) and EQE measurements, which will be discussed later.

3.5 Unintentional doping of GaInNAsSb

For GaInNAsSb solar cells one key material parameter is the background doping type and density. GaInNAs typically has relatively short minority carrier diffusion lengths and this limits the design of the cells to the p-i-n type configuration, where it is preferable that the GaInNAs region is fully depleted [67]. In practice, full depletion sets the maximum concentration for the GaInNAs i-region to the 10^{15} 1/cm^3 range and due to the higher mobility of electrons [37; 133],

the i-region has p-type preference. The unintentional doping of GaInNAs can be either n or p type and the background doping depends on annealing conditions [40; 133]

To analyze the GaInNAs solar cell performance, Tukiainen et al. [37] have modeled the effect of background doping on the solar cell performance. For the analysis, we have measured Hall effect characterization using simple epitaxial layers and CV spectroscopy for p-i-n junctions. From the GaInNAs Hall effect data we see that for GaInNAs the p-doping level has an exponential dependence on the N composition and goes over 10^{15} 1/cm^3 when N composition is over ~1.5%. A similar trend has been seen also for MOCVD grown materials [109; 134]. For 1 eV GaInNAs the doping rises to the ~10^{16} 1/cm^3 level, which is not the ideal case for high performance p-i-n GaInNAs solar cells.

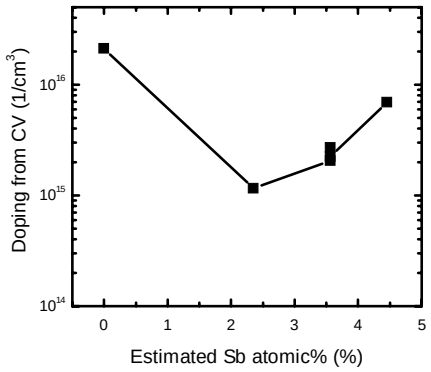

Figure 3.9. *Estimated background doping as a function of Sb composition for GaInNAsSb p-i-n structures measured by CV spectroscopy.*

It has been reported that the incorporation of Sb can reduce GaInNAsSb background doping, thus making wide depletion regions plausible for 1 eV dilute nitrides [71; 135]. We also studied the effect of Sb on the background doping and came to the same conclusion; levels as low as 10^{15} 1/cm^3 were achieved by incorporation of Sb (see Figure 3.9).

Chapter 4

4 Performance of GaInNAsSb solar cells

This chapter connects the findings made on the crystallization processes and crystal characteristics of GaInNAsSb with the performance of single junction solar cells. First we analyze the GaInNAs solar cells and then move on to GaInNAsSb solar cells. For the relative comparison between the samples with different growth parameters, we used heterostructures consisting of p-GaAs/GaInNAs/n-GaAs grown on n-GaAs and p-GaAs. Figure 4.1 presents a schematic structure of cells grown on n-GaAs. In this chapter, all N compositions refer to solar cell materials, where we have 2.7 times more In than N, also for some cells part of the In has been replaced by Sb while maintaining the same lattice constant. This ensured lattice matching and made possible the growth of thick structures necessary for solar cell applications.

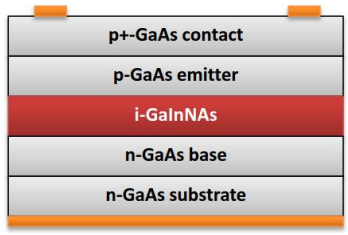

Figure 4.1. *Simple heterostructure used for growth dynamics study.*

4.1 Thermal annealing of GaInNAs solar cells

In chapter 3.3, it was briefly discussed how the annealing affects the N-atom bonding environment and the charge carrier lifetime. This chapter focuses on the effects of annealing on solar cell performance. Annealing has multiple effects on the GaInNAs crystal. It has been observed that the doping density and doping type can change [40; 133]. Also, the annealing introduces a band gap blue-shift that reduces the bandwidth for photon absorption under GaAs band gap energy [119]. The effect of RTA on the solar cell performance is presented in Figure 4.2. After optimized RTA, the GaInNAs solar cell power generation, fill factor and open circuit voltage increase significantly, but RTA may result in lower current generation, as shown in this example. The current generation is dependent on the resulting band gap and the type and density of the GaInNAs background doping. The improved voltage and fill factor are caused by the improved charge carrier lifetimes, as reported by, for example, Gubanov et al. [41].

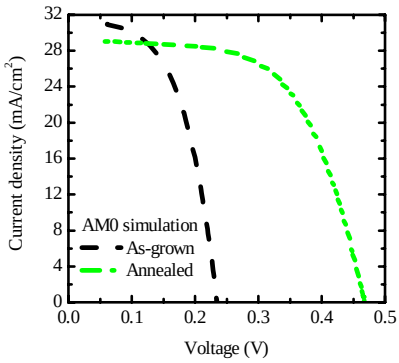

Figure 4.2. *The effect of post growth annealing on the IV-performance of a 1 eV GaInNAs solar cell. The annealing improves the open circuit voltage significantly and reduces device shunt resistance. On the other hand, the cell current generation is sacrificed slightly.*

The changes in the doping prolife of a p-i-n diode has been studied by kelvin probe force microscopy (KPFM), where the internal potential of the junction is profiled by atomic force microscopy [136]. The analyzed KPFM measurements reveal that the GaInNAs material has n-type background doping without annealing and becomes p-type after annealing. The doping type change observed here is also supported by Hall-measurements of 3000 nm thick samples grown on semi insulating GaAs substrates, where the background doping changed from ~10^{15} 1/cm^3 n-type to high 10^{16} 1/cm^3 p-type. All these findings were confirmed by simulation of the

structure with the obtained parameters (results to be published by Tukiainen et al). The simulated IV and EQE characteristics fitted each other well, confirming the physical phenomenon. Doping profile changes have also been reported based on observed changes in the IQE profile [133; 137]. The Optimal RTA treatment depends on the growth parameters and on the N composition, the observations made on these dependencies will be discussed in chapter 4.3.

4.2 The effect of N composition on the GaInNAs solar cell performance

The band gap of GaInNAs shrinks as a function of N and In composition. In theory, the current generation increases nearly linearly with N and In composition, as can be seen from Figure 4.3. Figure 4.3 shows three different current density curves calculated from an AM1.5G spectrum [72] by assuming three different average EQEs of 45%, 70% and 100% (theoretical maximum value). Our experiments show that for thin solar cells (~300 nm) the current generation increases with increasing N composition, up to an N composition of 4%. However, with higher compositions, the growth of uniform GaInNAs crystals becomes extremely challenging, as described in chapter 3.4. The formation of clusters results in an increase of the device shunt leakage and far from ideal cell performance is thus achieved (see results reported in [P1]). For high quality GaInNAs crystals with long charge carrier lifetimes and low background doping, it is possible to increase the current generation with thicker GaInNAs i-regions of a few microns. The optimal thickness depends on the diffusion length of the material and on the i-region doping density [37; 67; 135].

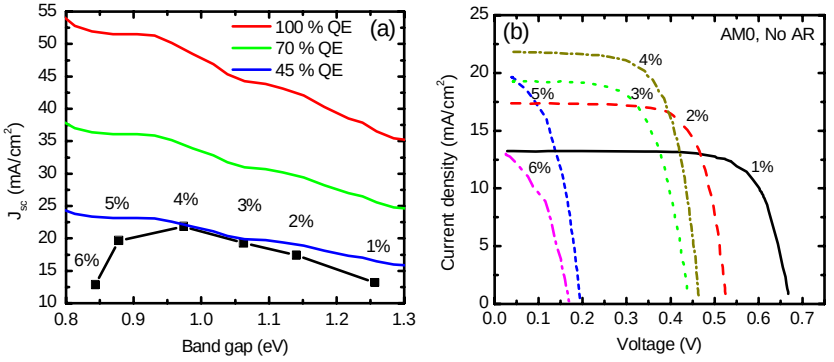

Figure 4.3. *(a) Calculated current densities obtainable for GaInNAs solar cells with different band gaps. Solid lines present the constant average EQE lines for the current generation potential and data points present the results obtained for thin 300 nm thick GaInNAs solar cells. (b) Measured IV-characteristics of thin lattice matched GaInNAs solar cells with N compositions up to 6%.*

GaInNAs solar cell performance is not only dependent on the maximum current achievable, but also on the maximum voltage obtainable under open circuit conditions. The V_{oc} values for GaInNAs cells with different band gaps are presented in Figure 4.4. In addition, the *FF* of the GaInNAs cell is dependent on the N composition and band gap; Figure 4.4 also presents the *FF* dependencies for GaInNAs cells. To maximize the output power from the full multijunction device the dilute nitride cell I_{sc}, V_{oc} and *FF* should have the maximum possible values, and therefore the selection of the correct band gap plays a significant role in the multijunction cell efficiency, as can be seen in the following chapter.

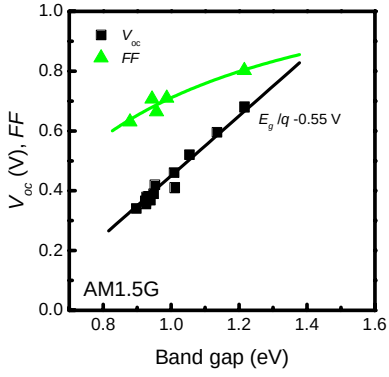

Figure 4.4. *Measured V_{oc} and FF values for GaInNAs solar cells measured at close to AM1.5G conditions.*

4.3 Growth optimization for GaInNAsSb single junction solar cells

Growth conditions play a significant role in achieving high efficiency III-V solar cells [67; 119; 126; 133; 135; 138]. This chapter summarizes the interplay between the growth conditions and the performance of GaInNAsSb solar cells.

Growth temperature dynamics of GaInNAs solar cells

As a metastable compound, GaInNAs has a very narrow growth parameter window, when compared to GaAs. The window is limited by phase separation effects and point defect formation at the low growth temperatures required by the metastable nature of the compound. These effects were discussed on the bulk level in chapter 3.4. The influence of these effects on GaInNAs solar cell performance were studied in paper [P1]. In this paper, we observed that for high solar cell performance it is essential to grow uniform materials. This is especially true for V_{oc} performance, as if even a slight amount of clusterization or unideal short range ordering is present in the crystal, the V_{oc} will decrease, which can be seen from Figure 4.5. The growth temperature induced ordering and clustering effects also make the crystal harder to anneal, requiring longer annealing times, as seen in Figure 4.5 (c). It might be that the ordered or phase separated areas act as shunt channels that increase the leakage current and lower V_{oc}, but do not yet significantly decrease shunt resistance as was seen in Figure 4.3 (b) for 5% and 6% N compositions.

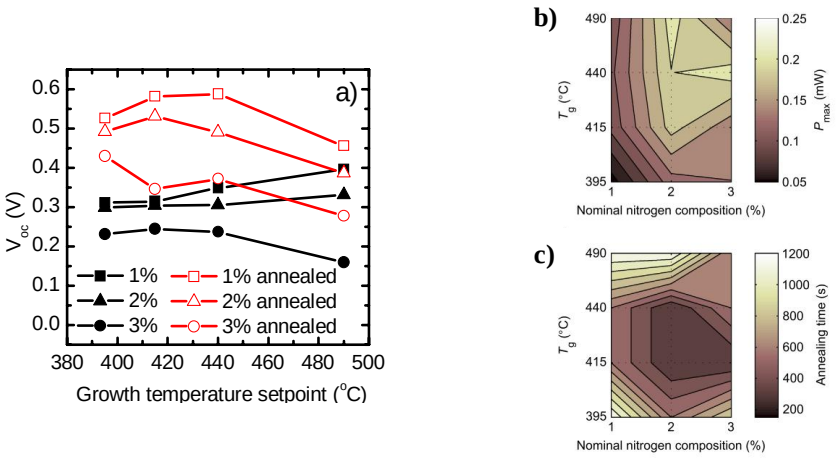

Figure 4.5. *Growth temperature dynamics of GaInNAs solar cell open circuit voltage (a), cell maximum power (b) and required annealing time for maximum power (c). Results published in P1.*

As a compromise for the growth temperature we found 440°C to yield the best results for the cell power and average EQE for the entire range of studied lattice matched compositions. At this growth temperature, the mutual sum of harmful point defect formation and the leakage caused by phase separation is minimized. Figure 4.6 presents a comparison of single wavelength EQE values for GaInNAs SCs grown with different growth temperatures and with 3% N.

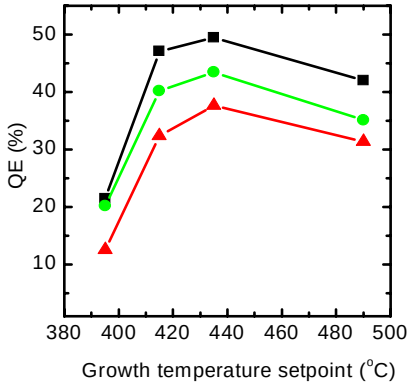

Figure 4.6. *Measured EQEs at 900 nm (squares), 1000 nm (circles) and 1100 nm (triangles) for optimally annealed 3% N solar cells grown at different growth temperature. Samples were left uncoated. Results published in P1.*

The second growth parameter studied in this thesis was the As/III BEP ratio. This ratio is between the measured As pressure value and the measured sum of group-III atomic fluxes. Because of low GaInNAs growth temperatures, it is logical that the compound defect density is sensitive to the selected As pressure. We have studied the As pressure related effects on the GaInNAs solar cell performance in P10 and P3 papers. Figure 4.7 shows the generic trend of the As/III-BEP ratio effect on the GaInNAs solar cell maximum performance. We see that between 7.5-10 the cell output power and efficiency peak. If the selected As pressure value is lower than 7.5, a rapid drop is observed for the cell performance and if the value is higher than 10, the drop is slower but the slope is almost constant.

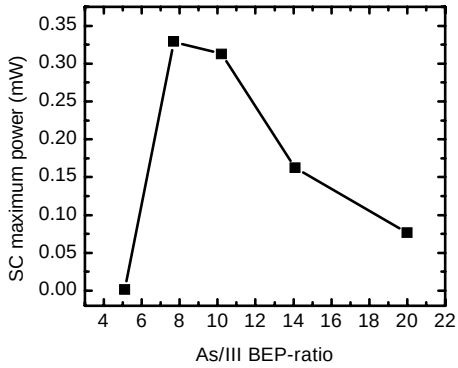

Figure 4.7. *GaInNAs SC power as a function of the As/III BEP-ratio. The plotted SC power for each data point is an average of two sample sets. Results published in P10.*

It is also possible to alloy atoms other than In for the lattice matching of the crystal, when N is used. Especially good results have been reported for the use of Sb to replace some of the In atoms in the crystal lattice [71; 115; 135]. In chapter 3.1 and [P8], we have shown how the incorporation of Sb has a faster band gap shrinking effect than In per composition percentage. In practice this means that slightly less N is needed to achieve the same band gap value, and it is therefore easier to avoid the phase separation effects. Another benefit is that Sb is known to be an effective surfactant for III-V semiconductor material growth and it therefore also aids the uniform distribution of atoms during the growth [97; 99; 115; 139]. In this thesis we did not perform any atomic level investigations on the Sb atomic spacing and incorporation, but the

macroscopic effect of the use of Sb atoms in the growth is reported as the total effect on the performance of single and multijunction solar cells.

4.4 Performance of optimized GaInNAsSb solar cells

This chapter summarizes the results obtained for optimized single solar cells in this work. In the previous chapter, we discussed the effect of the microscopic properties on the GaInNAsSb solar cell performance and the effect of annealing, N composition and growth parameters on the performance of single junction cells. In this chapter, the current generation of a 1 eV band gap GaInNAsSb sub-cell is pushed to the maximum, so that the maximum efficiency for dilute nitride multijunction concepts can be achieved. We also included phosphate based window layers in the structure to improve the surface recombination rates [4] of the devices. Figure 4.8 presents the solar cell layer structure for the studies in this section.

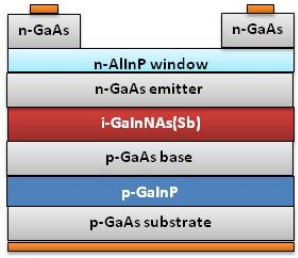

Figure 4.8. *Schematic structure of dilute nitride solar cell for high current generation.*

EQE performance of thick GaInNAsSb solar cells

Here we review how the performance of thick GaInNAsSb cells depend on the GaInNAsSb quality. Figure 4.9 presents the EQE performance of six thick GaInNAsSb solar cells with different performances. We have also calculated the J_{sc} values for AM1.5G, AM1.5D and AM0, the results are collected in Table 4.1. For the calculation of the J_{sc} values equation 4.1 [4] and the ASTM G 173-03 spectrum were used [72].

$J_{sc} = e\int_0^{\infty} QE(\lambda) f(\lambda) d\lambda$ (4.1), where $f(\lambda)$ is photon flux (1/s/nm).

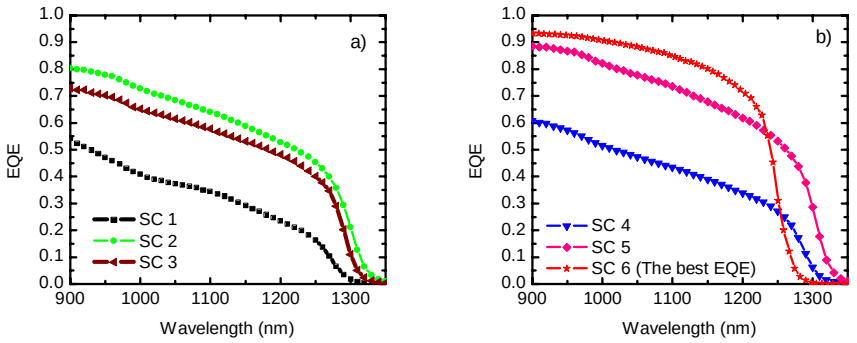

Figure 4.9. *EQE of GaInNAsSb solar cells with different performances. (a) Cells grown with different thicknesses and (b) cells with different background doping. The measured parameters from the cells are summarized in Table 4.1.*

Table 4.1. The performance of 1 eV band gap GaInNAsSb solar cells.

Cell	**J_{sc} (mA/cm^2) AM0/AM1.5G/AM1.5D above 900 nm**	**V_{oc} (V) at one sun**	**Thickness (nm)**	**Lifetime (ns)**	**Background doping (1/cm^3)**
1	7.4/5.8/5.4	0.44	300	~ 1 ns	2×10^{16}
2	14.7/11.1/10.5	0.43	1200	~ 1 ns	2×10^{16}
3	12.5/9.9/9.3	0.44	3000	~ 1 ns	2×10^{16}
4	9.6/7.5/7.1	0.41	1200	~ 1 ns	3×10^{16}
5	16.1/12.7/12.0	0.43	1200	~ 1 ns	8×10^{15}
6	17.3/13.6/13.0	0.44	2000	~ 1 ns	$\sim1\times10^{15}$
Est. from Ref. [71]	16.3/12.8/12.1	0.3	1000	0.2 ns	6.3×10^{15}
Est. from Ref. [133]	14.2/11.1/10.5	0.2	1500	-	-
Ideal cell (1 eV QE = 1)	19.4/15.2/14.3	0.6	thick	~14 ns*	1e17*

*Values assuming the performance level of GaAs, see Table 2.1 for details.

Table 4.1. also includes the measured variables from the cells: V_{oc} values for each cell at one sun excitation, i-region thickness, estimated charge carrier lifetimes, and background doping values. From the results it can be seen that the charge carrier lifetime limits the open circuit voltage, and that background doping limits the depletion of the GaInNAsSb region, which sets the depletion area width for efficient charge carrier collection. If the charge carrier lifetimes are

long and the i-region active doping is low enough, the charge carrier collection efficiency can be improved by increasing the i-region thickness up to approximately 3000 nm. In this work, we have limited the thickness to 2000 nm as a compromise for the highest performance. For ultimate performance it is clear that the thickness might be thinner or thicker than the selected value. By comparing the Table 4.1 values, we can see that the doping density needs to be below 8×10^{15} 1/cm^3 to achieve over 90% EQE values. The material quality of the crystal also effects the V_{oc} values and the best way to compare the values to each other is to use the term band gap voltage offset (W_{oc}), which is defined as $V_{oc}=E_g/q-W_{oc}$, where V_{oc} is measured under one sun conditions. For the highest quality III-V solar cells the W_{oc} value is close to 0.4 V, but traditionally for dilute nitrides the value has been larger, typically 0.6 V in many scientific reports [59]. We have measured values from 0.7 V to 0.47 V for non-optimized growth parameters and optimized parameters, respectively. Figure 4.10 (a) shows V_{oc} data from various GaInNAsSb solar cells studied in this work. The same figure also includes the values for typical GaInP and GaAs III-V solar cells grown by MBE in this work.

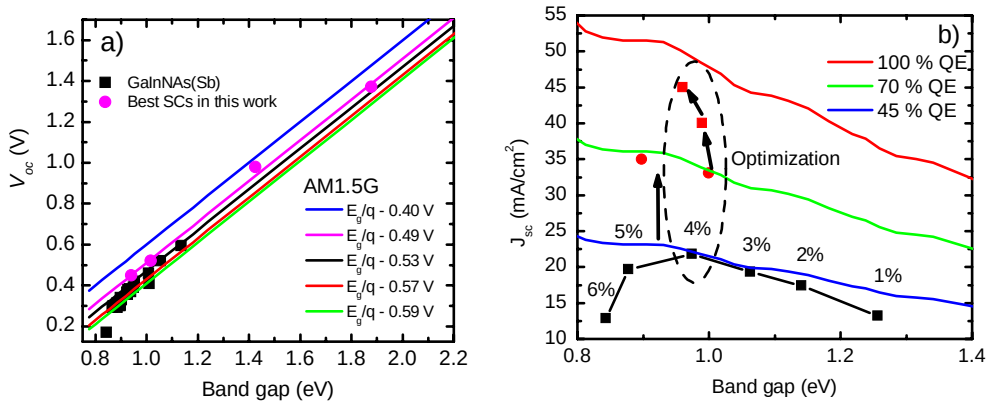

Figure 4.10. *(a) Measured open circuit voltage values for GaInNAsSb solar cells with different band gaps and best cell V_{oc} for this work up to 1.9 eV. To the same figure we have also added the values obtained for GaInP and GaAs solar cells in this work. (b) J_{sc} values for GaInNAsSb solar cells with different band gaps. Currently the current generation efficiency is approaching the ideality limit.*

The absolute current generation performance of the fabricated GaInNAsSb solar cells can be seen in Figure 4.10 (b), where the absolute performance is compared to the average EQE trends calculated for an ASTM 173-G AM1.5G spectrum as a function of GaInNAsSb solar cell band gap. The band gap is determined from the PL peak position.

Compared to the beginning of the thesis research plan we have been able to improve the GaInNAsSb cell average EQE values from 30% to close to 90% on average, over the whole measurement spectrum below the band gap wavelengths. For this development graph, the optimization iteration data points represent the best value for each iteration, so the practical number for grown solar cells is significantly larger. It also includes many different post process optimization rounds for each development step presented in this graph. The simulation of the structures plays a large role for the understanding and developing of the GaInNAsSb solar cells. Our preliminary simulation results have been published in [37]. Detailed simulation of cell performance for different charge carrier lifetimes, background doping levels and realistic mobility values also proved excellent fit (to be published) to the experimental EQE and IV characteristics demonstrated in this thesis.

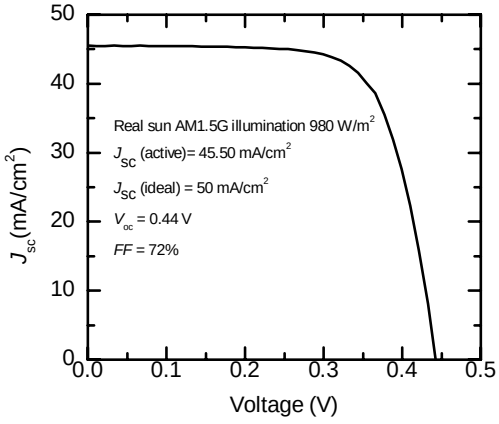

Figure 4.11. *IV-performance of the best GaInNAsSb solar cell measured under AM1.5G real sun conditions. The spectral irradiance was measured by a Kipp&Zonen pyranometer and the power density of the irradiation was 980 W/m^2.*

Figure 4.11 presents the best IV-performance achieved for a GaInNAsSb single junction solar cell fabricated in this work. The corresponding EQE of this cell is also presented in Figure 4.9 b. This result represents state-of-the-art GaInNAsSb cell performance and this material is also the workhorse for the GaInP/GaAs/GaInNAsSb solar cell results presented in the following chapter.

Chapter 5

5 Dilute nitride multijunction solar cells

In this chapter, we focus on the modeling, fabrication and characterization of high performance dilute nitride multijunction solar cells. For multijunction cells the same characterization methods can be used as for single junction cells, but the spectral sensitivity and accuracy of the measurements are more demanding.

5.1 Design of dilute nitride multijunction solar cells

For multijunction solar cells, the structural design plays a greater role in the device performance than it does for single junction solar cells. One key difference from the design point of view is that the top cell needs to pass a sufficient amount of photons to the cells below, so that the bottom cells can produce the same amount of current. How much light the top cell needs to pass to the bottom cells depends on the top cell and bottom cell(s) EQE performance. The design strategy starts from the setting of the top and bottom cell band gaps and the desired operation spectrum. Next, the number of sub cells needs to be decided and then the generated J_{sc} of the multijunction cell can be estimated. For the next step, the middle cell(s) band gap can be selected from the available materials. At this point, the theoretical maximum efficiency can already be estimated by assuming feasible average EQE values for the sub cells and diode

characteristics based on single junction cells. For the performance estimation of the multijunction devices, projective diode models were used. In papers [P5] and [P11] we estimated the efficiencies for AM1.5 and AM0 spectra. In the calculations, we used GaInP/GaAs/GaInNAsSb and GaInP/GaAs/GaInNAsSb/Ge architectures. An example of a GaInP/GaAs/GaInNAsSb structure is presented in Figure 5.1.

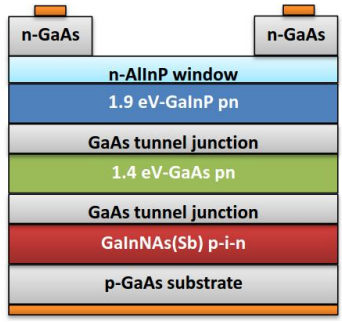

Figure 5.1. *Schematic picture of GaInP/GaAs/GaInNAs solar cell.*

Simulation of GaInNAsSb MJSC solar cell performance

We used diode equations for the simulation of the GaInP/GaAs/GaInNAsSb and GaInP/GaAs/GaInNAsSb/Ge solar cell performances based on equations 2.3 to 2.5 (chapter 2.3). Since the performance of GaInP/GaAs and GaInP/GaAs/Ge cells have already been optimized by many groups, the variables in our projective model were related to GaInNAsSb sub cells: quality measured by average EQE, band gap, and thickness. Figure 5.2 a presents the J_{sc} for GaInNAsSb sub-cells with different band gaps and with different average EQE performances. In Figure 5.2 b, the current matching window for GaInNAsSb placed under thick GaAs in the GaInP/GaAs/GaInNAsSb configuration is drawn. In this figure we have highlighted the average EQE and band gap area where the incorporation of a GaInNAsSb bottom cell is feasible. In practice, this sets the band gap window for the GaInNAsSb sub-junction in the GaInP/GaAs/GaInNAsSb device, from 0.9 to 1.04 eV.

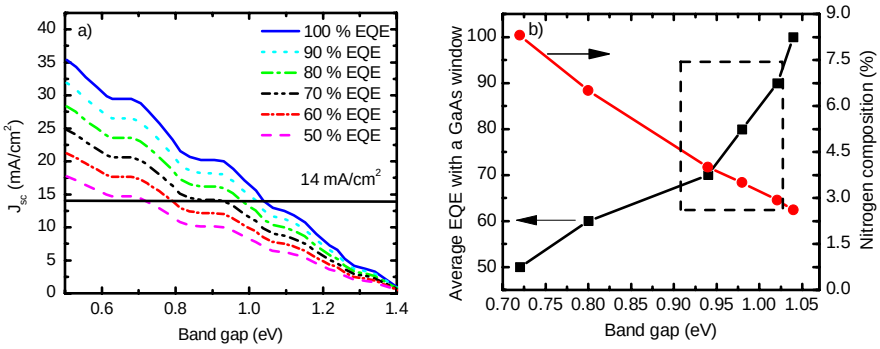

Figure 5.2. *Calculated J_{sc} for GaInNAsSb sub-cell (a) and realistic AM1.5G current matching window for GaInP/GaAs/GaInNAsSb SC (b).*

An attractive design aspect for the GaInNAsSb sub-cell is that the thickness and band gap of high quality GaInNAsSb can be rather freely optimized, so that the highest performance will be achieved for each application spectrum and concentration value. The generated current follows the absorbed light amount, which is close to exponentially dependent (Beer-Lambert law) on the semiconductor thickness. Figure 5.3 shows the thickness required for the current matching under thick GaAs in the GaInP/GaAs/GaInNAsSb/Ge configuration for different band gaps. The estimates for the required thicknesses are gathered from publications [42; 140].

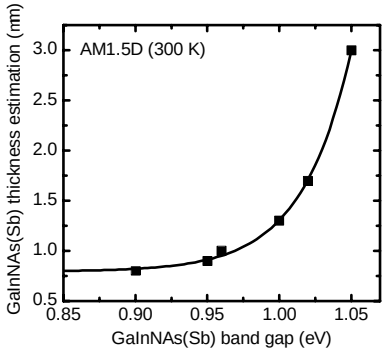

Figure 5.3. *Estimated GaInNAsSb junction thicknesses for current matched GaInP/GaAs/GaInNAsSb/Ge solar cell, the thicknesses are approximated from the publications by Friedman et al. [42] and Kirk et al. [140].*

It should be noticed that thicker cells are more demanding in terms of background doping and diffusion length limits for the GaInNAsSb junction. Therefore, an understanding of the optimal

band gap and thickness combinations becomes essential, especially if the material has high background doping and short diffusion lengths [37; 67; 104]. The option to use different band gaps for the GaInNAsSb junction gives the advantage that the junction can be significantly thinned down with the same current generation if the band gap is shifted towards smaller values. These thicknesses are calculated for GaInP/GaAs/GaInNAsSb/Ge devices, but they also provide a good understanding of how much the cell can be thinned down for triple junction cell if the cell band gap is reduced by, for example, 0.1 eV. The drawback of reducing the band gap is that the voltage of the multijunction cell will be lower, but simultaneously the cell fabrication costs can be reduced significantly by faster and cheaper epitaxy. This option was used as an input for the performance modelling. Figure 5.4 presents the estimated potential of GaInP/GaAs/GaInNAsSb and GaInP/GaAs/GaInNAsSb/Ge cells incorporated with GaInNAsSb cells with different performances. The individual sub-cell performances for GaInP, GaAs and Ge were estimated from publications and datasheets [141; 142] and the GaInNAsSb cell performance was estimated from the data gathered for GaInNAsSb single junction cells during this work. A detailed description of the modelling process for the sub-cells and multijunction cells is given in [P5] and [P11].

The simulation results for AM1.5G and AM1.5D from paper P5 show that, especially for the AM1.5D spectrum, the four junction design can provide a significant efficiency improvement when compared to the triple junction design. For the calculations with the AM1.5D spectrum, the GaInAsSb sub-cell was set to be current matched or to be overgenerating current in the triple junction cell. Similarly, for four junction cell calculations, the cell was set to be undergenerating and to be current matched. For the triple junction design the calculated practical maximum efficiency is 33.6% at one sun, and up to 1.7 percentage points higher efficiencies can be calculated for the four junction design. For a band gap of 0.9 eV instead of 1.0 eV, the cell will have only 1.4 percentage points lower efficiency, so with cell production in mind the 0.9 eV junction might be an attractive choice, since the sub cell could be ~2 μm thinner. The results, however, depend on the spectrum, and since for an AM1.5G spectrum the J_{sc} of the triple junction (3J) can be significantly higher than for a four junction cell (4J), the practical efficiency for this band gap combination will be ~1 percentage points higher for the triple junction cell. For better four junction cell design, all the sub-cell band gaps should be better matched to the AM1.5G spectrum. The simulation results for AM1.5D are listed in the Table 5.1 and the calculated IV-curves are plotted in Figure 5.4. For increased AM1.5D

concentrations, the efficiency increases significantly for both designs. By assuming a realistic series resistance value of ~5 mΩcm^2 for the multijunction cells, the cell efficiency can improve up to 46% for a triple junction cell and between 47 to 50% for a four junction cell at 300 suns concentration. Therefore it is clear that for new world records with over ~46% efficiency [143; 144], at least four junctions are needed.

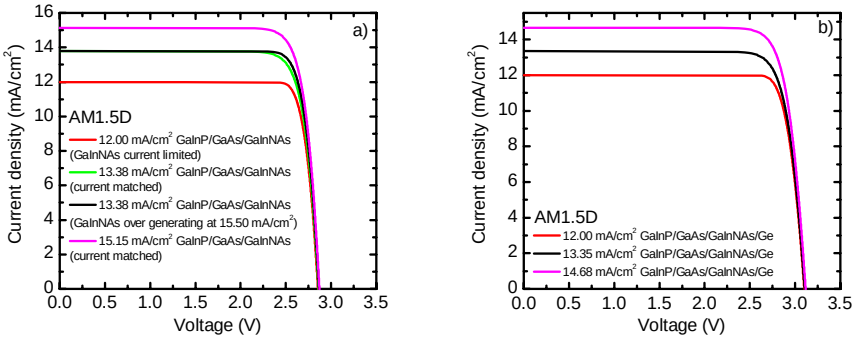

Figure 5.4. *(a) The calculated I-V-performance for GaInP/GaAs/GaInNAs triple junction solar cell structures and GaInP/GaAs/GaInNAs/Ge four junction devices with AM1.5D excitation.*

Table 5.1. Estimated one sun efficiencies of GaInNAsSb multijunction solar cells at AM1.5D.

Structure	Spectrum	J_{sc} (mA/cm^2)	V_{oc} (V)	*FF*	*h* (%)
GaInP/GaAs/GaInNAs	AM1.5D	13.79	2.86	83.05	32.76
GaInP/GaAs/GaInNAsSb (0.90 eV)	AM1.5D	13.79	2.76	82.52	31.36
GaInP/GaAs/GaInNAs (15.5 mA/cm2)	AM1.5D	13.79	2.87	84.98	33.58
GaInP/GaAs/GaInNAs	AM1.5D	15.15 (Ideal 3J)	2.87	82.97	36.08
GaInP/GaAs/GaInNAs/Ge	AM1.5D	12.00	3.10	86.20	32.08
GaInP/GaAs/GaInNAs/Ge	AM1.5D	13.35	3.11	82.71	34.36
GaInP/GaAs/GaInNAs/Ge	AM1.5D	14.68 (Ideal 4J)	3.12	82.65	37.79

Similar calculations were also performed for AM0 in the paper P11, but in this paper we focused only on the 1-sun calculations, since currently the majority of space photovoltaic applications are based on one sun AM0 concentrations (see Table 5.2. for calculated performance). As the for simulation results, we calculated that by changing the performance of the limiting GaInNAs sub-cell within reasonable limits, efficiencies from 25.6% to 30.7% could be achieved for the triple junction design. We do anticipate that the voltage of the GaInNAsSb

sub-cell can be improved, so that the ultimate efficiency may be at least 1 percentage point higher.

Table 5.2. Calculated efficiencies for dilute nitride based 3J and 4J space solar cells under AM0 excitation.

Structure	Spectrum	J_{sc} (mA/cm^2)	V_{oc} (V)	*FF*	η (%)
GaInP/GaAs/Ge commercial ref. [145]	AM0	17.7	2.746	86	30.6
GaInP/GaAs/GaInNAs (GaInNAs lim.)	AM0	14.1	2.849	87	25.6
GaInP/GaAs/GaInNAs	AM0	17.7	2.861	83	30.7
GaInP/GaAs/GaInNAs/Ge (GaInNAs lim,)	AM0	14.1	3.134	87	28.1
GaInP/GaAs/GaInNAs/Ge	AM0	17.7	3.144	82	33.5

The GaInP/GaAs/GaInNAsSb/Ge four junction cell can have up to 2.8 percentage points higher efficiency than the triple junction cell, resulting in efficiencies between 28.1 to 33.5%, depending on the GaInNAsSb sub-cell J_{sc} performance. Also in this case we believe that the GaInNAsSb sub-junction V_{oc} can be significantly improved, since the calculation in [PP3] was based on a GaInNAs cell with poorer performance than the best GaInNAsSb cell. This means that the best GaInP/GaAs/GaInNAsSb/Ge might break the 35% efficiency barrier.

5.2 Epitaxy optimization for multijunction architectures

For three and four junction cells, well over 40% cell efficiencies are possible under concentrated light. The epitaxy of such devices is indeed very demanding. For efficiencies over 40%, the first requirement for the grown wafer is that the multijunction solar cell structure to be incorporated with proper thicknesses, band gaps, doping levels and diffusion lengths. Simultaneously, the interfaces need to be sharp and the roughness of the whole grown structure low enough to meet the demands of post processing and thin tunnel junctions. The growth is also followed by post processing, which includes thermal treatments, etching steps and contact metal depositions with and without metal grid patterns. Altogether the III-V multijunction solar cell process is dependent on many different processes. Therefore, if some of the steps are not optimized, the resulting cell's performance is limited by the non-optimized process step. This

chapter focuses on the description of the multijunction solar cell growth optimization steps aiming to achieve efficiencies of over 40%.

Designing growth for dilute N multijunction solar cells

Traditionally it has been a challenge to achieve high enough current generation for dilute nitride cells with close to 1 eV band edges [64; 65; 67; 107; 109; 133-135; 137]. It is highly probable that if the dilute nitride growth is not optimized, the current generation in GaInP/GaAs/GaInNAsSb will be approximately half of the achievable maximum, and therefore roughly only half of the efficiency potential can be harvested. For this reason, it was clear during the early stages of this thesis that we could utilize the highest development potential by first developing the dilute N cell process to a sufficient level, so that the use of GaInNAsSb sub-cells would be viable in real world applications. In the beginning, we saw rapid improvements in GaInNAsSb cell performance; Figure 5.5 summarizes the development trend for the 1 eV band gap cell during the development years.

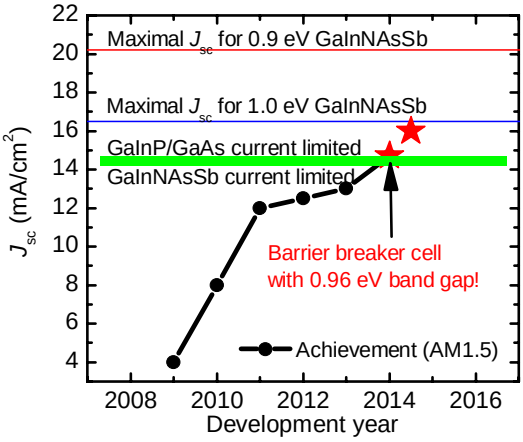

Figure 5.5. *J_{sc} development for the 1 eV GaInNAsSb cell plotted for years of dilute nitride solar cell projects. The stars represent the data points that surpassed the current limitation condition for GaInNAsSb sub-cell in GaInP/GaAs/GaInNAsSb cell.*

From Figure 5.5 we also see how extremely challenging it became to improve the current generation, and during the years 2010 to 2012 no significant breakthroughs were made. Starting from 2013, however, the cumulative understanding of the GaInNAsSb growth dynamics started to result in significant and constant progress for the current generation performance, and during

spring 2014 we were able to produce a cell that generated more than the GaInP and GaAs top cells generate at AM1.5G and AM1.5D, meaning that the dilute nitride junction was no longer the limiting junction for the GaInP/GaAs/GaInNAsSb cell, making high efficiencies possible.

We had already started to incorporate dilute N sub-junctions into a 3J cell in 2011, and the first structure was not only current limited by the dilute N sub-junction, but also by the performance of all of the five pn-junctions (three cell solar cell junctions and two tunnel junctions) incorporated into the 3J cell structure. After incorporation of one extra sub-junction and tunnel junction, it was clear that everything needed to be optimized together for the final integration of all five sub-junctions. Problems for multijunction integration arise from many different origins, and one of the greatest problems is how to handle the thermal stress for the junctions below when the top junctions are grown. In order to understand all the different MBE process related variables, a graphic was drawn where the main variables are linked together by a sphere. The optimization sphere is presented in Figure 5.6.

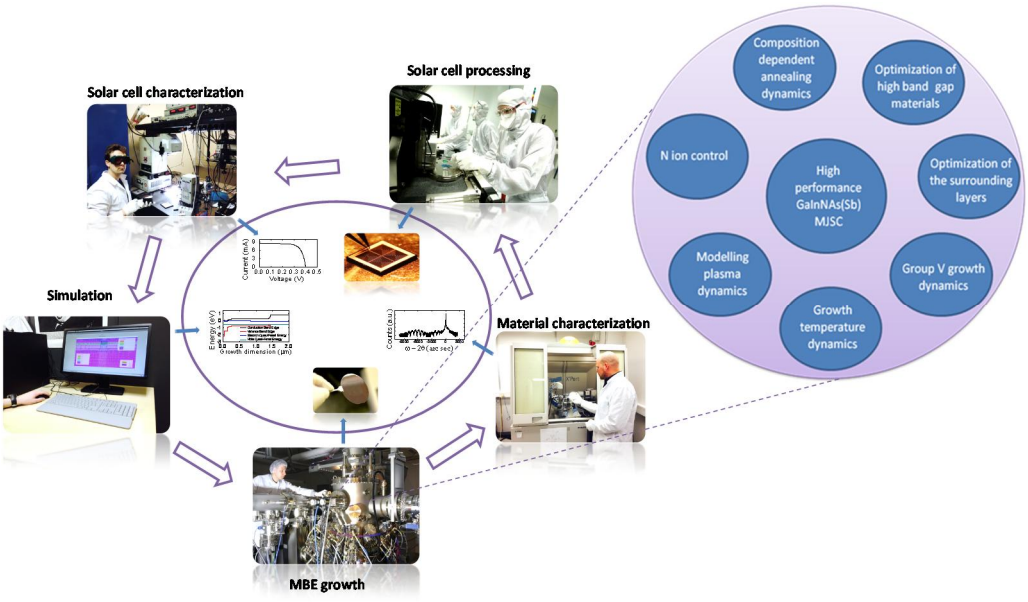

Figure 5.6. *Growth optimization space of GaInNAsSb multijunction solar cells.*

Fortunately MBE is a flexible tool so that many of these variables can be optimized separately, but the separately optimized sub-sections always need to be tested in larger sub-pieces and

finally incorporated into the final 3J structure. The sphere was drawn as a dilute N centered approach, but the same kind of strategy can be centered on tunnel junctions other sub-junctions.

Generally speaking, the thermal stress bottleneck for multijunction cells is the diffusion and activation of dopants in the tunnel junction, where the junction should have as high as possible doping levels and atomically sharp interfaces. For Be and Si, which are the traditional MBE dopants for p and n doping, respectively, there are a few problems related to the tunnel interface. Be, as a small atom, tends to have a high diffusion constant [146] and Si on the other hand has an amphoteric nature, causing compensation of the n type doping level at the close to 10^{19} 1/cm^3 concentrations that are needed for high current and low resistance tunnel junctions [58]. Both these processes are thermally activated, and therefore low temperature growth makes high concentrations and sharp interfaces plausible. For growth condition tuning, with the tunnel junctions in mind, the MBE process is more flexible for fine tuning of the growth than MOCVD, since the precursors in the MBE process do not need to be thermally activated or cracked at the growth front for the efficient incorporation of the dopants or group III or group V atoms [22].

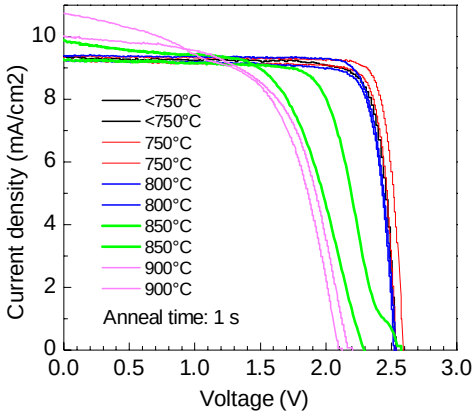

Figure 5.7. *IV-performance of GaInP/GaAs/GaInNAsSb solar cell annealed at different RTA temperatures. Tunnel junction(s) start to fail at high annealing temperatures; the physical reason for the exact process is under investigation.*

Figure 5.7 presents the *IV*-performance of a 3J cell structure annealed using RTA at different temperatures. From here it is clear that if the temperature is kept under 800°C, the tunnel junctions can withstand the annealing related thermal load. At higher temperatures the active

doping of the tunnel junction starts to change, and the possible reasons for this phenomenon could be inter diffusion of doping atoms near the tunnel junction interface, or the changes in the type and activation of the doping species on either side of the pn-tunnel junction. The performance of a single tunnel junction can be evaluated from separately processed and mesa etched tunnel junction diodes. Table 5.3 lists the key parameters of tunnel junction devices reported in the literature. The table also lists the tunnel junction results achieved in this thesis.

Table 5.3. Performance of GaAs based tunnel junctions designed for multijunction solar cells.

Growth method	Structure	Maximum tunneling current density (A/cm^2)	Forward tunneling peak voltage (V)	Series resistance ($m\Omega cm^2$)	Voltage drop at 1 sun (mV)	Voltage drop at 1000 suns (mV)	Voltage drop at 5000 suns (mV)
MBE	n-GaAs/p-GaAs [this work]	493	0.15	0.19	2.7×10^{-3}	2.7	14
MBE	n-GaInP/p-AlGaAs [this work]	181	0.09	0.33	4.7×10^{-3}	4.7	24
MBE	GaAs/ErAs/GaAs [147]	20 000	0.13	0.18	2.5×10^{-3}	2.5	12
MOCVD	n-GaAs/p-AlGaAs [148]	10 100	0.25	0.02	0.3×10^{-3}	0.3	1.5
MOCVD	p-AlGaAs/GaInP [149]	996	0.10	0.07	1.0×10^{-3}	1.0	4.7

Figure 5.8 presents the efficiency optimization results of the iterative process starting from 2011. We have been able to improve the 3J cell efficiency by a slope of 5.2 points efficiency per year, and this year the projection hits the efficiencies predicted from the calculations discussed in chapter 5.1. From this point the trend for the 3J cell will start to saturate due to physical limitations of the design. Therefore, we have started to focus on the optimization of 4J design that would enable the trend to continue. In addition we are developing our metal grids and cell dimensions to work better with higher concentrations, making it possible to utilize the full

potential of our epitaxial chip. The characteristics of the cells with the highest efficiencies under one sun conditions and at elevated concentrations are discussed further in the following chapter.

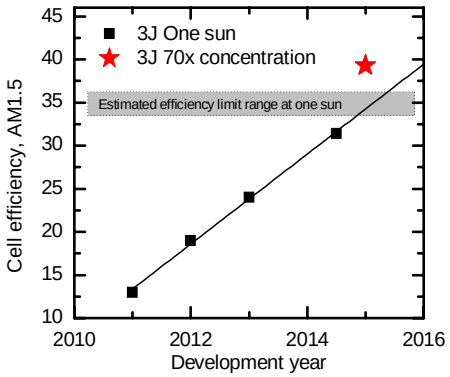

Figure 5.8. *Estimated cell efficiencies for triple junction cells fabricated in dilute nitride multijunction solar cell projects.*

5.3 Performance of GaInP/GaAs/GaInNAsSb solar cells

This chapter focuses on the performance of GaInP/GaAs/GaInNAsSb solar cells. The cells were measured by real sun illumination, by an Oriel solar simulator with an AM1.5G filter, by an in-house built three band solar simulator and by EQE. We also measured the cell characteristics at different cell temperatures and at elevated concentrations.

EQE performance and one sun performance of GaInP/GaAs/GaInNAsSb cell

As the basis of the efficiency determination for the GaInP/GaAs/GaInNAsSb cell, the EQE performance for each sub-cell was measured. For the EQE measurements of the GaInP/GaAs/GaInNAsSb cell careful optical and sometimes electrical biasing is needed. Light biasing with a nearly monochromatic bias light band is needed to make the sub-cells that are not under investigation produce more current than the cells being measured [150]. An additional electric bias might be needed for some junctions such as Ge, where electric breakdown may happen with relatively low voltages, or for junctions with low shunt resistance [151]. The EQE measurements have been used in this thesis for the analysis of the spectral response of GaInP/GaAs/GaInNAsSb cells in papers [P6] and [P7].

Figure 5.9 presents the performance of a GaInP/GaAs/GaInNAsSb solar cell measured at 22°C and at 80°C. These data are based on article P7. From the results it can be seen that all the sub-cells have a maximum EQE around 90% and that the integration of all the sub-junctions has been successful, with high EQE levels. When the cell is heated up from 22°C to 80°C we can see the EQE edges shifting towards longer wavelengths, which is caused by the band gap shrinking with temperature. This band gap shift typically increases the current generation of the multijunction device and reduces the V_{oc}. As an end result, the cell efficiency generally becomes lower when the cell is heated up. More details about the temperature dependencies of GaInP/GaAs/GaInNAsSb cells can be found from [P7].

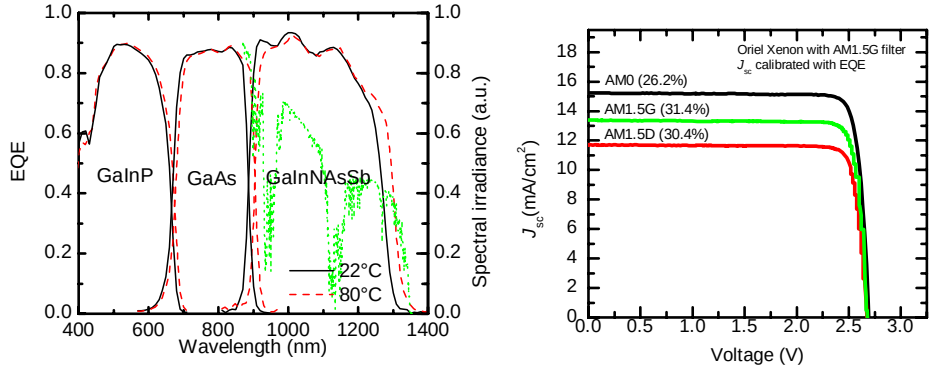

(a) (b)

Figure 5.9. *(a) EQE performance of GaInP/GaAs/GaInNAsSb cell measured at 22°C and 80°C. (b) IV-characteristics for a GaInP/GaAs/GaInNAsSb biased with Oriel Xenon solar simulator equipped with AM1.5G filter. The current of the 3J cell was calibrated to the minimum current calculated from the EQE measurements shown in Figure 5.9 a.*

The absolute performance for this cell was estimated from the light biased IV-measurements, where the 3J current generation was calibrated to the value of the cell which generated the lowest current. The IV-results are presented in Figure 5.9 b, from which the calculated efficiencies for ASTM G-173 AM1.5G, AM1.5D and AM0 are 31.4%, 30.4% and 26.2%, respectively. The maximum performance for the 3J cell under AM1.5D one sun conditions is 91%, from the predicted ultimate efficiency presented in chapter 5.1. This can be considered a remarkably good result achieved at the academic level.

The performance of GaInP/GaAs/GaInNAsSb cells under concentrated light

Our measurement set-up allowed assessments under concentrated light up to the 70-suns level. The performance of a GaInP/GaAs/GaInNAsSb 3J cell is presented in Figure 5.10 for a AM1.5G 1-sun spectrum and at ~70 suns real sun concentration. The sun intensity was recorded before the measurements by a calibrated pyranometer. Most of the concentrated power consisted only of direct irradiation, which is 900 W/m^2, but also some of the diffuse light, being less than 0.1 suns of 70 suns, was passed to the sample. For the one sun measurement the estimated cell efficiency was 31%, and the efficiency increased to 37-39% when the concentration was increased to 70 suns. The uncertainty for the cell efficiency at 70 suns comes mainly from the deviation of the cell temperature under concentrated sunlight conditions, which means that the estimated cell temperature was between 25 and 40°C. In practice the cell temperature was closer to 40°C than 25°C, because the cell stage was set to 25°C. For future developments better current matching between the sub-cells is essential and overall structural optimization and fewer interface recombinations will result in higher conversion efficiency. These targets can be achieved by more advanced processing and by improvement of the epitaxy process.

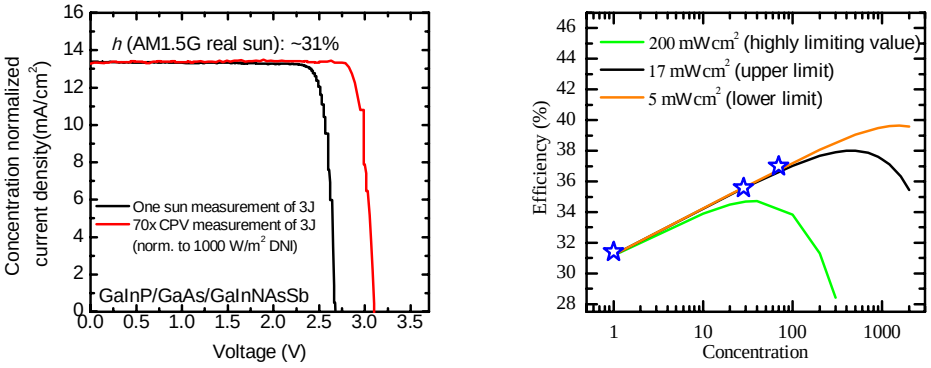

Figure 5.10. *(a) Measured GaInP/GaAs/GaInNAsSb cell performance at AM1.5G one sun excitation and at 70 suns excitation, both measurements were normalized to one sun intensity of 1000 W/cm^2. (b) Solar cell efficiencies under concentration and modelled efficiencies of GaInP/GaAs/GaInNAsSb solar cells with three different series resistance values.*

The efficiencies of the concentration dependent measurements are presented in Figure 5.10 b. In this graph, the efficiency trends are also calculated with lower and upper limits for the series resistance. One can see that the efficiency grows logarithmically with the concentration as presented in equation 2.6. The saturation of the three different efficiency trends are caused by the existing device series resistance, which can be due to the metal contact and metal transfer resistance or to the spreading resistance of the current within the cell. To estimate the potential of the measured cell we have used three different values for the series resistance; 200 mΩcm^2, 17 mΩcm^2 and 5 mΩcm^2. Based on the diode analysis of the 3J cell, the most probable series resistance values are between 17 and 5 mΩcm^2, which are reported in paper P7. This suggest that the cell efficiency may improve from 1.0 to 2.6 percentage points at higher concentration levels.

5.4 AlInP moth eye coated GaInP/GaAs/GaInNAs SC

For the future development of ultra-high efficiency solar cells it is essential to develop new concepts aiming at improved performance. Many modern concepts have been introduced, which include utilization of photonic 3D-stuctures with more than three junctions, and tailoring of the absorption bands of the solar cell absorber materials by quantum wells, quantum dots and intermediate band engineering [5]. To this end, we have studied the potential of moth eye nanostructures fabricated on the AlInP window layer of a GaInP/GaAs/GaInNAs solar cell. The purpose of this nano-pattern is to mimic the structure of the eye cornea layer surface pattern of the nocturnal butterfly, a pattern that has been optimized by nature for maximum light transmission and highest sensitivity for the eye at low light intensity levels during nighttime. This nano-sized pattern can be used as an antireflection coating [152]. The patterning process was developed by Tommila et al. [153-155] and the detailed spectral response for the moth eye patterned GaInP/GaAs/GaInNAs cell was studied in this thesis [P6]. The paper also compared moth eye anti reflection performance to a similar GaInP/GaAs/GaInNAs cell with a traditional two layer TiO_2/SiO_2 dielectric antireflection coating. Figure 5.11 shows the nano-pattern of the solar cell and the antireflective properties of moth eye patterned cell and TiO_2/SiO_2 comparison structure.

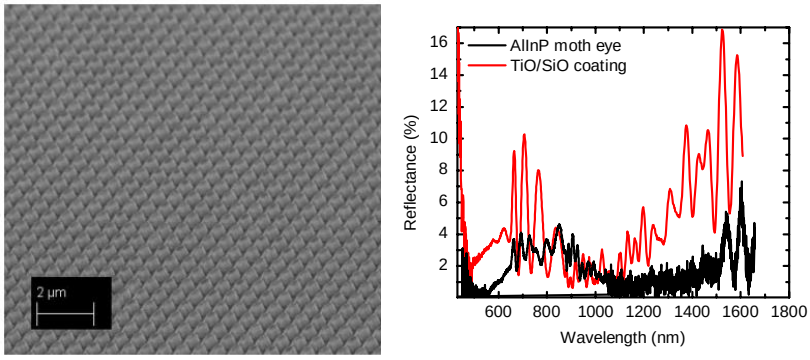

Figure 5.11. *SEM picture of the moth eye surface pattern fabricated on the AlInP surface by nano imprint lithography and reflectance of the fabricated GaInP/GaAs/GaInNAs cells with ARC.*

The antireflection performance of the patterned AlInP surface is compared to the different antireflection coatings published in the literature and fabricated in this work. The comparision in Table 5.4 shows that the average reflection of the AlInP moth eye pattern is extremely low, only 2.1% to 1.6%, and agrees well with the simulated average reflectivity of 1.7% [155]. The pattern outperforms the comparison structure reflectivity, having less than half of the latter's reflectivity. Also, the reflectivities of the published nano pattern structures collected in Table 5.4 are significantly higher than for the AlInP nano pattern demostrated in this work.

Table 5.4. Reflectivities of ARC on MJSCs.

ARC Structure	Average reflectivity 400-1000 nm	Average reflectivity 1000-1700 nm
AlInP moth eye, [this work]	2.09	1.62
AlInP moth eye simulation [155]	1.7	1.7
TiO_2/SiO_2, [this work]	4.24	5.83
TiO2 or SiNx nanostructure [156]	7.28	7.28
Patterned PVC film [157]	9.08	-
SiO_2 moth eye on conventional ARC [158]	3.45	4.25
4 layer ARC (simulation) [159]	4.16	3.80
SiO_2-nanopillars on conventional ARC [160]	11.4	-

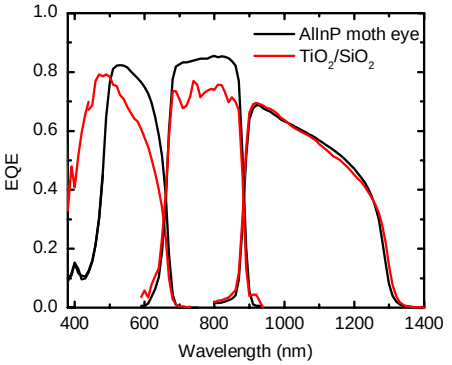

Figure 5.12. *a) Reflectivity of ARC coated 3J cell surfaces. (b) EQE of moth eye and TiO_2/SiO_2 coated 3J SCs.*

Table 5.5. Calculated AM1.5G current densities from EQE.

ARC	Sub-cell	Calculated AM1.5G J_{sc} (mA/cm^2)
AlInP moth eye	GaInP	10.1
AlInP moth eye	GaAs	13.9
AlInP moth eye	GaInNAs	10.4
TiO_2/SiO_2	GaInP	11.0
TiO_2/SiO_2	GaAs	13.3
TiO_2/SiO_2	GaInNAs	10.6

From the point of view of the reflectivity values the results looked very promising and the next step for the performance evaluation was to measure the 3J cell performances with real sun illumination. The results show [P6] that the moth eye cell has higher current generation and better fill factor. A more detailed analysis, however, showed that the AlInP moth eye structure is not perfect. In Figure 5.12 the comparison of the measured EQE values of GaInP/GaAs/GaInNAs solar cells with an AlInP moth eye and a TiO_2/SiO_2 antireflection coating are presented. Differences are seen for the spectral responces especially at short wavelengths below 500 nm, where the absoprtion of the remaining AlInP window causes the extinction of the photons. For wavelengths longer than 500 nm, the moth eye pattern is significanly better than the TiO_2/SiO_2 coating which was used as a reference. Significantly better performance at long wavelengths indicates a highly promising future for the developed nano-pattern, if the losses at wavelengths below 500 nm can be reduced by structural optimization of the pattern.

Chapter 6

6 Conclusions

This thesis focused on the growth optimization of GaInNAsSb compounds for III-V multijunction cells fabricated by plasma assisted molecular beam epitaxy. The growth, characteristics and multijunction cell design aspects were reported in 11 scientific papers. The outcome of the thesis work was that it is possible to fabricate GaInNAsSb solar cell materials for a GaInP/GaAs/GaInNAsSb cell without GaInNAsSb being the current limiting junction. The growth dynamics of GaInNAsSb crystals demand careful control of the growth temperatures, N plasma parameters, arsenic overpressure and annealing conditions.

The GaInNAsSb semiconductor materials were evaluated by testing them in simple bulk structures, single junction GaInNAsSb cells, and in GaInP/GaAs/GaInNAsSb multijunction cells. Altogether over 300 structures have been fabricated and more than 1000 components with different post growth treatments and optimizations steps were tested. The results show that the average EQE of GaInNAsSb in the spectral range of 1.4 eV to 1.0 eV can exceed 90%. The cells with high EQE can also be integrated into GaInP/GaAs/GaInNAsSb cells with excellent voltage and fill factor characteristics. For single junction 1 eV cells V_{oc} values of ~0.5 V and fill factor values of ~70% were achieved. The GaInP/GaAs/GaInNAsSb integration yielded one sun efficiencies of 30%, 31% and 26%, for AM1.5D, AM1.5G and AM0 spectra, respectively. For the concentrated sun light measurements at 70 suns the efficiency increased to 37-39%. For future improvements, detailed optimization of the growth interfaces and post processing optimizations, especially for front grid design, are needed. In order to approach 50% cell efficiencies more junctions are needed, and based on the calculations in this thesis the

GaInP/GaAs/GaInNAsSb/Ge cell concept can almost reach the target, with a projected efficiency of 47% to 50% at over 300 suns. In addition, an AlInP moth eye nanopattern antireflection coating was developed on top of a GaInP/GaAs/GaInNAs triple junction cell. The pattern performed well above 500 nm and exhibited less than 2% average reflectivity for the spectral band from 400 to 1700 nm. For the future usage of the structure in wide spectral range cells with more than 3 junctions, the pattern should be further optimized by minimizing the absorption in the patterned AlInP below 500 nm wavelengths. Our target in the near future is to achieve well over 30% conversion efficiency under AM0 illumination and to reach the 50 % efficiency limit with a multijunction solar cell with at least 4 junctions, under high concentration.

Bibliography

[1] Ohl, R.S. Light-sensitive electric device, US patent 2402662 A. (1946).

[2] NREL Research solar cell efficiency records, Cited:25/10/2015, http://www.nrel.gov/ncpv/images/efficiency_chart.jpg.

[3] Green, M.A., Emery, K., Hishikawa, Y., Warta, W. & Dunlop, E.D. Solar cell efficiency tables (Version 45). Progress in Photovoltaics: Research and Applications 23(2015)1, pp. 1-9.

[4] Friedman, D.J., Olson, J.M. & Kurtz, S. High-Efficiency III-V Multijunction Solar Cells. (2011) pp. 314-364.

[5] López, A.B.C., Vega, A.M., Cristobal, A. & López, A.L. Next Generation of Photovoltaics: New Concepts. 2012, Springer Science & Business Media.

[6] Shockley, W. & Queisser, H.J. Detailed balance limit of efficiency of p-n junction solar cells. Journal of Applied Physics 32(1961)3, pp. 510-519.

[7] Henry, C.H. Limiting efficiencies of ideal single and multiple energy gap terrestrial solar cells. Journal of Applied Physics 51(1980)8, pp. 4494-4500.

[8] Gillette, R. & Tallent, R. Discussion:“Performance of Silicon Solar Cells at High Levels of Solar Radiation”(Pfeiffer, C., Schoffer, P., Spars, BG, and Duffie, JA, 1962, ASME J. Eng. Power, 84, pp. 33–38). Journal of Engineering for Gas Turbines and Power 84(1962)1, pp. 38-38.

[9] Swanson, R.M. Photovoltaic Concentrators. In: Anonymous (ed.). Handbook of Photovoltaic Science and Engineering. 1st ed. 2005, John Wiley & Sons, Ltd. pp. 449-503.

[10] Gleckman, P., O'Gallagher, J. & Winston, R. Concentration of sunlight to solar-surface levels using non-imaging optics. Nature 339(1989)6221, pp. 198-200.

[11] Philpps, S.P., Bett, A.W., Horowitz, K. & Kurtz, S. Current Status of Concentrator Photovoltaic (CPV) Technology. (2015)TP-6A20-63916.

[12] Kost, C., Mayer, J., Thomsen, J., Hartmann, N., Senkpiel, C., Philipps, S., Nold, S., Lude, S., Saad, N. & Schlegl, T. Levelized cost of electricity renewable energy technologies. Fraunhofer Institute for Solar Energy Systems ISE (2013).

[13] King, R., Sherif, R., Kinsey, G., Kurtz, S., Fetzer, C., Edmondson, K., Law, D., Cotal, H., Krut, D. & Ermer, J. Bandgap engineering in high-efficiency multijunction concentrator cells. International Conference on Solar Concentrators for the Generation of Electricity or Hydrogen, 1-5 May 2005, Scottsdale, Arizona (NREL/CD-520-38172) (2005).

[14] Sandwell, P., Duggan, G., Nelson, J. & Ekins-Daukes, N. Life Cycle Analysis of a new HCPV Module. 11th International Conference on Concentrator Photovoltaic systems, Aix-Les Bains France(2015).

[15] Zech, T., Gerstmaier, T., Röttger, M., Moretta, R., Braun, C. & Gombert, A. Return of Experience from 5 Years of Field Data: Long Term Performance Reliability of Soitec's CPV Technology. 29th EU-PVSEC proceedings, DOI: 10.13140/2.1.2992.4164(2014).

[16] Muller, M., Jordan, D. & Kurtz, S. Degradation Analysis of a CPV Module After Six Years On-sun. Proceedings of 11th International Conference on Concentrator Photovoltaic systems, Aix-Les Bains France(2015).(2015).

[17] Yamaguchi, M., Okuda, T., Taylor, S.J., Takamoto, T., Ikeda, E. & Kurita, H. Superior radiation-resistant properties of InGaP/GaAs tandem solar cells. Applied Physics Letters 70(1997)12, pp. 1566-1568.

[18] Kazantsev, A.B., Lammasniemi, J., Jaakkola, R., Pessa, M., Rajatora, M. & Jain, R.K. Proton irradiated MBE grown GaInP/GaAs single junction and tandem solar cells. Photovoltaic Specialists Conference, 1997., Conference Record of the Twenty-Sixth IEEE, 1997, pp. 1003-1006.

[19] AZUR SPACE Solar Power GmbH, Space solar cell efficiencies,Cited:5/10/2015, http://www.azurspace.com/index.php/en/products/products-space/space-solar-cells.

[20] Law, D.C., Edmondson, K.M., Siddiqi, N., Paredes, A., King, R.R., Glenn, G., Labios, E., Haddad, M.H., Isshiki, T.D. & Karam, N.H. Lightweight, Flexible, High-Efficiency III-V Multijunction Cells. Photovoltaic Energy Conversion, Conference Record of the 2006 IEEE 4th World Conference on, 2006, pp. 1879-1882.

[21] Dimroth, F., Peharz, G., Wittstadt, U., Hacker, B. & Bett, A.W. Hydrogen Production in a PV Concentrator using III-V Multi-Junction Solar Cells. Conference Record of the 2006 IEEE 4th World Conference on Photovoltaic Energy Conversion, 2006, pp. 640-643.

[22] Pelzel, R. A Comparison of MOVPE and MBE Growth Technologies for III-V Epitaxial Structures. CS MANTECH Conference, May 13th-16th, New Orleans, Louisiana, USA, 2013.

[23] Gray, J.L. The Physics of the Solar Cell. Handbook of Photovoltaic Science and Engineering. 1st ed. 2005, John Wiley & Sons, Ltd. pp. 61-112.

[24] Vurgaftman, I., Meyer, J.R. & Ram-Mohan, L.R. Band parameters for III/V compound semiconductors and their alloys. Journal of Applied Physics 89(2001)11, pp. 5815-5875.

[25] Streetman, B.G. & Banerjee, S. Solid State Electronic Devices. 2006, Pearson Prentice Hall.

[26] Kurtz, S.R., Olson, J., Friedman, D., Geisz, J., Bertness, K. & Kibbler, A. Passivation of interfaces in high-efficiency photovoltaic devices. MRS Proceedings, 1999, Cambridge Univ Press. pp. 95.

[27] Lammasniemi, J., Tappura, K. & Smekalin, K. Recombination mechanisms at window/emitter interface in InP and other III-V semiconductor based solar cells. Photovoltaic Energy Conversion, 1994., Conference Record of the Twenty Fourth. IEEE Photovoltaic Specialists Conference - 1994, 1994 IEEE First World Conference on, 1994, pp. 1771-1774 vol.2.

[28] King, R.R., Ermer, J.H., Joslin, D.E., Haddad, M., Eldredge, J.W., Karam, N., Keyes, B. & Ahrenkiel, R.K. Double heterostructures for characterization of bulk lifetime and interface recombination velocity in III-V multijunction solar cells. Proceedings of the 2nd World Conference on Photovoltaic Solar Energy Conversion, 6-10 July. Vienna, Austria 1998.

[29] Ottaviani, G., Reggiani, L., Canali, C., Nava, F. & Alberigi-Quaranta, A. Hole drift velocity in silicon. Phys.Rev.B 12(1975)8, pp. 3318-3329.

[30] Norton, P., Braggins, T. & Levinstein, H. Impurity and Lattice Scattering Parameters as Determined from Hall and Mobility Analysis in n-Type Silicon. Phys.Rev.B 8(1973)12, pp. 5632-5653.

[31] Tyagi, M.S. & Van Overstraeten, R. Minority carrier recombination in heavily-doped silicon. Solid-State Electronics 26(1983)6, pp. 577-597.

[32] del Alamo, J.A. & Swanson, R.M. Modelling of minority-carrier transport in heavily doped silicon emitters. Solid-State Electronics 30(1987)11, pp. 1127-1136.

[33] Jellison, G.E. & Modine, F.A. Optical absorption of silicon between 1.6 and 4.7 eV at elevated temperatures. Applied Physics Letters 41(1982)2, pp. 180-182.

[34] Ioffe Physico-Technical Institute, Electrical Properties of Germanium, Cited: 06/06/2015, http://www.ioffe.ru/SVA/NSM/Semicond/Ge/electric.html#Basic.

[35] Kurtz, S.R., Myers, D. & Olson, J.M. Projected performance of three- and four-junction devices using GaAs and GaInP. In 26th IEEE, Photovoltaic specialists conference September 29- October 3, Anaheim: IEEE(1997).

[36] Pankove, J.I. & Aigrain, P. Optical Absorption of Arsenic-Doped Degenerate Germanium. Phys.Rev. 126(1962)3, pp. 956-962.

[37] Tukiainen, A., Aho, A., Polojärvi, V. & Guina, M. Modeling of MBE-Grown GaInNAs Solar Cells. 10th European Space Power Conference ESPC 2014, 13-17 April, 2014, Noordwijkerhout, the Netherlands 719(2014) pp. 1-4.

[38] Sturge, M.D. Optical Absorption of Gallium Arsenide between 0.6 and 2.75 eV. Phys.Rev. 127(1962)3, pp. 768-773.

[39] Adachi, S. Optical dispersion relations for GaP, GaAs, GaSb, InP, InAs, InSb, AlxGa1−xAs, and In1−xGaxAsyP1−y. Journal of Applied Physics 66(1989)12, pp. 6030-6040.

[40] Kurtz, S., Geisz, J.F., Friedman, D.J., Metzger, W.K., King, R.R. & Karam, N.H. Annealing-induced-type conversion of GaInNAs. Journal of Applied Physics 95(2004)5, pp. 2505-2508.

[41] Gubanov, A., Polojärvi, V., Aho, A., Tukiainen, A., Tkachenko, N.V. & Guina, M. Dynamics of time-resolved photoluminescence in GaInNAs and GaNAsSb solar cells. Nanoscale Research Letters 9(2014)1, pp. 1-4.

[42] Friedman, D.J. & Kurtz, S.R. Breakeven criteria for the GaInNAs junction in GaInP/GaAs/GaInNAs/Ge four-junction solar cells. Progress in Photovoltaics: Research and Applications 10(2002)5, pp. 331-344.

[43] Yao, L. & He, J. Recent progress in antireflection and self-cleaning technology – From surface engineering to functional surfaces. Progress in Materials Science 61(2014) pp. 94-143.

[44] Imenes, A.G. & Mills, D.R. Spectral beam splitting technology for increased conversion efficiency in solar concentrating systems: a review. Solar Energy Materials and Solar Cells 84(2004)1–4, pp. 19-69.

[45] Sasaki, K., Agui, T., Nakaido, K., Takahashi, N., Onitsuka, R. & Takamoto, T. Development of InGaP/GaAs/InGaAs inverted triple junction concentrator solar cells. AIP Conference Proceedings 1556(2013)1, pp. 22-25.

[46] King, R.R., Law, D.C., Edmondson, K.M., Fetzer, C.M., Kinsey, G.S., Yoon, H., Sherif, R.A. & Karam, N.H. 40% efficient metamorphic GaInP/GaInAs/Ge multijunction solar cells. Applied Physics Letters 90(2007)18.

[47] Sheng, X., Bower, C.A., Bonafede, S., Wilson, J.W., Fisher, B., Meitl, M., Yuen, H., Wang, S., Shen, L. & Banks, A.R. Printing-based assembly of quadruple-junction four-terminal microscale solar cells and their use in high-efficiency modules. Nature materials 13(2014)6, pp. 593-598.

[48] Yamaguchi, M. III–V compound multi-junction solar cells: present and future. Solar Energy Materials and Solar Cells 75(2003)1–2, pp. 261-269.

[49] Law, D.C., King, R.R., Yoon, H., Archer, M.J., Boca, A., Fetzer, C.M., Mesropian, S., Isshiki, T., Haddad, M., Edmondson, K.M., Bhusari, D., Yen, J., Sherif, R.A., Atwater, H.A. & Karam, N.H. Future technology pathways of terrestrial III–V multijunction solar cells for concentrator photovoltaic systems. Solar Energy Materials and Solar Cells 94(2010)8, pp. 1314-1318.

[50] King, R.R., Bhusari, D., Larrabee, D., Liu, X.-., Rehder, E., Edmondson, K., Cotal, H., Jones, R.K., Ermer, J.H., Fetzer, C.M., Law, D.C. & Karam, N.H. Solar cell generations over 40% efficiency. Progress in Photovoltaics: Research and Applications 20(2012)6, pp. 801-815.

[51] Dimroth, F. High-efficiency solar cells from III-V compound semiconductors. physica status solidi (c) 3(2006)3, pp. 373-379.

[52] Wiemer, M., Sabnis, V. & Yuen, H. 43.5% efficient lattice matched solar cells. SPIE Solar Energy Technology, 2011, International Society for Optics and Photonics. pp. 810804-810804-5.

[53] Sala, G. & Anton, I. Photovoltaic Concentrators. In: Anonymous (ed.). Handbook of Photovoltaic Science and Engineering. 2011, John Wiley & Sons, Ltd. pp. 402-451.

[54] Lammasniemi, J., Kazantsev, A.B., Jaakkola, R., Toivonen, M., Jalonen, M., Aho, R. & Pessa, M. GaInP/GaAs cascade solar cells grown by molecular beam epitaxy. Photovoltaic Specialists Conference, 1997., Conference Record of the Twenty-Sixth IEEE, 1997, pp. 823-826.

[55] Hermle, M., Létay, G., Philipps, S.P. & Bett, A.W. Numerical simulation of tunnel diodes for multi-junction solar cells. Progress in Photovoltaics: Research and Applications 16(2008)5, pp. 409-418.

[56] Bedair, S.M., Roberts, J.C., Jung, D., Moody, B.F., El-Masry, N.A. & Katsuyama, T. Analysis of p^+-AlGaAs/n^+-InGaP tunnel junction for high solar concentration cascade solar cells. Photovoltaic Specialists Conference, 2000. Conference Record of the Twenty-Eighth IEEE, 2000, pp. 1154-1156.

[57] Harris, J.J., Joyce, B.A., Gowers, J.P. & Neave, J.H. Nucleation effects during MBE growth of Sn-Doped GaAs. Applied Physics A 28(1982)1, pp. 63-71.

[58] Silveira, J.P. & Briones, F. Low temperature growth of highly doped GaAs:Si by atomic layer molecular beam epitaxy. Applied Physics Letters 65(1994)5, pp. 573-574.

[59] King, R.R., Bhusari, D., Boca, A., Larrabee, D., Liu, X.-., Hong, W., Fetzer, C.M., Law, D.C. & Karam, N.H. Band gap-voltage offset and energy production in next-generation multijunction solar cells. Progress in Photovoltaics: Research and Applications 19(2011)7, pp. 797-812.

[60] Friedman, D.J. Progress and challenges for next-generation high-efficiency multijunction solar cells. Current Opinion in Solid State and Materials Science 14(2010)6, pp. 131-138.

[61] Barnett, A., Honsberg, C., Kirkpatrick, D., Kurtz, S., Moore, D., Salzman, D., Schwartz, R., Gray, J., Bowden, S., Goossen, K., Haney, M., Aiken, D., Wanlass, M. & Emery, K. 50% Efficient Solar Cell Architectures and Designs. Photovoltaic Energy Conversion, Conference Record of the 2006 IEEE 4th World Conference on, 2006, pp. 2560-2564.

[62] Sabnis, V., Yuen, H. & Wiemer, M. High-efficiency multijunction solar cells employing dilute nitrides. AIP Conference Proceedings 1477(2012)1, pp. 14-19.

[63] Vurgaftman, I. & Meyer, J.R. Band parameters for nitrogen-containing semiconductors. Journal of Applied Physics 94(2003)6, pp. 3675-3696.

[64] Friedman, D.J., Geisz, J.F., Kurtz, S.R. & Olson, J.M. 1-eV solar cells with GaInNAs active layer. Journal of Crystal Growth 195(1998)1–4, pp. 409-415.

[65] Geisz, J.F., Friedman, D.J., Olson, J.M., Kurtz, S.R. & Keyes, B.M. Photocurrent of 1 eV GaInNAs lattice-matched to GaAs. Journal of Crystal Growth 195(1998)1–4, pp. 401-408.

[66] Geisz, J.F., Friedman, D.J. & Kurtz, S. GaNPAs solar cells lattice-matched to GaP. Photovoltaic Specialists Conference, 2002. Conference Record of the Twenty-Ninth IEEE, 2002, pp. 864-867.

[67] Ptak, A., Friedman, D., Kurtz, S. & Reedy, R. Low-acceptor-concentration GaInNAs grown by molecular-beam epitaxy for high-current pin solar cell applications. Journal of Applied Physics 98(2005)9, pp. 094501-094501-5.

[68] Korpijarvi, V.-M., Kantola, E.L., Leinonen, T., Isoaho, R. & Guina, M. Monolithic GaInNAsSb/GaAs VECSEL Operating at 1550 nm. Selected Topics in Quantum Electronics, IEEE Journal of 21(2015)6, pp. 1-5.

[69] Konttinen, J. & Korpijärvi, V.-M. Frequency-converted dilute nitride laser diodes for mobile display applications. Nanoscale research letters 9(2014)1, pp. 1-5.

[70] Korpijärvi, V. -M., Guina, M., Puustinen, J., Tuomisto, P., Rautiainen, J., Härkönen, A., Tukiainen, A., Okhotnikov, O. & Pessa, M. MBE grown GaInNAs-based multi-Watt disk lasers. Journal of Crystal Growth 311(2009)7, pp. 1868-1871.

[71] Jackrel, D.B., Bank, S.R., Yuen, H.B., Wistey, M.A., Harris, J.S., Ptak, A.J., Johnston, S.W., Friedman, D.J. & Kurtz, S.R. Dilute nitride GaInNAs and GaInNAsSb solar cells by molecular beam epitaxy. Journal of Applied Physics 101(2007)11, .

[72] ASTM G 173–03: *Standard tables for reference solar spectral irradiances: direct normal and hemispherical on 37° tilted surface*. West Conshohoken, PA: ASTM International. 2003, .

[73] Siefer, G. & Bett, A.W. Analysis of temperature coefficients for III-V multi-junction concentrator cells. Progress in Photovoltaics: Research and Applications 22(2014)5, pp. 515-524.

[74] Bailey, S. & Raffaelle, R. Space Solar Cells and Arrays. (2011) pp. 365-401.

[75] Zdanowicz, T., Rodziewicz, T. & Zabkowska-Waclawek, M. Theoretical analysis of the optimum energy band gap of semiconductors for fabrication of solar cells for applications in higher latitudes locations. Solar Energy Materials and Solar Cells 87(2005)1–4, pp. 757-769.

[76] Kinsey, G.S., Hebert, P., Barbour, K.E., Krut, D.D., Cotal, H.L. & Sherif, R.A. Concentrator multijunction solar cell characteristics under variable intensity and temperature. Progress in Photovoltaics: Research and Applications 16(2008)6, pp. 503-508.

[77] Steiner, M.A. & Geisz, J.F. Non-linear luminescent coupling in series-connected multijunction solar cells. Applied Physics Letters 100(2012)25, .

[78] Friedman, D.J., Geisz, J.F. & Steiner, M.A. Effect of Luminescent Coupling on the Optimal Design of Multijunction Solar Cells. Photovoltaics, IEEE Journal of 4(2014)3, pp. 986-990.

[79] Derkacs, D., Bilir, D.T. & Sabnis, V.A. Luminescent Coupling in GaAs/GaInNAsSb Multijunction Solar Cells. Photovoltaics, IEEE Journal of 3(2013)1, pp. 520-527.

[80] Steiner, M., Philipps, S.P., Hermle, M., Bett, A.W. & Dimroth, F. Front contact grid optimization of III-V solar cells with SPICE network simulation. 24th European Photovoltaic Solar Energy Conference, 21-25 September 2009, Hamburg, Germany 2009, pp. 721 - 724.

[81] Bett, A.W., Jaus, J., Peharz, G., Siefer, G., Hakenjos, A., Heile, I., Lerchenmuller, H. & Wullner, J. Outdoor evaluation of flatcon® modules and systems. Photovoltaic Specialists Conference, 2008. PVSC '08. 33rd IEEE, 2008, pp. 1-6.

[82] Bird, R.E. & Riordan, C. Simple solar spectral model for direct and diffuse irradiance on horizontal and tilted planes at the earth's surface for cloudless atmospheres. Journal of Climate and Applied Meteorology 25(1986)1, pp. 87-97.

[83] Franchi, S. Chapter 1 - Molecular beam epitaxy: fundamentals, historical background and future prospects. In: Henini, M. (ed.). Molecular Beam Epitaxy. Oxford 2013, Elsevier. pp. 1-46.

[84] Herman, M.A. & Sitter, H. Molecular beam epitaxy: fundamentals and current status. 2012, Springer Science & Business Media.

[85] Farrow, R.F. Molecular beam epitaxy: applications to key materials. 1995, Elsevier.

[86] Shaw, M., Yu, K., Ting, M., Powell, R., Sarney, W., Svensson, S., Kent, A., Walukiewicz, W., Foxon, C. & Novikov, S. Composition and optical properties of dilute-Sb $GaN_{1-x}Sb_x$

highly mismatched alloys grown by MBE. Journal of Physics D: Applied Physics 47(2014)46, pp. 465102.

[87] E Luna and A Trampert and E-M Pavelescu and,M.Pessa Nitrogen-enhanced indium segregation in (Ga,In)(N,As)/GaAs multiple quantum wells grown by molecular-beam epitaxy. New Journal of Physics 9(2007)11, pp. 405.

[88] Neugebauer, J. & Van de Walle, C.G. Electronic structure and phase stability of GaAs1-$_x$N$_x$ alloys. Phys.Rev.B 51(1995)16, pp. 10568-10571.

[89] Schlenker, D., Miyamoto, T., Pan, Z., Koyama, F. & Iga, K. Miscibility gap calculation for Ga1−xInxNyAs1−y including strain effects. Journal of Crystal Growth 196(1999)1, pp. 67-70.

[90] Xin, H.P., Kavanagh, K.L., Zhu, Z.Q. & Tu, C.W. Observation of quantum dot-like behavior of GaInNAs in GaInNAs/GaAs quantum wells. Applied Physics Letters 74(1999)16, pp. 2337-2339.

[91] McGee, W.M., Williams, R.S., Ashwin, M.J., Jones, T.S., Clarke, E., Zhang, J. & Tomic, S. Structure, morphology, and optical properties of GaxIn1-xN0.05As0.95 quantum wells: Influence of the growth mechanism. Phys.Rev.B 76(2007)8, pp. 085309.

[92] Ho, I. & Stringfellow, G.B. Solubility of nitrogen in binary III–V systems. Journal of Crystal Growth 178(1997)1–2, pp. 1-7.

[93] Kong, X., Trampert, A., Tournie, E. & Ploog, K.H. Decomposition in as-grown (Ga,In)(N,As) quantum wells. Applied Physics Letters 87(2005)17, pp. -.

[94] Pan, Z., Li, L.H., Zhang, W., Lin, Y.W. & Wu, R.H. Kinetic modeling of N incorporation in GaInNAs growth by plasma-assisted molecular-beam epitaxy. Applied Physics Letters 77(2000)2, pp. 214-216.

[95] Pavelescu, E.-M., Wagner, J., Komsa, H.-., Rantala, T.T., Dumitrescu, M. & Pessa, M. Nitrogen incorporation into GaInNAs lattice-matched to GaAs: The effects of growth temperature and thermal annealing. Journal of Applied Physics 98(2005)8, .

[96] Chauveau, J., Trampert, A., Ploog, K., Pinault, M. & Tournié, E. Interplay between the growth temperature, microstructure, and optical properties of GaInNAs quantum wells. Applied Physics Letters 82(2003)20, pp. 3451-3453.

[97] Massies, J. & Grandjean, N. Surfactant effect on the surface diffusion length in epitaxial growth. Phys.Rev.B 48(1993)11, pp. 8502-8505.

[98] Shimizu, H., Kumada, K., Uchiyama, S. & Kasukawa, A. High performance CW 1.26 um GaInNAsSb-SQW and 1.20 um GaInAsSb-SQW ridge lasers. Electronics Letters 36(2000)20, pp. 1701-1703.

[99] Tournié, E., Grandjean, N., Trampert, A., Massies, J. & Ploog, K.H. Surfactant-mediated molecular-beam epitaxy of III–V strained-layer heterostructures. Journal of Crystal Growth 150, Part 1(1995) pp. 460-466.

[100] Yang, X., Jurkovic, M.J., Heroux, J.B. & Wang, W.I. Molecular beam epitaxial growth of InGaAsN:Sb/GaAs quantum wells for long-wavelength semiconductor lasers. Applied Physics Letters 75(1999)2, pp. 178-180.

[101] Tixier, S., Adamcyk, M., Young, E.C., Schmid, J.H. & Tiedje, T. Surfactant enhanced growth of GaNAs and InGaNAs using bismuth. Journal of Crystal Growth 251(2003)1–4, pp. 449-454.

[102] Albrecht, M., Abu-Farsakh, H., Remmele, T., Geelhaar, L., Riechert, H. & Neugebauer, J. Compositional Correlation and Anticorrelation in Quaternary Alloys: Competition Between Bulk Thermodynamics and Surface Kinetics. Phys.Rev.Lett. 99(2007)20, pp. 206103.

[103] Miguel-Sanchez, J., Guzman, A. & Munoz, E. Role of N ions in the optical and morphological properties of InGaAsN quantum wells for 1.3-1.5 um applications. Applied Physics Letters 85(2004)11, pp. 1940-1942.

[104] Oye, M.M., Mattord, T.J., Hallock, G.A., Bank, S.R., Wistey, M.A., Reifsnider, J.M., Ptak, A.J., Yuen, H.B., Harris, J.S. & Holmes, A.L. Effects of different plasma species (atomic N, metastable N2*, and ions) on the optical properties of dilute nitride materials grown by plasma-assisted molecular-beam epitaxy. Applied Physics Letters 91(2007)19.

[105] Liu, X., Prasad, A., Nishio, J., Weber, E.R., Liliental-Weber, Z. & Walukiewicz, W. Native point defects in low- temperature- grown GaAs. Applied Physics Letters 67(1995)2, pp. 279-281.

[106] Tan, S.L., Hunter, C.J., Zhang, S., Tan, L.J.J., Goh, Y.L., Ng, J.S., Marko, I.P., Sweeney, S.J., Adams, A.R., Allam, J. & David, J.P.R. Improved Optoelectronic Properties of Rapid Thermally Annealed Dilute Nitride GaInNAs Photodetectors. Journal of Electronic Materials 41(2012)12, pp. 3393-3401.

[107] Volz, K., Lackner, D., Németh, I., Kunert, B., Stolz, W., Baur, C., Dimroth, F. & Bett, A.W. Optimization of annealing conditions of (GaIn)(NAs) for solar cell applications. Journal of Crystal Growth 310(2008)7–9, pp. 2222-2228.

[108] Kurtz, S.R., Allerman, A.A., Jones, E.D., Gee, J.M., Banas, J.J. & Hammons, B.E. InGaAsN solar cells with 1.0 eV band gap, lattice matched to GaAs. Applied Physics Letters 74(1999)5, pp. 729-731.

[109] Kurtz, S., Johnston, S.W., Geisz, J.F., Friedman, D.J. & Ptak, A.J. Effect of nitrogen concentration on the performance of $Ga_{1-x}In_xN_yAs_{1-y}$ solar cells. Photovoltaic Specialists Conference, 2005. Conference Record of the Thirty-first IEEE, 2005, pp. 595-598.

[110] Kurtz, S., Geisz, J.F., Friedman, D.J., Olson, J.M., Duda, A., Karam, N.H., King, R.R., Ermer, J.H. & Joslin, D.E. Modeling of electron diffusion length in GaInAsN solar cells. Photovoltaic Specialists Conference, 2000. Conference Record of the Twenty-Eighth IEEE, 2000, pp. 1210-1213.

[111] Matthews, J.W. & Blakeslee, A.E. Defects in epitaxial multilayers: I. Misfit dislocations. Journal of Crystal Growth 27(1974) pp. 118-125.

[112] Zolper, J.C. & Barnett, A.M. The effect of dislocations on the open-circuit voltage of gallium arsenide solar cells. Electron Devices, IEEE Transactions on 37(1990)2, pp. 478-484.

[113] Maree, P.M.J., Barbour, J.C., van der Veen, J.F., Kavanagh, K.L., Bulle-Lieuwma, C.W.T. & Viegers, M.P.A. Generation of misfit dislocations in semiconductors. Journal of Applied Physics 62(1987)11, pp. 4413-4420.

[114] Suzuki, T. & Nishinaga, T. Surface diffusion and atom incorporation kinetics in MBE of InGaAs and AlGaAs. Journal of Crystal Growth 111(1991)1–4, pp. 173-177.

[115] Harris, J.S., Kudrawiec, R., Yuen, H., Bank, S., Bae, H., Wistey, M., Jackrel, D., Pickett, E., Sarmiento, T. & Goddard, L. Development of GaInNAsSb alloys: growth, band structure, optical properties and applications. Physica Status Solidi-B-Basic Solid State Physics 244(2007)8, pp. 2707-2729.

[116] Egorov, A.Y., Bernklau, D., Borchert, B., Illek, S., Livshits, D., Rucki, A., Schuster, M., Kaschner, A., Hoffmann, A., Dumitras, G., Amann, M.C. & Riechert, H. Growth of high quality InGaAsN heterostructures and their laser application. Journal of Crystal Growth 227–228(2001) pp. 545-552.

[117] Jaschke, G., Averbeck, R., Geelhaar, L. & Riechert, H. Low threshold InGaAsN/GaAs lasers beyond 1500 nm. Journal of Crystal Growth 278(2005)1–4, pp. 224-228.

[118] Odnoblyudov, V.A., Kovsh, A.R., Zhukov, A.E., Maleev, N.A., Semenova, E.S. & Ustinov, V.M. Thermodynamic analysis of the growth of GaAsN ternary compounds by molecular beam epitaxy. Semiconductors 35(2001)5, pp. 533-538.

[119] Korpijärvi, V.-M., Aho, A., Laukkanen, P., Tukiainen, A., Laakso, A., Tuominen, M. & Guina, M. Study of nitrogen incorporation into GaInNAs: The role of growth temperature in molecular beam epitaxy. Journal of Applied Physics 112(2012)2.

[120] Carrère, H., Arnoult, A., Ricard, A. & Bedel-Pereira, E. RF plasma investigations for plasma-assisted MBE growth of (Ga,In)(As,N) materials. Journal of Crystal Growth 243(2002)2, pp. 295-301.

[121] Voulot, D., McCullough, R.W., Thompson, W.R., Burns, D., Geddes, J., Cosimini, G.J., Nelson, E., Chow, P.P. & Klaassen, J. Characterisation of an RF atomic nitrogen plasma source. Journal of Crystal Growth 201–202(1999) pp. 399-401.

[122] Reifsnider, J.M., Govindaraju, S. & Holmes Jr., A.L. Use of optical emission intensity to characterize an RF plasma source for MBE growth of GaAsN. Journal of Crystal Growth 243(2002)3–4, pp. 396-403.

[123] Ma, T., Lin, Y. & Lin, H. Incorporation behaviors of group V elements in GaAsSbN grown by gas-source molecular-beam epitaxy. Journal of Crystal Growth 310(2008)11, pp. 2854-2858.

[124] Lin, Y., Ma, T., Chen, T. & Lin, H. Energy gap reduction in dilute nitride GaAsSbN. Applied Physics Letters 93(2008)17.

[125] Kudrawiec, R., Pavelescu, E.-M., Andrzejewski, J., Misiewicz, J., Gheorghiu, A., Jouhti, T. & Pessa, M. The energy-fine structure of GaInNAs/GaAs multiple quantum wells grown at different temperatures and postgrown annealed. Journal of Applied Physics 96(2004)5, pp. 2909-2913.

[126] Kudrawiec, R., Korpijärvi, V.-M., Poloczek, P., Misiewicz, J., Laukkanen, P., Pakarinen, J., Dumitrescu, M., Guina, M. & Pessa, M. The influence of As/III pressure ratio on nitrogen nearest-neighbor environments in as-grown GaInNAs quantum wells. Applied Physics Letters 95(2009)26, .

[127] Pavelescu, E.-M., Jouhti, T., Dumitrescu, M., Klar, P.J., Karirinne, S., Fedorenko, Y. & Pessa, M. Growth-temperature-dependent (self-)annealing-induced blueshift of photoluminescence from 1.3 um GaInNAs/GaAs quantum wells. Applied Physics Letters 83(2003)8, pp. 1497-1499.

[128] S Karirinne and E-M Pavelescu and J Konttinen and T Jouhti and,M.Pessa The behaviour of optical and structural properties of GaInNAs/GaAs quantum wells upon annealing. New Journal of Physics 6(2004)1, pp. 192.

[129] Klar, P.J., Gruning, H., Koch, J., Schafer, S., Volz, K., Stolz, W., Heimbrodt, W., Saadi, A.M.K., Lindsay, A. & O'Reilly, E.P. (Ga, In)(N, As)-fine structure of the band gap due to nearest-neighbor configurations of the isovalent nitrogen. Phys.Rev.B 64(2001)12, pp. 121203.

[130] Murdick, D.A., Zhou, X.W. & Wadley, H.N.G. Low-temperature atomic assembly of stoichiometric gallium arsenide from equiatomic vapor. Journal of Crystal Growth 286(2006)1, pp. 197-204.

[131] Novikov, S.V., Staddon, C.R., Foxon, C.T., Yu, K.M., Broesler, R., Hawkridge, M., Liliental-Weber, Z., Denlinger, J., Demchenko, I., Luckert, F., Edwards, P.R., Martin, R.W. & Walukiewicz, W. Growth by molecular beam epitaxy of amorphous and crystalline GaNAs alloys with band gaps from 3.4 to 0.8 eV for solar energy conversion devices. Journal of Crystal Growth 323(2011)1, pp. 60-63.

[132] Wang, X.J., Puttisong, Y., Tu, C.W., Ptak, A.J., Kalevich, V.K., Egorov, A.Y., Geelhaar, L., Riechert, H., Chen, W.M. & Buyanova, I.A. Dominant recombination centers in Ga(In)NAs alloys: Ga interstitials. Applied Physics Letters 95(2009)24.

[133] Langer, F., Perl, S., Höfling, S. & Kamp, M. p-to n-type conductivity transition in 1.0 eV GaInNAs solar cells controlled by the V/III ratio. Applied Physics Letters 106(2015)6, pp. 063905.

[134] Friedman, D.J., Ptak, A.J., Kurtz, S.R. & Geisz, J.F. Analysis of depletion-region collection in GaInNAs solar cells. Photovoltaic Specialists Conference, 2005. Conference Record of the Thirty-first IEEE, 2005, pp. 691-694.

[135] Ptak, A.J., Friedman, D.J. & Kurtz, S. Effects of temperature, nitrogen ions, and antimony on wide depletion width GaInNAs. Journal of Vacuum Science & Technology B 25(2007)3, pp. 955-959.

[136] Tukiainen, A., Aho, A., Polojärvi, V., Salmi, J., Gubanov, A., Ahorinta, R. & Guina, M. MBE-grown dilute nitride materials: Ready for high-efficiency III-V multijunction solar cells? Physics Days Annual Conference of the Finnish Physical Society and the Second Nordic Physics Meeting HU-P-D178(2011) pp. 295-295.

[137] Kurtz, S., King, R., Law, D., Ptak, A., Geisz, J. & Karam, N. Effects of in situ annealing on GaInNAs solar cells. Photovoltaic Specialists Conference (PVSC), 2013 IEEE 39th, 2013, pp. 2095-2099.

[138] Pavelescu, E.-M., Hakkarainen, T., Dhaka, V.D.S., Tkachenko, N.V., Jouhti, T., Lemmetyinen, H. & Pessa, M. Influence of arsenic pressure on photoluminescence and structural properties of GaInNAs/GaAs quantum wells grown by molecular beam epitaxy. Journal of Crystal Growth 281(2005)2–4, pp. 249-254.

[139] Miyashita, N., Ahsan, N. & Okada, Y. Effect of antimony on uniform incorporation of nitrogen atoms in GaInNAs films for solar cell application. Solar Energy Materials and Solar Cells 111(2013)0, pp. 127-132.

[140] Kirk, A. High efficacy thinned four-junction solar cell. Semiconductor Science and Technology 26(2011)12, 125013.

[141] Takamoto, T., Ikeda, E., Kurita, H. & Ohmori, M. Over 30% efficient InGaP/GaAs tandem solar cells. Applied Physics Letters 70(1997)3, pp. 381-383.

[142] AZUR SPACE Solar Power GmbH, Azur space CPV triple junction solar cell - Type 3C40C (5.5*5.5mm^2), Cited: 06/14/2015, http://www.azurspace.com/images/pdfs/CPV%20TJ%20Solar%20Cell%203C40C%205.5x5.5 mm.pdf.

[143] Dimroth, F., Grave, M., Beutel, P., Fiedeler, U., Karcher, C., Tibbits, T.N.D., Oliva, E., Siefer, G., Schachtner, M., Wekkeli, A., Bett, A.W., Krause, R., Piccin, M., Blanc, N., Drazek, C., Guiot, E., Ghyselen, B., Salvetat, T., Tauzin, A., Signamarcheix, T., Dobrich, A., Hannappel, T. & Schwarzburg, K. Wafer bonded four-junction GaInP/GaAs//GaInAsP/GaInAs concentrator solar cells with 44.7% efficiency. Progress in Photovoltaics: Research and Applications 22(2014)3, pp. 277-282.

[144] Green, M.A., Emery, K., Hishikawa, Y., Warta, W. & Dunlop, E.D. Solar cell efficiency tables (Version 45). Progress in Photovoltaics: Research and Applications 23(2015)1, pp. 1-9.

[145] Bett, A.W., Dimroth, F., Guter, W., Hoheisel, R., Oliva, E., Philipps, S.P., Schöne, J., Siefer, G., Steiner, M. & Wekkeli, A. Highest efficiency multi-junction solar cell for terrestrial and space applications. 24th European Photovoltaic Solar Energy Conference, 21-25 September 2009, Hamburg, Germany (2009) pp. 1-6.

[146] Ilegems, M. Beryllium doping and diffusion in molecular beam epitaxy of GaAs and AlxGa1-xAs. Journal of Applied Physics 48(1977)3, pp. 1278-1287.

[147] Nair, H.P., Crook, A.M. & Bank, S.R. Enhanced conductivity of tunnel junctions employing semimetallic nanoparticles through variation in growth temperature and deposition. Applied Physics Letters 96(2010)22.

[148] García, I., Rey-Stolle, I. & Algora, C. Performance analysis of AlGaAs/GaAs tunnel junctions for ultra-high concentration photovoltaics. Journal of Physics D: Applied Physics 45(2012)4, pp. 045101.

[149] Barrigón, E., García, I., Barrutia, L., Rey-Stolle, I. & Algora, C. Highly conductive p ++-AlGaAs/n++-GaInP tunnel junctions for ultra-high concentrator solar cells. Progress in Photovoltaics: Research and Applications 22(2014)4, pp. 399-404.

[150] Siefer, G., Gandy, T., Schachtner, M., Wekkeli, A. & Bett, A.W. Improved grating monochromator set-up for EQE measurements of multi-junction solar cells. Photovoltaic Specialists Conference (PVSC), 2013 IEEE 39th, 2013, pp. 0086-0089.

[151] Meusel, M., Baur, C., Létay, G., Bett, A.W., Warta, W. & Fernandez, E. Spectral response measurements of monolithic GaInP/Ga(In)As/Ge triple-junction solar cells: Measurement artifacts and their explanation. Progress in Photovoltaics: Research and Applications 11(2003)8, pp. 499-514.

[152] CLAPHAM, P.B. & HUTLEY, M.C. Reduction of Lens Reflexion by the "Moth Eye" Principle. Nature 244(1973)5414, pp. 281-282.

[153] Tommila, J., Aho, A., Tukiainen, A., Polojärvi, V., Salmi, J., Niemi, T. & Guina, M. Moth-eye antireflection coating fabricated by nanoimprint lithography on 1 eV dilute nitride solar cell. Progress in Photovoltaics: Research and Applications 21(2013)5, pp. 1158-1162.

[154] Tommila, J., Polojärvi, V., Tukiainen, A., Salmi, J., Puustinen, J., Aho, A., Ranta, S., Niemi, T. & Guina, M. Moth-eye antireflection coatings fabricated by nanoimprint lithography on dilute nitride solar cell. European Photovoltaic Solar Energy Conference and Exhibition EU PVSEC (2011) pp. 367-369.

[155] Tommila, J., Polojrvi, V., Aho, A., Tukiainen, A., Viheril, J., Salmi, J., Schramm, A., Kontio, J.M., Turtiainen, A., Niemi, T. & Guina, M. Nanostructured broadband antireflection

coatings on AlInP fabricated by nanoimprint lithography. Solar Energy Materials and Solar Cells 94(2010)10, pp. 1845-1848.

[156] Yu, P., Chiu, M., Chang, C., Hong, C., Tsai, Y., Han, H. & Wu, Y. Towards high-efficiency multi-junction solar cells with biologically inspired nanosurfaces. Progress in Photovoltaics: Research and Applications 22(2014)3, pp. 300-307.

[157] Han, K., Shin, J., Yoon, W. & Lee, H. Enhanced performance of solar cells with anti-reflection layer fabricated by nano-imprint lithography. Solar Energy Materials and Solar Cells 95(2011)1, pp. 288-291.

[158] Perl, E.E., Chieh-Ting Lin, McMahon, W.E., Bowers, J.E. & Friedman, D.J. Design of ultra-broadband antireflection coatings utilizing integrated moth-eye structures for multi-junction device applications. Photovoltaic Specialists Conference (PVSC), 2013 IEEE 39th, 2013, pp. 1902-1906.

[159] Aiken, D.J. High performance anti-reflection coatings for broadband multi-junction solar cells. Solar Energy Materials and Solar Cells 64(2000)4, pp. 393-404.

[160] Liu, J., Ho, W., Syu, J., Lee, Y., Lin, C. & Shiao, H. Performance improvement of a triple-junction GaAs-based solar cell using a SiO 2-nanopillar/SiO 2/TiO 2 graded-index antireflection coating. International Journal of Nanotechnology 11(2014)1-234, pp. 311-321.

P1

Publication 1

Aho, A., Polojärvi, V., Korpijärvi, V.-M., Salmi, J., Tukiainen, A., Laukkanen, P. & Guina, M. Composition dependent growth dynamics in molecular beam epitaxy of GaInNAs solar cells. Solar Energy Materials and Solar Cells 124(2014), pp. 150-158.

Solar Energy Materials & Solar Cells 124 (2014) 150–158

Contents lists available at ScienceDirect

Solar Energy Materials & Solar Cells

journal homepage: www.elsevier.com/locate/solmat

Composition dependent growth dynamics in molecular beam epitaxy of GaInNAs solar cells

Arto Aho [a,*], Ville Polojärvi [a], Ville-Markus Korpijärvi [a], Joel Salmi [a], Antti Tukiainen [a], Pekka Laukkanen [b], Mircea Guina [a]

[a] Tampere University of Technology, Optoelectronics Research Centre, Korkeakoulunkatu 3, Tampere FI-33720, Finland
[b] University of Turku, Department of Physics and Astronomy, Finland

ARTICLE INFO

Article history:
Received 3 May 2012
Received in revised form
23 January 2014
Accepted 31 January 2014
Available online 21 February 2014

Keywords:
Plasma-assisted molecular beam epitaxy
Multi-junction solar cells
Dilute nitrides
GaInNAs
Concentrated photovoltaics

ABSTRACT

We have investigated the role of the nitrogen content, the growth parameters, and the annealing processes involved in molecular beam epitaxy of GaInNAs solar cells lattice-matched to GaAs. The nitrogen composition was varied between 1% and 5%. The influence of the growth temperature was assessed by performing photoluminescence, atomic force microscopy, X-ray diffraction, reflection high-energy electron diffraction, quantum efficiency and light-biased current–voltage measurements. The growth temperature ensuring the best cell parameters was found to be 440 °C. At this temperature we were able to incorporate up to 4% of nitrogen and achieve a good material quality. Further increase of the N composition to 5% led to phase separation. For the lattice matched samples grown within the optimal temperature range, we have identified a clear (1 × 3) surface reconstruction. Using the optimized growth we have demonstrated a GaInNAs p-i-n solar cell structure containing 4% nitrogen, that exhibited a short-circuit current density as high as 33.8 mA/cm^2 in respect to effective area illuminated. These measurements have been performed under real sun AM1.5 (~1000 W/m^2) illumination.

1. Introduction

Multi-junction III–V solar cells (MJSCs) with efficiencies above 40% are poised to make a strong impact on the development of concentrated photovoltaic (CPV) systems [1,2]. Solar cells (SC) with efficiency above this level would make CPV systems even more attractive and could accelerate the penetration and the development of more advanced solutions to the market. This goal can be achieved by using MJSCs with 4 or even 5 junctions collecting efficiently the solar energy spectrum down to 1 eV and below. However, the developments are daunted by a lack of high-quality 1 eV band gap materials that are lattice matched to GaAs and Ge and can ensure high current generation. The state-of-the-art commercial solar cells that are based on 3 junctions, i.e. GaInP/GaInAs/Ge, can reach efficiencies slightly above 41% under concentrated sunlight [3,4]. SCs making use of GaInAs with small band gaps need to be grown metamorphically which complicates the fabrication and increases the number of crystalline defects. A very promising alternative for the development of 1 eV compounds lattice-matched to GaAs is to use dilute nitrides, i.e. GaInNAs [5,6] with an N content of only a few percent. Replacing a small fraction of the As atoms with N induces a strong reduction of the band gap and reduces the lattice constant enabling lattice matching to GaAs [7]. Despite these prospects, achieving a sufficiently high material quality for SC applications of dilute nitrides has remained elusive, at least when it comes to the use of metal–organic chemical vapor deposition (MOCVD), which is currently adopted for the commercial fabrication of III–V SCs. Generally speaking, the synthesis of dilute nitride materials is rather challenging because these alloys are metastable and have a large miscibility gap [8,9]. Therefore, they have to be grown under non-equilibrium conditions to incorporate even small amounts of N. We note here that in order to achieve 1 eV GaInNAs material lattice-matched to GaAs, we would need to incorporate about 3% of N, which is already a high value and can lead to significant defect densities. In particular, the use of dilute nitrides has been hampered by the rather complex defects associated with N incorporation [10] and relatively low growth temperature used in the epitaxy of dilute nitrides [11]. Such defects decrease the carrier lifetimes and diffusion lengths. These effects get more severe when the amount of nitrogen is increased leading to reduced voltages and poor quantum efficiencies [10,12].

* Corresponding author. Tel.: +358 40198 1053.
E-mail address: arto.j.aho@tut.fi (A. Aho).

http://dx.doi.org/10.1016/j.solmat.2014.01.044
0927-0248

Despite the complexity of GaInNAs material system, there are means to reduce the number of defects associated with N incorporation. First of all, when it comes to epitaxial techniques used for fabricating dilute nitrides, molecular beam epitaxy (MBE) offers clear advantages over MOCVD, as it avoids issues related to C doping and hydrogen related complexes [16]. MBE also allows operation at relatively low growth temperatures to avoid phase separation and clustering effects. The most common way of incorporating N in MBE uses a radio frequency (RF) plasma source to crack high purity N_2 molecules into N atoms. The down side of using RF plasma source is that it simultaneously generates N ions that cause additional defects within the epitaxial structure. Fortunately, in plasma assisted molecular beam epitaxy (PAMBE), the detrimental effect of the ions can be reduced by optimizing the design of the RF plasma source and using ion deflecting electric or magnetic fields [13–15]. The use of surfactants [15], post growth annealing [16,17], and the overall growth parameter optimization in MBE [12,18–20] have also a remarkable effect on the number and the type of defects.

The fundamental surface processes involved in dilute nitride growth by PAMBE are mainly controlled by thermal energy applied to the substrate [11,18,21–23]. The optimal growth temperature (T_g) window for the epitaxy of GaInNAs is defined by different processes limiting the crystal quality at high and low T_g. In the low T_g range (defined as $T_g < 420$ °C), high quality epitaxy is hindered by the formation of various point defects that appear due to lack of thermal energy. The point defects have been identified as group-III vacancies [24], arsenic anti-sites [24], interstitial nitrogen [18] and even arsenic dimers [25]. GaAs [26] and GaNAs [27] growth also evolves to an amorphous growth mode if the T_g is lowered below 300 °C, and thus similar effect can be predicted for GaInNAs. At the high T_g range (i.e. $T_g > 480$ °C) the high quality two-dimensional (2D) growth is mainly limited by the phase separation of the GaInNAs crystal to InAs and GaN rich phases [38]. It has also been proposed that the phase separation takes place because the N segregation to the surface leads to enhanced In segregation, which eventually leads to a three dimensional growth mode and poor interfaces [21–23]. After growth, the defect density can be reduced by annealing the crystal at high temperatures [16,17]. The main effects of annealing are related to a change of the neighboring configuration of atoms in the crystal lattice. Essentially, the amount of Ga–N bonds is reduced compared to In–N bonds [16,28] while there is also a substantial decrease of the point defects, leading to higher crystal quality [15,16].

The temperature related processes involved in the epitaxy of dilute nitride quantum wells (QW) have been thoroughly studied [11,21–23]. However, in most of the published reports, the GaInNAs layers have been compressively strained or the studies have been carried out only for a specific N composition. Much less is known about the composition dependent growth dynamics in thick GaInNAs layers lattice matched to GaAs or about the effect of the growth processes on the operation of solar cells using such GaInNAs heterostructures. In this paper, we report a study focused on improving the understanding of the relation between the MBE growth temperature and the quality of GaInNAs solar cells with various N contents in connection with annealing processes. Finally, we assess the performance of 1 eV GaInNAs solar cell containing 4% N and which was grown under optimized conditions. We have also incorporated the 1 eV absorbing region within a GaInP/GaAs/GaInNAs solar cell with an AlInP window to show that the growth conditions we have devised are suitable for the fabrication of multijunction solar cells.

2. Description of structures and the experiments

2.1. Growth and processing

The GaInNAs heterostructures were grown on n-GaAs(1 0 0) and p-GaAs(1 0 0) substrates using a Veeco GEN20 solid source MBE equipped with a Veeco Uni-Bulb RF plasma source for nitrogen activation. For all samples, we used a As/III beam equivalent pressure (BEP) ratio of 10; this ratio was shown to result in high optical quality GaInNAs [20]. For the GaInNAs experiments, the In compositions were calibrated using $Ga_{0.9}In_{0.10}As$/GaAs superlattice structures comprised of four periods of 6-nm-thick GaInAs and 10-nm-thick GaAs layers grown on n-GaAs (1 0 0) substrates. The In compositions of GaInAs were analyzed from high-resolution x-ray diffraction (XRD) rocking curves using dynamical diffraction theory and commercial fitting algorithms. The N composition was varied by changing the plasma power between 150 W and 300 W, and the N_2 flow between 0.15 sccm and 0.53 sccm. This parameter range corresponds to a variation of the N content from 1% to 5%. After the composition calibrations, we fabricated three sets of GaInNAs samples.

The first set of samples was grown on n-GaAs(1 0 0) and consisted of GaInNAs bulk layers without contact layers. This set was used for structural characterization and optimization of the growth temperature. The samples' structure is shown in Fig. 1. The N compositions were 3% and 5% while the In flux was fixed and corresponded to a composition of 8%. Therefore, for 3% N, the GaInNAs layers were lattice matched to GaAs and their thickness was 500 nm. Accordingly, for the 5% N, the GaInNAs layer was tensile-strained and had a thickness of 200 nm (below the critical thickness). For this set, the growth temperature was changed between 375 °C and 525 °C.

The second set of samples was grown on n-GaAs(1 0 0) and consisted of an undoped GaInNAs layer with a thickness of 320 nm, which was incorporated between Si- and Be-doped GaAs layers, as shown in Fig. 1. This set was used for optical and electrical characterization. The In and N compositions were 2.7%, 5.6% and 8.0%, and 1%, 2%, and 3%, respectively, as required for lattice matching to GaAs. The growth temperature for the GaInNAs region was changed between 395 °C and 495 °C, while the In and N fluxes were kept fixed for each lattice-matched compositions targeted. We should note here that the effective N composition

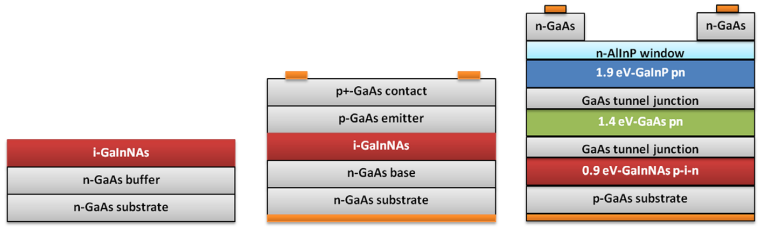

Fig. 1. Generic structure of the bulk sample for structural characterization, the p-i-n solar cell including a 320 nm thick InGaAsN absorber lattice matched to n-GaAs(1 0 0) substrate and GaInP/GaAs/GaInNAs MJSC.

increases with the growth temperature for constant N flux leading to slight decrease of the lattice constant and band gap [29]. After growth, these p-i-n samples were thermally annealed at 800 °C and electrical contacts were processed using shadow masks. We used Ni/Ge/Au for n-side contact grid metallization and Ti/Pt/Au on the p-side. The total solar cell area was 0.157 cm^2 with a metal coverage of 25% and an active area of 0.117 cm^2. For these tests the top surface was not antireflection coated.

The third set of samples was fabricated taking into account the identified optimal growth parameters and was used to assess the performance of more realistic GaInNAs-based solar cells. To this end, we fabricated a GaInNAs p-i-n single-junction solar cell and a GaInP/GaAs/GaInNAs MJSC, both grown on p-GaAs(1 0 0). The N composition for the two solar cells was 4% and the growth temperature was 440 °C. A schematic structure of the MJSC is also shown in Fig. 1. After the growth, the optimized SCs were processed and coated by plasma-enhanced chemical vapor deposition. We used a SiN_x/SiO_2 antireflection (AR) coating designed to have minimum reflectivity at 1000 nm.

2.2. Characterization

The surface structure of the bulk GaInNAs samples incorporating 3% N was studied in-situ by reflection high energy electron diffraction (RHEED). After growth, the first set of samples with 3% and 5% N were studied by XRD and atomic force microcopy (AFM). The p-i-n structures were studied by photoluminescence (PL), time-resolved PL (TRPL) and XRD. For a differential comparison of the p-i-n structures, we measured light-biased current–voltage (LIV) characteristics using a solar simulator (Thermo Oriel, 1000 W) equipped with a Xe-lamp and an AM0 filter. In addition, we used a 900 nm high pass filter (Thorlabs FEL900 filter) to simulate the cell operation in a MJSC configuration where the short wavelength spectrum below 900 nm would be absorbed by the top cells. The lamp excitation power was fixed using a known solar cell without 900 nm filter. Based on the separate external quantum efficiency (EQE) measurements of GaInNAs p-i-n SCs, the LIV measurement conditions corresponded approximately to one sun illumination with an ideal 900 nm high pass filter. During the experiments, the dark current–voltage characteristics of the SCs were also measured.

The EQEs were measured for p-i-n SCs with N-content ranging from 1% to 3% (second set of samples) and for the optimized single junction GaInNAs SC (third set). As a light source we used an Oriel 250 W QTH lamp. The narrow excitation wavelength span was chosen by using a Digikrom DK240 monochromator and a proper combination of long-pass and short-pass filters. The system also contained a Gigahertz Optik P-9202-4 detector amplifier which was used as a current-to-voltage converter. The signal from solar cells and reference detectors were measured using an SRS SR830 lock-in amplifier and chopped light. We use NIST-calibrated Si and Ge reference detectors for the wavelength ranges of 400–1000 nm and 800–1600 nm, respectively.

The GaInNAs p-i-n and GaInP/GaAs/GaInNAs SCs with 4% N were measured under real sun illumination in Tampere, Finland. The illumination intensity was assessed using a Kipp & Zonen CM11 pyranometer and the air masses were determined for each measurement based on the measurement location and time.

3. Experimental results and discussions

This chapter presents the structural, optical and electrical characteristics of the GaInNAs crystals. Section 3.1 is concerned with the structural characteristics of bulk heterostructure (first set of samples) and the optical characteristics p-i-n GaInNAs structures (second set). The performance of processed p-i-n SCs are presented in Section 3.2. The results described in Sections 3.1 and 3.2 are discussed and analyzed in detail in Section 3.3. Finally, in Section 3.4, we present and discuss the results of the single junction and triple junction SC incorporating GaInNAs grown under optimized conditions.

3.1. Structural and optical characterization of the GaInNAs heterostructures

The composition and structural quality were first assessed by XRD. Because the bulk samples used for growth temperature optimization were grown with constant In and N fluxes, we can assume that all the crystallographic changes would arise from the variation of the T_g. For these samples, we observed that GaInNAs XRD peak shifted from compressive to tensile side when T_g was increased from 375 °C to 465 °C (see Fig. 2). This corresponds to an absolute compositional change of ± 0.33 percentage points for N or -1.0 percentage points for In, leading to approx $\pm 0.04\%$ maximum lattice mismatch. The Pendellösung oscillations were observed to be stronger at low growth temperatures indicating sharper interfaces and better crystal quality. The observations based on XRD measurements are supported by in-situ RHEED patterns measured during the crystal growth. As shown in Fig. 3, the RHEED pattern for the lattice matched bulk samples with 3% N exhibited a clear (1×3) surface reconstruction, which was the clearest at $T_g \approx 450$ °C but became spotty when the temperature was increased above this point. This was the only reconstruction observed during the growth of GaInNAs. The (1×3) reconstruction is interesting because usually it is not seen on the III–As(1 0 0) binary surfaces but has been previously observed for $Ga_{0.90}In_{0.10}As$

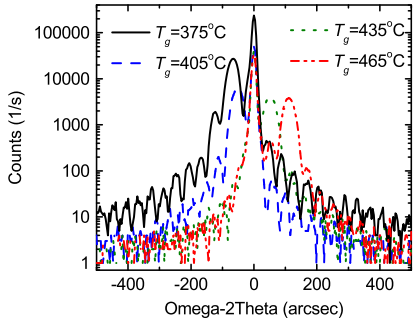

Fig. 2. Omega-2Theta XRD scan over the GaAs(0 0 4) reflection of GaInNAs SCs grown at different temperatures. Pendellösung oscillations are the strongest for the samples grown at low T_g.

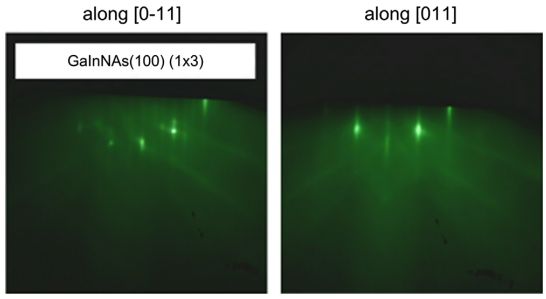

Fig. 3. RHEED patterns observed during the growth of $Ga_{0.92}In_{0.08}N_{0.03}As_{0.97}$ on GaAs(1 0 0) revealing a 1×3 surface reconstruction at 450 °C.

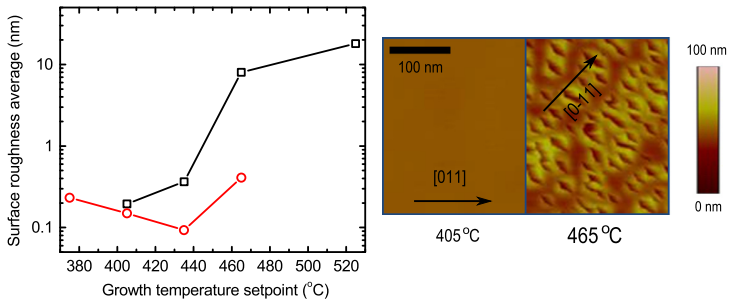

Fig. 4. Surface roughnesses from $Ga_{0.92}In_{0.08}N_{0.03}As_{0.97}$ (circles) and $Ga_{0.92}In_{0.08}N_{0.05}As_{0.95}$ (squares) layers grown at different temperatures. Right-hand side: AFM surface images taken from $Ga_{0.92}In_{0.08}N_{0.05}As_{0.95}$ grown at 405 °C and 465 °C. Deep holes (28 nm) are seen on the surface of the sample grown at 465 °C. Holes are elongated in [0–1 1] direction.

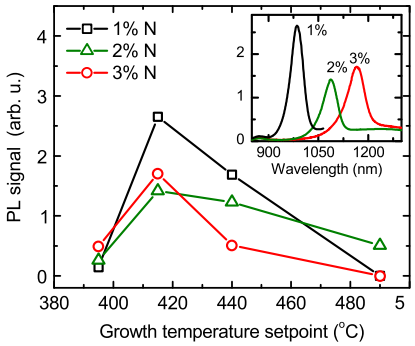

Fig. 5. PL signal of the SCs with 1%, 2% and 3% N measured at 300 K as a function of growth temperature. Inset: PL emission peaks at room temperature for the annealed GaInNAs SCs lattice matched to GaAs. Samples were grown at 415 °C and contained 1%, 2%, 3% N.

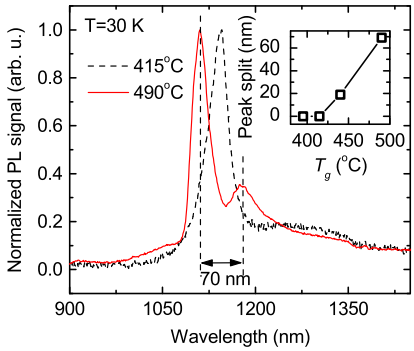

Fig. 6. LTPL measurements. The PL peak of samples with 3% N splits when T_g is increased. The inset shows how spectral splitting depends on the T_g. Dashed lines are used to indicate the 70 nm spectral splitting for the sample grown at 490 °C.

growth at ~450 °C [30]. Furthermore, we have used AFM for the surface structure and roughness analysis. We measured AFM in tapping mode and the presented roughness values are arithmetic averages. These measurements were done for samples where GaInNAs was the top-most layer. The results are summarized in Fig. 4. Clear minima of the surface roughness were detected near 440 °C for the samples with 3% N. For higher N composition and higher T_g the surface roughness increases; in fact we observed formation of surface pits elongated along the [0–1 1], as revealed in Fig. 4. This leads to a conclusion that higher nitrogen content shifts the 2D growth temperature window to lower temperatures.

The optical quality of the as-grown and thermally annealed GaInNAs p-i-n structures was assessed by measuring the PL properties. The room temperature PL and carrier lifetime improved remarkably with the annealing for the entire N composition range between 1% and 3% [31]. Annealing also caused a slight blue shift of the photoluminescence emission peak of GaInNAs. The blue shift increases with T_g, being 10 meV for T_g=400 °C and reaching 40 meV when T_g approaches 500 °C [29]. The blue shift is caused by changes in the short range ordering of GaInNAs crystal during thermal annealing. The changes in the short range ordering are rapid with annealing but no further changes take place after the atomic rearrangement [29]. For the annealed samples, the band-gaps of the GaInNAs layers with N compositions of 1%, 2% and 3%, were approximately 1.25 eV, 1.14 eV and 1.06 eV, respectively. As it can be seen in Fig. 5, the p-i-n samples grown at 415 °C had the highest PL intensities for all compositions. The PL intensity dropped rapidly on both sides of 415 °C. Moreover, higher T_g resulted in longer PL wavelengths for the annealed samples. For samples with N fluxes targeting nominal composition of 3%, the PL wavelength increased linearly from 1161 nm to 1194 nm when T_g was increased from 395 °C to 490 °C. Since the In incorporation in MBE does not depend on the T_g within the studied temperature range [32] and since the In flux was fixed during the experiment, the red-shift of the PL wavelength is associated with an increase of the N concentration with increasing the T_g. Using the band anticrossing model [33] we have estimated the change of N-composition corresponding to this wavelength shift to be close to +0.42 percentage points, which is in a good agreement with the XRD analysis that provided an estimation of 0.33 percentage points for N increase (see previous section). This phenomenon has also been confirmed by other samples and measurement methods [30].

Furthermore, we performed low temperature PL (LTPL) measurements at 30 K for the p-i-n samples with 3% N; these measurements are summarized in Fig. 6. We found that the PL peak splits into two components and the split is dependent on T_g for temperatures above 415 °C. For compositions below 3% we did not observe any clear evidence of spectral splitting in this T_g range. The linewidths of the PL peaks were also dependent on T_g: they were broadened at the low T_g and the high T_g ranges. At high T_g, the PL lines broadened due to spectral splitting while the individual peaks remained quite narrow. The splitting of the spectrum is considered to be an indication of partial phase separation of GaInNAs into In and N rich areas. The peak splitting observed for samples grown at high T_g is in a good agreement with previously observed peak splitting of 40 meV for phase separated compressive $GaIn_{0.30}N_{0.03}As$ QWs [34]. In our case, the splitting is between 0 meV and 66 meV (70 nm) depending on T_g. Phase separation

could also explain why the compositional changes of N determined by XRD and PL measurements differ by about 0.09 percentage points from each other. For phase separated bulk GaInNAs material we assume to have undulating In and N composition and band structure. Deterioration of crystal structure seen earlier by XRD [31] for all samples with 5% of N and the large surface roughness observed by AFM, lead to a conclusion that phase separation takes place in samples with high N composition already at growth temperatures which are otherwise optimal for lower N compositions.

3.2. Properties of the GaInNAs solar cells

3.2.1. The general effect of N composition and annealing on SC performance

For the processed p-i-n structures (second set of samples), we performed LIV measurements with a Xenon simulator and 900 nm high-pass filter to reveal how thermal annealing and nitrogen incorporation affect the cell parameters. In general, with differential comparison of the cells, the annealing has a drastic effect on the open circuit voltage (V_{oc}). For optimized parameters, V_{oc} was roughly doubled. After the annealing, the band-gap-voltage offset ($W_{oc}=E_g/q-V_{oc}$) was 0.58 V which is only 0.18 V higher than the typical experimental value (0.4 V) for high quality SCs at one sun [35]. Typical W_{oc} values for GaInNAs SC are close to 0.6 V [35]. Annealing improved the fill factors of the SCs remarkably—an increase of about 20% was observed for all samples. On the other hand, increasing the nitrogen composition from 1% to 3% reduced the fill factors of annealed samples from 74% to 68%. Based on dark-IV analysis, the improvements in fill factor and V_{oc} of 1 J GaInNAs SCs are related to a decrease of the dark current by about 10–15 times, an increase of the shunt resistance from 10–100 kΩ to 1–5 MΩ, and a small improvement of the series resistance. By far, the largest effect on V_{oc} and fill factor improvements at one sun is the decrease of the dark current.

3.2.2. The effect of the growth temperature on LIV characteristics, EQE and the annealing time required to achieve maximum power

For all N compositions the short circuit current (I_{sc}) of annealed samples increased up to T_g=440 °C and then saturated. We found that I_{sc} for annealed samples grown at 440 °C was about doubled when compared to samples grown at 395 °C; this was valid for the nominal N compositions of 1%, 2%, and 3%. As it can be seen in Fig. 7(a), the PL wavelength for a certain nominal composition of N, increases with T_g owing to increased N incorporation. Accordingly, the I_{sc} increases with the nominal N composition and T_g for annealed p-i-n SCs as shown in and Fig. 7(b), except for the lowest T_g of 395 °C where I_{sc} drops rapidly and highest T_g of 490 °C where the I_{sc} growth saturates.

The V_{oc} results as a function of the growth temperature are presented in Fig. 8. As-grown samples with less than 2% N showed a maximum V_{oc} when grown at the highest T_g. As seen in Fig. 8, the V_{oc} for not-annealed samples grown at low T_g is not as strongly dependent on the N composition as it is for the samples grown at higher T_g. The V_{oc} for the not-annealed samples with 3% N degrades when T_g is higher or lower than the optimal value. Fig. 8 also reveals that for an optimized annealing, the V_{oc} for SCs with larger N content was maximized for structures grown at lower T_g. The maximal V_{oc} for 1%, 2% and 3% N corresponded to growth temperatures of 440 °C, 415 °C and 395 °C, respectively. Moreover, SCs grown at high T_g have clearly lower V_{oc} after annealing compared to samples grown at temperatures below 450 °C.

The maximum output powers (P_{max}) of the SCs as a function of T_g and annealing time are summarized in Fig. 9(a) and (b).

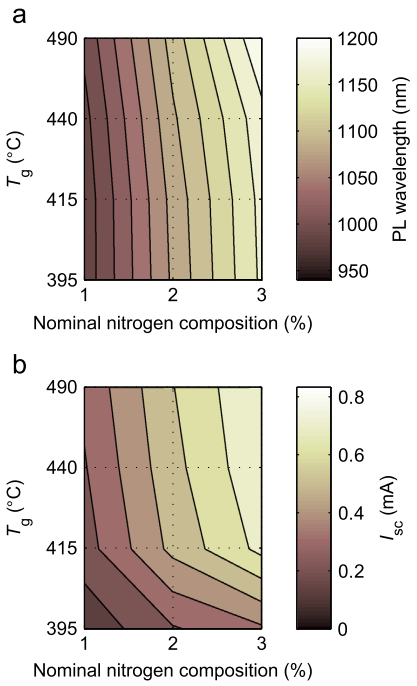

Fig. 7. (a) PL wavelength of the annealed GaInNAs p-i-n SC structures as a function of nominal N composition and growth temperature. (b) GaInNAs p-i-n SC I_{sc} as the function of nominal N composition and T_g.

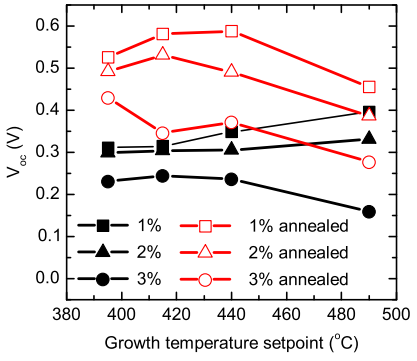

Fig. 8. V_{oc} before annealing (black and filled symbols) and after annealing (red and open symbols) as a function of T_g for SCs with 1%, 2% and 3% N. It can be seen that V_{oc} difference between the different N compositions at the high temperature (V_L) is bigger than at low temperature (V_H). V_H-V_L=0.16 V. (For interpretation of the references to color in this figure legend, the reader is referred to the web version of this article.)

The main findings of this analysis are: (i) the P_{max} corresponded to samples grown at T_g=440 °C and, (ii) the annealing time needed to achieve P_{max} was found to be dependent on the T_g. Related to annealing time, Fig. 9(b) reveals that the optimized annealing time is shortest for growth temperatures between 415 °C and 440 °C. Moreover, this temperature range leads to the highest P_{max} irrespective of N composition.

EQE measurements were performed on optimally annealed p-i-n SCs. Fig. 10(a) shows that the highest EQE was achieved for samples with 3% N. The inset of Fig. 10(a) presents the EQE at 900 nm and 1000 nm. The best SCs with 3% N had the highest EQE throughout

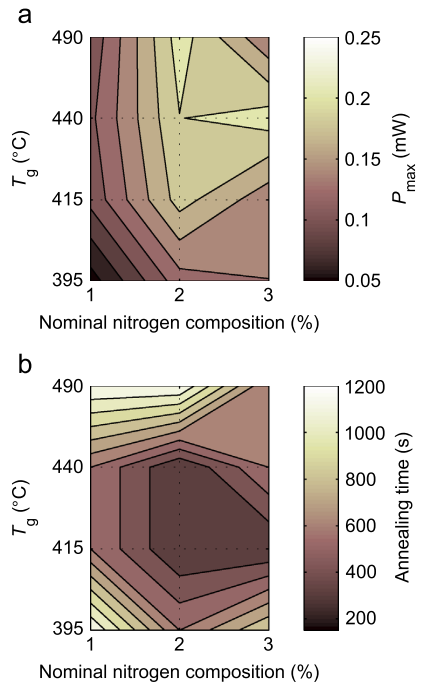

Fig. 9. A contour map of the maximum SC output power (a) and annealing time for the maximized SC output power (b) as a function of T_g and nominal N composition.

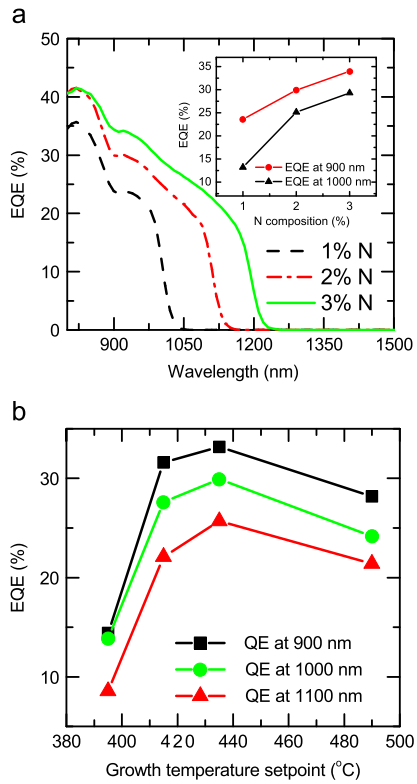

Fig. 10. (a) Measured EQE from optimally annealed 1%, 2% and 3% N SCs grown at 440 °C and EQE at 900 nm and 1000 nm (inset) with different N composition (T_g=440 °C). (b) Measured EQEs at 900 nm (squares), 1000 nm (circles) and 1100 nm (triangles) for optimally annealed 3% N solar cells grown at different T_g. Samples were left uncoated.

the whole measured spectral range starting from 800 nm. Fig. 10 (b) also shows the dependence of EQE for 3% N SCs grown at different temperatures. EQE increased rapidly when T_g was increased up to 440 °C and decreased after that. For 1% and 2% N compositions, we did not detect a significant drop of EQE at high T_g and the EQE remained almost constant in T_g range from 415 °C to 490 °C. In general, the EQEs were quite low. This is understandable as the thickness of the light absorbing undoped GaInNAs layer was only 320 nm and no antireflection coating was used. Moreover, the test samples did not have any back-surface field (BSF) or window layers that would also have further improved the EQE [36]. Ultimately we would also expect some decrease of EQE due to detrimental effects related to N incorporation [10].

3.3. Combined analysis of structural, optical, and electrical measurements

For the as-grown samples with less than 2% N, the V_{oc} increased with T_g, which can be explained by fewer point defects generated during the growth. The drastic increase of V_{oc} and the decrease of dark currents for annealed samples are directly related to the annihilation or transformations of point defects or defect complexes in GaInNAs [10]. The V_{oc} difference between the as-grown samples with different nitrogen composition also gets smaller when the T_g is lowered. This presumably indicates that not only nitrogen-related defects are limiting the V_{oc} and that unusual Ga-interstitial formation [37] or As antisites should be also taken into account. The reason for this behavior could be the high group V flux and the lack of thermal energy for the surface migration of group III atoms. Poor room temperature PL signal, broadening of LTPL peak, rapid decrease of I_{sc} and decrease of EQE for the samples grown at lowest T_g are all related to the increase of the defect density.

Generally, the increase of I_{sc} with higher growth temperatures can be explained by the shift of the absorption edge to longer wavelengths, which is revealed by PL and EQE measurements. Although the EQE decreased on both ends of the T_g range (see Fig. 10(b)), for samples with 3% N the efficiency decrease at highest T_g compensated the effect of band gap reduction (due to increased N composition) leading to saturation of I_{sc}. This behaviour has been confirmed by calculated I_{sc} from the EQE data. The reason for lower EQE for SC grown at T_g of 490 °C is considered to be partial phase separation. The onset of phase separation is clearly seen as increased surface roughness detected by spotty RHEED during the growth and ex-situ AFM measurements. No phase separation could be detected for the 1% and 2% N SCs even at high T_g; accordingly, we did not observe a drop in EQE and peak broadening of the LTPL signal. This is indeed expected when considering that the T_g limit for the phase separation shifts to higher temperatures when the N composition is decreased [9]. The effect of high T_g in annealed SCs is still seen as lower V_{oc} for all compositions from 1 to 3%. For SCs with 1% and 2% N, we assume that lower V_{oc} of samples grown at high T_g are caused by the short range ordering towards Ga–N and In–As rich configuration [38], which finally leads to observable phase separation in samples with higher N content. This phenomenon leads to a need to lower the T_g for the GaInNAs SCs with high N compositions.

The optimal annealing time for maximizing the P_{max} was the shortest within the growth temperature range of 415 °C to 440 °C.

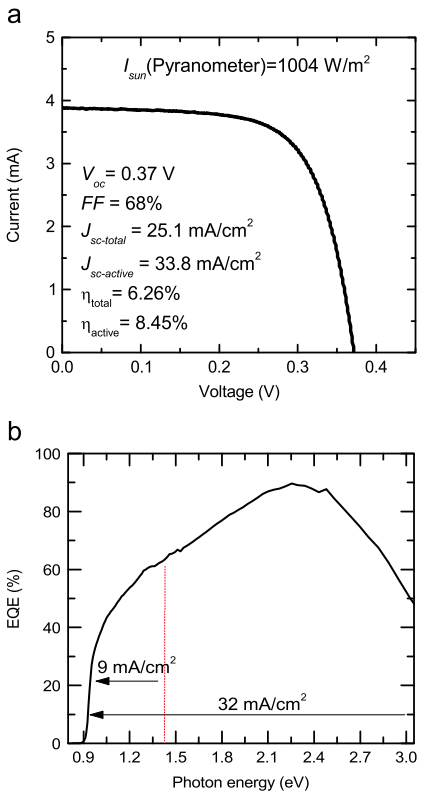

Fig. 11. (a) LIV characteristics and (b) EQE of $Ga_{0.89}In_{0.11}N_{0.04}As_{0.96}$ SC. The measurements were done at AM1.52 real sun illumination. The shown current densities were integrated from the measured EQE assuming AM1.5 G spectrum with and without a GaAs filter. The vertical line indicates the bandgap of GaAs (1.42 eV).

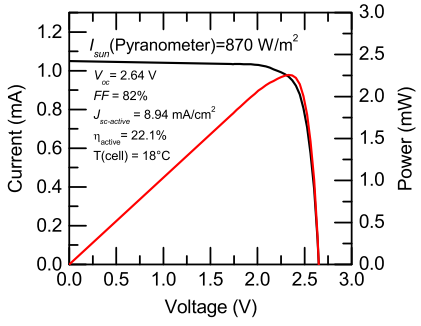

Fig. 12. GaInP/GaAs/GaInNAs MJSC with SiN_x/SiO_2 anti-reflection coating. Measurements were done at real sun illumination.

The need for longer annealing time, for samples grown at 395 °C, can be explained by a rapid increase of low temperature defects. Assuming that the optimal annealing time is only proportional to the number of defect species, it should decrease for samples grown at high T_g because of the reduced point defect density. The result, however, is the opposite. The need for longer annealing is presumably caused by partial phase separation and the increase in the number of Ga–N and In–As bonds in GaInNAs grown at high T_g. Phase separated quantum dot (QD) like areas are far away from each other compared to low T_g point defects resulting in the need for a longer annealing. Similar behavior has been observed for GaInNAs QW structures [39]. The QD-like areas lower the effective material band gap [23] resulting in lower V_{oc} and P_{max}. On the other hand, Ga–N bond rich material leads to reduced V_{oc} since it has been addressed to have high recombination currents [16]. Therefore, we conclude that the 415–440 °C is the growth temperature window where the defect populations in the GaInNAs crystal can be efficiently suppressed by annealing resulting in highest quality GaInNAs crystal.

3.4. The performance of growth-optimized GaInNAs solar cells

For GaInP/GaAs/GaInNAs multi junction SC, the thickness of i-GaInNAs and its band gap has to be optimized in order to achieve ~14 mA/cm^2 current matching at AM 1.5 G. Based on the photon flux at AM1.5G illumination, the average EQE of the junction with E_g=0.9 eV has to be only ~70% instead of 100% for E_g=1.04 eV for current matching. As the growth of GaInNAs with 5% N is already challenging we propose that the optimal N concentration SCs should be close to 4%. Based on this target and growth temperature optimization presented in this paper, we prepared an AR-coated single junction p-i-n structure on p-GaAs(1 0 0) with 1300 nm thick undoped GaInNAs region and 4% N. The LIV curve shown in Fig. 11(a) reveals promising short-circuit current densities (J_{sc}). When referred to the total illuminated area, the $J_{sc\text{-}total}$ was ~25.1 mA/cm^2. The $J_{sc\text{-}active}$ in respected to the metal-less effective area was 33.8 mA/cm^2. The measurements were performed at real sun illumination level of 1004 W/m^2 and AM1.52 [40]. The V_{oc} and fill factor values were 0.37 V and 68%, respectively. The band-gap-voltage offset for this SC was only 0.55 V, while for thin p-i-n structures it was 0.58 V (see Section 3.2.1). The band-gap of GaInNAs was estimated from the absorption edge observed in EQE characteristics (see Fig. 11(b)) and it was ~0.92 eV. When calculated from EQE, GaInNAs p-i-n produces a J_{sc} of 9 mA/cm^2 for spectrum filtered by GaAs (1.42 eV) and 32 mA/cm^2 with the whole AM1.5G illumination spectrum.

Finally, the optimized GaInNAs sub-junction was embedded into a SiN_x/SiO_2 AR-coated GaInP/GaAs/GaInNAs triple junction SC in which AlInP and GaInP (E_g(GaInP)=1.88 eV) were lattice-matched to GaAs. The SC measured at 870 W/m^2 and AM3.2 real sun illumination [41], produced a $J_{sc\text{-}active}$=8.94 mA/cm^2, a V_{oc}=2.64 V, a fill factor of 82%, and an efficiency of 22.1% (see Fig. 12 for details). If the power level is normalized to 1000 W, it would give a $J_{sc\text{-}active}$ of 10.3 mA/cm^2, which correlates well with the 1 J current calculated from EQE. Even though the MJSC was current limited by GaInNAs SC to ~10 mA/cm^2, we were able to integrate the GaInNAs SC to triple junction device without sacrificing the GaInNAs SC current generation. We estimate that the J_{sc}s of single and triple junction SCs were limited by the background doping level of the dilute nitride i-region (estimated by Hall effect measurements to be ~10^{16} cm^{-3}), the non-ideal AR-coating reflectivity (~10%), and partly by the charge carrier lifetimes (~0.5 ns). For current matching, the background doping level for GaInNAs i-region has to be in the range of ~10^{15} cm^{-3} and charge carrier lifetime needs to be over 0.5 ns [42]. We deem these parameters as feasible for MBE technology.

4. Conclusion

We have performed a thorough study to identify the effects of growth temperature and N composition on the quality of lattice matched GaInNAs materials required for multijunction solar cells. We observed that the optimum T_g window is 415–440 °C and that

post growth annealing is needed for all compositions in order to improve material quality. This growth temperature window is the best compromise to reduce the density of point defects associated with low growth temperature, the phase separation effects acting at high growth temperatures, as well as short range ordering effects making the crystal easy to anneal. The point defects at low T_g easily limit the SC current generation. These defects are most likely not originated from N since the V_{oc} difference between the samples with different N compositions is very small. On the other hand, high T_g crystal ordering and phase separation clusters limit the V_{oc} and EQE at high N compositions. At high T_g the surface roughness increases rapidly with N composition, and therefore planar growth of crystal with 5% N is difficult even at 440 °C. It is clear that it would be challenging to grow the top junctions on such material which has poor morphology. Therefore, the realistic N-composition of lattice-matched GaInNAs junctions to be incorporated in GaInP/GaAs/GaInNAs SCs for AM1.5 applications is limited on one hand by the 100% EQE level that can be achieved for a N composition of ~2.6% (1.04 eV band gap), and on the other hand, by the phase separation limit occurring at compositions of ~5% at 440 °C. Based on these facts, we demonstrated a 0.9 eV GaInNAs single junction and a triple junction SC incorporating GaInNAs with 4% N. The single-junction SC exhibited a high crystal quality and produced a $J_{sc\text{-}active}$ of 33.8 mA/cm^2 at ~1000 W/m^2 real sun illumination. The calculated current density of this device from EQE and AM1.5G spectrum assuming perfectly absorbing GaAs junction was ~9 mA/cm^2. This result is well in line with the projected triple junction J_{sc} of 10 mA/cm^2 assuming a current limit imposed by GaInNAs junction. The result also demonstrates a successful integration of dilute nitride materials in GaInP/GaAs/GaInNAs multijunction solar cell. Further work will be directed towards optimization of the triple junction solar cell design, related AR coating, and contacts technology.

Acknowledgements

The authors would like to thank Juha Tommila, Andreas Schramm, Alexander Gubanov, Wenxin Zhang, Miki Tavast, Pekka Malinen and Prof. Nikolai Tkachenko for their high-quality experimental support. For the financial support, we would like to thank Finnish Funding Agency for Technology and Innovation—TEKES (project 40120/09 Solar III–V), County Administrative Board of Oulu for ENNA Project (project number S11249), National Graduate School in Material Physics, Graduate School in Electronics, Telecommunications and Automation, Ulla Tuominen Foundation, Finnish Foundation for Technology Promotion, Emil Aaltonen Foundation, and Wärtsilä Foundation.

References

[1] A. Luque, Will we exceed 50% efficiency in photovoltaics? J. Appl. Phys. 110 (2011) 031301.
[2] S. Kurtz, J. Geisz, Multijunction solar cells for conversion of concentrated sunlight to electricity, Opt. Express 18 (2010) A73–A78.
[3] M.A. Green, K. Emery, Y. Hishikawa, W. Warta, E.D. Dunlop, Solar cell efficiency tables (version 39), Prog. Photovoltaics Res. Appl. 20 (2012) 12–20.
[4] W. Guter, J. Schöne, S.P. Philipps, M. Steiner, G. Siefer, A. Wekkeli, E. Welser, E. Oliva, A.W. Bett, F. Dimroth, Current-matched triple-junction solar cell reaching 41.1% conversion efficiency under concentrated sunlight, Appl. Phys. Lett. 94 (2009) 223504.
[5] D.J. Friedman, J.F. Geisz, S.R. Kurtz, J.M. Olson, 1-eV Solar cells with GaInNAs active layer, J. Cryst. Growth 195 (1998) 409–415.
[6] J.F. Geisz, D.J. Friedman, J.M. Olson, S.R. Kurtz, B.M. Keyes, Photocurrent of 1 eV GaInNAs lattice-matched to GaAs, J. Cryst. Growth 195 (1998) 401–408.
[7] M. Kondow, K. Uomi, A. Niwa, T. Kitatani, S. Watahiki, Y. Yazawa, GaInNAs: a novel material for long-wavelength-range laser diodes with excellent high-temperature performance, Jpn. J. Appl. Phys. 35 (1996) 1273–1275.
[8] J. Neugebauer, C.G. Van de Walle, Electronic structure and phase stability of GaAs1$_{-x}$N$_x$ alloys, Phys. Rev. B: Condens. Matter 51 (1995) 10 568–10 751.
[9] D. Schlenker, T. Miyamoto, Z. Pan, F. Koyama, K. Iga, Miscibility gap calculation for Ga$_{1-x}$In$_x$NyAs$_{1-y}$ including strain effects, J. Cryst. Growth 196 (1999) 67–70.
[10] A. Khan, S.R. Kurtz, S. Prasad, S.W. Johnson, J. Gou, Correlation of nitrogen related traps in InGaAsN with solar cell properties, Appl. Phys. Lett. 90 (2007) 243509.
[11] Z. Pan, L.H. Li, W. Zhang, Y.W. Lin, R.H. Wu, Kinetic modeling of N incorporation in GaInNAs growth by plasma-assisted molecular-beam epitaxy, Appl. Phys. Lett. 77 (2000) 214.
[12] A.J. Ptak, R. France, C.-S. Jieang, M.J. Romero, Improved performance of GaInNAs solar cells grown by molecular-beam epitaxy using increased growth rate instead of surfactants, J. Cryst. Growth 311 (2009) 1876–1880.
[13] M.M. Oye, T.J. Mattord, G.A. Hallock, S.R. Bank, M.A. Wistey, J.M. Reifsnider, A.J. Ptak, H.B. Yuen, J.S. Harris , A.L. Holmes , Effects of different plasma species (atomic N, metastable N2*, and ions) on the optical properties of dilute nitride materials grown by plasma-assisted molecular-beam epitaxy, Appl. Phys. Lett. 91 (2007) 191903.
[14] J. Miguel-Sánchez, A. Guzmán, E. Muñoz, Role of N ions in the optical and morphological properties of InGaAsN quantum wells for 1.3–1.5 μm applications, Appl. Phys. Lett. 85 (2004) 1940.
[15] D.B. Jackrell, S.R. Bank, H.B. Yuen, M.A. Wistey, J.S. Harris , Dilute nitride GaInNAs and GaInNAsSb solar cells by molecular beam epitaxy, J. Appl. Phys. 101 (2007) 114916.
[16] K. Voltz, D. Lackner, I. Nemeth, B. Kunert, W. Stolz, C. Baur, F. Dimroth, A.W. Bett, Optimization of annealing conditions of (GaIn)(NAs) for solar cell applications, J. Cryst. Growth 310 (2008) 2222–2228.
[17] S.R. Kurtz, A.A. Allerman, E.D. Jones, J.M. Gee, J.J. Banas, InGaAsN solar cells with 1.0 eV band gap, lattice matched to GaAs, Appl. Phys. Lett. 74 (1999) 729.
[18] E.–M. Pavelescu, J. Wagner, H.-P. Komsa, T.T. Rantala, M. Dumitrescu, M. Pessa, Nitrogen incorporation into GaInNAs lattice-matched to GaAs: the effects of growth temperature and thermal annealing, J. Appl. Phys. 98 (2005) 083524.
[19] R. Kudrawiec, V.-M. Korpijärvi, P. Poloczek, J. Misiewicz, P. Laukkanen, J. Pakarinen, M. Dumitrescu, M. Guina, M. Pessa, The influence of As/III pressure ratio on nitrogen nearest-neighbor environments in as-grown GaInNAs quantum wells, Appl. Phys. Lett. 95 (2009) 261909.
[20] E.–M. Pavelescu, T. Hakkarainen, V.D.S. Dhaka, N.V. Tkachenko, T. Jouhti, H. Lemmetyinen, M. Pessa, Influence of arsenic pressure on photoluminescence and structural properties of GaInNAs/GaAs quantum wells grown by molecular beam epitaxy, J. Cryst. Growth 281 (2005) 249–254.
[21] E. Luna, A. Trampert, E.-M. Pavelescu, M. Pessa, Nitrogen-enhanced indium segregation in (Ga,In)(N,As)/GaAs multiple quantum wells grown by molecular-beam epitaxy, New J. Phys. 9 (2007) 405.
[22] J.–M. Chaveau, A. Trampert, K.H. Ploog, M.–A. Pinault, E. Tournie, Interplay between the growth temperature, microstructure, and optical properties of GaInNAs quantum wells, Appl. Phys. Lett. 82 (2003) 3451.
[23] W.M. McGee, R.S. Williams, M.J. Ashwin, T.S. Jones, E. Clarke, J. Zhang, S. Tomic, Structure, morphology, and optical properties of Ga$_x$In$_{1-x}$N$_{0.05}$As$_{0.95}$ quantum wells: influence of the growth mechanism, Phys. Rev. B: Condens. Matter 76 (2007) 085309.
[24] X. Liu, A. Prasad, J. Nishio, E.R. Weber, Z. Liliental-Weber, W. Walukiewicz, Native point defects in low-temperature-grown GaAs, Appl. Phys. Lett. 67 (1995) 279.
[25] E.S. Tok, J.H. Neave, J. Zhang, B.A. Joyce, T.S. Jones, Arsenic incorporation kinetics in GaAs(001) homoepitaxy revisited, Surf. Sci. 374 (1997) 397–405.
[26] D.A. Murdick, X.W. Zhou, H.N.G. Wadley, Low-temperature atomic assembly of stoichiometric gallium arsenide from equiatomic vapor, J. Cryst. Growth 286 (2006) 197–204.
[27] S.V. Novikov, C.R. Staddon, C.T. Foxon, K.M. Yu, R. Broesler, M. Hawkridge, Z. Liliental-Weber, J. Denlinger, I. Demchenko, F. Luckert, P.R. Edwards, R.W. Martin, W. Walukiewicz, Growth by molecular beam epitaxy of amorphous and crystalline GaNAs alloys with band gaps from 3.4 to 0.8 eV for solar energy conversion devices, J. Cryst. Growth 323 (2011) 60–63.
[28] S. Kurtz, J. Webb, L. Gedvilas, D. Friedman, J. Geisz, J. Olson, R. King, D. Joslin, N. Karam, Structural changes during annealing of GaInAsN, Appl. Phys. Lett. 78 (2001) 748.
[29] V.-M. Korpijärvi, A. Aho, P. Laukkanen, A. Tukiainen, A. Laakso, M. Tuominen, M. Guina, Study of nitrogen incorporation into GaInNAs: the role of growth temperature in molecular beam epitaxy, J. Appl. Phys. 112 (2012) 023504.
[30] P.A. Bone, J.M. Riplada, G.R. Bell, T.S. Jones, Surface reconstructions of InGaAs alloys, Surf. Sci 600 (2006) 973–982.
[31] A. Aho, A. Tukiainen, V. Polojärvi, A. Gubanov, J. Salmi, M. Guina, P. Laukkanen, Lattice matched dilute nitride materials for III–V high-efficiency multi-junction solar cells: growth parameter optimization in molecular beam epitaxy, EU PVSEC 2011, in: 26th European Photovoltaic Solar Energy Conference and Exhibition, 2011, pp. 58–61, http://dx.doi.org/10.4229/26thEUPVSEC2011-1AO.8.3.
[32] T. Suzuki, T. Nishinaga, Surface diffusion and atom incorporation kinetics in MBE of InGaAs and AlGaAs, J. Cryst. Growth 111 (1991) 173–177.
[33] I. Vurgaftman, J.R. Meyer, Band parameters for nitrogen-containing semiconductors, J. Appl. Phys. 94 (2003) 3675.
[34] H.P. Xin, K.L. Kavanagh, Z.Q. Zhu, C.W. Tu, Observation of quantum dot-like behavior of GaInNAs in GaInNAs/GaAs quantum wells, Appl. Phys. Lett. 74 (1999) 2337.
[35] R.R. King, D. Bhusari, A. Boca, D. Larrabee, X.–Q. Liu, W. Hong, C.M. Fetzer, D.C. Law, N.H. Karam, Band gap-voltage offset and energy production in next-generation multijunction solar cells, Prog. Photovoltaics Res. Appl. 19 (2011) 797–812.

[36] M. Yamaguchi, K.I. Nishimura, T. Sasaki, H. Suzuki, k. Arafune, N. Kojima, Y. Ohsita, Y. Okada, A. Yamamoto, T. Takamoto, K. Araki, Novel materials for high-efficiency III–V multi-junction solar cells, Sol. Energy 82 (2008) 173–180.
[37] X.J. Wang, Y. Puttisong, C.W. Tu, Aaron J. Ptak, V.K. Kalevich, A. Yu. Egorov, L. Geelhaar, H. Riechert, W.M. Chen, I.A. Buyanova, Dominant recombination centers in Ga(In)NAs alloys: Ga interstitials, Appl. Phys. Lett. 95 (2009) 241904.
[38] X. Kong, A. Trampert, E. Tournie, K.H. Ploog, Decomposition in as-grown (Ga,In)(N,As) quantum wells, Appl. Phys. Lett. 87 (2005) 171901.
[39] A. Hierro, J.-M. Ulloa, J.-M. Chauveau, A. Trampert, M.-A. Pinault, E. Tournié, A. Guzmán, J.L. Sánchez-Rojas, E. Calleja, Annealing effects on the crystal structure of GaInNAs quantum wells with large In and N content grown by molecular beam epitaxy, J. Appl. Phys. 94 (2003) 2319.
[40] Real Sun Measurement, Coordinates: 61.26°N, 23.51°E, Date: 23.5.2012, Time: 15:02 (GMT+2), Solar Zenith Angle, (⟨http://solardat.uoregon.edu/SolarPositionCalculator.html⟩): 49°, Temperature: ∼20 °C, Normal Incidence.
[41] Real Sun Measurement, Coordinates: 61.26°N, 23.51°E, Date: 08.5.2012, Time: 12:54 (GMT+2), Solar Zenith Angle, (⟨http://solardat.uoregon.edu/SolarPositionCalculator.html⟩): 72°, Temperature: ∼−5 °C, Normal Incidence.
[42] A.J. Ptak, D.J. Friedman, S. Kurtz, R.C. Reedy, Low-acceptor-concentration GaInNAs grown by molecular-beam epitaxy for high-current p-i-n solar cell applications, J. Appl. Phys. 98 (2005) 094501.

Publication 2

P2

Aho, A., Korpijärvi, V.-M., Tukiainen, A., Puustinen, J. & Guina, M. Incorporation model of N into GaInNAs alloys grown by radio-frequency plasma-assisted molecular beam epitaxy. Journal of Applied Physics 116(2014) 21.

Incorporation model of N into GaInNAs alloys grown by radio-frequency plasma-assisted molecular beam epitaxy

A. Aho, V.-M. Korpijärvi, A. Tukiainen, J. Puustinen, and M. Guina
Optoelectronics Research Centre, Tampere University of Technology, Korkeakoulunkatu 3, FI-33720 Tampere, Finland

(Received 19 September 2014; accepted 22 November 2014; published online 3 December 2014)

We present a Maxwell-Boltzmann electron energy distribution based model for the incorporation rate of nitrogen into GaInNAs grown by molecular beam epitaxy (MBE) using a radio frequency plasma source. Nitrogen concentration is predicted as a function of radio-frequency system primary resistance, N flow, and RF power, and group III growth rate. The semi-empirical model is shown to be repeatable with a maximum error of 6%. The model was validated for two different MBE systems by growing GaInNAs on GaAs(100) with variable nitrogen composition of 0%–6%.
 [http://dx.doi.org/10.1063/1.4903318]

I. INTRODUCTION

Plasma-assisted molecular beam epitaxy (PAMBE) is an attractive technique for growing III-N-V alloys[1] and has been used for demonstrating a wide range of heterostructures. In particular, the MBE growth has led to state-of-the-art demonstrations of GaInNAs(Sb)-based lasers[2,3] and 1 eV GaInNAs(Sb) solar cells.[4,5] However, the N incorporation processes using radio-frequency (RF) N plasma source requires a thorough optimization of the growth conditions and understanding of the N incorporation processes.[1,5] First of all, the growth parameters and plasma settings do not translate to a simple linear relation for the incorporation rate of N. Also, the N-ions generated by the plasma source can easily lead to poor epitaxial quality of the semiconductor wafer,[6–8] which leads to a dependence of the epitaxial quality on the selected N flow and RF power,[9–11] largely due to variations of the N ion fluxes and energies.[12] By optimizing the plasma parameters for a given N composition, the effect of the N-ions can be minimized. Thus, a useful model predicting the N composition as a function of plasma parameters could result in significantly faster calibration and optimization of GaInNAs growth. The predictive model could also be used for growth of complicated structures with different N compositions in the same growth run. So far, some incorporation models for MBE have been presented,[13–15] but they are not practical on a daily basis, since they do not predict the dissociation efficiency of N as a function of the RF power (P_{RF}). In this paper, we introduce a Maxwell-Boltzmann electron energy distribution based rate equation predicting the N composition as a function of PAMBE parameters, namely, the N flow and RF power, and group III growth rate.

II. THEORY AND MODEL

In an RF plasma source, the N_2 molecules are bombarded with RF powered electrons; the RF oscillation mainly energizes the electrons and leaves the ions unperturbed due to a large mass to charge ratio. The electron oscillation intensity is increased when the RF power is increased leading eventually to excitation, dissociation, and ionization of N species.[16] RF plasma activated N incorporates to the crystal mainly in the form of atomic N,[17] but also the other plasma activated N species contribute to the growth.[6] In general, the N RF plasma consists of electrons and the following N species (ordered descending in terms of their amount): neutral molecules (N_2), excited molecule radicals, neutral atoms, molecular ions, and atomic ions, with formation energies ~6–8, 9.7, 15.8, and 14.5 eV, respectively.[6] To establish a model for the incorporation of N, we first need to estimate the electron energy distribution and the average energy of the electrons in nitrogen plasma. The electrons are approximated to be nearly free and to move in a loop trajectory confined into a symmetric volume V_L with a loop cross-section area A_L and a loop length L_L. The plasma electrons are confined by a time variable magnetic field induced by a solenoid coil of the plasma source and the strength of the field is dependent on the intensity of the transmitted RF power (P_p). The average free electron energy E_e can be expressed as

$$E_e = \frac{E_{RF-plasma}}{n_e V_L} = kT_e, \tag{1}$$

where n_e is the free electron density, $E_{RF\text{-}plasma}$ is the time-averaged total transmitted RF energy, T_e is the average electron temperature, and k is the Boltzmann constant. If we assume the plasma loop as a conductor, where the electrons carry the current with mobility μ_e, we can estimate n_e from the plasma resistance

$$R_p = \frac{1}{e n_e \mu_e} \frac{L_L}{A_L}. \tag{2}$$

When n_e is solved from Eq. (2) and inserted to Eq. (1), we obtain

$$E_e = \frac{E_{RFtot}}{\frac{1}{R_p e \mu_e}\frac{L_L}{A_L}V_L} = \frac{2R_p \int_0^{T/2} P_p(t)dt}{\frac{1}{e\mu_e}\frac{L_L}{A_L}V_L} = \frac{2R_p P_p \int_0^{T/2} dt}{\frac{1}{e\mu_e}\frac{L_L}{A_L}V_L} = \frac{R_p P_p}{\frac{1}{e\mu_e}C(P_p,T)}, \tag{3}$$

where we define $C(P_p, T)$ as an effective electron confinement factor dependent on P_p and RF oscillation period (T). In the case of low pressure plasma, a collisionless plasma approximation can be used and therefore the energy distribution of electrons is assumed to follow a Maxwell-Boltzmann distribution, otherwise electrons follow a Druyvesteyn distribution.[16,18] In our case, the pressure of the plasma system is low and therefore it is justified to use Maxwell-Boltzmann distribution for the modelling.[16] The dissociation rate R_d of the molecules becomes[16]

$$R_d = N_m \delta(T_e) \left(\frac{8kT_e}{\pi m_e}\right)^{1/2} e^{\frac{-Ead}{kT_e}}. \tag{4}$$

Then by using Eq. (3), we get

$$\begin{aligned} R_d &= N_m \delta(T_e) \left(\frac{8e\mu_e R_p P_p}{\pi m_e C(P_p)}\right)^{1/2} \exp\left(\frac{-E_{ad} C(P_p, T)}{\mu_e R_p P_p}\right) \\ &= N_m \delta(T_e) \left(\frac{8e\mu_e}{\pi m_e C(P_p, T)}\right)^{1/2} (R_p P_p)^{1/2} \\ &\quad \times \exp\left(\frac{-E_{ad} C(P_p, T)}{e\mu_e R_p P_p}\right), \end{aligned} \tag{5}$$

where δ is the absorption cross section for inelastic electron collision processes in N_2, N_m is the density of nitrogen molecules, and E_{ad} is the activation energy for N_2 dissociation.[16] N_m can be solved from the ideal gas law

$$p_{eq} V = N_m k T_{N2} \tag{6}$$

and the Knudsen equation[19]

$$\frac{dN_{N_2}}{dt} = A(p_{eq} - p)\sqrt{\frac{N_a}{2\pi M_{N_2} k T_{N_2}}} \overset{Eq.(6)}{\approx} \frac{A N_m k T_{N_2}}{V}\sqrt{\frac{N_a}{2\pi M_{N_2} k T_{N_2}}}, \tag{7}$$

where V is the plasma source volume, p_{eq} is the plasma chamber equilibrium pressure, p is MBE system pressure, and A is the plasma source aperture area; here, we assume that

$$p_{eq} - p \approx p_{eq}. V = n \times V_m, \tag{8}$$

where n is the concentration of N_2 molecules in moles and V_m is the molar volume (22.4 l/mol). By differentiating Eq. (8) with respect to time, a relation between the molecular flows F(sccm) and $\frac{dN_2}{dt}$ (1/s) is found

$$\frac{dV}{dt} = V_m \frac{dn}{dt} = \frac{V_m}{N_a}\frac{dN_{N_2}}{dt} = \frac{1}{60s/\text{min}} F \tag{9}$$

resulting in

$$\frac{dN_{N_2}}{dt} = \frac{F \times N_a}{60s/\text{min} \times V_m}, \tag{10}$$

where N_a is the Avogadro constant. Next, we combine Eqs. (7) and (10) yielding

$$N_m = \frac{F(sccm) \times N_a \times V}{60s/\text{min} \times A \times V_m k T_{N_2} \sqrt{\frac{N_a}{2\pi M_{N_2} k T_{N_2}}}}. \tag{11}$$

From Eqs. (5) and (11), we obtain

$$\begin{aligned} R_d = &\frac{F\delta(T_e) \times V}{60s/\text{min} \times A \times V_m \times \sqrt{\frac{kT_m}{2\pi M_{N_2} N_A}}} \\ &\times \left(\frac{8e\mu_e}{\pi m_e C}\right)^{1/2} (R_p P_P)^{1/2} \exp\left(\frac{-EadC}{e\mu_e R_p P_P}\right). \end{aligned} \tag{12}$$

Next, we need to link the R_p and P_p to the system primary resistance (R_{sp}) and P_{RF}. The changes in the R_p as a function of P_{RF} and F can be estimated from the primary circuit, and the changes in the system primary resistance are directly related to the power transferred to the plasma.[20] Here, we use the plasma transformer formalism for the estimation of R_p.[21] In this model, the primary coil has n turns and the plasma itself can be modeled as a single turn coil. In an ideal transformer, where the plasma loop is modeled with a single loop coil, R_p is seen on the primary circuit as a transformed resistance[21]

$$R_{pt} = n^2 R_p. \tag{13}$$

We therefore get

$$R_{sp} = R_c + n^2 R_p, \tag{14}$$

where R_c is the resistance that simulates the RF matcher and system losses. P_p can be also estimated from the system resistances with the relation[22]

$$P_p = \frac{n^2 R_p}{R_{sp}} P_{RF} = \varepsilon P_{RF}, \tag{15}$$

where ε is the power transfer efficiency.

$$\begin{aligned} R_d \overset{Eq.15}{=} &\frac{F\delta(T_e) \times V}{60s/\text{min} \times A \times V_m \times \sqrt{\frac{kT_m}{2\pi M_{N_2} N_A}}} \left(\frac{8e\mu_e}{\pi m_e C}\right)^{1/2} \\ &\times \left(\frac{\varepsilon^2 R_{sp}}{n^2} P_{RF}\right)^{1/2} \exp\left(\frac{-E_{ad}C}{e\mu_e \frac{\varepsilon^2 R_{sp}}{n^2} P_{RF}}\right). \end{aligned} \tag{16}$$

Nitrogen incorporation is estimated by scaling R_d with a geometrical factor G accounting for the reactor and plasma source and the nitrogen sticking coefficient $S \leq 1$. S is a function of growth temperature,[23,24] nitrogen composition,[25] and arsenic flux.[15,26] Nitrogen incorporation is also inversely proportional to the group III growth rate GR_{III}.[26] Finally, for fitting with experimental data, Eq. (16) is simplified with parameters B and D, which are dependent on P_{RF} and F. Finally, we obtain an equation for the nitrogen composition

$$N(\%) = \frac{SGR_d}{GR_{III}} = \frac{B}{GR_{III}} F (R_{sp} P_{RF})^{1/2} \exp\left(\frac{-E_{ad} D}{R_{sp} P_{RF}}\right). \tag{17}$$

III. EXPERIMENTS

In order to verify the model, we grew a series of samples with two MBE systems: Veeco GEN20 and VG Semicon V80. Both systems were equipped with Veeco Sumo cells for In and Ga, cracker for As and Veeco UNI-Bulb autotuned RF (13.56 MHz) N plasma source. The plasma systems contained a commercial automatic matcher unit with L-topology. The matcher units are used for the compensation of plasma and coil reactance ensuring maximum power transfer from the RF power source to the plasma.

The GEN20 samples consisted of 200 nm thick GaInNAs layers, which were grown on n-GaAs(100) wafers. Before the epitaxial growth of GaInNAs, desorption of the native oxides was performed at 620 °C followed by growth of a GaAs buffer at 580 °C. The growth rate was 0.75 μm/h, the beam equivalent pressure ratio of As and group III atoms was 10, and the growth temperature setpoint was 440 °C. The indium composition was calibrated to 8% by separately grown GaInAs/GaAs superlattice samples. After calibration of the In composition, multiple samples were grown with different N fluxes. The active N flux was varied by changing both P_{RF} and F. The P_{RF} was varied between 150 and 350 W, while F was varied from 0.15 to 0.63 sccm. The N plasma system primary resistance was estimated from the RF power-voltage data with different powers and fluxes collected from the GEN20 reactor.

The samples grown at the V80 MBE system were 3-period GaAs/GaNAs superlattice structures composed of 20 nm GaNAs and 50 nm GaAs layers. The superlattices were grown on semi-insulating or n-doped GaAs(100). The growth rate was 0.5 μm/h and the growth temperature setpoint was 475 °C for the superlattice region. F was varied from 0.05 to 0.25 sccm and P_{RF} from 250 to 450 W. All the samples were grown in a short period of time to minimize fluctuations in the growth parameters.

X-Ray diffraction (XRD) spectra from (004) planes for both sets of samples were measured with either Philips' triple-axis or BEDE's double crystal x-ray diffractometers. The N compositions were obtained by fitting the measured XRD data to rocking curves simulated by the BEDE RADS software using dynamical diffraction theory. The N composition values were fitted to Eq. (17)[27] using the Levenberg-Marquardt algorithm. After the fitting, the model was tested by growing three GaInNAs quantum well samples (QW) with a nitrogen concentration of 1.2% with the GEN20 reactor, while varying the plasma parameters to following values: 150 W and 0.45 sccm; 227 W and 0.17 sccm; 304 W and 0.15 sccm. The quality of QW samples and corresponding emission wavelengths were compared by photoluminescence (PL) measurements. A second test with the GEN20 reactor was made for lattice matched bulk samples with 0%–6% N composition. In these samples, the In composition was tuned to 2.7 times the N composition ensuring lattice matching to GaAs.

IV. RESULTS AND DISCUSSION

First the measured RF power-voltage-data for the GEN20 reactor was analyzed; the data are summarized in Fig. 1(a). The calculated primary resistances for different F values are presented in Fig. 1(b). Primary resistance was found to be a function of F and nearly independent of the P_{RF}. Therefore, for the incorporation model, a linear interpolation for plasma resistance as a function of F was used as shown in Fig. 1(b).

The nearly monotonic decrease of plasma system resistance with F could be explained by the fact that every new nitrogen molecule inserted to the system can free more electrons to the plasma. Eventually, we expect that the resistance would start to rise as a reduction of the electron mobility in the plasma at higher flows.

The measured N compositions for the samples grown with two MBE systems and the corresponding fitted curves are presented in Fig. 2. The curves follow the N incorporation rate reported elsewhere.[13,14,17] The incorporation shows a linear growth at low F values followed by a saturation region at high F. The fitted dependence also predicts that the incorporation rate should start to decrease for the high flows. This is actually seen for the samples grown with 150 W RF power on Gen20 reactor. With our plasma systems, the descending sides were not studied thoroughly due to plasma instability in this parameter range, which often leads to unwanted plasma shut-off. However, the decrease of the

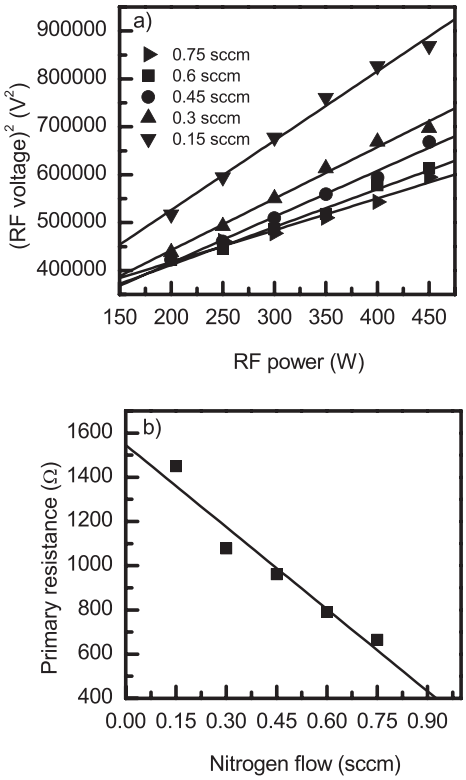

FIG. 1. (a) Square of the RF plasma voltage as a function of the plasma RF power. The linear behavior indicates that the plasma primary resistance remains constant as a function of P_{RF}, but depends on the nitrogen flow. (b) Primary resistance as a function of N_2-flow.

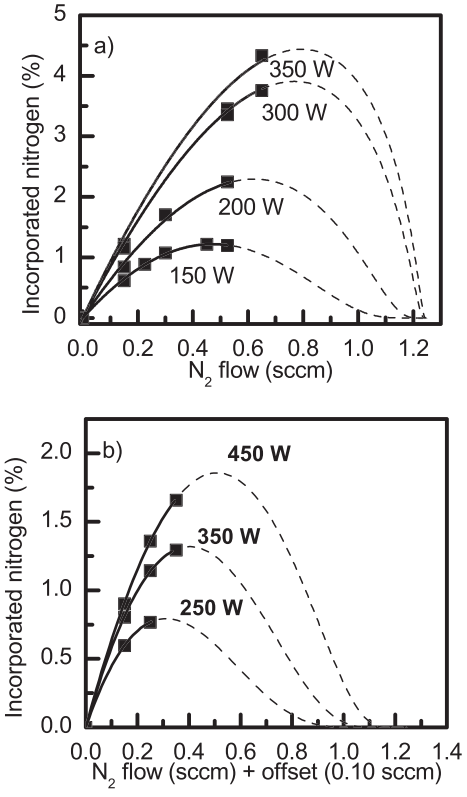

FIG. 2. Measured nitrogen compositions and the fitted curves predicted by the model for GEN20 (a) and V80 (b) reactors. The results were normalized to 1 μm/h growth rate. The fitted lines are drawn as solid in the experimentally tested range and as dashed lines on the range that was not tested in this study.

incorporation rate at high flows has been reported elsewhere in connection with the growth of GaN.[17]

Using the nominal F values for the V80 reactor, the curves could not be fitted with the requirement that they start from zero incorporation. Therefore, a constant offset of +0.10 sccm was added to the F values for the V80 reactor. This offset could be caused by an inherent offset in the N mass flow controller. For the GEN20, no offset was used. The shape differences between the curves also arise from different N-source nozzles, R_c values, reactor geometries, and configurations. Additionally, the V80 samples comprised of GaAsN, which has been observed to deviate from Vegard's law at high N compositions (although we note that in this study all but one GaAsN sample had N composition below 3% so a clear deviation is not expected[25]). The curves in Fig. 2 have only 2.6% and 0.2% deviations from the measured values in average for GEN20 and V80 reactors, respectively.

The fitting parameters B and $E_{ad}D$ are plotted in Fig. 3 as a function of P_{RF}. $R_{sp}(F)$ for the V80 reactor was adopted from the GEN20 reactor, they were not separately measured. The fitting parameters are assumed to be independent of F. In other words, the electrons are assumed to be free and only the RF power can affect the average thermal energy of the electrons. This assumption is well supported by the measured system primary resistance. In order to clarify the power dependencies of the $B(P_{RF})$ and $E_{ad}D(P_{RF})$ parameters, we used exponential fitting functions. The functions are

$$B(P_{RF}) = a_B \exp(P_{RF} t_B) + b_B \tag{18}$$

and

$$E_{ad}D(P_{RF}) = a_d \exp(P_{RF} t_d) + b_d, \tag{19}$$

where a_B, a_d, b_B, b_d, t_B, and t_d are constants. For simplicity, we use here unity power transfer efficiency and $n = 1$ for the primary coil. Fitting parameters for the GEN20 and V80 reactors are presented in Table I and Fig. 3. The fitting parameters can be interpolated accurately by the exponential functions described above. The B-parameter for both reactors decreases monotonically as a function of power, which could be linked to changes in the absorption cross section or to a power dependent plasma chamber pressure. The shape differences between the GEN20 and V80H curves may be linked to different plasma source aperture nozzles. The power dependence of E_{ad}D could be explained by changes in the effective activation energy E_{ad} or by the fact that the plasma is tighter confined when the P_{RF} is increased. The latter is considered the most probable reason. The fitting parameters also include the effect of the RF power and the N flow on the power transfer efficiency, which can be significantly lower at low plasma powers and low flows.[20–22]

To test the accuracy of the model, we used it to predict the N composition in grown crystals. To this end, we grew three QW samples with different combinations of P_{RF} and F, yet all aimed at having the same N composition. In the same way, we forecasted the compositions of five lattice matched

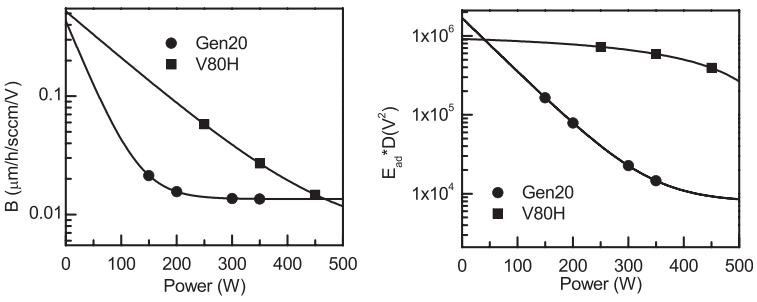

FIG. 3. Fitting parameters B and E_{ad}D as a function of the RF power.

TABLE I. Fitting parameters for the GEN20 and V80 reactors.

Reactor	a_B (μm/h/sccm/V)	t_B(1/W)	b_B (μm/h/sccm/V)	a_d (V^2)	t_d (1/W)	b_d (V^2)
GEN20	4.204×10^{-1}	-2.650×10^{-2}	1.352×10^{-2}	1.680×10^{6}	-1.578×10^{-2}	7.879×10^{3}
V80H	5.155×10^{-1}	-9.230×10^{-3}	6.640×10^{-3}	-1.280×10^{5}	3.610×10^{-3}	1.042×10^{6}

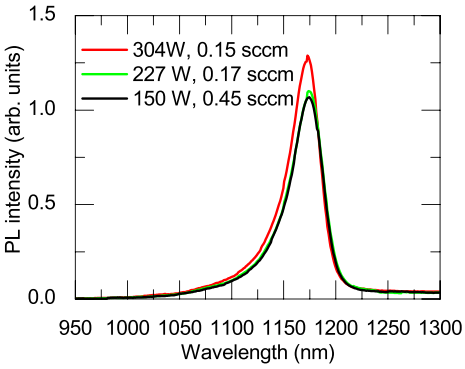

FIG. 4. PL from GaInNAs QW samples grown with different plasma parameters aimed at the same N composition.

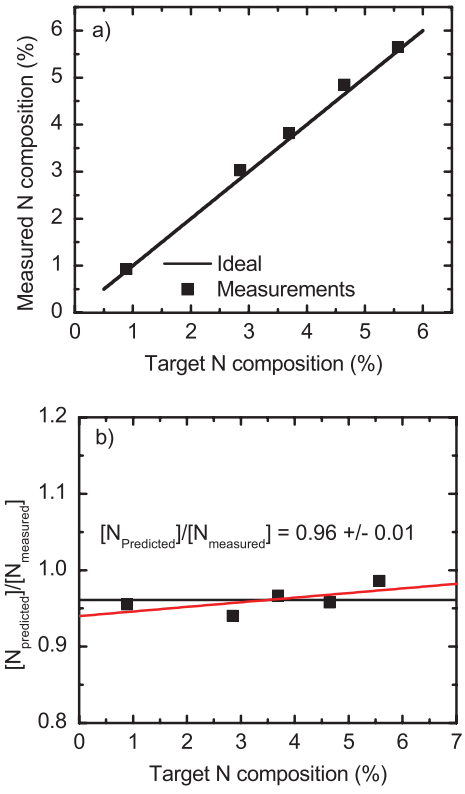

FIG. 5. (a) Comparison of predicted and measured N composition for the GaInNAs bulk samples. (b) Division of the target and measured composition. Results show that the model has 4% average error with 6% maximum error.

bulk samples with N composition form 1%–6% grown with different plasma parameters. The results are presented in Fig. 4, in which we can see that the QWs emit at precisely the same emission wavelength. This is a clear indication that all samples have same N composition despite the fact that various combinations of plasma power and flow were used. The slight differences in the peak intensities can be explained by the differences in the ratio of atomic N and N-ions produced.

For the bulk layers, the targeted N composition corresponds very well to the values from XRD simulations, as revealed in Fig. 5. The values seem to have a small calibration related drift, which becomes smaller when the N composition is increased. Nevertheless, all the samples have a maximum deviation of 6% from the model, and the average deviation is only 4%. The error is mainly systematic and can be easily corrected. After the correction, the prediction would deviate only approximately 1% from the measured values. This means that the N incorporation can be estimated with the same precision as the group III fluxes can be determined from ion gauge measurements. Furthermore, the model has been used on a daily basis at the GEN20 reactor for numerous samples; it has proved to be a helpful tool for complex GaInNAsSb solar cell and laser epitaxy.

V. CONCLUSION

We have derived a Maxwell-Boltzmann electron energy distribution based equation for the incorporation rate of N from a plasma source as a function of RF power, N flow, and group III growth rate. The model was tested for GaInNAs samples grown using Veeco GEN20 and VG Semicon V80H reactors with Veeco UNI-bulb nitrogen RF plasma sources. For both reactors, the model can be used with an absolute deviation better than 6%. The model has also been reliable in the long term use and has proved to be a versatile tool for dilute nitride epitaxy. The model and the same calibration sequence should be applicable to other nitride based PAMBE systems and RF plasma sources.

ACKNOWLEDGMENTS

The authors would like to thank colleagues at Optoelectronics Research Centre for their high-quality experimental support. For the financial support, we would like to thank Finnish Funding Agency for Technology and Innovation—TEKES (Project Nos. #40120/09 “Solar III–V” and #40239/12 “Nextsolar”), Graduate School in Electronics, Telecommunications and Automation, Ulla Tuominen Foundation, Finnish Foundation for Technology Promotion, and Wärtsilä Foundation.

[1]M. Guina and S. M. Wang, "Chapter 9—MBE of dilute-nitride optoelectronic devices," in *Molecular Beam Epitaxy*, edited by M. Henini (Elsevier, Oxford, 2013), pp. 171-187.
[2]J. Konttinen and V.-M. Korpijärvi, Nanoscale Res. Lett. **9**, 82 (2014).
[3]M. Guina, T. Leinonen, A. Härkönen, and M. Pessa, New J. Phys. **11**, 125019 (2009).
[4]M. Wiemer, V. Sabnis, and H. Yuen, "High and low concentrator systems for solar electric applications VI," Proc. SPIE **8108**, 810804 (2011).
[5]A. Aho, V. Polojärvi, V.-M. Korpijärvi, J. Salmi, A. Tukiainen, P. Laukkanen, and M. Guina, Sol. Energy Mater. Sol. Cells **124**, 150–158 (2014).
[6]N. Newman, J. Cryst. Growth **178**, 102–112 (1997).
[7]M. M. Oye, T. J. Mattord, G. A. Hallock, S. R. Bank, M. A. Wistey, J. M. Reifsnider, A. J. Ptak, H. B. Yuen, J. S. Harris, Jr., and A. L. Holmes, Appl. Phys. Lett. **91**, 191903 (2007).
[8]J. Miguel-Sánchez, A. Guzmán, and E. Muñoz, Appl. Phys. Lett. **85**, 1940 (2004).
[9]D. J. Economou, D. R. Evans, and R. C. Alkire, J. Electrochem. Soc. **135**(3), 756 (1988).
[10]T. Kageyama, T. Miyamoto, S. Makino, F. Koyama, and K. Iga, J. Cryst. Growth **209**, 350–354 (2000).
[11]M. A. Wistey, S. R. Bank, H. B. Yuen, H. Bae, and J. S. Harris, Jr., J. Cryst. Growth **278**, 229–233 (2005).
[12]J. M. Reifsnider, S. Govindaraju, and A. L. Holmes, Jr., J. Cryst. Growth **243**, 396–403 (2002).
[13]H. Carrere, A. Arnoult, A. Ricard, and E. Bedel-Pereira, J. Cryst. Growth **243**, 295–301 (2002).
[14]D. Voulot, R. W. McCullough, W. R. Thompson, D. Burns, J. Geddes, G. J. Cosimini, E. Nelson, P. P. Chow, and J. Klaassen, J. Cryst. Growth **201**/**202**, 399–401 (1999).
[15]V. A. Obnoblyudov, A. R. Kovsh, A. E. Zhukov, N. A. Maleev, E. S. Semenova, and V. M. Ustinov, Semiconductors **35**(5), 533–538 (2001).
[16]J. A. Thornton, Thin Solid Films **107**, 3–19 (1983).
[17]J. Osaka, M. Senthil Kumar, H. Toyoda, T. Ishijima, H. Sugai, and T. Mizutani, Appl. Phys. Lett. **90**, 172114 (2007).
[18]M. Druyvesteyn and F. Penning, Rev. Mod. Phys. **12**(2), 87–174 (1940).
[19]M. A. Herman and H. Sitter, *Molecular Beam Epitaxy, Fundamentals and Current Status*, 2 ed. (Springer, 1996).
[20]V. A. Godyak, R. B. Piejak, and B. M. Alexandrovich, Plasma Sources Sci. Technol. **3**, 169 (1994).
[21]R. B. Piejak, V. A. Godyak, and B. M. Alexandrovich, Plasma Sources Sci. Technol. **1**, 179–186 (1992).
[22]V. A. Godyak, R. B. Piejak, and B. M. Alexandrovich, J. Appl. Phys. **85**, 703 (1999).
[23]Z. Pan, L. H. Li, W. Zhang, Y. W. Lin, and R. H. Wu, Appl. Phys. Lett. **77**, 214 (2000).
[24]V.-M. Korpijärvi, A. Aho, P. Laukkanen, A. Tukiainen, A. Laakso, M. Tuominen, and M. Guina, J. Appl. Phys. **112**, 023504 (2012).
[25]W. Li, M. Pessa, and J. Likonen, Appl. Phys. Lett. **78**(19), 2864 (2001).
[26]G. Jaschke, R. Averbeck, L. Geelhaar, and H. Riechert, J. Cryst. Growth **278**, 224–228 (2005).
[27]Origin 8.0, OriginLab, Northampton, MA.

Publication 3

P3

Aho, A., Tukiainen, A., Polojärvi, V., Salmi, J. & Guina, M. High current generation in dilute nitride solar cells grown by molecular beam epitaxy. SPIE Conference Proceedings 8620 (2013) 55, pp. 1-6.

High current generation in dilute nitride solar cells grown by Molecular Beam Epitaxy

A. Aho, A. Tukiainen, V. Polojärvi, J. Salmi, and M. Guina*
Optoelectronics Research Centre, Tampere University of Technology
P.O.B. 692, FIN-33101, Finland

ABSTRACT

We review our recent work concerning the development of dilute nitride solar cells by molecular beam epitaxy. This epitaxial technology enables a high level of control of the growth conditions and alleviates known issues related to epitaxy of dilute nitrides ultimately enabling to achieve high quality materials suitable for solar cell developments. In particular, we focus on discussing the mechanisms linking the epitaxial and annealing conditions to the operation of dilute nitride solar cells. We also report operation of a single junction dilute nitride solar cell with a short circuit current density as high as ~39 mA/cm^2 under 1 sun illumination.

Keywords: multi-junction solar cells, dilute nitrides, molecular beam epitaxy, high efficiency solar cells,

1. INTRODUCTION

Multi-junction (MJ) III-V compound semiconductor solar cells (SC) are the prime choice for efficient solar energy harvesting. MJSC based on semiconductor heterostructure made of InGaP/(In)GaAs/Ge p-n junctions are the core of the satellite solar energy generators and are gaining increased attention also for terrestrial applications. For example, when combined with concentrator photovoltaic (CPV) techniques, high efficiency III-V solar cells offer attractive opportunities for achieving the price target required to make solar energy competitive with traditional energy sources. The high impact of these applications has generated even more need to surpass the current technological barriers that limit the efficiency of 3-junction solar cells to ~30% for 1 sun AM0 condition, and the ~40% range for CPV AM1.5 illumination . In order to surpass these efficiency limits one needs to deploy device architectures with more than three p-n junctions to absorb the solar spectrum more efficiently. One of the most attractive development approaches to increase the number of absorbing junctions is to use GaInNAs, i.e. dilute nitride, alloy integrated with the "standard" lattice matched 3-junction materials [1-3].

Dilute nitrides, are compounds that incorporate a small amount of N, typically below 5%, and exhibit extraordinary optical and electrical properties. Most important for solar cell applications is the fact that their band-gap can be engineered to cover the entire range from 1.4 eV down to 0.8 eV while preserving lattice matching to GaAs. Thus they are ideal candidates for the development of multijunction solar cells; their potential has been proved recently by demonstrating triple-junction solar cells incorporating GaInNAs with a record high conversion efficiency of 44% [4]. Their deployment as a practical development path for high efficiency solar cells has been daunted by difficulties encountered when using metal-organic vapor-phase epitaxy (MOVPE) technology, the standard technique used in industry to fabricate III-V solar cells. On the other hand, dilute nitrides have been intensively studied by using molecular beam epitaxy (MBE), the epitaxial technology widely adopted for research of novel materials. MBE has clear advantages over MOVPE when it comes to epitaxy of dilute nitrides, as it avoids issues related to C-doping and hydrogen related complexes [5]. Moreover, MBE enables a higher level of control of growth conditions; in particular, it enables operation at relatively low growth temperatures to avoid phase separation and clustering effects, while the ratio of group V elements to group III as well as the amount of N available for nucleation can be controlled more accurately.

Despite the proven advantages of MBE for fabrication of GaInNAs alloys, this remains a challenging material that requires optimization of several interdependent fabrication parameters, such as growth temperature (T_g), V/III flux ratio, post growth annealing conditions and nitrogen composition. For example, we have earlier shown that T_g has to be set in a rather narrow window centered at ~440 ^{o}C in order to achieve adequate quality for solar cells developments [6, 7]. This window is limited by point defects generated on the low temperature side of the window, and on the other hand, phase

Physics, Simulation, and Photonic Engineering of Photovoltaic Devices II, edited by Alexandre Freundlich, Jean-Francois Guillemoles, Proc. of SPIE Vol. 8620, 86201I · © 2013 SPIE
CCC code: 0277-786X/13/$18 · doi: 10.1117/12.2002972

separation and segregation effects taking place at higher temperatures. This temperature range was also linked to preferential surface morphology with (1x3) surface reconstruction on GaInNAs surface [8]. We have also demonstrated that the incorporation mechanism is thermally activated and therefore our observations challenge the commonly accepted understanding that N concentration is temperature independent at temperatures below the phase segregation regime. In this paper we provide further insights into physical processes linking the growth parameters and the properties of GaInNAs solar cells. In particular we have analyzed the effect of growth temperature, As/III beam equivalent pressure (BEP), and annealing on the characteristics of dilute nitride solar cells. As a result of the growth optimization steps we demonstrate a 1 eV GaInNAs solar cell exhibiting a short circuit current density of ~39 mA/cm^2 and a V_{oc} of 0.41 V.

2. DESCRIPTION OF EXPERIMENTAL STRUCTURES

The set of GaInNAs p-i-n junctions was grown using a Veeco GEN20 solid source MBE equipped with a Uni-Bulb RF plasma source. A first set of GaInNAs p-i-n structures was grown on n-GaAs(100) substrate. These structures comprised undoped GaInNAs layers placed between 250-nm-thick p-GaAs emitter and a 600-nm-thick n-GaAs buffer layers. The doping levels of the p- and n-GaAs were 1x10^{18} cm^{-3} and 5x10^{17} cm^{-3}, respectively. The thickness of GaInNAs layers was varied from 150 nm to 1200 nm. The structures did not contain window layers; the main purpose of this test set was to study the effect of different growth conditions on the formation of GaInNAs current generation layer without targeting high conversion efficiency. In order to adjust the amount of N required for lattice matching with different In compositions, the N-plasma power was varied between 150 W and 300 W at flow rates between 0.15 and 0.53 sccm; the corresponding amount of N incorporated was varied between 1% and 6%. For the lattice matching In concentration was set to ~ 2.7 x N concentration. The growth temperature used for the epitaxy of GaInNAs layer was varied between 400 ^{o}C and 500^{o}C. The samples were studied using various methods including reflection high-energy electron diffraction (RHEED), photoluminescence, time-resolved photoluminescence, x-ray diffraction, light-biased current-voltage (LIV) and quantum efficiency (QE) measurements. These samples were processed into solar cell components using a simple shadow mask process.

After optimizing the growth parameter using the set of structures described above, we have fabricated a single-junction GaInNAs solar cell on p-GaAs(100) substrates. The thickness of the undoped GaInNAs i-region was 1300 nm. This was placed between a n-GaAs emitter with a thickness of 100 nm and a 600-nm-thick p-GaAs base layers. In addition, the structure incorporated a p-GaInP back surface field layer with a thickness of 100-nm and an n-AlInP window layer with a thickness of 25 nm. For contacting we have used n$^+$GaAs layer with a thickness of 300 nm. The samples were processed in devices with an area of 0.1 cm^2 using standard photolithography followed by the deposition of a TiO_2/SiO_2 antireflective coating.

As the carrier concentrations and mobilities are strongly linked to solar cell parameters, we have performed standard Hall measurements at room temperature on undoped GaInNAs layers grown on semi-insulating GaAs substrates to determine the carrier concentrations and mobilities corresponding to GaInNAs layers. The undoped GaInNAs turns out to have p-type conduction with carrier concentrations in the range of 10^{16} cm^{-3}. The mobility for holes was measured to be 100 cm^2/Vs, which is in good accordance with published results [9, 10].

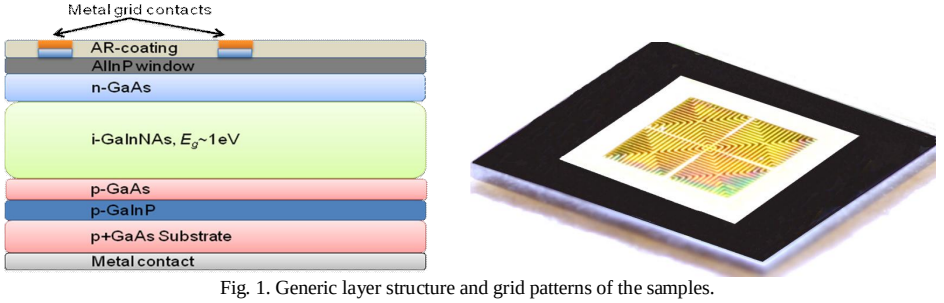

Fig. 1. Generic layer structure and grid patterns of the samples.

3. INFLUENCE OF THE GROWTH PARAMETERS

One of the growth parameter that has a strong influence on the properties of GaInNAs material is the T_g. A number of physical processes taking place on the sample surface during the growth are temperature dependent, including atomic surface migration, desorption, and defect formation. Generally speaking, there are three temperature regions in which the epitaxy is affected by different physical mechanisms [11]. In the low T_g regime, which can be regarded as temperatures below ~420°C, thermal energy of the atoms migrating on the sample surface is not enough to drive them to their right lattice sites, which eventually leads to formation of a large population of point defects. In the high-temperature regime, starting from ~460°C, the segregation and phase separation processes are predominant and lead to formation of very rough sample surfaces during growth [12-13]. In between these ranges there is a narrow window of temperatures at which our test structures exhibited a good materials quality for N content of 1−4%. More precisely we have found that the optimum T_g for solar cells is close to 440 °C [6]. Our interpretation is that at this temperature range the phase separation and segregation are not effective and that temperature is not too low to cause formation of considerable amounts of point defects. The optimal temperature window is revealed in Fig. 2 for a N content of 3%; in this figure we have plotted the normalized output power (P_{max}) of GaInNAs junctions as a function of the growth temperature. There are also other T_g related effects that need to be discussed here in conjunction with the N-content. For example, it is known that the sticking coefficient of In starts to decrease at higher temperatures than those identified as optimal for N incorporation [14]. Also it has been shown that at higher temperatures nitrogen starts to desorb from the sample surface [15] and furthermore annealing at elevated temperatures lead to changes in the N bond environment [16].

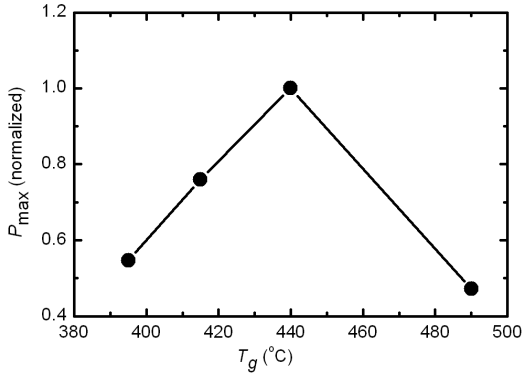

Fig. 2. Normalized P_{max} for GaInNAs p-i-n samples grown different growth temperatures. Measurements were performed at AM0 and with a 900 nm long-pass filter.

Another parameter which directly affects the growth of GaInNAs is the As/III beam equivalent pressure ratio. For good quality GaAs-based materials grown by MBE at 580 °C the optimal BEP ratio values are often in the range of 10 [17, 18]. For the samples studied here we have changed the As/III BEP ratios between 5 and 20 for N contents ranging from 1 to 3 % [19]. As a monitoring parameter used in optimization we have used again the maximum power generated by the cells. The results are summarized by the contour map shown in Fig. 3 which collects all measurements for AM0 illumination. The results show that the lower limit for the BEP ratio is ~7 and the upper limit is ~14. Other observations here are that the more nitrogen is inserted to the material the more sensitive the growth becomes in terms of As-flux.

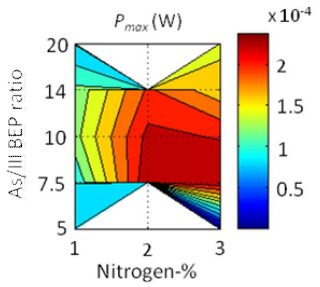

Fig. 3. The effect of As/III BEP ratio on the solar cell parameters for different N compositions. Measurements have been performed at AM0 and with a 900 nm long-pass filter.

The amount of N has a direct effect on the bandgap and hence on the current and voltage characteristics; the more nitrogen is introduced, the smaller E_g becomes and the absorption edge shifts towards longer wavelengths enabling higher current production. On the other hand smaller bandgap decreases the open circuit voltage and therefore the N content should be optimized for specific current matching conditions. However, there are quite strict limitations when it comes to the maximum amount of N that can be incorporated substitutionally; incorporation of N content higher than 4% typically makes extremely challenging the use of material for solar cells applications [6]. Fig. 4 plots the V_{oc} for GaInNAs solar cells with different bandgaps (i.e. N contents). Here the bandgaps are depicted by corresponding maximum of the room temperature photoluminescence emission. Besides the direct effect of the N content on V_{oc} via the bandgap, higher densities of nonradiative recombination centers corresponding to higher N content would lead to a reduction of the V_{oc} compared to the ideal values. As it can be seen in Fig. 3, the V_{oc} dependence on N follows a linear behavior with $V_{oc}=E_g/q$-0.55 V indicating good electrical properties of the material.

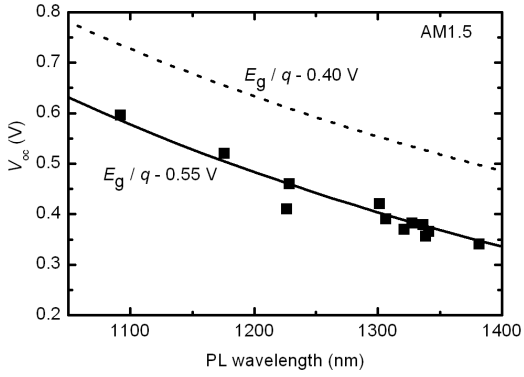

Fig. 4. V_{oc} values for test GaInNAs single junction devices.

4. INFLUENCE OF ANNEALING

The properties of GaInNAs are strongly affected by thermal annealing process. In general annealing leads to a significant reduction of the defect densities accompanied also by a change of the N environment. The effect of annealing can be assessed in a simple way by measuring the photoluminescence (PL) intensity in steady-state or time-resolved domains. For example, in non-annealed samples we have measured carrier lifetimes in the range of 10-30 ps reflecting partially the low growth temperature and on the other hand the existence of nitrogen-induced defects in the crystal lattice. However, when the crystal was thermally annealed, we observed a strong increase in the photoluminescence

lifetime in particular for samples with a nitrogen content of 2% N; the corresponding lifetime was in the range of 900 ps. For samples with more nitrogen a drastic lifetime increase was also observed but to a lesser amount compared to samples with 2% N. Lifetimes as long as 500 ps and 300 ps were obtained for GaInNAs samples with 3% and 4% nitrogen after thermal annealing, respectively.

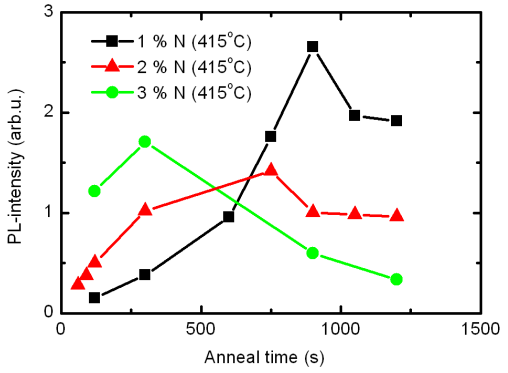

Fig. 5. PL intensities versus annealing time at 800 °C from GaInNAs p-i-n structures with 1-3% N.

In correlation with time-resolved data, the steady-state PL experiences drastic changes upon RTA. We have studied the PL from GaInNAs p-i-n structures with different N-contents and growth parameters subjected to different annealing conditions; in particular we have tried to identify the optimal annealing conditions for samples with different N-contents. These results are summarized in Fig. 4. For example, the samples grown at 415 °C and annealed at 800 °C, exhibited maximum PL after 900 s for N compositions of 1% , 700s for samples with 2% N and 300s for samples with 3% N; the general trend behind the measurements reveal that more N is inserted, the lower is the required time for attaining the maximum PL intensity.

5. SINGLE JUNCTION SOLAR CELL RESULTS AND CONCLUSIONS

The LIV measurement on the optimized GaInNAs solar cell devices were measured using AM1.5 illumination at 1000 W/cm^2 (a solar simulator calibrated against a set of 1 eV single, dual and triple-junction solar cells, real sun illumination and a Kipp&Zonen pyranometer, model CM11). The LIV and external quantum efficiency (EQE) measurement results are shown in Fig. 6.

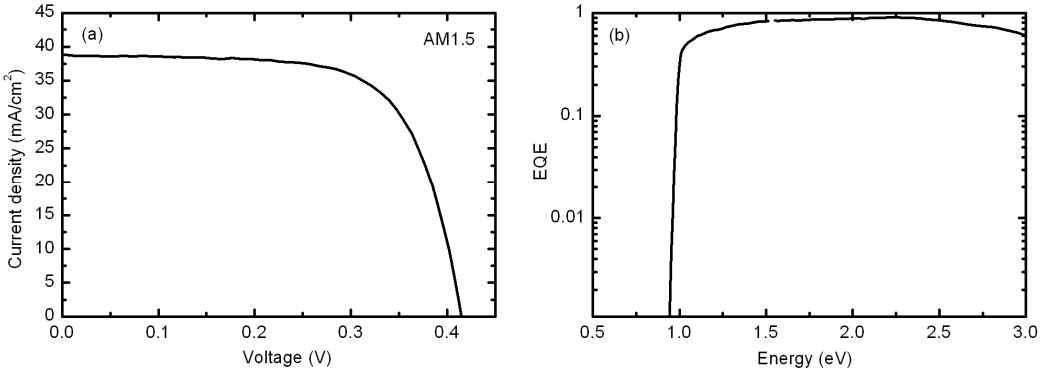

Fig. 6. (a) LIV and (b) (EQE) measured for the optimized GaInNAs single junction cell.

As a result of the growth parameter optimization, we have demonstrated single junction GaInNAs SCs with high short circuit current densities of J_{sc}=38.8 mA/cm^2 at simulated AM1.5 illumination. The device V_{oc} was 0.41 V. The peak external quantum efficiency of the single junction GaInNAs cell was 90% at 2.2 eV and still almost 80% at the energies just below the bandgap of GaAs. These results are the basis for future integration of the GaInNAs sub-junction in multi-junction solar cell configurations.

ACKNOWLEGEMENTS

The work was financially supported by Finnish Funding Agency for Technology and Innovation – TEKES (projects Solar III-V and NextSolar), the National Graduate School in Electronics, Telecommunications and Automation, Ulla Tuominen Foundation, Finnish Foundation for Technology Promotion and Wärtsilä Foundation.

REFERENCES

[1] D.J. Friedmann, J.F. Geisz, S.R. Kurtz, J.M.Olson, J. Crystal Growth 195 409–415 (1998).
[2] D. J. Friedman, S. R. Kurtz, and J. F. Geisz, in Conference Record of the Twenty-ninth IEEE Photovoltaic Specialists Conference, New Orleans, Louisiana, 19–24 May, p. 856–859 (2002).
[3] A. J. Ptak, D. J. Friedman, S. Kurtz, and R. C. Reedy, J. Appl. Phys. 98, 094501 (2005).
[4] www.sj-solar.com/downloads/Solar_Junction_44_Percent_WR_15Oct12.pdf
[5] A.J. Ptak, S.W. Johnston, S. Kurtz, D.J. Friedman, W.K. Metzger, J. Crystal Growth 251 392–398 (2003).
[6] A. Aho, A. Tukiainen, V. Polojärvi, A. Gubanov, J. Salmi, M. Guina, P. Laukkanen, 26th EU PVSEC 58-61 (2011), doi:10.4229/26thEUPVSEC2011-1AO.8.3.
[7] A. Aho, A. Tukiainen, V.-M. Korpijärvi, V. Polojärvi, J. Salmi, and M. Guina, AIP Conf. Proc. 1477, pp. 49–52; doi:10.1063/1.4753831, 8th International Conference on Concentrating Photovoltaic Systems, CPV-8, April 16 - 18, 2012, Toledo, Spain (2012).
[8] V.-M. Korpijärvi, A. Aho, P. Laukkanen, A. Tukiainen, A. Laakso, M. Tuominen, M. Guina, J. Appl. Phys. 112, 023504 (2012).
[9] J. Geisz, D.J. Friedman, J.M. Olson, S.R. Kurtz, P.M. Keyes, J. Crystal Growth 195, 401–408 (1998).
[10] W. Li, M. Pessa, J. Toivonen, H. Lipsanen, Phys. Rev. B 64, 113308 (2001).
[11] James S. Harris Jr., R. Kudrawiec, H. B. Yuen, S. R. Bank, H. P. Bae, M. A. Wistey, D. Jackrel, E. R. Pickett, T. Sarmiento, L. L. Goddard, V. Lordi, and T. Gugov, Phys. Stat. Sol. (b) 244, 2707–2729 (2007); DOI 10.1002/pssb.200675620.
[12] W.M. McGee, R.S. Williams, M. S. Ashwin, T. S. Jones, E. Clarke, J. Zhang, S. Tomic, Phys. Rev. B 76, 085309 (2007).
[13] E. Luna, A. Trampert, E. M. Pavelescu, and M. Pessa, New J. Phys. 9 405 (2007).
[14] T. Suzuki and T. Nishinaga, J. Crystal Growth 111, 173–177 (1991).
[15] Z. Pan, L. H. Li, W. Zhang, Y. W. Lin, and R. H. Wu, Appl. Phys. Lett. 77, 214 (2000); doi: 10.1063/1.126928.
[16] S.R. Kurtz, J. Webb, L. Gedvilas, D. Friedman, J. Geisz, and J. Olson, Appl. Phys. Lett. 78, 748–750 (2001).
[17] J. Pakarinen, V. Polojärvi, P. Laukkanen, A. Tukiainen, A. Laakso, C.S. Peng, P. Tuomisto, V.-M. Korpijärvi, J. Puustinen, M. Pessa, Appl. Surf. Sci. 255, 2985–2988 (2008).
[18] E.–M. Pavelescu, T. Hakkarainen, V. D. S. Dhaka, N. V. Tkachenko, T. Jouhti, H. Lemmetyinen, M. Pessa, J. of Crystal Growth 281, 249–254 (2005).
[19] A. Aho, A. Tukiainen, V. Polojärvi, J. Salmi, M. Guina, 27th EU PVSEC, 290-292 (2012), ISBN: 3-936338-28-0, DOI: 10.4229/27thEUPVSEC2012-1BV.7.13.

Publication 4

Aho, A., Tukiainen, A., Korpijärvi, V.-M., Polojärvi, V., Salmi, J. & Guina, M. Comparison of GaInNAs and GaInNAsSb solar cells grown by plasma-assisted molecular beam epitaxy. AIP Conference Proceedings 1477 (2012), pp. 49-52.

P4

Comparison Of GaInNAs And GaInNAsSb Solar Cells Grown By Plasma-Assisted Molecular Beam Epitaxy

Arto Aho, Antti Tukiainen, Ville-Markus Korpijärvi, Ville Polojärvi, Joel Salmi and Mircea Guina

Tampere University of Technology/Optoelectronics Research Centre, +358 40 198 1076, arto.j.aho@tut.fi, Korkeakoulunkatu 3, FI-33720 Tampere, Finland

Abstract. We compare dilute nitride GaInNAs and GaInNAsSb solar cells grown by molecular beam epitaxy. Single junction p-i-n diode solar cells were fabricated to test the dilute nitride and antimonide material fabrication process. Triple-junction solar cells were fabricated to test the behavior of single GaInNAs(Sb) junctions in multi-junction configuration. When nitrogen was added to the growth of GaInNAs, good crystal quality was maintained up to 4% of nitrogen at the used growth conditions. Short circuit current densities of the devices could be increased by adding Sb to the growth but at the same time the open circuit voltages decreased due to bandgap shrinkage induced by Sb. In multijunction configuration, the samples with Sb showed inferior properties to ones without it. Lower currents and voltages of Sb-containing cells may be linked to segregation of Sb and transfer to the upper junctions.

Keywords: Solar cells, Molecular beam epitaxy, III-V semiconductors, dilute nitrides, dilute antimonides.
PACS: 78.55.Cr, 81.15.Hi, 81.05.Ea, 88.40.jp

INTRODUCTION

Dilute nitride (GaInNAs/GaAs) materials with a few percent of nitrogen are well suited for sub-junctions of ultra-high efficiency multijunction solar cells (MJSC) used in concentrated photovoltaic (CPV) systems. GaInNAs junctions lattice-matched to GaAs or Ge and tuned to have their absorption edge close to 1 eV or slightly below allow high-quality pseudomorphic fabrication of MJSCs without strain-induced misfit dislocations. When adding more than 4% of nitrogen into GaInNAs it becomes difficult to maintain the crystalline quality good enough for SCs. One option to overcome this problem is to add a small amount of antimony into GaInNAs [1] which enables to reduce the amount of N required for achieving a certain bandgap and also allows fabrication of solar cell active materials with their bandgaps less than 0.9 eV [2]. In this paper we compare the properties of GaInNAs and GaInNAsSb p-i-n SCs with high nitrogen content.

EXPERIMENTAL

The SC structures were grown using RF plasma-assisted molecular beam epitaxy system equipped with Knudsen-type cells for group-III elements and cracker sources for arsenic and phosphorus. Nitrogen was provided from a RF-plasma source. For GaInNAsSb samples the nitrogen flux and other growth parameters were kept the same, only antimony was added to the growth. Growth rates were ~1 μm/h for both materials. Silicon and beryllium dopants were used for the n- and p-type GaAs, respectively. The sample structure was the following: 600 nm thick n-GaAs buffer (n=1x10^{18} cm^{-3}) layer was grown onto n-GaAs(100) substrate followed by 324 nm of undoped, nearly lattice-matched, GaInNAs, and 250 nm of p-GaAs (p=1x10^{18} cm^{-3}) emitter. On top, a 50 nm thick p++ GaAs contact was grown. GaAs layers were grown at 580 ^{o}C whereas GaInNAs layers were grown at various temperatures ranging from 390 to 490 ^{o}C with As/III BEP ratio of ~10. With the optimized growth temperature (T_g~440 ^{o}C), another set of samples was grown with reverse polarity on p-GaAs(100) and with different nominal antimony compositions of 0, 0.02 and 0.04. In this sample set the thickness of GaInNAs(Sb) layer was 1.3 μm. Top emitter thickness for the latter set was 100 nm and a 25 nm thick AlInP window layer was grown between the emitter layer and the 600 nm thick highly doped contact n-GaAs. Thermal annealing was done ex-situ to reduce the amount of growth-related and nitrogen-related defects [3, 4].

To maintain close lattice matching between the substrate and the GaInNAs layer, the amount of indium in GaInNAs was ~2.7 x [N]. Grid patterns were formed using shadow masks.

PHOTOLUMINESCENCE

The GaInNAs(Sb) cells were characterized using room temperature photoluminescence. Table 1 lists the emission wavelengths and peak full-width-at-half-maximum (FWHM) values of annealed GaInNAs cells with different nitrogen contents. The general observation is that the higher the nitrogen content the longer the emission wavelength. Also,

8th International Conference on Concentrating Photovoltaic Systems
AIP Conf. Proc. 1477, 49-52 (2012); doi: 10.1063/1.4753831

TABLE 1. Room temperature photoluminescence data from annealed GaInNAs cells with different nitrogen compositions and without addition of Sb.

GaInNAs composition	PL wavelength (nm)	FWHM (meV)
GaAs	870	42.5
GaIn $N_{0.01}As$	985	60
$GaInN_{0.02}As$	1090	58
$GaInN_{0.03}As$	1160	63.5
$GaInN_{0.04}As$	1265	64.5
$GaInN_{0.05}As$	N.A.	N.A.
$GaInN_{0.06}As$	N.A.	N.A.

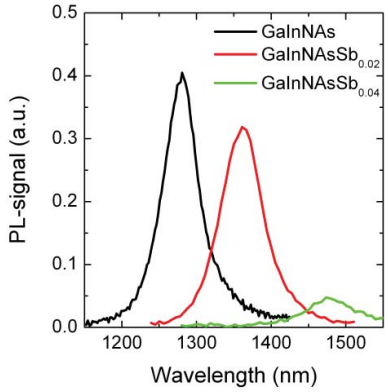

FIGURE 1. Room temperature photoluminescence measurements on GaInNAs(Sb) with different nominal antimony contents.

the peak width increases as nitrogen introduces a number of defects species in the crystal lattice. The FWHM values for 3 and 4 % nitrogen are nominally in the range of 60 meV, but for optimally annealed GaInNAs cells we were able to reduce this value to ~34 meV. Very weak not easily resolvable PL was obtained from samples with 5 and 6% nitrogen.

Figure 1 shows the evolution of photoluminescence spectra of GaInNAs(Sb) cells with 3.5% nitrogen when the amount of antimony is increased. With higher amounts of Sb the emission wavelength gets longer indicating a drastic reduction of the band gap. With addition of 4% of Sb one can easily shift the PL emission ~200 nm to longer wavelengths compared to material without Sb. For a moderate amount of Sb the PL peak width does not considerably change. For the optimized samples we observe only a slight increase in the peak width from ~34 meV to 38 meV when 4% of Sb is added, indicating a relatively good crystal quality.

LIGHT *I-V* MEASUREMENTS ON GAINNAS(SB) SOLAR CELLS

Light *I-V* measurements were done for the first sample set at AM0 conditions. The results are shown in Figure 2a. When the growth temperature is increased from 390 °C the maximum output power of the cells increases until 440 °C, after which it starts to decrease for all samples with nitrogen contents up to 4%. There seems to be a quite narrow temperature range from ~410 to 450 °C where GaInNAs grows with good crystalline quality. High-resolution x-ray diffraction measurements have shown that the crystal quality starts to deteriorate when when nitrogen content exceeds 4% for the used growth parameters. [5]

Figure 2b shows the variation of open circuit voltage (V_{oc}) along the PL emission wavelength of GaInNAsSb cells with different nominal Sb contents. In general, one observes a clear difference in V_{oc} between GaInNAs and GaInNAsSb samples; samples without Sb have always higher V_{oc}. This originates from the larger material band gap evidenced by the PL peak wavelength.

There seems to be a slight offset in V_{oc} between the samples without and with antimony. This offset, ~15-30 meV in total, might be caused by formation of defect states or dopant states in Sb-containing material [6,7]. To test whether this offset is real we plotted into figure 2b a curve showing $V_{oc}=Eg/q-0.4V$, which is the case for high-quality GaAs solar cells. At the radiative limit the V_{oc} should be higher compared the expression above and thus the V_{oc} offset to the Eg/q should be smaller [Viite]. Instead, all the samples with Sb exhibit larger offset – 0.56 V for GaInNAs, 0.575 V for $GaInNAsSb_{0.04}$ and 0.59 V for $GaInNAsSb_{0.02}$. Although there is no overlapping points between the PL emission wavelengths of the samples with and without Sb, the results suggest that the additional offset component is there and is related to addition of Sb.

To test the uniformity of GaInNAsSb on 2" wafers we grew two otherwise identical samples with and without antimony. The composition uniformity of the grown cells is quite good as the PL wavelength varies less than 4 nanometers across the wafers for both samples.

We measured the light *I-V* characteristics at AM1.5G for the optimized GaInNAs and GaInNAsSb cells (The cell size was 0.117 cm^2). The results indicated that uncoated GaInNAs cells produced a short circuit current density (J_{sc}) of ~25 mA/cm^2. The maximum open circuit voltage for the GaInNAs cells was 0.39 V. When Sb was added, there was a 6.4% increase in the short circuit current to 26.6 mA/cm^2. The open circuit voltage for GaInNAsSb was reduced to 0.30 V most likely due to reduced bandgap, which is also responsible for higher current generation. Defect formation might explain part of the V_{oc} reduction for the GaInNAsSb cell [1,2,6,7]. Also, it has been found that Sb may increase the dark current of GaInNAs SCs [8].

With SiO_2/SiN_x antireflection coatings the optimized GaInNAs cells produced current densities of ~33 mA/cm^2 at 950 W/m^2 excitation in outdoor conditions (Figure 3). At the same conditions, GaInNAsSb cells produced 35.5 mA/cm^2.

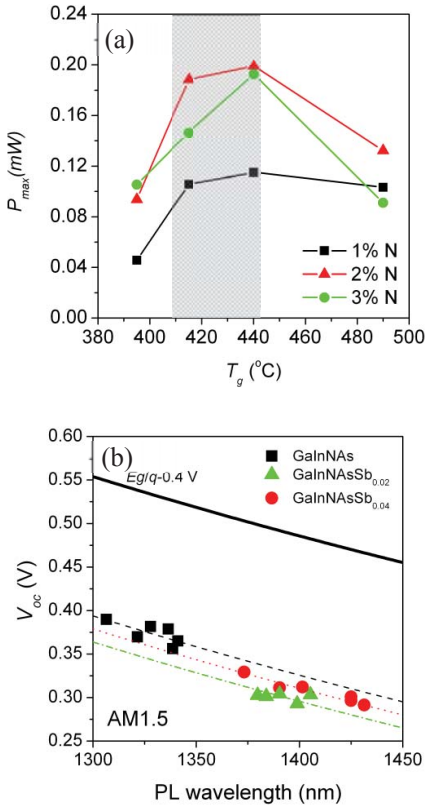

FIGURE 2. (a) Maximum output power (P_{max}) of test GaInNAs cells with different nitrogen contents and grown at different temperatures. Shaded area denotes the growth temperature window. (b) V_{oc} values measured for GaInNAsSb cells with different amounts of antimony: GaInNAs (black squares), $GaInNAsSb_{0.02}$ (green triangles) and $GaInNAsSb_{0.04}$ (red circles). Thick black curve shows the $Voc=Eg/q$-0.4V line which is commonly measured for high quality GaAs solar cells. The thin lines (dashed black, dotted red and dash-dotted green) denote best fits of the V_{oc} offset for the GaInNAs, $GaInNAsSb_{0.04}$ and $GaInNAsSb_{0.02}$ respectively.Nominal N composition was 0.035.

The highest V_{oc} value of 0.5 V was obtained for the optimized GaInNAs cell. For GaInNAsSb cell the highest V_{oc} was 0.35 V. There is not very large difference between the GaInNAs and GaInNAsSb cells in J_{sc} and thus it is tempting to think whether it is even necessary to insert Sb into crystal. Provided that one could fabricate GaInNAs cell with high enough current, then one could take the advantage of the high V_{oc} obtained for the cells made out of this material.

To test whether the GaInNAsSb sub-junctions work in actual MJSCs we prepared GaInP/GaAs/GaInNAs(Sb) 3J solar cells with GaInNAs and

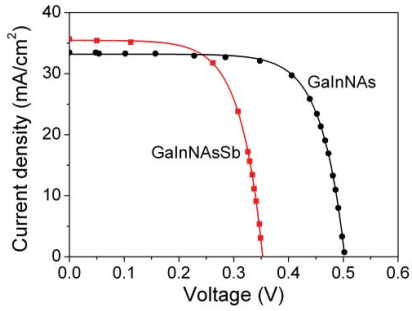

FIGURE 3. Outdoor light *I-V* measurements performed on GaInNAs (black circles) and GaInNAsSb (red squares) antireflection-coated single-junction SCs at one sun (950 W/m^2, measured by a CM11 pyranometer, T_{cell}=0 °C).

GaInNAsSb sub-junctions. The light *I-V* results measured for these cells at AM1.5G are shown in Figure 4.

Although GaInNAsSb single-junction cells had larger J_{sc} compared to GaInNAs cells, 3J cells fabricated using closely similar GaInNAsSb sub-junction did not perform well compared to 3J cells with GaInNAs sub-junction. To test which sub-junction is the limiting one, we applied an external monochromatic light with different wavelengths of 488 nm, 690 nm and 980 nm in addition to the AM1.5G excitation. It turned out that the only way to increase the I_{sc} of the devices for samples with and without Sb was using 488 nm light bias. The longer wavelength illuminations did not affect the I_{sc}. These results indicated that the limiting sub-junction in both 3J cells was made of GaInP.

Currently we do not know the exact reason for inferior behavior with Sb but it may be related to segregation of Sb and transfer to the upper junctions. It is known that Sb acts as surfactant on GaInP in MOVPE growth and is able to reduce the degree of ordering in this material [9,10]. In such a case, the subsequent increase in the bandgap could lead to observed reduction in short circuit current (I_{sc}) but not V_{oc} of 3J cell. Furthermore, it is known that Sb reduces the carrier lifetimes in GaInP [11].

In our case we see slight changes in photoluminescence spectrum of the GaInP sub-junction when GaInNAsSb is used for the bottom junction. The main GaInP peak at room temperature is located at 647 nm but for the sample without Sb we see another shoulder ($\lambda \sim$ 655 nm) on the low energy side of the main peak. The position of the main peak does not change when Sb is added to the growth, but the shoulder disappears. This peak can be explained either by disappearance of another ordering variant due to Sb or reduction of slight tensile strain observed for the sample without Sb. We also observed reduction of the integrated luminescence intensity of GaInP top cell with GaInNAsSb bottom cell. This is most likely related

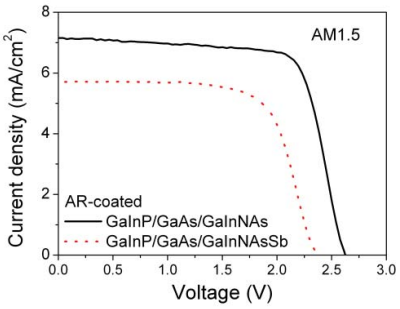

FIGURE 4. Light *I-V* curves for 3J SCs with GaInNAs (solid) and GaInNAsSb (dashed) sub-junctions.

to larger amount of point defects generated in GaInP top cells in samples with Sb. The shift of the band edge of GaInP to shorter wavelengths and reduced luminescence efficacy due to defects are the main factors to explain the reduced I_{sc} for the 3J cell with Sb.

Also, the reduction of V_{oc} for 3J cells with Sb is 0.25 V. This is ~0.1 V more than would be expected from GaInNAs(Sb) single-junction SC results. Although Sb is known to generate deep level defects in GaAs [12,7] and reduce recombination lifetime in GaInP [11], and we observe that the luminescence efficacy of GaInP is decreased for samples with Sb we are lacking more detailed information about the exact voltage losses inside the 3J cells and thus cannot refer at this point the missing voltage loss to changes in any specific sub-junction. This will be investigated in more detail in further studies.

CONCLUSIONS

We have obtained >35 mA/cm^2 short circuit current density for GaInNAsSb single-junction SCs at ~one sun illumination. When semiconductors with bandgap below 1 eV and high nitrogen contents are needed, replacement of the GaInNAs subcell with optimized GaInNAsSb subcell will provide enhanced flexibility to fulfill the current matching condition required for high-efficiency MJSCs once problems with possible segregation of Sb and transfer to the upper layers are solved. Also, low open circuit voltages for Sb-containing cells calls for optimization of growth parameters and the amount of Sb in GaInNAsSb.

ACKNOWLEDGMENTS

The authors want to thank the finnish funding agency for technology and innovation (TEKES) and all the other contributors and partners in Solar III-V project (#40120/09). Also, Mr. Pekka Malinen is greatly acknowledged for his valuable assistance in MBE and materials characterization related tasks.

REFERENCES

1. D. B. Jackrel, S. R. Bank, H. B. Yuen, M. A. Wistey, J. S. Harris, A. J. Ptak, S. W. Johnston, D. J. Friedman, and S. R. Kurtz, J. Appl. Phys. **101**, 114916 (2007).
2. S. L. Tan, W. M. Soong, S. Zhang, J. S. Ng, J. P. R. David, and M. J. Steer, Proc. SPIE **8256**, 82561E (2012).
3. S.R. Kurtz, A. A. Allerman, E. D. Jones, J. M. Gee, J. J. Banas, and B. E. Hammons, Appl. Phys. Lett. **74**, 729-731 (1999).
4. K. Voltz, D. Lackner, I. Németh, B. Kunert, W. Stolz, C. Baur, F. Dimroth, A.W. Bett, Journal of Crystal Growth **310** 2222-2228 (2008).
5. A. Aho, A. Tukiainen, V. Polojärvi, A. Gubanov, J. Salmi, M. Guina, P. Laukkanen, EU PVSEC 2011, 26th European Photovoltaic Solar Energy Conference and Exhibition, p.58-61, ISBN 3-936338-27-2, doi:10.4229/26thEUPVSEC2011-1AO.8.3 (2011).
6. W. K. Cheach, W. J. Fan, S. Wicaksono, S. F. Yoon, and K. H. Tan, J. Crystal Growth **254** 305-309 (2003).
7. W. K. Cheach, W. J. Fan, S. F. Yoon, K. H. Tan, R. Liu, and A. T. S. Wee, Thin Solid Films **488** 56-61 (2005).
8. A. J. Ptak, D. J. Friedman, and Sarah Kurtz, J. Vac. Sci. Technol. B 25, 955-959 (2007).
9. G. B. Stringfellow et al., J. Electron. Mat. **29** 134-139 (2000).
10. J. K. Shutleff et al., Appl. Phys. Lett. **75** 1914-1916 (1999).
11. C. M. Fetzer, R. T. Lee, G. B. Stringfellow, X. Q. Liu, A. Sasaki, and N.Ohno, J. Appl. Phys. **91**, 199-203 (2002).
12. R. Yakimova, P. Omling, B. H. Yang, L. Samuelson, J.-O. Fornell, and L. Ledebo, Appl. Phys. Lett. **59**, 1323-1325 (1991).

Publication 5

Aho, A., Tukiainen, A., Polojärvi, V. & Guina, M. Performance assessment of multijunction solar cells incorporating GaInNAsSb. Nanoscale Research Letters 9 (2014), 1 pp. 1-7.

P5

Nanoscale Research Letters
a SpringerOpen Journal

NANO EXPRESS Open Access

Performance assessment of multijunction solar cells incorporating GaInNAsSb

Arto Aho*, Antti Tukiainen, Ville Polojärvi and Mircea Guina

Abstract

We have measured the characteristics of molecular beam epitaxy grown GaInNAsSb solar cells with different bandgaps using AM1.5G real sun illumination. Based on the solar cell diode characteristics and known parameters for state-of-the-art GaInP/GaAs and GaInP/GaAs/Ge cells, we have calculated the realistic potential efficiency increase for GaInP/GaAs/GaInNAsSb and GaInP/GaAs/GaInNAsSb/Ge multijunction solar cells for different current matching conditions. The analyses reveal that realistic GaInNAsSb solar cell parameters, render possible an extraction efficiency of over 36% at 1-sun AM1.5D illumination.

Keywords: III-V Semiconductor multijunction solar cells; GaInNAsSb solar cells; Molecular beam epitaxy; High efficiency solar cells; Dilute nitrides

PACS: 88.40.hj; 88.40.jm; 88.40.jp; 81.15.Hi

Background

Multijunction solar cells (MJSC) are instrumental in concentrated (CPV) and space photovoltaic systems. The driving force for the material and technological development of MJSCs is the need for higher conversion efficiency. In CPV systems, the conversion efficiency is further increased owing to the use of concentrated light and therefore any efficiency gain that can be made by using more suitable materials and advanced design would lead to significant gain in overall system efficiency. The record CPV efficiency for lattice-matched GaInP/GaAs/GaInNAsSb SC is 44% [1]. On the other hand, the best lattice-matched GaInP/GaAs/Ge exhibit a peak efficiency of 43.3% under concentration [2] and 34.1% at 1 sun [3]. Efficiencies as high as 50% have been predicted for cells with a larger number of junctions and high concentration [4]. To this end, a promising approach is to integrate dilute nitrides and standard GaInP/GaAs/Ge. Yet, so far, such heterostructures have exhibited low current generation [5].

The GaInNAs and GaInNAsSb solar cells reported in the literature have typically high bandgap voltage offsets (W_{oc}), indicating poor junction properties [6,7]. The offsets can be higher than 0.6 V, which is a rather high value when compared to GaInAs materials exhibiting a W_{oc} of 0.4 V or even lower [4]. Recent studies on GaInNAs grown by molecular beam epitaxy (MBE) have demonstrated that by employing proper fabrication parameters [8-10], the W_{oc} can be reduced below 0.5 V [11]. Another peculiar feature of GaInNAs solar cells is their shunt-like junction operation [6,12]. This feature has been associated with clustering in GaInNAs due to phase separation of GaInNAs. Phase separation and shunt-like operation can also be avoided in MBE by the optimizing of the growth parameters [13]. In this paper, we focus on GaInNAsSb-based multijunction SCs, in particular on evaluating the practical bandgap and thickness limitations set by the subjunctions. Using realistic solar cell parameters for GaInNAsSb, based on the diode model and Kirchhoff's laws, we estimate the efficiency of GaInP/GaAs/GaInNAsSb and GaInP/GaAs/GaInNAsSb/Ge solar cells.

Methods

Experimental details and models

The experimental set consisted of single-junction GaInNAsSb p-i-n SCs with bandgaps ranging from 0.84 to 1.0 eV. The structures were grown by solid source MBE, equipped with SUMO cells for group III atoms, thermal crackers for group V elements and RF plasma source for atomic N flux generation. The N composition (y) of $Ga_{1-x}In_xN_yAs_{1-y}$ was 0.035 while the In composition

* Correspondence: arto.j.aho@tut.fi
Optoelectronics Research Centre, Tampere University of Technology, Korkeakoulunkatu 3, Tampere 33101, Finland

(x) was approximately 2.7 times the N composition to ensure lattice matching to GaAs. The GaInNAsSb samples were also closely lattice-matched to GaAs using Sb compositions of up to 0.04. For all structures, the lattice matching was verified by X-ray diffraction measurements.

We also fabricated a GaInP/GaAs/GaInNAs triple-junction test SC structure including a GaInNAs subjunction with a bandgap of 0.9 eV. The triple-junction solar cell and the fabrication details are described elsewhere [10]. After the MBE process, the samples were processed to solar cells having TiAu contact metals on p-side and NiGeAu for the n-side. Then the surface was coated with a two-layer TiO/SiO antireflection (AR) coating. The current–voltage (*I-V*) characteristics of single and multijunction solar cells were measured at the real sun (AM1.5G). The real sun intensity level was measured with a Kipp&Zonen CM11 pyranometer (Delft, the Netherlands). The external quantum efficiency (EQE) of the GaInNAs SC was also measured. Our EQE system was calibrated using NIST-calibrated Si and Ge detectors. Moreover, we measured the room-temperature photoluminescence (PL) spectra to determine the bandgaps of GaInNAsSb subjunction materials. The solar cell measurements and calculations are performed for one sun illumination unless otherwise stated when data is presented.

The theoretical efficiency of the multijunction solar cells incorporating 1 eV GaInNAsSb materials, was estimated using standard diode equations and AM1.5G/D current generation limits set by the absorbed light, bandgap value, and average EQE (EQE_{av}) of each junction. The equations below were used to estimate the I-V characteristics, and were derived from series-connected diodes with two terminals using Kirchhoff's laws.

$$I = I_i, \quad i = 1, 2, 3, 4 \tag{1}$$

$$V_i(I) = \frac{n_i k_B T}{e} \ln\left(\frac{I_{\mathrm{Li}}\left(E_{\mathrm{g}_i}, EQE_{\mathrm{av}\,i}\right) - I}{I_{0i}\left(T, E_{\mathrm{g}_i}\right)}\right) - IR_s \tag{2}$$

$$V(I) = \sum_{1}^{4} V_i(I) \tag{3}$$

Here, I is the current of the multijunction device which contains one to four junctions inside, I_i is the current through an individual solar cell, $V_i(I)$ is the voltage of single-junction device, n_i is the quality factor of the ith diode, k_B is the Boltzmann coefficient, T is the device temperature (T = 300 K), I_{Li} is the current generated by the junction i, E_{gi} is the bandgap (300 K) of the ith junction, I_{0i} is the reverse saturation current of the ith junction at 300 K, R_s is the device total series resistance, and V is the device total voltage. We have neglected the shunt resistance for simplicity, which is a good approximation for most of the high-quality SC devices. Here, we have also approximated the tunnel junctions as ideal lossless contacts between the solar cell junctions. One should keep in mind that this approximation is not valid at extremely high concentrations; the concentration limit depends strongly on the quality of the tunnel junctions.

Measurements

The *I-V* characteristics of single-junction GaInNAs SC, for AM1.5G real-sun illumination, are shown in Figure 1a. Measurements were done with and without a 900-nm long-pass filter inserted before the SC. The filter was used for simulating the light absorption into top junctions present in a multijunction device. The open circuit voltage (V_{oc}) and short-circuit current (J_{sc}) values for the GaInNAs SCs were 0.416 V and approximately 40 mA/cm^2, and 0.368 V and approximately 10 mA/cm^2, without and with a long-pass filter, respectively. The spectral behavior of PL and EQE is shown in Figure 1b. The bandgap of the GaInNAs was estimated from the PL peak maximum wavelength to be approximately 1 eV.

Examples of the measured PL spectra for GaInNAsSb structures with different amounts of Sb are presented in Figure 2a. As it can be seen, the bandgap of GaInNAsSb can be decreased down to 0.83 eV (1,500 nm). The *I-V* characteristics of a GaInNAsSb SC with E_g = 0.9 eV measured under real sun excitation at AM1.5G are presented in Figure 2b.

From the data presented in Figures 1 and 2b, we have calculated the W_{oc} values for selected GaInNAs and GaInNAsSb single-junction SCs. For GaInNAs SC with E_g = 1 eV the W_{oc} was 0.58 V and for GaInNAsSb with E_g = 0.90 eV, the W_{oc} was 0.59 V. The best W_{oc} we have achieved so far from GaInNAs single-junction SCs is 0.49 V [11]. The observations made here are in accordance with previously published reports which indicate that the Sb-based solar cells have a slightly higher W_{oc} values compared to GaInNAs SCs [6,9].

The J_{sc} values at AM1.5G for GaInNAsSb solar cells are summarized in Table 1 together with calculated EQE_{av} values for SCs with a thick GaAs filter. The fitted diode parameters for GaInNAsSb single-junction SCs are also included in Table 1. The performance of the GaInP/GaAs/GaInNAs SC, which we used for initial estimation, was current limited to 12 mA/cm^2 [10]; we note here that 14 mA/cm^2 would be needed for current matching with the two top junctions. Based on the J_{sc} = 12 mA/cm^2, we calculate that in our triple-junction SCs, the EQE_{av} of GaInNAs subjunction below a thick GaAs filter is approximately 0.6. For the current matching of this particular type of triple-junction device, one would need an EQE_{av} of 0.7. The V_{oc} improvement from double- to triple-junction SC due to adding GaInNAs subjunction was 0.35 V. Using this information and our

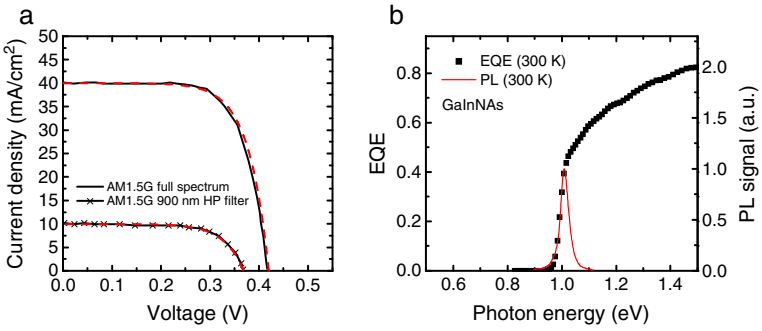

Figure 1 The *I-V* characteristics of single-junction GaInNAs SC (a) and EQE and PL spectra of GaInNAs (b).

model, we can approximate the behavior of the pure GaInNAs subjunction at different illumination conditions. At 1/3 suns - situation which occurs when a lattice-matched triple-junction cell is illuminated by 1 sun - the W_{oc} of GaInNAs subjunction is 0.56 V. At 1-sun illumination, which corresponds to a 3-sun illumination of a triple-junction device, the W_{oc} of GaInNAs subjunction is 0.53 V.

Theoretical and practical limits for current generation in GaInNAsSb SC

In order to estimate the performance of realistic MJSC-incorporating GaInNAsSb materials, one would need to use realistic data concerning current generation and current matching. The current generation in the GaInNAsSb subjunction has to be high enough to satisfy the current matching conditions of GaInP/GaAs/GaInNAsSb and GaInP/GaAs/GaInNAsSb/Ge solar cells. The current matching condition depends on the illumination spectrum, thickness, bandgap, and the EQE_{av} of GaInNAsSb sub-cell and the thickness of top subjunctions. The calculated J_{sc}s for GaInNAsSb at AM1.5G [14] are shown in Figure 3a. Again, in this case, it was considered that the dilute nitride cell is covered by a thick GaAs window layer, which practically absorbs all the photons with energy above 1.42 eV, to simulate the MJSC operation.

The theoretical upper limit for the bandgap of GaInNAsSb in GaInP/GaAs/GaInNAsSb solar cell operating at AM1.5G is 1.04 eV. In practice, the bandgap needs to be slightly smaller than this because the EQE_{av} target of approximately 100% is impractical for GaInNAsSb. EQE_{av} values of approximately 90% have been achieved for GaInP, GaAs, and Ge junctions [12,15], and thus, we set the EQE_{av} = 90% as a practical upper limit for GaInNAs subjunction operation which sets the upper limit for the GaInNAsSb bandgap to 1.02 eV. The current matching limits for different bandgaps of GaInNAsSb are presented in Figure 3b, where N compositions were calculated using the Vegard law and the band anti-crossing model [16].

To be usable for triple-junction SCs, the GaInNAsSb subjunction should produce higher V_{oc} than Ge. Therefore,

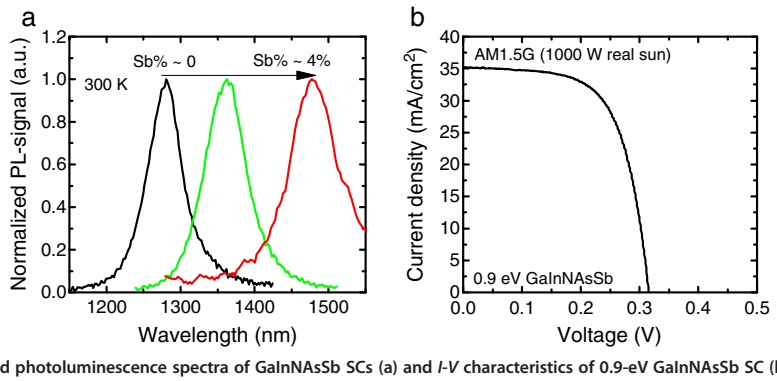

Figure 2 Measured photoluminescence spectra of GaInNAsSb SCs (a) and *I-V* characteristics of 0.9-eV GaInNAsSb SC (b).

Table 1 Characteristics of GaInNAsSb p-i-n diodes at different illumination conditions

Spectrum	Device	J_{sc} (mA/cm^2)	$J_{sc-ideal}$ (mA/cm^2)	EQE_{av}	V_{oc} (V)	FF	η	I_0 (mA/cm^2)	n
AM1.5G	GaInNAs (1 eV)	39.9	48.12	0.83	0.416	70%	11.6%	1.20E-03	1.55
AM1.5G (900-nm LP)	GaInNAs (1 eV)	9.98	16.48	0.61	0.368	68%	2.5%	1.20E-03	1.58
AM1.5G	GaInNAsSb (0.9 eV)	35.0	51.61	0.68	0.383	65%	7.2%	1.70E-02	1.60

FF, fill factor; η, solar cell efficiency.

the break-even limit for GaInP/GaAs/GaInNAsSb compared to GaInP/GaAs/Ge depends on the W_{oc} of GaInNAsSb subjunction. Note that the thickness and bandgap of GaInNAsSb can be rather freely optimized to fulfill the current matching criteria for a triple-junction device. However, the situation is very different when GaInP/GaAs/GaInNAsSb/Ge devices are considered. In four-junction devices, the total J_{sc} produced by photons with energies between 1.4 eV and approximately 0.7 eV needs to be shared equally by the GaInNAsSb and Ge junctions at various illumination conditions. The ideal amount of J_{sc} generated to be shared between GaInNAsSb and Ge regions are presented in Table 2. The intensities of AM1.5G/D are normalized to 1,000 W/m^2 and of AM0 illumination to 1,366 W/m^2. The data points out that for a GaInP/GaAs/GaInNAsSb/Ge solar cell, the AM1.5G spectrum turns out to be non-optimal for the current balance of the top and bottom junction pair and thus AM1.5D and AM0 are better for four-junction devices from the current matching point of view [12].

The optimal bandgap for GaInNAsSb junction of the triple- and four-junction SCs depends on the target spectrum and the performance of the subjunctions [12,15]. In a four-junction cell, it would be beneficial to have slightly larger bandgaps for the top junctions, especially for the AM1.5G spectrum. The GaInP/GaAs top cells have already been well optimized and that is the reason why the bandgap shifting is probably not the best practical step to start with, especially because the W_{oc} values of top junctions with larger bandgaps increase easily [4].

Efficiency estimations

For the efficiency simulation of MJSCs, we used the measured results for GaInNAsSb and parameters for state-of-the-art GaInP/GaAs [17] and GaInP/Ga(In)As/Ge [3] SCs with standard bandgaps of 1.9/1.4/0.70 eV. The calculated multijunction SC characteristics with GaInNAsSb subjunctions are based on the data presented in Tables 1 and 2 and the diode Equations 1 to 3.

To optimize four-junction SC efficiency, the thicknesses of top GaInP and GaAs cells need to be thinner because for AM1.5D, GaAs SC needs to bypass extra photons to produce additional current in the bottom junction pair and thus satisfy current matching condition. For four-junction devices, also the GaInNAsSb layer thickness needs to be lower than for triple-junction operation, if the bandgap were not optimal, which is close to approximately 1.04 eV (see Figure 3b for details). The estimated thicknesses of the GaInNAsSb junction to be used in four-junction devices operating at AM1.5D and 300 K, are approximately 3 μm for $E_g = 1.04$ eV and 0.8 μm for $E_g = 0.9$ eV [12,18]. One should note that the optimal GaInNAsSb thicknesses are different for AM1.5G and AM0 and that the thickness depends also on the SC operation temperature [12]. In our calculations, we have assumed that the device thicknesses have been optimized to maximize the current generation in every GaInNAsSb/Ge junction combination. GaInNAsSb MJSC performances at 1-sun excitation are presented in Figure 4a,b and in Tables 3 and 4. Figure 4 presents *I-V* estimations for AM1.5D, whereas Table 3 also contains estimations made for the AM1.5G performance.

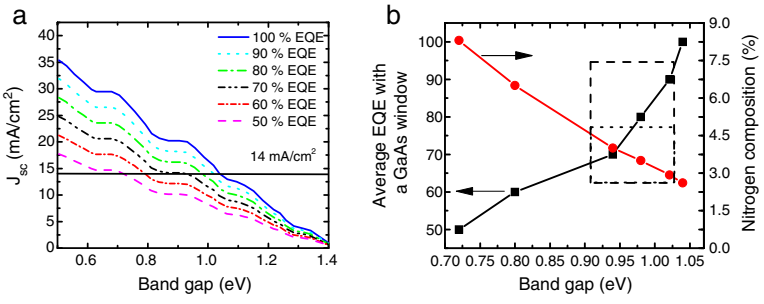

Figure 3 Calculated J_{sc} for GaInNAsSb sub-cell (a) and realistic AM1.5G current matching window for GaInP/GaAs/GaInNAs SC (b).

Table 2 Ideal and practical J_{sc} values for GaInP/GaAs/GaInNAsSb and GaInP/GaAs/GaInNAsSb/Ge SCs

	$J_{sc(GaInP)} + J_{sc(GaAs)}$ (mA/cm^2)	$J_{sc(GaInNAsSb)} + J_{sc(Ge)}$ (mA/cm^2)	Difference (mA/cm^2)	$J_{sc\text{-current matched 3J}}$ (mA/cm^2)	$J_{sc\text{-current matched 4J}}$ (mA/cm^2)
AM1.5G	31.9	25.0	−6.9	14.52	12.94
AM1.5D	30.3	28.4	−1.9	13.79	13.35
AM0	39.0	36.1	−2.9	17.75	17.09

J_{sc} values shared by GaInP/GaAs and GaInNAsSb/Ge junctions for different spectra at 300 K [12] and the current matching J_{sc} values with $EQE_{av} = 0.91$ for GaInP/GaAs/GaInNAsSb and GaInP/GaAs/GaInNAsSb/Ge. The J_{sc} differences between the two top junctions and the two bottom junctions are also given.

Results and discussion

According to our measurements and calculations, it would be beneficial to design the GaInNAs junction to overproduce current (see Figure 4a). Our calculations show that when GaInNAs junction generates more current than other junctions one would get approximately 1 percentage points higher efficiency compared to exactly current-matched triple-junction device. This is in line with reported data for GaInP/GaAs/GaInNAsSb triple-junction cells [19].

The efficiency improvement upon adding GaInNAsSb junction to a double- or triple-junction cell shows clear dependence on the illumination spectrum. When GaInP/GaAs/Ge triple-junction cells are compared with GaInP/GaAs/GaInNAs, one observes that at AM1.5G, the efficiency is 0.4 to 1.4 percentage points better when GaInNAs subjunction is used, depending of the design and the GaInNAs subjunction performance. However, it turns out that a four-junction SC with 1 eV GaInNAs, does not perform well at AM1.5G illumination. The added Ge junction does not improve the efficiency when compared to its triple junction reference (GaInP/GaAs/GaInNAs cell). This is simply due to the fact that the subjunctions of GaInP/GaAs/GaInNAs ($E_g = 1$ eV)/Ge SCs do not have the optimum bandgaps for current matching at AM1.5G conditions. When such a device is measured at AM1.5D, the situation changes and due to less blue rich spectrum, the multijunction device has better current matching between the subjunctions [12]. The studied four-junction device can have 1.6- to 1.7-percentage point higher efficiency at 1-sun than its GaInNAs triple-junction reference depending on the current matching. We have also compared the effect of bandgap on the efficiency of triple-junction devices. When a GaInNAsSb subjunction with $E_g = 0.9$ eV instead of GaInNAs with $E_g = 1.0$ eV is used at AM1.5D, the obtainable efficiency drops a 1.4 percentage points but since a device would be easier to realize with generation of excess current, the drop in practice would be smaller (see Figure 4a).

We have made a preliminary estimate for the performance of GaInP/GaAs/GaInNAs/Ge SC under concentrated sunlight at AM1.5D using GaInP/GaAs/Ge parameters from reference [20]. When compared to 1-sun results, the benefit of using a GaInNAs junction starts to be significant at concentrated sunlight. We estimate that GaInP/GaAs/GaInNAs triple-junction SCs operated at a concentration of 300 times have up to 3- to 6-percentage point higher efficiencies than GaInP/GaAs/Ge SCs. The situation gets even more favorable for using GaInNAs when four-junction devices are considered. Our calculations show that the efficiency can be further improved by approximately 3.5 percentage points compared with a GaInP/GaAs/GaInNAs triple-junction device by adding the fourth junction.

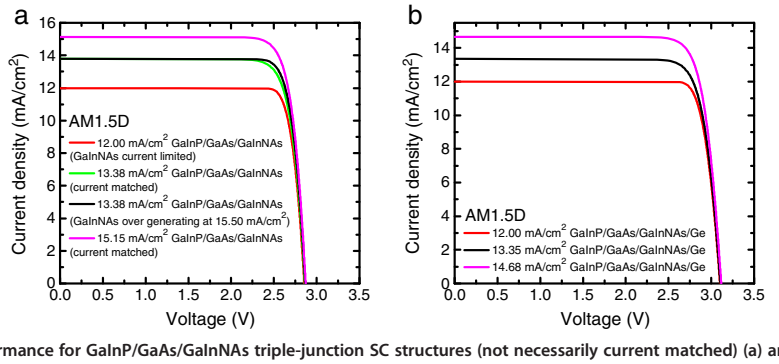

Figure 4 *I-V* performance for GaInP/GaAs/GaInNAs triple-junction SC structures (not necessarily current matched) (a) and current-matched GaInP/GaAs/GaInNAs/Ge four-junction devices (b).

Table 3 Estimated 1-sun efficiencies for GaInNAsSb multijunction solar cells at AM1.5G

Structure	Spectrum	J_{sc} (mA/cm^2)	V_{oc} (V)	FF	η (%)	Reference
2 J-GaInP/GaAs	AM1.5G	14.22	2.49	85.60	30.28	[17]
3 J-GaInP/GaAs/Ge	AM1.5G	14.70	2.69	86.00	34.10	[3]
3 J-GaInP/GaAs/GaInNAs	AM1.5G	12.00	2.86	87.52	30.02	This work, [17]
3 J-GaInP/GaAs/GaInNAs	AM1.5G	14.52	2.86	83.07	34.54	This work, [17]
3 J-GaInP/GaAs/GaInNAs (15.5 mA/cm^2)	AM1.5G	14.52	2.87	84.37	35.14	This work, [17]
3 J-GaInP/GaAs/GaInNAs (15.5 mA/cm^2)	AM1.5G	14.70	2.87	84.16	35.50	This work, [17]
4 J-GaInP/GaAs/GaInNAs/Ge	AM1.5G	12.00	3.10	83.93	31.19	This work, [3]
4 J-GaInP/GaAs/GaInNAs/Ge	AM1.5G	12.94	3.10	82.92	33.29	This work, [3]

Another important aspect that needs to be addressed to make sure of these advantages is the AR coating. The four-junction devices are already very demanding from the AR coating point of view since even the lowest short circuit current density of 13.79 mA/cm^2 used in the calculations requires an EQE_{av} of 91%. Commonly used AR coatings on GaInP/GaAs/Ge should be improved since the reflectance has traditionally been optimized for GaInP and GaAs subjunction current generation. This can be done in GaInP/GaAs/Ge SCs with almost no additional loss as Ge produces excess current that is able to accommodate the loss due to inappropriate AR coating. This leads to the fact that many Ge-based multijunction devices have EQE_{av} less than 90%. To improve the AR coating, one needs to adopt new schemes. One potential candidate is the moth eye pattern fabricated onto window layers of multijunction SCs. Such AR coatings are able to provide low reflectivity throughout the entire absorption spectrum of multijunction SCs [11].

Four-junction SCs are also sensitive to changes in spectral conditions since the photons need to be shared more equally than in Ge-based triple-junction devices. However, calculations have proved that inserting the fourth junction [12,15] or even more junctions would in fact be beneficial from the total yearly produced energy point of view, even if the changing spectral conditions were considered. Another positive factor for the GaInP/GaAs/GaInNAsSb/Ge SCs is the fact that the top cells can be made thin to obtain current matching. This will bring clear savings in fabrication costs, especially for CPV cells. There are indications that by using thin subjunctions, the epitaxial costs could be even cut by half [18]. The multijunction SC approach easily gets cost limited by the substrate costs and thus substrate recycling would be obvious companion to this approach. Therefore, the optimal GaInP/GaAs/GaInNAsSb/Ge structure would depend on the device efficiency, the cost of epitaxy and the cost of substrate and environment where the SC would be operated.

The efficiency improvements to GaInP/GaAs/GaInNAsSb SC after adding the Ge junction calculated in this paper may seem small but when calculating the SC system costs and generated energy factor, the grid-connected systems would provide better values since the total system costs do not increase too much [5]. In this paper, we have not estimated the effect of the lower Ge junction current generation on V_{oc} of Ge junction in the four-junction device. It was dropped out because of the lack of information on Ge subjunction performance in high-quality GaInP/GaAs/Ge SC. This might bias our results towards slightly overestimated V_{oc} and FF values for the four-junction SCs. On the other hand, in four-junction SCs, the quantum defect is lower in the Ge subjunction and the overall temperature of the whole SC will be lower, especially in CPV operation. In practice, this makes higher efficiencies and higher V_{oc} possible at high concentrations.

Table 4 Estimated 1-sun efficiencies for GaInNAsSb multijunction solar cells at AM1.5D

Structure	Spectrum	J_{sc} (mA/cm^2)	V_{oc} (V)	FF	η (%)
3 J-GaInP/GaAs/GaInNAs	AM1.5D	13.79	2.86	83.05	32.76
3 J-GaInP/GaAs/GaInNAsSb (0.90 eV)	AM1.5D	13.79	2.76	82.52	31.36
3 J-GaInP/GaAs/GaInNAs (15.5 mA/cm^2)	AM1.5D	13.79	2.87	84.98	33.58
3 J-GaInP/GaAs/GaInNAs	AM1.5D	15.15 (Ideal 3 J)	2.87	82.97	36.08
4 J-GaInP/GaAs/GaInNAs/Ge	AM1.5D	12.00	3.10	86.20	32.08
4 J-GaInP/GaAs/GaInNAs/Ge	AM1.5D	13.35	3.11	82.71	34.36
4 J-GaInP/GaAs/GaInNAs/Ge	AM1.5D	14.68 (Ideal 4 J)	3.12	82.65	37.79

Conclusion

We have presented our GaInNAsSb diode characteristics with different N and Sb compositions and estimated the efficiency of GaInP/GaAs/GaInNAsSb and GaInP/GaAs/GaInNAsSb/Ge solar cells. Our calculations based on measurements and a diode model reveal that at AM1.5G and at current matching condition, the use of GaInNAsSb junction as the bottom junction of a triple junction SC can increase the efficiency by approximately 4 percentage points compared to GaInP/GaAs double junction SC and have 1.4 percentage points higher efficiency than a GaInP/GaAs/Ge SC. At AM1.5D, the GaInNAsSb-based four-junction cell has a potential to show 1.7 percentage points higher efficiency than the GaInP/GaAs/GaInNAsSb triple-junction device. The achievable efficiencies for GaInNAsSb four-junction solar cells at AM1.5D 1-sun illumination are estimated to be over 36%. Our future target is to increase the GaInNAsSb EQE close to 100%, minimize the losses in front surface reflection and develop low-loss tunnel junctions.

Abbreviations

AR: antireflection; CPV: concentrated photovoltaics; E_{gi}: the bandgap (300 K) of the ith junction; EQE: external quantum efficiency; EQE_{av}: average EQE; FF: fill factor; I: current of the two-terminal solar cell; I_{0i}: reverse saturation current of the ith junction at 300 K; I_i: current through an individual solar cell; I_{Li}: current generated by the ith junction; I-V: current–voltage; k_B: Boltzmann coefficient; MBE: molecular beam epitaxy; MJSC: multijunction solar cell; n_i: quality factor of the ith diode; PL: photoluminescence; R_s: device total series resistance; SC: solar cell; T: SC temperature; V: device total voltage; V_{oc}: open circuit voltage; $V_i(I)$: voltage of a single-junction device; W_{oc}: bandgap open circuit voltage offset; η: solar cell efficiency.

Competing interests

The authors declare that they have no competing interests.

Authors' contributions

AA carried out the MBE growth, calculated the efficiency estimation, and drafted the manuscript. AA, AT, VP, and MG contributed to finalizing the manuscript. AT and AA contributed to the epitaxial design. VP processed the solar cells and designed the device processes. AA, AT, and VP measured the solar cell materials. MG is the head of the research group and he contributed to writing the manuscript. All authors read and approved the final manuscript.

Acknowledgements

The authors acknowledge the Finnish Funding Agency for Technology and Innovation, Tekes, via projects 'Solar III-V' #40120/09 and 'Nextsolar' #40239/12, and European Space Agency via project Contract N.: 4000108058/13/NL/FE. A. Aho acknowledges Graduate School in Electronics, Telecommunications and Automation, Wärtsilä Foundation, Finnish Foundation for Technology Promotion, and Ulla Tuominen Foundation for financial support. The authors also acknowledge MSc Ville-Markus Korpijärvi, DSc Juha Tommila, Wenxin Zhang, BSc Joel Salmi and BSc Pekka Malinen for their technical support.

Received: 18 November 2013 Accepted: 24 January 2014
Published: 5 February 2014

References

1. Green MA, Emery K, Hishikawa Y, Warta W, Dunlop ED: **Solar cell efficiency tables (version 41).** *Prog Photovolt Res Appl* 2013, **21**(1):1–11.
2. *CPV World Record by AZUR SPACE Solar Power: 43.3 Percent Efficiency.* http://www.azurspace.com/images/pdfs/pi-2012-AzurSpace-Rekord_EN.pdf.
3. Bett AW, Dimroth F, Guter W, Hoheisel R, Oliva E, Phillips SP, Schöne J, Siefer G, Steiner M, Wekkeli A, Welser E, Meusel M, Köstler W, Strobl G: **Highest efficiency multi-junction solar cell for terrestrial and space applications.** In *24th European Photovoltaic Solar Energy Conference and Exhibition.* Hamburg; 2009:1–6.
4. King RR, Bhusari D, Boca A, Larrabee D, Liu XQ, Hong W, Fetzer CM, Law DC, Karam NH: **Band gap-voltage offset and energy production in next-generation Multijucntion Solar Cells.** *Prog Photovol: Res Appl* 2011, **19:**797–812. doi:10.1002/pip.1044.
5. King RR, Sherif RA, Kinsey GS, Kurtz S, Fetzer CM, Edmondson KM, Law DC, Cotal HL, Krut DD, Karam NH: **Bandgap engineering in high-efficiency multijunction concentrator cells.** In *International Conference on Solar Concentrators for the Generation of Electricity or Hydrogen May 1–5, 2005.* Scottsdale, Arizona; 2005. NREL/CD-520-38172.
6. Jackrell DB, Bank SR, Yuen HB, Wistey MA, Harris JS Jr: **Dilute nitride GaInNAs and GaInNAsSb solar cells by molecular beam epitaxy.** *J Appl Phys* 2007, **101:**114916.
7. Khan A, Kurtz SR, Prasad S, Johnson SW, Gou J: **Correlation of nitrogen related traps in InGaAsN with solar cell properties.** *Appl Phys Lett* 2007, **90:**243509.
8. Aho A, Tukiainen A, Polojärvi V, Salmi J, Guina M: **High current generation in dilute nitride solar cells grown by molecular beam epitaxy.** In *Proceedings of the SPIE 2013 volume 8620.* San Francisco; 2013. doi:10.1117/12.2002972.
9. Aho A, Tukiainen A, Korpijärvi VM, Polojärvi V, Salmi J, Guina M: **Comparison of GaInNAs and GaInNAsSb solar cells grown by plasma-assisted molecular beam epitaxy**. In *AIP Conference Proceedings*, Volume 1477. Toledo; 2012:49–52. http://dx.doi.org/10.1063/1.4753831.
10. Aho A, Tukiainen A, Polojärvi V, Salmi J, Guina M: **MBE growth of high current dilute III-V-N single and triple junction solar cells**. In *EU Pvsec 2012 27th European Photovoltaic Solar Energy Conference and Exhibition.* Frankfurt; 2012:290–292. doi:10.4229/27thEUPVSEC2012-1BV.7.13.
11. Tommila J, Aho A, Tukiainen A, Polojärvi V, Salmi J, Niemi T, Guina M: **Moth-eye antireflection coating fabricated by nanoimprint lithography on 1 eV dilute nitride solar cell.** *Prog Photovolt Res Appl* 2013, **21:**1158–1162. doi:10.1002/pip.2191.
12. Friedman DJ, Kurtz SR: **Breakeven criteria for the GaInNAs junction in GaInP/GaAs/GaInNAs/Ge four-junction solar cells.** *Prog Photovolt Res Appl* 2002, **10:**331–344. doi:10.1002/pip.430.
13. Aho A, Tukiainen A, Polojärvi V, Gubanov A, Salmi J, Guina M, Laukkanen P: **Lattice matched dilute nitride materials for III-V high-efficiency multi-junction solar cells: growth parameter optimization in molecular beam epitaxy**. In *EU Pvsec 2011 26th European Photovoltaic Solar Energy Conference and Exhibition.* Hamburg; 2011:58–61. doi:10.4229/26thEUPVSEC2011-1AO.8.3.
14. ASTM G 173–03: *Standard tables for reference solar spectral irradiances: direct normal and hemispherical on 37° tilted surface.* West Conshohoken, PA: ASTM International; 2003. doi:10.1520/G0173-03R12.
15. Kurtz SR, Myers D, Olson JM: **Projected performance of three- and four-junction devices using GaAs and GaInP**. In *26th IEEE, Photovoltaic specialists conference September 29- October 3, 1997.* Anaheim: IEEE; 1997. doi:10.1109/PVSC.1997.654226.
16. Vurgaftman I, Meyer JR: **Band parameters for nitrogen-containing semiconductors.** *J Appl Phys* 2003, **94:**3675.
17. Takamoto T, Ikeda E, Kurita H, Ohmori M: **Over 30% efficient InGaP/GaAs tandem solar cell.** *Appl Phys Lett* 1997, **70:**381. doi:10.1060/1.118419.
18. Kirk AP: **High efficacy thinned four-junction solar cell.** *Semicond Sci Technol* 2011, **26:**155013. doi:10.1088/0268-1242/26/12/125013.
19. Wiemer M, Sabnis V, Yuen H: **43.5% efficient lattice matched solar cells**. In *Proceedings of SPIE 8108 High and Low Concentrator Systems for Solar Electric Applications VI.* San Diego, CA; 2011. doi:10.1117/12.897769.
20. *Azur space CPV triple junction solar cell - Type 3C40C (5.5*5.5mm^2).* http://www.azurspace.com/images/pdfs/CPV%20TJ%20Solar%20Cell%203C40C%205.5x5.5mm.pdf.

doi:10.1186/1556-276X-9-61
Cite this article as: Aho *et al.*: Performance assessment of multijunction solar cells incorporating GaInNAsSb. *Nanoscale Research Letters* 2014 **9**:61.

Publication 6

Aho, A., Tommila, J., Tukiainen, A., Polojärvi, V., Niemi, T. & Guina, M. Moth eye antireflection coated GaInP/GaAs/GaInNAs solar cell. AIP Conference Proceedings 1616 (2014), pp. 33-36.

P6

Moth Eye Antireflection Coated GaInP/GaAs/GaInNAs Solar Cell

Arto Aho, Juha Tommila, Antti Tukiainen, Ville Polojärvi, Tapio Niemi, and Mircea Guina

Optoelectronics Research Centre, Tampere University of Technology, P.O.Box 692, FIN-33101 Tampere, Finland, email: arto.j.aho@tut.fi

Abstract. The performance of a GaInP/GaAs/GaInNAs solar cell incorporating AlInP moth eye antireflection coating is reported and compared with the performance of a similar cell comprising TiO_2/SiO_2 antireflection coating. The moth eye coating exhibits an average reflectance of only 2% within the spectral range from 400 nm to 1600 nm. EQE measurements revealed absorption-related losses in the AlInP moth eye coating at wavelengths below 510 nm. Short wavelength absorption decreases the current generation in the top GaInP junction by 10%. Despite the absorption losses, the moth eye patterned GaInP/GaAs/GaInNAs solar cell exhibited higher current generation under AM1.5G real sun illumination.

Keywords: Antireflection coating, AlInP moth eye, GaInNAs, multijunction solar cell, MBE
PACS: 88.40.jp, 88.40.jm, 88.40.hj, 78.20.-e

INTRODUCTION

The efficient utilization of the broad solar spectrum in multijunction solar cells (MJSC) calls for the development of advanced antireflection coatings (ARCs) that operate in a broad spectral range [1]. Triple junction solar cell employing dilute nitrides have shown efficiencies of about 44% and improvements towards reaching efficiencies as high as 50% have been predicted, when using more junctions and advanced low loss ARCs [2]. One of the advanced approaches for fabricating high quality ARCs is to utilize bio-mimicked "moth eye" nanostructures processed on top of the MJSC.

The advantageous features of such nanostructures fabricated in AlInP, which is typically used as a window layer on GaAs based MJSCs, have been already demonstrated [3, 4]. Moreover, we have also demonstrated a moth eye ARC fabricated on top of a single junction dilute nitride solar cell with a bandgap (E_g) of 1 eV [4]. For the sake of generality we note that there are also other materials that can be used as the basis for the moth eye pattern, for example polymers, semiconductor nanowires and patterned dielectrics [5, 6, 8, 9, 10, 11, 12]. In this paper, we utilized the nanoimprint lithography (NIL) technique to integrate an AlInP moth eye ARC with a multijunction GaInP/GaAs/GaInNAs solar cell and we compared its performance against a GaInP/GaAs/GaInNAs solar cell comprising a TiO_2/SiO_2 ARC.

EXPERIMENTS

The GaInP/GaAs/GaInNAs MJSCs were grown by molecular beam epitaxy (MBE). The band gaps of the active regions were 1.9, 1.4 and 1 eV for the GaInP, GaAs and GaInNAs junctions, respectively. After the MBE growth the wafers were processed and moth eye ARC patterns were fabricated using NIL technique. The moth eye coating was fabricated directly on the monolithically grown AlInP surface of the triple junction MJSC. Prior patterning, the thickness of the AlInP window layer was 700 nm. The reference sample consisted of a similar triple junction solar cell with the only difference being a thinner AlInP window of only 40 nm. The reference sample was e-beam coated with a TiO_2/SiO_2 ARC. Details of the MJSC growth and the moth eye ARC fabrication have been reported elsewhere [3, 4, 13]. Ni/Ge/Au contact fingers and the Ti/Au back contact were deposited by e-beam evaporation on the n-side and p-side, respectively.

The solar cells were characterized by measuring the reflectance, the current-voltage (*I–V*) characteristics, and the external quantum efficiency (EQE). The textures of the patterned surfaces were studied using scanning electron microscopy (SEM). The reflectance was measured with an automated Accent RPM 2000 photoluminescence mapping tool calibrated with a gold mirror. Real sun I–V characteristics were measured at AM1.5G spectral conditions. The corresponding radiation power density was 860 W/m^2 as determined with a Kipp & Zonen

10th International Conference on Concentrator Photovoltaic Systems
AIP Conf. Proc. 1616, 33-36 (2014); doi: 10.1063/1.4897022

CM11 pyranometer. The measurements were performed in Tampere Finland. We performed the EQE measurements with an in-house build monochromator-based measurement system, which was calibrated using NIST-calibrated Si and Ge reference cells. All measurements were done at 300 K.

RESULTS, SIMULATION AND DISCUSSION

The AlInP moth eye structure processed on top of the MJSC was characterized first by SEM. The SEM picture in Fig. 1 reveals the pattern, with periodicity of 500 nm, arranged into a triangular lattice. The surface reflection properties of the AlInP moth eye are compared with the TiO_2/SiO_2 reference structure in Fig. 2. Both ARCs show good antireflection properties but at wavelengths above 1200 nm the moth eye ARC shows clearly lower reflectivity.

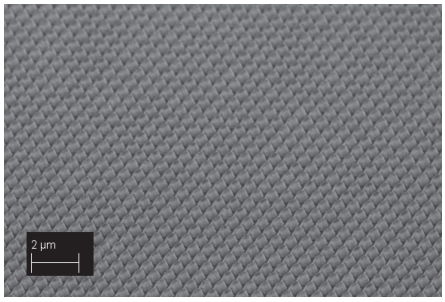

FIGURE 1. SEM picture of the moth eye surface pattern.

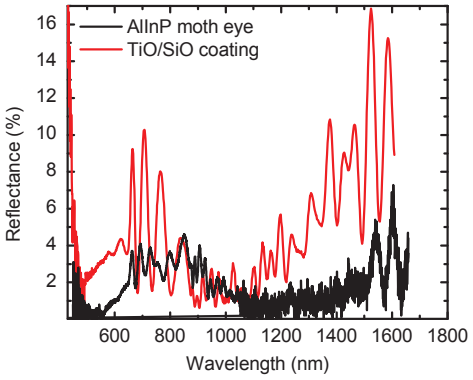

FIGURE 2. Reflectance measurements of the GaInP/GaAs/GaInNAs solar cells with AlInP moth eye and TiO_2/SiO_2 ARC.

Table 1 shows the performance of the ARCs fabricated in our study and performance of various ARCs reported in literature. We have also included corresponding reflectance simulation results for our AlInP moth eye structure. In addition to the simulated reflectance in Ref. [4], the angular performance of the moth-eye-patterned 1 eV GaInNAs SC was also evaluated. The reflectance was found to remain below 5% up to incident angles of 45° and less than 10% even up to 60°. Such low reflectance in a wide angular range is an important figure of merit for CPV solar cell performance.

TABLE 1. Reflectivities of ARC on MJSCs.

ARC Structure	Average reflectivity 400-1000 nm (%)	Average reflectivity 1000-1700 nm (%)
AlInP moth eye, measured [this work]	2.09	1.62
AlInP moth eye simulation [3]	1.7	1.7
TiO_2/SiO_2, [this work]	4.24	5.83
TiO_2 or SiN_x nanostructure [6]	7.28	7.28
Patterned PVC film [9]	9.08	-
SiO_2 moth eye on conventional ARC [7]	3.45	4.25
4 layer ARC (simulation) [14]	4.16	3.80
SiO_2-nanopilars on conventional ARC [5]	11.4	-

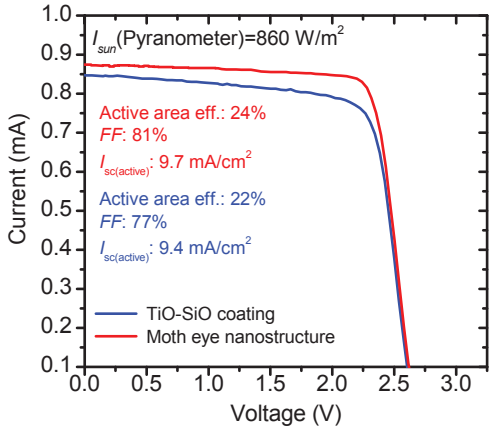

FIGURE 3. IV-characterics of GaInP/GaAs/GaInNAs SC coated with AlInP moth eye ARC and TiO/SiO ARC measured at AM1.5G.

The *I–V* performance of the GaInP/GaAs/GaInNAs solar cells with AlInP moth eye and TiO_2/SiO_2 ARC are shown in the Fig. 3. In real sun measurement conditions, the moth eye patterned cell outperforms the TiO_2/SiO_2 coated reference structure. The active area efficiencies of the processed solar cells are 24% for the moth eye cell and 22% for the TiO_2/SiO_2-coated structure.

The spectral responses of the sub-junctions were estimated from the EQE measurements. The results are presented in the Fig. 4. The results reveal that the AlInP moth eye pattern is performing well at long wavelengths above 510 nm but at short wavelengths, collected by the GaInP SC, we see a drop of EQE. The largest advantage of using AlInP moth eye in this comparison is seen for the GaAs sub-cell. Also one can see that the close band gap EQE has been enhanced for every sub cell, especially for GaInP SC. One possible reason for the decreased performance of the GaInP cell at short wavelength, besides the absorption losses, could be the difference in surface recombination rate at AlInP surface. Based on the geometry, we estimate that the surface area of the moth eye structure is approximately three times larger than that for the TiO_2/SiO_2 reference structure [3]. However, based on PC1D simulations with different AlInP window thicknesses, we did not see remarkable differences even when a recombination velocity as high as 10^7 cm/s was considered instead of more typical 10^4 cm/s to 10^5 cm/s rates [15]. We believe that the most of the losses are caused by the absorption losses of AlInP [3]. Therefore, for future developments the AlInP layer thickness should be optimized to maximize the current generation in the top junction.

Table 2 summarizes the calculated current densities (J_{sc}) based on the EQE measurements and AM1.5G reference spectrum [16]. The calculated J_{sc} values are slightly lower than J_{sc} values obtained from real sun *I–V* measurements, especially for the AlInP moth eye MJSC. Based on these calculations, the MJSC with AlInP moth eye ARC is current limited by the GaInP top cell while the MJSC with TiO_2/SiO_2 ARC is current limited by the GaInNAs bottom cell. Moreover, based on the EQE analysis, the MJSC with TiO_2/SiO_2 ARC should produce ~5% more current at AM1.5G conditions. However, as it is shown in Fig. 3, for the real sun conditions the AlInP moth eye ARC MJSC produces 3% higher current. This could be explained by an EQE calibration error or by the fact that the SCs operate differently with direct EQE beam signal and with wide incident angle of the AM1.5G global spectra. Therefore, we have made additional *I–V* measurements for AM1.5G and AM1.5 semi-direct spectrum conditions (a cone installed in front of the SC with 20° acceptance angle). We observed that the moth eye ARC solar cell operates better with AM1.5G conditions than the MJSC with TiO_2/SiO_2 ARC. With direct configuration, both SCs had the same J_{sc}. For the AM1.5G illumination, the MJSC with AlInP moth eye had again 3% higher current.

The benefits of the AlInP moth eye structure are clearly at long wavelengths and the situation would get more favorable if one would consider GaInP/GaAs/GaInNAs/Ge four junction designs. The flat low reflection band starting from 400 nm can have clear design advantage if the current generation of the top cell at short wavelength can be further boosted. By comparing the studied ARCs for the operation band of Ge SC (from 1240 nm to 1600 nm) the average reflectivities are 2% and 8% for the AlInP moth eye ARC and TiO_2/SiO_2 ARC respectively. This would give approximately 0.8 mA/cm^2 higher current density and 2.0 percentage point higher efficiency for a moth eye patterned four junction cell operating at AM1.5G. The corresponding numbers for AM1.5D are 0.9 mA/cm^2 and 2.3 percentage point higher efficiency. These estimations are based on the calculations presented in the literature [1].

TABLE 2. Calculated AM1.5G current densities from EQE.

ARC	Sub-cell	Calculated AM1.5G J_{sc} (mA/cm^2)
AlInP moth eye	GaInP	10.1
AlInP moth eye	GaAs	13.9
AlInP moth eye	GaInNAs	10.4
TiO_2/SiO_2	GaInP	11.0
TiO_2/SiO_2	GaAs	13.3
TiO_2/SiO_2	GaInNAs	10.6

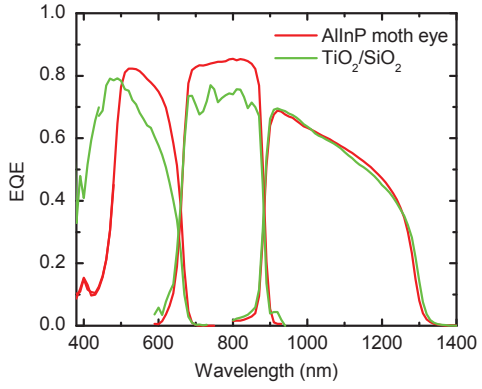

FIGURE 4. EQE measurements for GaInP, GaAs and GaInNAs sub-cells with AlInP moth eye ARC and TiO2/SiO2 ARC.

CONCLUSION

We have demonstrated the performance of AlInP moth eye ARC structure fabricated on a thick AlInP window layer of a MJSC. The performance comparison between moth-eye and TiO_2/SiO_2 ARC shows that the AlInP moth eye has excellent anti-reflection performance starting from 510 nm exhibiting an average reflectivity of only 2% within the spectral range from 400 nm to 1600 nm. This is significantly lower than the 5% average reflectance of the TiO_2/SiO_2 ARC. Low average reflectivity in a wide wavelength range brings clear advances when four junction GaInP/GaAs/GaInNAs/Ge solar cells are considered. Below 510 nm, the absorption of the AlInP moth eye layer limits the GaInP top junction current generation by approximately 10%. Based on the EQE measurements, the SC with TiO_2/SiO_2 ARC should generate higher current but in practice it was observed that the SC with an AlInP moth eye ARC generates 3% higher current under AM1.5G conditions. This is caused by the better response of the moth eye coating for wide incident angle photons.

ACKNOWLEDGMENTS

The authors acknowledge the financial support provided by the Finnish Funding Agency for Technology and Innovation, Tekes (projects 'Solar III-V' #40120/09 and 'Nextsolar' #40239/12). A. Aho acknowledges the Graduate School in Electronics, Telecommunications and Automation, Wärtsilä Foundation, Finnish Foundation for Technology Promotion, and Ulla Tuominen Foundation for financial support. For the technical support, the authors acknowledge: Mr Joel Salmi and Mr Pekka Malinen: Tampere University of Technology, Prof. Yuan Xiaofeng and Peng Changsi: Institute of Information Optical Engineering, Soochow University and Mr. Zhang Yuxiang: Suzhou Institute of Nano-Tech and Nano-Bionics, Chinese Academy of Sciences.

REFERENCES

1. A. Aho, A. Tukiainen, V. Polojärvi and M. Guina, *Nanoscale Research Letters* **9**:61 (2014)
2. R. R. King, D. Bhusari, A. Boca, D. Larrabee, X. Q. Liu, W. Hong, C. M. Fetzer, D. C. Law and N. H. Karam, *Prog Photovol: Res Appl*, **19**, 797–812. (2011)
3. J. Tommila, V. Polojärvi, A. Aho, A. Tukiainen, J. Viheriälä, J. Salmi, A. Schramm, J. M. Kontio, A. Turtiainen, T. Niemi, M. Guina, *Solar Energy Materials & Solar Cells*, **94**, 1845–1848 (2010)
4. J. Tommila, A. Aho, A. Tukiainen, V. Polojärvi, J. Salmi, T. Niemi and M. Guina, *Prog. Photovolt: Res. Appl.* DOI: 10.1002/pip.2191 (2012)
5. J.J. Liu, W-J. Ho, J-K. Syu, Y-Y. Lee, C-F. Lin and H-P. Shiao, *International Journal of Nanotechnology*, **11**, No. 1/2/3/4, Special Issue on Sustainable Nanoelectronics, DOI: 10.1504/IJNT.2014.059832 (2014)
6. P. Yu, M-Y. Chiu, C-H. Chang, C-Y. Hong, Y-L. Tsai, H-V. Han and Y-R. Wu, *Prog. Photovolt: Res. Appl.*, **22**, 300 – 307 (2014)
7. E. E. Perl, C-T. Lin, W. E. McMahon, J. E. Bowers 1 , and Daniel J. Friedman 2, *Photovoltaic Specialists Conference (PVSC), IEEE 39th*, 16-21 June, 14115971, 1902 – 1906 (2013) DOI:10.1109/PVSC.2013.6744515 (2013)
8. L. Yao, J. He, *Prog. Mat. Science*, **61**, 94-143 (2014)
9. K-S. Han ,J-H. Shin,W-Y. Yoon and H. Lee, *Solar Energy Materials & Solar Cells*, **95**, 288-291 (2011)
10. S. L. Diedenhofen, G. Grzela, E. Haverkamp, G. Bauhuis, J. Schermer, J. Gómez Rivas, *Solar Energy Materials & Solar Cells*, **101**, 308-314 (2011)
11. J-L. Hou, S-J. Chang, T-J. Hsueh, C-H. Wu, W-Y. Weng and J-M. Shieh, *Prog. Photovolt: Res. Appl.*, **21**, 1645–1652 (2013)
12. Q. Chen, G. Hubbard, P. A. Shields, C. Liu, D. W. E. Allsopp, W. N. Wang, and S. Abbott, *Applied Physics Letters* **94**, 263118 (2009)
13. A. Aho, V. Polojärvi, V-M. Korpijärvi, J. Salmi, A. Tukiainen, P. Laukkanen, M. Guina, *Solar Energy Materials & Solar Cells*, **124**, 150-158 (2014)
14. D. J. Aiken, *Solar Energy Materials & Solar Cells*, **64**, 393-404 (2000)
15. S.R. Kurtz, J.M. Olson, D.J. Friedman, J.F. Geisz and A.E. Kibbler, *Compound Semiconductor Surface Passivation and Novel Device Processing: Proceedings of the Materials Research Society Symposium, 5-7 April 1999, San Francisco, California. Materials Research Society Symposium Proceedings*, **573**, 95-106 (1999)
16. ASTM G 173–03: Standard tables for reference solar spectral irradiances: direct normal and hemispherical on 37° tilted surface. West Conshohoken, PA: ASTM International; 2003. doi:10.1520/G0173-03R12.

Publication 7

Aho, A., Isoaho, R., Tukiainen, A., Polojärvi, V., Aho, T., Raappana, M. & Guina M. Temperature Coefficients for GaInP/GaAs/GaInNAsSb Solar Cells, AIP Conference Proceedings 1679 (2015) 050001.

P7

Temperature Coefficients for GaInP/GaAs/GaInNAsSb Solar Cells

Arto Aho, Riku Isoaho, Antti Tukiainen, Ville Polojärvi, Timo Aho, Marianna Raappana and Mircea Guina

Optoelectronics Research Centre, Tampere University of Technology, P.O. Box 692, FIN-33101 Tampere, Finland

Corresponding author: arto.j.aho@tut.fi

Abstract. We report the temperature coefficients for MBE-grown GaInP/GaAs/GaInNAsSb multijunction solar cells and the corresponding single junction sub-cells. Temperature-dependent current-voltage measurements were carried out using a solar simulator equipped with a 1000 W Xenon lamp and a three-band AM1.5D simulator. The triple-junction cell exhibited an efficiency of 31% at AM1.5G illumination and an efficiency of 37–39% at 70x real sun concentration. The external quantum efficiency was also measured at different temperatures. The temperature coefficients up to 80°C, for the open circuit voltage, the short circuit current density, and the conversion efficiency were determined to be -7.5 mV/°C, 0.040 mA/cm^2/°C, and -0.09%/°C, respectively.

INTRODUCTION

Dilute nitride antimonides offer a great potential for efficiency improvement in concentrated photovoltaics (CPV) and space photovoltaic panels using multijunction solar cells architectures [1-4]. In the quest for optimizing the multijunction structure for specific application, it is essential to understand the temperature dynamics of the performance for the integrated cell and its sub-cells. This is particularly important for GaInP/GaAs/GaInNAsSb architectures since the corresponding absorption bands are significantly narrower than those for GaInP/GaAs/Ge cells, where Ge generates significantly more current than the top cells [1]. Additionally, air humidity plays also a significant role for the current generation in GaInNAsSb sub-cell; this is due to the presence of two water absorption bands in the spectral range from 1.0 eV to 1.4 eV, covered by GaInNAsSb absorption [5]. GaInP top cell on the other hand is more sensitive to the changes in the UV spectral band, which is dependent at least on the ozone level in the upper atmosphere [6, 7]. Moreover, for space applications, a proper balance between the current generated by the sub-junctions at different temperatures is instrumental for the achieving the highest average efficiency and highest energy production. Generally speaking, for single junction solar cells, the voltage decreases with the temperature increase and the generated current increases due to band gap narrowing with temperature increase. These effects result in typically lower cell efficiencies at higher temperatures. In this paper, the temperature behavior of the current voltage (*I–V*) and external quantum efficiency (EQE) characteristics, for molecular beam epitaxy (MBE) grown single and triple-junction GaInP/GaAs/GaInNAsSb solar cells are reported.

EXPERIMENTS

The solar cells were grown by plasma assisted solid source MBE. The structures were processed into cells with metal contact grid on the n-side and were coated with a TiO_2/SiO_2 antireflection film. More detailed description of the growth and processing can be found elsewhere [8-10]. The EQE measurements were performed with a monochromator based measurement system which was calibrated using NIST-calibrated Si and Ge reference cells. Suitable combinations of long-pass and short-pass optical filters were used for different spectral band investigations. For EQE measurements, the temperature was varied from 22°C (room temperature) to 80°C. The *I–V* characteristics

11th International Conference on Concentrator Photovoltaic Systems
AIP Conf. Proc. 1679, 050001-1–050001-5; doi: 10.1063/1.4931522

of the cells were measured in three different conditions: (i) using a 1000 W Oriel solar simulator equipped with an AM1.5G filter, (ii) using real sun illumination at one sun and ~100 suns and (iii) using an in-house build three-band solar simulator calibrated with single junction GaInP, GaAs and GaInNAsSb solar cells. The short circuit current densities of single junction cells were calibrated by EQE measurements. For the real sun measurements, the corresponding global radiation power density was measured using a Kipp & Zonen CM11 pyranometer. All the measurements were performed in Tampere, Finland. During the real sun measurements the integrated spectral irradiance was close to 1000 W/m^2 and the air mass was close to 1.5. For the real sun measurements, the temperature of the sample mount was set to 25°C. For simulator based measurements, the cell temperature was varied from 25°C to 150°C. For the short circuit current density (J_{sc}) and efficiency calculations, ASTM G173–03 spectrum [11] and EQE measurement data were used. For the concentrated real sun measurements, a simple lens and tracking device was used, which in practice limited the concentration to 70-100 suns. The potential efficiency trends and cell temperature under CPV operation were estimated by utilization of projective diode model for the GaInP/GaAs/GaInNAsSb cell [1].

RESULTS AND DISCUSSION

First the temperature dependent *I–V* characteristics of a GaInP/GaAs/GaInNAsSb triple-junction cell and GaInP, GaAs, GaInNAsSb single junction cells were determined at one sun conditions. Figure 1a summarizes the temperature dependencies of open circuit voltages (V_{oc}) for studied GaInP/GaAs/GaInNAsSb, GaInP/GaAs, GaInP, GaAs and GaInNAsSb cells. The V_{oc} measurements for single junction cells were carried out using one band Oriel solar simulator, equipped with an AM1.5G filter, calibrated close to one sun. For the triple-junction cell, the temperature dependencies of V_{oc} were measured by three-band solar simulator calibrated to AM1.5D; the temperature dependent *I–V* characteristics for the triple-junction cell are presented in Figure 1b.

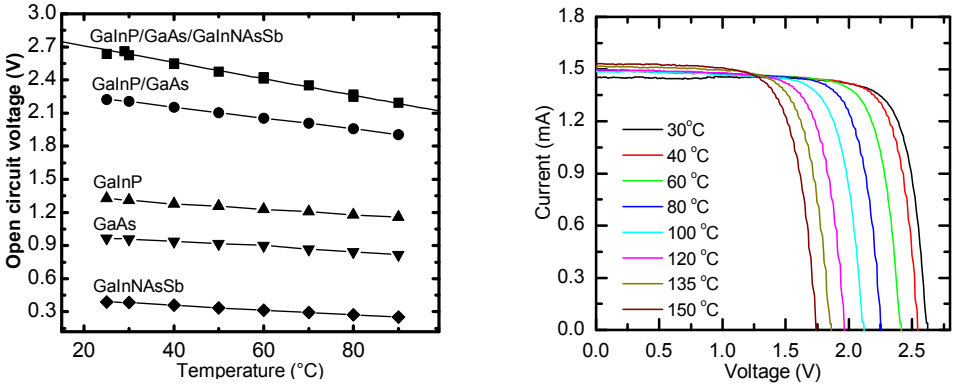

(a) (b)

FIGURE 1. (a) Temperature dependence of V_{oc} for the GaInP/GaAs/GaInNAsSb multijunction cell and single junction cells in the temperature range from 25°C to 90°C. All the cells were measured at AM1.5G except the triple junction cell which was measured at AM1.5D (b) Measured *I–V* characteristics of GaInP/GaAs/GaInNAsSb cell with a three-band solar simulator set to AM1.5D in the temperature range of 30°C to 150°C.

In order to understand the measured *I–V* characteristics of the GaInP/GaAs/GaInNAsSb cell, temperature dependent EQE measurements were also done. The EQE data taken at 22°C and at 80°C are presented in Figure 2a. The corresponding J_{sc} values were obtained by integrating the product of EQE values and the spectral irradiance values at each wavelength for each sub-cell at each temperature. The integration was done by using AM1.5D ASTM G173–03 reference spectrum [11]. The calculated J_{sc} values are presented in Figure 2b, which also presents the measured current densities for the GaInP/GaAs/GaInNAsSb cell illuminated by the three-band solar simulator. The current densities for the GaInP, GaAs, and GaInP/GaAs/GaInNAsSb devices show linear increase of J_{sc} as a function of temperature, but for GaInNAsSb sub-cell the slope of J_{sc} is negative. This observation can be understood

by analysing the properties of the AM1.5D spectrum in the wavelength range from 900 nm to 1350 nm, where the operation band of GaInNAsSb sub-cell is set. A portion of the AM1.5D spectrum [11] is also included in Figure 2a to support the discussion. In this wavelength range, two H_2O related absorption bands are visible [6, 7, 11]. The H_2O absorption band on the shorter wavelengths is close to the spectral boundary between GaAs and GaInNAsSb sub-cells on the GaInNAsSb cell side. Therefore, when the GaAs cell temperature increases and the band edge of GaAs shifts towards longer wavelengths the usable band for GaInNAsSb narrows down. On the other hand, more photons can be collected from the long wavelengths near 1300 nm due to red-shifting absorption edge of GaInNAsSb at least up to ~100°C when yet another water absorption peak begins to reduce the current production of GaInNAsSb cell [12]. This dependence makes the designing of the triple-junction cells particularly challenging for different geographical locations with different combinations of humidity and temperature. For robust cell operation in different conditions it is suggested that the GaInNAsSb cell should be designed to over-generate current. It would also be important to further improve the near band edge EQE of the GaInNAsSb sub cell, which is currently limited by the used antireflection coating materials and coating design. Ultimately, the non-ideality of the GaInNAsSb sub-cell also limits the near band edge performance of the triple-junction device [8].

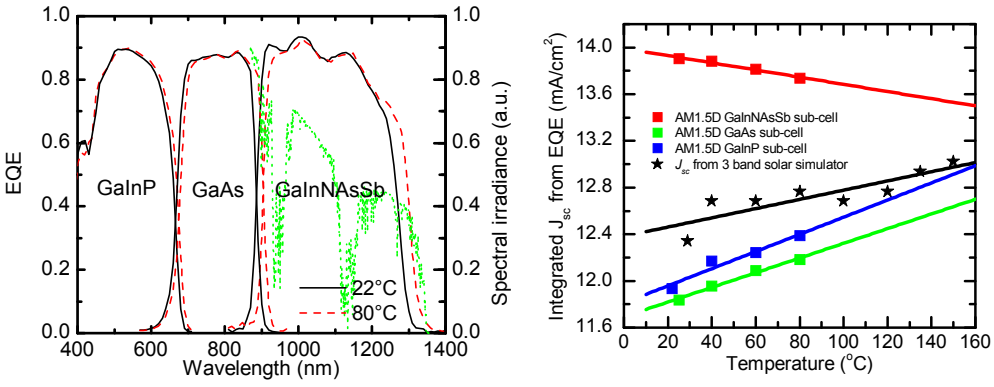

(a) (b)

FIGURE 2. (a) Measured EQE spectra for GaInP, GaAs and GaInNAsSb sub-cells at temperatures of 22°C and 80°C. The spectral window relevant for GaInNAsSb sub-cell of the AM1.5D ASTM G173–03 spectrum is also plotted with a green dotted line [11]. (b) Temperature dependence of J_{sc} values of sub-cells calculated from EQE measurements made on the 3J cell assuming AM1.5D ASTM G173-03 excitation spectrum (900 W/m^2) [11]. The measured temperature dependence of J_{sc} values for 3J cell is also presented for comparison.

The temperature slopes for the J_{sc} and V_{oc} are summarized in Table 1. The obtained V_{oc} slope for GaInP/GaAs/GaInNAsSb cell is similar to those reported earlier for GaInP/GaAs/Ge cells [13, 14]. The measured J_{sc} values are slightly higher than the J_{sc} values calculated from the EQEs of the limiting GaAs sub-cell. The measured and estimated values however are close to each other and the differences possibly arising from the calibration accuracy of the triple band simulator would not lead to significant variation of the total cell efficiency. By using three-band AM1.5D simulation at 900 W/m^2, the cell efficiency temperature coefficient was -0.09%/°C.

TABLE 1. Temperature coefficients for J_{sc} and V_{oc} for GaInP, GaAs, GaInNAsSb, and GaInP/GaAs/GaInNAsSb cells.

Sub-cell	**J_{sc} slope (mA/cm^2)**	**V_{oc} slope from 1J cells** (mV/°C)
GaInNAsSb	-0.031 mA/°C/cm^2	-2.0 mV/°C
GaAs	0.073 mA/°C/cm^2	-2.2 mV/°C
GaInP	0.063 mA/°C/cm^2	-2.5 mV/°C
GaInP/GaAs/GaInNAsSb *I–V*	0.040 mA/°C/cm^2	-7.5 mV/°C

The performance assessment of the fabricated GaInP/GaAs/GaInNAsSb cell was also done under concentrated light conditions. For this, a simple test bench was built in which light concentration level up to 70 suns could be achieved. The measurement for 70 suns concentration is presented in Figure 3a – the concentration level was determined by assuming linear dependence between J_{sc} and concentration factor. For the measurement system, higher concentrations were not possible without sacrificing the beam uniformity and quality. During the measurement the stage temperature was set at 25°C and continuous real sun illumination was used. The measured *I–V* characteristics are presented in Figure 3a. The Figure 3a also shows the *I–V* measurements done at one sun (AM1.5G, 1000 W/m^2) and at concentrated illumination. The spectral irradiance was measured by pyranometer and the *I–V*-curves shown in Figure 3a are normalized to 1000 W/m^2. Due to uncertainty of the real cell junction temperature and concentration during the CPV measurement, there is some margin in the estimated efficiencies. The estimation indicated that the lower limit for the cell efficiency was 37 % when the cell temperature was assumed to match that of the stage. In reality, the junction temperature most likely is somewhat higher under concentrated illumination. Junction temperature of 40°C was estimated from the diode analysis done on the cells at different temperatures. This gives the upper limit for the efficiency to be 39% at 70 suns. The diode analysis was also used for estimating the lower and upper limits for the series resistance of the cell. Thus, the efficiency trends for the measured cell at different concentration levels with lower and upper limits of the cell series resistance could be calculated and they are shown in Figure 3b.

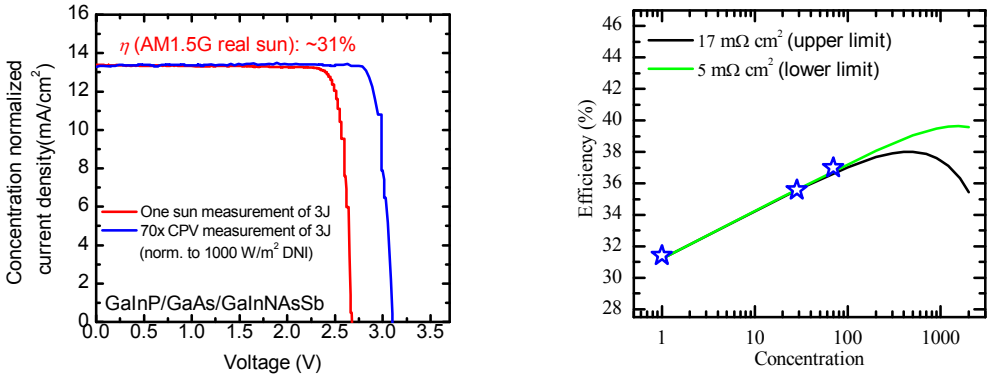

FIGURE 3. (a) *I–V* measurements done for the GaInP/GaAs/GaInNAsSb cell under one sun and concentrated sun light. Measurement stage temperature was set to 25°C. J_{sc} calculated from EQE for the limiting sub-cell at AM1.5G (13.0 mA/cm^2) fits well to the measured J_{sc}. (b) Efficiency of GaInP/GaAs/GaInNAsSb cell as the function of concentration factor. The blue stars represent the efficiencies estimated for the cells measured at 25°C. The solid lines are calculated cell efficiency trends with lower and upper series resistance values of 5 mΩ·cm^2 and 17 mΩ·cm^2.

For the future development steps, we expect to get further improvements for the cell efficiency from better current matching between the cells through anti-reflection coating optimization, improved cell design and by integrating GaInP/GaAs/GaInNAsSb structures into four-junction cells grown on germanium [1]. For GaInP/GaAs/GaInNAsSb/Ge four-junction solar cells thorough understanding of the temperature dependence of the sub-cell current generation balance would be even more critical, especially when efficiencies reaching 50% are targeted.

CONCLUSION

The efficiency for the active area of the triple-junction solar cell was estimated to be 31% at AM1.5G. Heating the cell reduced the cell efficiency and the temperature coefficient for conversion efficiency of a triple-junction GaInP/GaAs/GaInNAsSb cell was -0.09%/°C for AM1.5D (900 W/m2) excitation. For the same device, the temperature coefficient for the open circuit voltage was -7.5 mV/°C, which is close to the -7 mV/°C reported for lattice-matched GaInP/GaInAs/Ge solar cells [14]. The temperature coefficient for J_{sc} of the triple-junction cell was

0.04 mA/cm^2/°C. The temperature coefficient for the short circuit current was positive for GaInP and GaAs sub-cells and negative for GaInNAsSb sub-cell. This dependence is caused by changes in GaInP/GaAs/GaInNAsSb absorption bands with respect to the H_2O absorption bands in the AM1.5D spectrum. At 70 suns, the cell efficiency was estimated to be 37–39%.

ACKNOWLEDGMENTS

The authors would like to thank colleagues at Optoelectronics Research Centre for their high-quality experimental support, in particular we acknowledge the support of Ville-Markus Korpijärvi and Pekka Malinen. For the financial support, we would like to thank Finnish Funding Agency for Technology and Innovation—TEKES (projects#40120/09 'Solar III–V' and #40239/12 'Nextsolar'), Graduate School in Electronics, Telecommunications and Automation, Ulla Tuominen Foundation, Finnish Foundation for Technology Promotion, and Wärtsilä Foundation.

REFERENCES

1. A. Aho, A. Tukiainen, V. Polojärvi and M. Guina, Nanoscale Research Letters, **9**, 1-7 (2014).
2. R. R. King, D. Bhusari, D. Larrabee, X. Liu, E. Rehder, K. Edmondson, H. Cotal, R. K. Jones, J. H. Ermer, C. M. Fetzer, D. C. Law and N. H. Karam, Prog Photovoltaics Res Appl, **20**, 801-815 (2012).
3. A. Barnett, C. Honsberg, D. Kirkpatrick, S. Kurtz, D. Moore, D. Salzman, R. Schwartz, J. Gray, S. Bowden, K. Goossen, M. Haney, D. Aiken, M. Wanlass and K. Emery, "50% efficient solar cell architectures and designs," in *Photovoltaic Energy Conversion, Conference Record of the 2006 IEEE 4th World Conference,* (2006), pp. 2560-2564.
4. F. Dimroth, Physica Status Solidi (C), **3**, 373-379 (2006).
5. S. R. Kurtz, D. Myers and J. M. Olson, "Projected performance of three- and four-junction devices using GaAs and GaInP," vol. In 26th IEEE, Photovoltaic specialists conference September 29- October 3, Anaheim, 1997
6. T. Zdanowicz, T. Rodziewicz and M. Zabkowska-Waclawek, Solar Energy Mater. Solar Cells, **87**, 757-769 (2005).
7. R. E. Bird and C. Riordan, Journal of Climate and Applied Meteorology, **25**, 87-97 (1986).
8. A. Aho, V. Polojärvi, V. -M. Korpijärvi, J. Salmi, A. Tukiainen, P. Laukkanen and M. Guina, Solar Energy Mater. Solar Cells, **124**, 150-158 (2014).
9. A. Aho, J. Tommila, A. Tukiainen, V. Polojärvi, T. Niemi and M. Guina, AIP Conference Proceedings 1616, 33-36 (2014). DOI: http://dx.doi.org/10.1063/1.4897022
10. A. Aho, V. -M. Korpijärvi, A. Tukiainen, J. Puustinen and M. Guina, J. Appl. Phys., **116**(21) (2014). DOI: http://dx.doi.org/10.1063/1.4903318
11. ASTM G 173–03: Standard tables for reference solar spectral irradiances: direct normal and hemispherical on 37° tilted surface, West Conshohoken, PA: ASTM International (2003).
12. D. Derkacs, R. Jones-Albertus, F. Suarez and O. Fidaner, Journal of Photonics for Energy, **2**, 021805-1-021805-8 (2012).
13. G. S. Kinsey, P. Hebert, K. E. Barbour, D. D. Krut, H. L. Cotal and R. A. Sherif, Prog Photovoltaics Res Appl, **16**, 503-508 (2008).
14. G. Siefer and A. W. Bett, Prog Photovoltaics Res Appl, **22**, 515-524 (2014).

Publication 8

Aho, A., Korpijärvi, V.-M., Isoaho, R., Malinen, P., Tukiainen, A., Honkanen, M. & Guina, M., Determination of composition and energy gaps of GaInNAsSb layers grown by MBE, (Submitted to Journal of Crystal Growth).

P8

P9

Publication 9

Aho, A., Tukiainen, A., Polojärvi, V., Korpijärvi, V.-M., Gubanov, A., Salmi, J. & Guina, M. and P. Laukkanen, Lattice matched dilute nitride materials for III-V high-efficiency multi-junction solar cells: growth parameter optimization in molecular beam epitaxy, European Photovoltaic Solar Energy Conference and Exhibition EU PVSEC (2011), pp. 58-61.

LATTICE MATCHED DILUTE NITRIDE MATERIALS FOR III-V HIGH-EFFICIENCY MULTI-JUNCTION SOLAR CELLS: GROWTH PARAMETER OPTIMIZATION IN MOLECULAR BEAM EPITAXY

Arto Aho, Antti Tukiainen*, Ville Polojärvi, Ville Korpijärvi, Alexander Gubanov, Joel Salmi, Mircea Guina
Optoelectronics Research Centre, Tampere University of Technology, Tampere, Finland
P.O. Box 692, FIN-33101 Tampere, Finland, http://www.tut.fi/orc, *e-mail: antti.tukiainen@tut.fi

Pekka Laukkanen,
University of Turku, Department of Physics and Astronomy,
Vesilinnantie 5, FI-20014 Turku. Phone +358 2 333 6659, pekka.laukkanen@utu.fi

ABSTRACT: We report on growth parameter optimization for fabrication GaInNAs materials with nitrogen concentrations ranging from 1 to 6%. These compounds, refered as dilute nitrides, are a promising choice for developing 1-eV sub-cells required in III-V high-efficiency multi-junction solar cells. Specifically, we have compared the effects of growth temperature and thermal annealing onto optical and structural properties of GaInNAs p-i-n diodes lattice matched to GaAs. When used in a 3-junction GaInP/GaAs/GaInNAs solar cell, the dilute nitride structure could generate a short-circuit current density of ~12 mA/cm2 measured in outdoor conditions.

Keywords: III-V Semiconductors, Gallium Arsenide Based Solar Cells, Dilute Nitride Materials, Multijunction Solar Cell, Molecular Beam Epitaxy

1 INTRODUCTION

The increasing need to improve the efficiency of multi-junction solar cells (SC) used in concentrated photovoltaic systems, calls for advancing the development of GaAs-based materials able to absorb effectively the solar spectrum within 1100-1400 nm. Dilute nitrides (GaInNAs) are promising materials for this wavelength range but, so far, they have been rarely used for this purpose because they exhibit high defect densities. Despite of this the new world record conversion efficiency has recently been achieved using multijunction solar cells which employ dilute nitride material containing subcells [1]. To reach an absorption edge at ~1400 nm with GaInNAs lattice matched to GaAs one needs to incorporate a substantial amount of nitrogen (4% or more) into crystal. This is not an easy task due to large miscibility gap of GaInNAs and the high number of N-related defects, which are increasing rapidly with N composition [2-6]. High nitrogen content leads to degradation of electrical and optical properties of the material. Although the dilute nitrides can be grown by metalorganic chemical vapor deposition, there are challenges related to high background doping level and increased carbon and hydrogen-related defect species, which have a detrimental effect on electrical and optical properties [7,8]. In our studies we are employing molecular beam epitaxy (MBE) as this technique allows a high level of independent control of the growth conditions (e.g. growth temperature and III-As ratio) and provides low level of hydrogen and carbon contamination. We should note here that the growth parameter window is very narrow for metastable materials such as GaInNAs [9]. In particular, MBE enables to operate at relative low growth temperatures to avoid phase separation and clustering effects, while the ratio of As to group III ratio can be accurately controlled. Moreover, with MBE we can employ reflection high-energy electron diffraction (RHEED) to observe the surface reconstructions during the growth and thus optimize the growth conditions.

Here, we present a thorough optimization of the growth parameters for lattice matched and slightly mismatched GaInNAs having nitrogen compositions ranging from 1 to 6%. We focus especially on comparing the properties of materials with 2% and 4% of N-content.

2 SAMPLE FABRICATION AND EXPERIMENTAL METHODS

For fabrication we have used plasma-assisted MBE that provides flexible means to control the N incorporation. The epitaxy system was equipped with a cracker source for arsenic and RF-plasma source for nitrogen. Group III elements were provided from standard Knudsen-type cells and SUMO cells. Sample fabrication started by thermal oxide desorption and growth of a 600 nm thick n-GaAs:Si buffer layer on n-GaAs(100) substrates. The buffer layer was n-type doped at a concentration of $1x10^{18}$ cm^{-3}. Then we grow nearly lattice-matched, 324 nm thick, undoped GaInNAs layers using a wide range of substrate temperatures (Tg from 395 to 525ºC) and a V/III ratio of 10. Then, p-i-n structures were formed by growing 250 nm of p-GaAs:Be doped to $n=1x10^{18}$ cm^{-3} and the structure was finalized by growth of 50 nm thick highly Be-doped contact layer ($p=2x10^{19}$ cm^{-3}). The nitrogen content of the undoped GaInNAs region was varied from 1% to 6%. After growth, the samples were thermally annealed in a rapid thermal annealing (RTA) system using proximity capping and temperatures and times to correlate possible changes in material quality with the growth parameters. The best quality GaInNAs material was used in a GaInP/GaAs/GaInNAs 3-junction device lattice matched to GaAs to demonstrate its usability in real devices.

The GaInNAs/GaAs p-i-n structures were studied using photoluminescence (PL), x-ray diffraction (XRD), atomic force microscopy (AFM), RHEED and light-biased current-voltage (LIV) and external quantum efficiency measurements.

3 RESULTS AND DISCUSSION

GaInNAs samples with variable nitrogen content exhibited small or non-existent room temperature PL

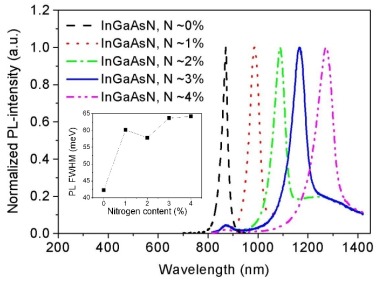

Figure 1: Normalized room temperature PL emission peaks at room temperature for annealed GaInNAs material with 0–4% N-content. The FWHM value of the PL signal are given in the inset.

intensities when PL was measured from as-grown samples. However, thermal annealing drastically improved the room temperature PL of GaInNAs for the entire N composition range of 1–4%. The emission wavelengths of annealed samples ranged from 970 nm (1% N) to 1300 nm (4% N) corresponding to material bandgaps of 1.28 eV and 0.95 eV, respectively. The measured PL signals are shown in Figure 1.The peak widths (FWHM) were increasing from 42.5 to 64.5 meV for samples without any nitrogen (GaAs p-i-n diode) and samples with 4% nitrogen.

For the N compositions between 1 and 4%, the maximum PL intensity after annealing was found to correspond to a growth temperature of ~415ºC. For samples with 5–6% of nitrogen we did not detect PL at temperature even after annealing. XRD measurements are shown in Figure 2. The diffraction peaks remain sharp up

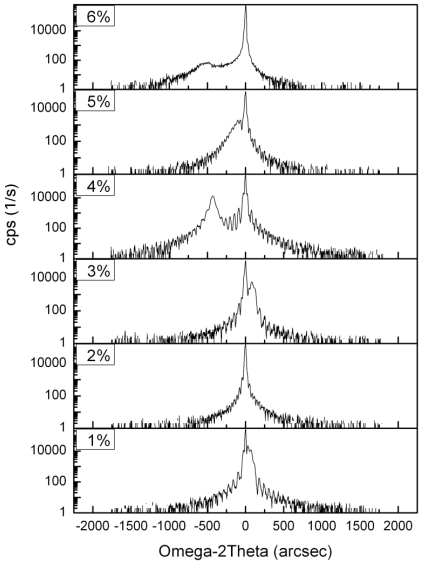

Figure 2: XRD rocking curves for GaInNAs with 1-6% nitrogen.

to 4% N, but for 5 and 6% N the diffraction peaks are getting wider. Also, the diffraction peak intensity drops drastically for samples with 5 and 6% nitrogen. Wider and smaller diffraction peaks mean inferior crystalline quality and can be related to either phase separation or segregation effects that set in for the used growth parameters with higher N concentrations [10-13].

Annealing introduced a complex N-composition and growth parameter dependent PL wavelength blue shift (BS). Optimized annealing process for GaInNAs with 2% and 4% N increased the PL lifetimes from τ_{PL}<20 ps to τ_{PL} ~900 ps and τ_{PL}~300 ps, respectively. Such TRPL lifetimes are among the longest ever reported for GaInNAs material lattice-matched to GaAs with 2% and 4% nitrogen.

The LIV measurements for samples with 1-6% N are shown in Figure 3. The highest short circuit currents were obtained for the as-grown samples with T_g=440-490ºC, while the open circuit voltage, fill factor and cell power were maximized for thermally annealed SCs grown at 440ºC for all N-compositions ranging from 1 to 4%. The optimum growth temperature for GaInNAs SCs was found to be close to 450ºC. At this temperature we identified a (1x3) surface reconstruction during the growth of GaInNAs sample with 3% N. At higher temperatures the RHEED pattern became spotty indicating increased surface roughness, which was also confirmed by XRD and AFM measurements. The best measured roughness average values were about 0.3 nm and even at their worst the value was still clearly below 1 nm.

The fact that the overall SC parameters are maximized at T_g=440ºC is thought to be due to multiple simultaneous processes such as nitrogen incorporation probability, defect generation and annihilation, phase separation and indium segregation. I_{sc} is inversely proportional to the bandgap of GaInNAs and can thus be used in part as a measure of nitrogen incorporation into crystal in as-grown samples. After annealing the BS-induced changes in I_{sc} due to formation of In-N bonds through atomic rearrangements in the lattice [7,14]. The drastic increase of V_{oc} for annealed samples is directly

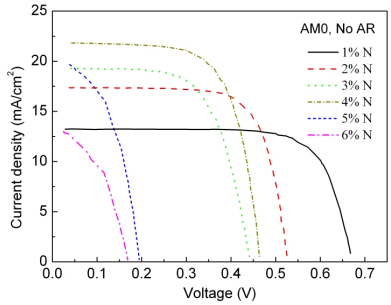

Figure 3: Light-biased current-voltage measurements for annealed GaInNAs/GaAs p-i-n diodes at AM0 simulation. No antireflection coating was applied on the samples.

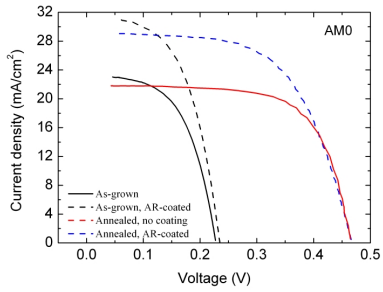

Figure 4: LIV characteristics of as-grown and annealed GaInNAs p-i-n diodes with and without AR-coatings compared at AM0 simulation.

related to annihilation of point defects or defect complexes in GaInNAs [2,6]. Also, phase separation and segregation effects are more probable at high temperatures leading finally to rough surfaces and poor crystal quality [12]. At low temperature side, high number of point defects is generated partially due to high group V flux [15,16] and lack of thermal energy for surface migration [10].

The effect of annealing on GaInNAs p-i-n diodes with 4% nitrogen is shown in Figure 4. We compared as-grown samples with and without standard 2-layer antireflection (AR) coating made of SiN_x/SiO_2 and samples with and without closely optimized annealing under AM0 simulation. The AR-coating increased the short circuit current density >30%. Annealing was found to drastically increase the V_{oc}. In annealed samples V_{oc} was doubled from ~0.23V to 0.47 V. The increase in I_{sc} can be linked to improvements in quantum efficiency whereas the improvement in V_{oc} upon annealing is related to reduction of number of defects characteristic to GaInNAs material [2].

After multiple optimization rounds of separate GaInNAs p-i-n diodes, we included a GaInNAs sub-junction within a GaInP/GaAs/GaInNAs 3-junction solar cell. The real one sun characteristics of the device are shown in Figure 5. The measured I_{sc} was 11.8 mA/cm^2. On the downside, the LIV measurement shows detrimental effects related to current mismatch between

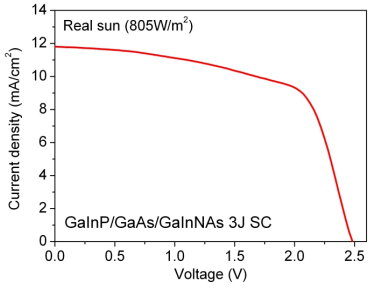

Figure 5: Real one-sun LIV-measurements of GaInP/GaAs/GaInNAs 3J solar cell. The measured light irradiance at the time of measurement was 805 W/m^2 based on a pyranometer reading [18].

the sub-junctions and carrier leakage. This was confirmed by shading 808 nm laser light on the structure to generate more current in the GaAs sub-cell.

Nevertheless, we have demonstrated a 3J solar cell with GaInNAs-containing subjunction which produces a current density of almost 12 mA/cm^2 without addition of Sb [17].

4 CONCLUSIONS

In conclusion, we report on optimization of GaInNAs material for multi-junction solar cells. GaInNAs materials and p-i-n solar cells with 1–6% nitrogen were studied. Fabrication of good quality GaInNAs material requires thermal annealing which reduces the number of defects in the material and causes growth parameter dependent blueshift. Optimized GaInNAs was used in a GaInP/GaAs/GaInNAs 3J solar cell to demonstate its capabilities for multi-junction devices. The short-circuit current of the 3J solar cell measured in outdoor conditions was almost 12 mA/cm^2.

5 ACKNOWLEDGEMENTS

This work was supported by the Finnish Funding Agency for Technology and Innovation (TEKES) project Solar III-V (#210024). A. Aho wants to thank National Graduate School in Materials Physcis for financial support.

6 REFERENCES

[1] Compound Semiconductor, July 2011, http://compoundsemiconductor.net/csc/features-details.php?cat=features&id=19733899, (15/08/2011)
[2] A. Khan, S. R. Kurtz, S. Prasad, S. W. Johnson, J. Gou, Applied Physics Letters, 90 (2007) 243509
[3] Z. Pan, L. H. Li, W. Zhang, Y. W. Lin, R. H. Wu, Applied Physics Letters, Vol. 77, No. 2 (2000)
[4] J. Neugebauer, C. G. Van de Walle, Physical Review B, Vol. 51, No. 16 (1995)
[5] D. Schlenker, T. Miyamoto, Z. Pan, F. Koyama, K. Iga, Journal of Crystal Growth, Vol. 196 (1999) 67-70
[6] S. R. Kurtz, S. W. Johnson, and H. M. Branz, Applied Physics letters, Vol. 86 (2005) 072109
[7] K. Voltz, D. Lackner, I. Nemeth, B. Kunert, W. Stolz, C. Baur, F. Dimroth, A. W. Bett, Journal of Crystal Growth Vol. 310 (2008) 2222-2228
[8] J. F. Geisz, D. J. Friedman, J. M. Olson, S. R. Kurtz and B. M. Keyes, Journal of Crystal Growth Vol. 195 (1998) 401–408
[9] D. Schlenker, T. Miyamoto, Z. Pan, F. Koyama, K. Iga, Journal of Crystal Growth, Vol. 196 (1999) 67-70
[10]Z. Pan, L. H. Li, W. Zhang, Y. W. Lin, R. H. Wu, Applied Physics Letters, Vol. 77, No. 2 (2000)
[11]E. Luna, A. Trampert, E-M Pavelescu, M. Pessa, New Journal of Physics, Vol. 9 (2007) 405
[12]J. –M. Chaveau, A. Trampert, K. H. Ploog, M. –A. Pinault, E. Tournie, Applied Physics Letters, Vol. 82, No. 20 (2003)
[13]W. M. McGee, R. S. Williams, M. J. Ashwin, T. S. Jones, E. Clarke, J. Zhang, S. Tomic, Physical

Review B Vol. 76 (2007) 085309
[14]S. Kurtz, J. Webb, L. Gedvilas, D. Friedman, J. Geisz, J. Olson, R. King, D. Joslin, N. Karam, Applied Physics letters, vol. 78 No. 6 (2006)
[15]E. S. Tok, J. H. Neave, J. Zhang, B. A. Joyce, T. S. Jones, Surface Science, Vol. 374 (1997) 397-405
[16]X. Liu, A. Prasad, J. Nishio, E.R. Weber, Z. Liliental-Weber, W. Walukiewicz, Appl. Phys. Lett. Vol. 67 (1995) 279
[17]D. B. Jackrel, S. R. Bank, H. B. Yuen, M. A. Wistey, J. S. Harris Jr., Journal of Applied Physics vol. 101 (2007) 114916
[18]http://webhotel2.tut.fi/units/set/research/solar/index.php (09/02/2011)

Publication 10

P10

Aho, A., Tukiainen, A., Polojärvi, V., Salmi J., & Guina, M., MBE Growth of High Current Dilute III-V-N Single and Triple Junction Solar Cells, European Photovoltaic Solar Energy Conference (2012), pp. 290-292.

MBE GROWTH OF HIGH CURRENT DILUTE III-V-N SINGLE AND TRIPLE JUNCTION SOLAR CELLS

Arto Aho, Antti Tukiainen, Ville Polojärvi, Joel Salmi, Mircea Guina
Tampere University of Technology, Optoelectronics Research Centre
Korkeakoulunkatu 3, FI-33720 Tampere, Finland.

ABSTRACT: We report on the optimization of growth temperature and As flux for fabrication of 1 eV GaInNAs solar cell using plasma assisted molecular beam epitaxy. Two sets of samples were grown at different temperatures and As beam equivalent pressures, keeping the As flux fixed in the first set and the growth temperature in the other. The p-i-n-solar cell structures were grown on n-GaAs(100) substrates. The output power exhibited a clear maximum within a narrow growth temperature and As pressure window. Based on this optimization, an AlInP-windowed GaInNAs p-i-n solar cell was grown on p-GaAs(100) substrate; the specific growth temperature was 440°C and the As/III beam equivalent pressure ratio was ~10. This solar cell exhibited a short circuit current density of ~29 mA/cm^2. Moreover, we demonstrated a GaInP/GaAs/GaInNAs triple junction solar cell that exhibited a short circuit current density of 12 mA/cm^2 under real sun illumination.

Keywords: III-V semiconductors, epitaxy, multijunction solar cell

1 Introduction

Multijunction solar cells (MJSC) produce efficiencies over 40% in concentrator applications [1]. Further improvement of MJSC efficiency requires development of a new sub-junction material to be combined with the conventional GaInP, GaAs and Ge semiconductors. An attractive option is the lattice matched 1 eV $Ga_{0.92}In_{0.08}N_{0.03}As_{0.97}$, so called dilute nitrides, which can improve the MJSC efficiency above 50% under concentrated sun light [2]. The GaInNAs material quality is however adversely affected by many material defects, which has so far led to poor MJSC current matching and low solar cell (SC) open circuit voltages (V_{oc}). Typically, the V_{oc} is smaller by about 0.2 V compared to ideal values and the external quantum efficiency (EQE) is below 0.5 [2, 3, 4]. In order to satisfy the current matching requirements for MJSC operation (i.e. short-circuit current densities >14 mA/cm^2) much higher quantum efficiencies are needed. To this end the limiting material property is the short carrier diffusion lengths arising from the defects [2].

The material defects in diluted nitrides can be categorized in two groups. At low temperature the growth is limited by point defect formation [5] while at high temperature the defect formation is mainly related to phase separation [6 ,7 ,8]. Growth related defects are also depended on the fabrication method. Metal organic chemical vapour deposition (MOCVD) suffers from carbon and hydrogen contamination, which both can significantly reduce the performance of GaInNAs solar cells [9]. On the other hand, the use of plasma-assisted molecular beam epitaxy (PAMBE) alleviates these issues but is not free of technological challenges, in particular related to stability of plasma sources and production of undesired N ions [10]. Overall, PAMBE is a more versatile growth method allowing to directly control the growth front related ordering by independently adjustable growth parameters. Therefore, the best GaInNAs SC results so far have been obtained using MBE [1, 11, 12].

In general, the GaInNAs SC material related defects can be engineered also by employing post-growth annealing [3, 9, 13] in addition to tuning the growth parameters [4, 8, 14]. Post growth thermal annealing leads to significant improvement of GaInNAs SC quality, which can be seen for instance as remarkable improvement of the V_{oc} [11]. When combined with appropriate growth parameters, annealing results in significant improvements of SC performance. One example is the demonstration of a 1 eV GaInNAs SC exhibiting a high V_{oc} of ~ 0.5 V [11, 15].

In this paper we present a systematic study focused on optimizing the growth parameters of GaInNAs SC, in particular concerning the effect of the growth temperature and As pressure.

2 Experiments

The solar cell structures were grown by PAMBE using Sumo cells for group III atoms, an RF plasma source for N, and valved crackers for As and P. The substrate native oxide was desorbed at 620°C and then an n-doped (Si) GaAs buffer layer was grown at 580°C on the n-GaAs(100) substrate to smooth the growth front. The GaAs buffer was followed by a 320 nm thick GaInNAs i-region. Two different sample sets were grown at growth temperatures ranging from 395°C to 490°C and As/III BEPs ranging from 5 to 20. As flux was kept fixed for the first set while the growth temperature was constant for the other. The GaInNAs regions were capped with 300 nm p-GaAs doped with Be.

After the growth, rapid thermal annealing (RTA) was carried out at 800°C for 300 s. The RTA was followed by processing of contacts using e-beam and shadow mask. Ni/Ge/Au metals were used as back contacts on the n-side. For the front side contact we used an Au/Ge top grid metal. The grid metal coverage was 25%, therefore in this paper we report only active area current densities and efficiencies.

The SCs were studied with light-biased current-voltage measurements (LIV) using a 1000 W solar simulator from Thermo Oriel equipped with an AM0 filter. The AM0 spectrum was further filtered using a 900 nm high pass filter to simulate the operation of the 1-eV junction inside a MJSC. After the measurements, the best growth parameters were combined in a AlInP-windowed GaInNAs single junction solar cell and a GaInP/GaAs/GaInNAs triple-junction solar cell, which

both were grown on p-GaAs(100) substrates. For comparison, we grew a GaInP/GaAs reference tandem SC using the same growth parameters as for the triple junction SC.

3 Results and discussion

The LIV measurements revealed a clear power optimum in a narrow growth temperature range, as shown in Fig. 1. We believe that near 440°C the combination of the intrinsic GaInNAs defects population enhances favourable the post growth annealing processes.

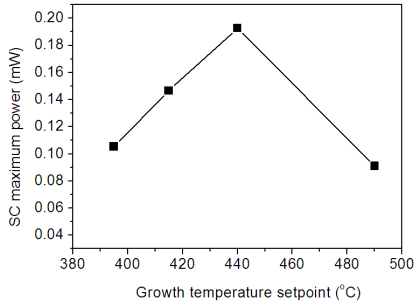

Figure 1: The maximum power for the GaInNAs SC as the function of the growth temperature. The best SC performance is achieved when the growth temperature was 440°C for the annealed samples.

We observed that the maximum power is highly sensitive to the As/III-ratio (see Fig. 2 below). These measurements are summarized in Fig. 2. Using a ratio between 8 and 10, we could achieve up to 3-times higher maximum power levels as compared to As/III ratio of 20. The lower limit for the As/III ratio was observed to be between 8 and 5. With an As/III ratio of 5 the SC performance can be considered poor and this is clearly too small value for the GaInNAs epitaxy even for an optimal growth temperature.

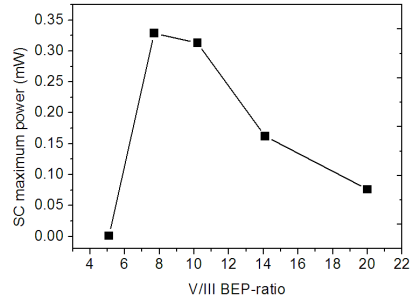

Figure 2: GaInNAs SC power as a function of the As/III BEP-ratio. The plotted SC power for each data point is an average of two annealed sample sets.

Following this optimization we have grown an AlInP-windowed p-i-n SC on p-GaAs(100) substrate. Specifically, we used a growth temperature of 440°C and an As/III BEP ratio of ~10. For this SC a short circuit current density (J_{SC}) of 29 mA/cm^2 was measured at AM1.5G. This measurement is presented in Fig. 3.

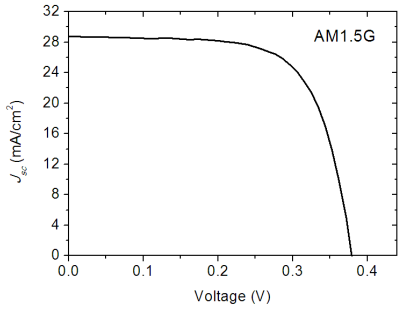

Figure 3: IV-characteristics of a GaInNAs p-i-n single junction SC with optimized growth parameters. The SC has an AlInP-window and SiO_2/SiN_x AR-coating.

The optimized p-i-n GaInNAs heterostructure was also incorporated into a GaInP/GaAs/GaInNAs triple junction SC. For this we have achieved a J_{SC} of 9 mA/cm^2 under AM1.5G simulation (see Fig. 4 below).

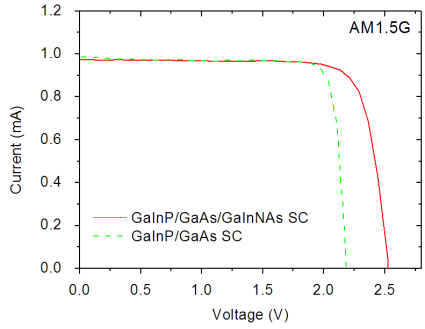

Figure 4: IV-characteristics of a GaInP/GaAs tandem and a GaInP/GaAs/GaInNAs triple junction SC with optimized GaInNAs growth. SCs are illuminated with simulated AM1.5G spectrum.

Table I lists the J_{sc}, V_{oc} and fill factor (*FF*) corresponding to AM1.5G measurements. It also shows how GaInP/GaAs and GaInP/GaAs/GaInNAs SCs are producing almost the same current, which indicates that adding GaInNAs sub-cell does not significantly limit the current in our multi-junction SC under AM1.5 simulated spectrum.

Table I: IV results for AM1.5G simulated spectrum

	J_{sc} (mA/cm^2)	V_{oc} (V)	*FF* (%)
GaInNAs	29	0.38	69
GaInP/GaAs	9	2.2	86
GaInP/GaAs/GaInNAs	9	2.5	81

The GaInP/GaAs/GaInNAs SC was also tested with real sun illumination. In this case, the current matching was not perfect (*FF*~70%), but the J_{sc} increased to 12 mA/cm^2. The illumination intensity was estimated by Kipp & Zonen CM11 pyranometer; both air mass and

illumination intensity were close to AM1.5 and 1000 W/m^2 [16]. We believe that with further optimization steps and current matching studies the SC efficiency can be significantly improved reaching the current matching target of ~14 mA/cm^2.

4 Conclusions

In summary, we have performed a PAMBE growth parameter optimization of 1 eV GaInNAs SC material. As a result we observed a rather narrow growth window with the optimum growth temperature of 440°C and the As/III BEP ratio of 10. With these growth parameters a high J_{SC} of 29 mA/cm^2 was demonstrated for the single junction p-i-n. A triple junction GaInP/GaAs/GaInNAs SC produced a J_{SC} of 12 mA/cm^2 with real sun illumination.

Acknowledgements

The authors would like to thank, Wenxin Zhang, Ville-Markus Korpijärvi and Pekka Malinen for their experimental support. For the financial support, we would like to thank Finnish Funding Agency for Technology and Innovation – TEKES (project 40120/09 Solar III-V), County Administrative Board of Oulu for ENNA Project (project number S11249), National Graduate School in Material Physics, Graduate School in Electronics, Telecommunications and Automation, Ulla Tuominen Foundation, Finnish Foundation for Technology Promotion, and Wärtsilä Foundation.

References

[1] A. Luque, J. of Appl. Phys., Will we exceed 50% efficiency in photovoltaics?, 110 (2011) 031301

[2] D. J. Friedman, J. F. Geisz, S. R. Kurtz, J. M. Olson, 1-eV solar cells with GaInNAs active layer, Journal of Crystal Growth, 195 (1998) 409-415

[3] A. Khan, S. R. Kurtz, S. Prasad, S. W. Johnson, J. Gou, Correlation of nitrogen related traps in InGaAsN with solar cell properties, Appl. Phys. Lett. 90 (2007) 243509

[4] J. Ptak, R. France, C.-S. Jieang, M. J. Romero, Improved performance of GaInNAs solar cells grown by molecular-beam epitaxy using increased growth rate instead of surfactants, Journal of Crystal Growth 311 (2009) 1876-1880

[5] X. Liu, A. Prasad, J. Nishio, E.R. Weber, Z. Liliental-Weber, Native point defects in low-temperature-grown GaAs, W. Walukiewicz, Appl. Phys. Lett. 67 (1995) 279

[6] J. Neugebauer, C. G. Van de Walle, Electronic structure and phase stability of GaAs1-*x*N*x* alloys, Phys. Rev. B, 51 (1995) 10 568-10 751

[7] D. Schlenker, T. Miyamoto, Z. Pan, F. Koyama, K. Iga, Miscibility gap calculation for Ga1−xInxNyAs1−y including strain effects, Journal of Crystal Growth 196 (1999) 67-70

[8] J. –M. Chaveau, A. Trampert, K. H. Ploog, M. –A. Pinault, E. Tournie, Interplay between the growth temperature, microstructure, and optical properties of GaInNAs quantum wells, Appl. Phys. Lett. 82 (2003) 3451

[9] K. Voltz, D. Lackner, I. Nemeth, B. Kunert, W. Stolz, C. Baur, F. Dimroth, A. W. Bett, Journal of Crystal Growth 310 (2008) 2222-2228

[10] M. M. Oye, T. J. Mattord, G. A. Hallock, S. R. Bank, M. A. Wistey, J. M. Reifsnider, A. J. Ptak, H. B. Yuen, J. S. Harris, Jr., and A. L. Holmes, Jr., Effects of different plasma species (atomic N, metastable N2*, and ions) on the optical properties of dilute nitride materials grown by plasma-assisted molecular-beam epitaxy, Appl. Phys. Lett. 91 (2007) 191903

[11] A. Aho, A. Tukiainen, V. Polojärvi, A. Gubanov, J. Salmi, M. Guina, P. Laukkanen, EU PVSEC 2011, 26th European Photovoltaic Solar Energy Conference and Exhibition, doi:10.4229/26thEUPVSEC2011-1AO.8.3 (2011)

[12] D. B. Jackrell, S. R. Bank, H. B. Yuen, M. A. Wistey, J. S. Harris Jr., Dilute nitride GaInNAs and GaInNAsSb solar cells by molecular beam epitaxy, J. Appl. Phys. 101 (2007) 114916

[13] S. Kurtz, J. Webb, L. Gedvilas, D. Friedman, J. Geisz, J. Olson, R. King, D. Joslin, N. Karam, Structural changes during annealing of GaInAsN, Appl. Phys. Lett. (2001)78 748

[14] E. –M. Pavelescu, T. Hakkarainen, V. D. S. Dhaka, N. V. Tkachenko, T. Jouhti, H. Lemmetyinen, M. Pessa, Influence of arsenic pressure on photoluminescence and structural properties of GaInNAs/GaAs quantum wells grown by molecular beam epitaxy, Journal of Crystal Growth 281(2005) 249-254

[15] J. Tommila, A. Aho, A. Tukiainen, V. Polojärvi, J. Salmi, T. Niemi and M. Guina, Prog. Photovolt: Res. Appl.. doi: 10.1002/pip.2191 (2012)

[16] Real sun measurement, Co-ordinates: 61.26°N, 23.51°E Date: 08.5.2012 Time: 15:00-16:00 (GMT+2), Solar zenith angle 54°, Temperature: ~14°C, Normal incidence

Publication 11

P11

Aho, A., Tukiainen, A., Polojärvi, V., & Guina, M., Dilute Nitride Space Solar Cells: Towards 4 Junctions, 10th European Space Power Conference ESPC 2014, 13-17 April, 2014, Noordwijkerhout, the Netherlands, vol. 719 (2014), pp. 1-3.

DILUTE NITRIDE SPACE SOLAR CELLS: TOWARDS 4 JUNCTIONS

Arto Aho, Antti Tukiainen, Ville Polojärvi and Mircea Guina

Optoelectronics Research Centre, Tampere University of Technology
FIN-33101, Tampere, Finland, Email:arto.j.aho@tut.fi

ABSTRACT

The use of 1 eV band gap GaInNAs heterostructures is an important step towards the development of monolithic solar cells with more than three junctions. We report current-voltage and external quantum efficiency characteristics of GaInNAs single-junction solar cells. Using known characteristics for standard double and triple-junction solar cells, we estimate the AM0 efficiency for GaInP/GaAs/GaInNAs and GaInP/GaAs/GaInNAs/Ge solar cells. The improvement in conversion efficiency upon adding the 1 eV GaInNAs sub-junction would correspond to at least 3 percentage points compared to state-of-the-art GaInP/GaAs and GaInP/GaAs/Ge solar cells.

1. INTRODUCTION

The development of GaAs based materials is currently reaching a level at which the triple junction solar cells (SC) are highly optimized and the AM0 beginning-of-life conversion efficiencies are leveling at ~30% [1]. The efficiency can be further increased by using lattice-matched ~1 eV band gap GaInNAs(Sb) and 1.4-2.0 eV (AlGaInAsP) materials to form 4-6 junctions [2]. The drawback in using GaInNAs(Sb) are related to challenges in material fabrication [3, 4] and defect population control [5]. Both these challenges easily lead to poor current generation [6] and low open circuit voltages [2]. However, recent development steps in molecular beam epitaxy (MBE) of dilute nitride SCs have overcome the most critical performance limits [7, 8, 9] and led to demonstration of record conversion efficiencies [10]. In this paper, we focus on evaluating the characteristics of GaInNAs SCs grown by MBE. Based on the experimental results we estimate the performance rendered possible by GaInNAs materials, when used in four-junction solar cells operating at AM0 conditions.

2. EXPERIMENTS

The structures consisted of a single junction GaInNAs p-i-n and a triple junction GaInP/GaAs/GaInNAs SC. Both GaInNAs junctions had a 1 eV band gap and thickness of 1.3 µm. The SC structures were fabricated by solid source MBE equipped with an RF plasma source for incorporation of atomic nitrogen. The layers were grown on p-GaAs(100) substrates and the wafers were processed into 4x4 mm^2 solar cells. TiAu and NiGeAu were used for contacts, on p- and n-side, respectively. The metal finger patterns were made using photolithography. The structures were antireflection (AR) coated with TiO_x/SiO_x. More detailed information about the SCs and fabrication is provided elsewhere [3, 8, 9]. The current-voltage (I-V) characteristics were measured using real sun conditions at light intensities close to 1000 W/m^2 and air masses close to 1.5. During the real sun measurements the temperature of the SCs was 300 K. The external quantum efficiency (EQE) was measured using a system incorporating a halogen lamp, a monochromator, lock-in technique, and Si and Ge reference cells. For the diode curve fitting and efficiency calculation, we used diode equations for multijunction solar cells [11] and the current density limits corresponding to band gaps of GaInP, GaAs, GaInNAs and Ge at AM0 excitation [12].

3. RESULTS AND DISCUSSION

The EQE of the GaInNAs cell is shown in Fig. 1a. From the EQE the estimated short circuit current density (J_{sc}) at AM1.5G conditions is 36.8 mA/cm^2, for the full spectrum excitation, and 11.2 mA/cm^2 when light is filtered by GaAs. The corresponding J_{sc} values for AM0 ASTM E490 are 45.2 mA/cm^2 and 14.1 mA/cm^2, respectively.

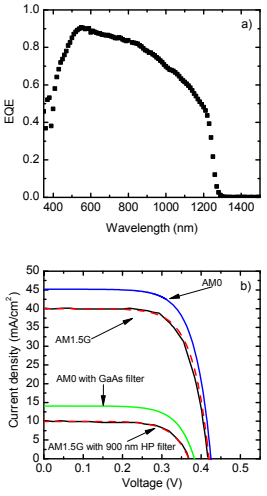

Figure 1. a) EQE measurement of a single junction GaInNAs device. b) Single junction GaInNAs solar cell performance under AM1.5G excitation, fitted diode equations, and estimated I-V-curves for the AM0 ASTM E490 excitation.

The measured I-V-characteristics of a single junction GaInNAs SC with and without a 900 nm long-pass filter at AM1.5G excitation are presented in Fig. 1b. Based on the EQE and using a simple diode model to fit the AM1.5G I-V-characteristics, we also calculated the AM0 performance of this device with and without long-pass filter (Fig. 1b). The AM0 saturation current (I_0) and the ideality factor (n) values were taken from the fitted AM1.5G diode curves. The AM0 generation currents were calculated from EQE. The measured and calculated I-V-results and fitting parameters for the single GaInNAs junction are summarized in Tab. 1.

Table 1. The I-V-results and fitting parameters for GaInNAs SC at different excitations.

Spectrum	I_{sc} (mA/cm2)	V_{oc} (V)	*FF*	η	I_0 (mA/cm²)	*n*
AM1.5G	39.9	0.416	70 %	11.6 %	1.2×10^{-3}	1.55
AM1.5G with 900 nm HP filter	10.0	0.368	69 %	2.5 %	1.2×10^{-3}	1.58
AM0 estimation	45.2	0.424	70 %	9.9 %	1.2×10^{-3}	1.55
AM0 estimation with GaAs filter	14.1	0.383	69 %	2.7 %	1.2×10^{-3}	1.58

The performance of the GaInP/GaAs/GaInNAs cell is compared against an un-optimized double junction SC in Fig. 2a. The real sun AM1.5G measurements at 1000 W/m^2 reveal that the triple junction cell is current limited by GaInNAs to 12 mA/cm^2. The fill factors (*FF*) of the double and triple junction SCs are 82% and 76%, respectively. The open circuit voltage (V_{oc}) increase, owing to incorporation of GaInNAs, was 0.42 V.

The potential of the GaInNAs for developing multijunction SCs was then analyzed by using the obtained fitting parameters and assuming state-of-the-art double-junction GaInP/GaAs and triple-junction GaInP/GaAs/Ge SCs as a starting point. The AM0 I–V characteristics of current-matched SCs were calculated for J_{sc} =14.1 mA/cm^2 (corresponds to the measured GaInNAs SCs) and J_{sc}=17.7 mA/cm^2 (the condition at which current matching would be fulfilled for state-of-the-art SC). Estimation was based on the characteristics given in [1] and [13] and the diode equations given in [11]. The results of the calculations are shown in Fig. 2b and Tab. 2. To fulfil the current matching requirement of J_{sc}=17.7 mA/cm^2 by using 1 eV GaInNAs an average EQE of ~90% is needed.

Table 2: Performance of reference SCs (red background) and estimated performance for GaInP/GaAs/GaInNAs (light blue) and GaInP/GaAs/GaInNAs/Ge (dark blue) SCs.

Structure	J_{sc} (mA/cm2)	V_{oc} (V)	*FF*	η (%)	Reference
GaInP/GaAs	16.85	2.451	0.88	26.9	[13]
GaInP/GaAs/Ge	17.7	2.746	0.86	30.6	[1]
GaInP/GaAs/GaInNAs	14.1	2.849	0.87	25.6	[This work, 1]
GaInP/GaAs/GaInNAs	17.7	2.861	0.83	30.7	[This work, 1, 13]
GaInP/GaAs/GaInNAs/Ge	14.1	3.134	0.87	28.1	[This work, 1]
GaInP/GaAs/GaInNAs/Ge	17.7	3.144	0.82	33.5	[This work. 1]

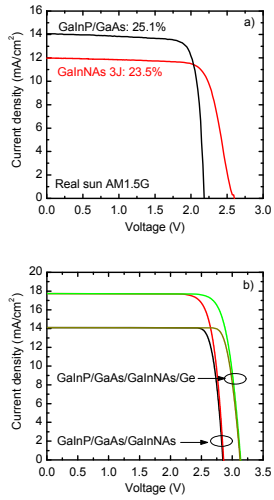

Figure 2: a) Measured I-V-curves for GaInP/GaAs and GaInP/GaAs/GaInNAs. b) Estimated performance for multijunction dilute nitride solar cell at AM0 based on GaInNAs junction reported here and the literature data for GaInP/GaAs and GaInP/GaAs/Ge SCs [1],[13].

The calculations show that by adding the 1 eV GaInNAs junction the efficiency of double and triple-junction SC can be increased by ~3 percentage points assuming current matching. However, in the four-junction structure, the EQEs for 1 eV GaInNAs and Ge junctions would need to be over 93% throughout the whole cell absorption spectral range. The absolute improvement can be even higher than 3 percentage points, since the GaInNAs SC used in the calculations did not have the highest open circuit voltage; it was chosen because of the best J_{sc} [8]. We believe that with further optimization we can get up to ~0.10 V higher V_{oc} for GaInNAs junctions. This and FF improvements can lead to additional 1-3 percentage points gain in efficiency at AM0.

4. CONCLUSIONS AND FUTURE WORK

We have fabricated GaInNAs single and GaInP/GaAs/GaInNAs triple-junction SCs which were measured at AM1.5G. Using the measured EQE, I-V characteristics at AM1.5G, and a diode model we estimated the behaviour of the GaInNAs junction at AM0 conditions. The data was then used to assess the potential of using the GaInNAs sub-junction as a part of triple and four-junction solar cells. If the average EQE of GaInNAs junction can be increased to ~90%, the efficiency of state-of-the-art triple-junction and four-junction SCs could be increased by at least 3 percentage points. Our future work aims at improving the performance of standard GaInP/GaAs cell, the EQE of

the GaInNAs SC, and to reduce the open circuit voltage band gap offset. Our preliminary results has indicated that the ~90% average EQE for a dilute nitride SC is a feasible target. These optimizations should lead to conversion efficiencies of >35% at AM0 with four-junction SCs.

5. Acknowledgements

The authors acknowledge the financial support provided by the Finnish Funding Agency for Technology and Innovation, Tekes (projects 'Solar III-V' #40120/09 and 'Nextsolar' #40239/12), and the European Space Agency (project Contract N.: 4000108058/13/NL/FE). A. Aho acknowledges support received from the Graduate School in Electronics, Telecommunications and Automation, Wärtsilä Foundation, Finnish Foundation for Technology Promotion, and Ulla Tuominen Foundation for financial support. The authors also acknowledge Dr. Juha Tommila, Wenxin Zhang, BSc Joel Salmi and BSc Pekka Malinen for their technical support.

6. REFERENCES

1. Bett, A. W., Dimroth, F., Guter, W., Hoheisel, R., Oliva, E., Phillips, S. P., Schöne, J., Siefer, G., Steiner, M., Wekkeli, A., Welser, E., Meusel, M., Köstler, W. & Strobl, G. (2009). Highest Efficiency Multi-Junction Solar Cell for Terrestrial and Space Applications, '*24th European Photovoltaic Solar Energy Conference and Exhibition*', Hamburg, Germany, pp1-6

2. King, R. R., Sherif, R. A., Kinsey, G. S., Kurtz, S., Fetzer, C. M., Edmondson, K. M., Law, D. C., Cotal, H. L., Krut, D. D., Ermer, J. H. & Karam, N. H. (2005). Bandgap Engineering in High-Efficiency Multijunction Concentrator Cells, '*Internaltional Conference on Solar Concentrators for the Generation of Electricity or Hydrogen*', Scottsdale, Arizona, USA, NREL/CD-520-38172

3. Aho, A., Tukiainen, A., Polojärvi, V., Gubanov, A., Salmi, J., Guina, M. & Laukkanen, P. (2011). Lattice Matched Dilute Nitride Materials for III-V High-Efficiency Multi-Junction Solar Cells: Growth Parameter Optimization in Molecular Beam Epitaxy, '*EU PVSEC 2011, 26th European Photovoltaic Solar Energy Conference and Exhibition*', Hamburg, Germary, pp58-61 doi:10.4229/26thEUPVSEC2011-1AO.8.3.

4. Luna, E., Trampert, A., Pavelescu, E.-M. & Pessa, M. (2007). Nitrogen-enhanced indium segregation in (Ga,In)(N,As)/GaAs multiple quantum wells grown by molecular-beam epitaxy, *New J. Phys.* **9** (405)

5. Khan, A., Kurtz, S. R., Prasad, S., Johnson, S. W. & Gou, J. (2007). Correlation of nitrogen related traps in InGaAsN with solar cell properties, *Appl. Phys. Lett.* **90**(243509)

6. Geisz, J. F., Friedman, D. J., Olson, J. M., Kurtz, S. R. & Keyes, B. M. (1998). Photocurrent of 1 eV GaInNAs latticematched to GaAs, *J. of Crystal Growth* **195,** pp401-408

7. Jackrell, D. B., Bank, S. R., Yuen, H. B., Wistey, M. A. & Harris Jr., J. S. (2007). Dilute nitride GaInNAs and GaInNAsSb solar cells by molecular beam epitaxy, *J. Appl. Phys.* **101**(114916)

8. Aho, A., Tukiainen, A., Polojärvi, V., Salmi, J. & Guina, M. (2013). High current generation in dilute nitride solar cells grown by molecular beam epitaxy. '*Proc. SPIE* **8620**, *Physics, Simulation, and Photonic Engineering of Photovoltaic Devices II*', San Francisco, USA, 86201I doi:10.1117/12.2002972

9. Aho, A., Tukiainen, A. , Polojärvi, V. , Salmi, J. & Guina, M. (2012). MBE Growth of High Current Dilute III-V-N Single and Triple Junction Solar Cells, '*EU PVSEC 2011, 27th European Photovoltaic Solar Energy Conference and Exhibition*', Frankfurt, Germany, pp290-292, 10.4229/27thEUPVSEC2012-1BV.7.13

10. Wiemer, M., Sabnis, V. & Yuen, H. (2011). 43.5% efficient lattice matched solar cells, '*Proc. SPIE **8108**, High and Low Concentrator Systems for Solar Electric Applications VI*', 810804, doi:10.1117/12.897769

11. King, R. R., Bhusari, D., Boca, A., Larrabee, D., Liu, X-Q., Hong, W., Fetzer, C. M., Law, D. C. & Karam, N. H. (2011). Band gap-voltage Offset and Energy Production in Next-generation Multijuntion Solar Cells, *Prog. Photovolt: Res. Appl.*; **19**, pp797-812, doi:10.1002/pip.1044

12. Friedman, D. J. & Kurtz, S. R. (2002). Breakeven Criteria for the GaInNAs Junction in GaInP/GaAs/GaInNAs/Ge Four-Junction Solar Cells, *Prog. Photovolt: Res. Appl.*; **10**, pp331-344, doi: 10.1002/pip.430

13. Takamoto, T., Ikeda, E., Kurita, H. & Ohmori, M. (1997). Over 30% efficient InGaP/GaAs Tandem Solar Cell, *Appl. Phys. Lett.* **70**, 381, doi:10.1060/1.118419

Tampereen teknillinen yliopisto
PL 527
33101 Tampere

Tampere University of Technology
P.O.B. 527
FI-33101 Tampere, Finland

ISBN 978-952-15-3613-7
ISSN 1459-2045